

**The Development of a Droplet Formation and Entrainment
Model for Simulations of Immiscible Liquid-Liquid Flows**

By

Wesley M. Wilson

A THESIS

**Submitted to
The College of Engineering and Mineral Resources
at
West Virginia University**

**in partial fulfillment of the requirements
for the degree of**

**Master of Science
in
Mechanical Engineering**

**Dr. Ismail Celik, Committee Chair
Dr. John Kuhlman
Dr. Nigel Clark**

Department of Mechanical and Aerospace Engineering

**Morgantown, West Virginia
1999**

Keywords: droplet formation, turbulent mixing, shear flow, droplet size, buoyant jet

Report Documentation Page

*Form Approved
OMB No. 0704-0188*

Public reporting burden for the collection of information is estimated to average 1 hour per response, including the time for reviewing instructions, searching existing data sources, gathering and maintaining the data needed, and completing and reviewing the collection of information. Send comments regarding this burden estimate or any other aspect of this collection of information, including suggestions for reducing this burden, to Washington Headquarters Services, Directorate for Information Operations and Reports, 1215 Jefferson Davis Highway, Suite 1204, Arlington VA 22202-4302. Respondents should be aware that notwithstanding any other provision of law, no person shall be subject to a penalty for failing to comply with a collection of information if it does not display a currently valid OMB control number.

1. REPORT DATE 1999	2. REPORT TYPE	3. DATES COVERED 00-00-1999 to 00-00-1999	
4. TITLE AND SUBTITLE The Development of a Droplet Formation and Entrainment Model for Simulation of Immiscible Liquid-Liquid Flows		5a. CONTRACT NUMBER	
		5b. GRANT NUMBER	
		5c. PROGRAM ELEMENT NUMBER	
6. AUTHOR(S)		5d. PROJECT NUMBER	
		5e. TASK NUMBER	
		5f. WORK UNIT NUMBER	
7. PERFORMING ORGANIZATION NAME(S) AND ADDRESS(ES) West Virginia University, Department of Mechanical and Aerospace Engineering, Morgantown, WV, 26506		8. PERFORMING ORGANIZATION REPORT NUMBER	
9. SPONSORING/MONITORING AGENCY NAME(S) AND ADDRESS(ES)		10. SPONSOR/MONITOR'S ACRONYM(S)	
		11. SPONSOR/MONITOR'S REPORT NUMBER(S)	
12. DISTRIBUTION/AVAILABILITY STATEMENT Approved for public release; distribution unlimited			
13. SUPPLEMENTARY NOTES			
14. ABSTRACT			
15. SUBJECT TERMS			
16. SECURITY CLASSIFICATION OF:			17. LIMITATION OF ABSTRACT Same as Report (SAR)
a. REPORT unclassified	b. ABSTRACT unclassified	c. THIS PAGE unclassified	
19a. NAME OF RESPONSIBLE PERSON			

ABSTRACT

The Development of a Droplet Formation and Entrainment Model for Simulations of Immiscible Liquid-Liquid Flows

Wesley M. Wilson

Droplet formation is a common phenomenon in turbulent mixing and has many practical applications in emulsion technology, surface agents, and liquid-liquid extraction. The ability to predict the relative sizes and distributions of fluid droplets formed from mixing events is a complex problem which is dependent on many different parameters including geometric considerations, the nature and physical properties of the fluids in question, turbulence parameters, buoyancy and body forces, and flow history. While there have been many researchers who have analyzed this problem for both liquid-liquid and gas-liquid systems, the present study will focus only on droplet formation in immiscible liquid-liquid systems.

A review of the literature has shown that previous attempts at describing fluid droplet sizes essentially fall into two categories: (1) phenomenological models, and (2) statistical models. The use of phenomenological models usually involves semi-empirical analyses of a particular liquid-liquid or gas-liquid system, and typically employs a force balance to determine the conditions under which droplet formation or breakage occurs. Statistical models, on the other hand, utilize flow history and probability density functions (PDF's) to determine the size and number distribution of daughter droplets formed from the splitting of larger droplets or the coalescence of smaller ones. In the present study we will adopt many of the methods of the former set of models, resulting in expressions which determine the sizes of the dispersed phase droplets based on local flow parameters including turbulence quantities, appropriate characteristic length scales, and dimensionless parameters such as the gradient Richardson number. While much of the development of the droplet formation/entrainment (DFE) model comes from results from the literature concerning stratified shear flows, the model can be calibrated through the adjustment of certain constants to conform to a wide variety of flow scenarios.

The present study is one element of a larger effort in cooperation with engineers and naval architects at the Naval Surface Warfare Center - Carderock Division (NSWC-CD) in Bethesda, Maryland, as well as faculty and students at Johns Hopkins University in Baltimore, Maryland, to study turbulent mixing events in compensated fuel/ballast tanks used in U.S. naval surface ships. The overall goal of this project at WVU is to develop sub-models for the prediction of the extent and location of mixing of fuel and water, and to estimate the total flow-through time for the fuel, as well as the amount of water-hideout. Water hideout involves the amount of water that remains inside the fuel tanks after refueling is complete (i.e. when the fuel stream reaches the outlet), and presents a concern with regard to efficiency. The fuel/water mixing, on the other hand, represents an environmental concern, as some of the fuel may become entrained in the

compensating water that is forced overboard during refueling. The prediction of the size and distribution of the fuel droplets that form during mixing is an integral part of the overall effort, both for accurate predictions of mixing events, as well as in estimating the amount of fuel entrainment that occurs.

Numerical simulations have been performed at West Virginia University using the commercial CFD (Computational Fluid Dynamics) code, CFX-4, developed by AEA Technologies, to assess the performance of the droplet formation/entrainment model for several different flow configurations. These include a stratified shear flow of two immiscible fluids of different densities, and a densely buoyant vertical jet flow of a higher density fluid impinging on a quiescent layer of lighter fluid. The multiphase model used in these simulations was a single fluid, scalar transport (SFST) model, which is a mixture model based on Ishii's drift flux model [22]. The turbulence model used was a modified form of the standard k- ϵ model that includes additional terms to account for the effects of buoyant production/destruction.

Both of the flow scenarios in question closely match the conditions for experiments currently being performed at Johns Hopkins University by Dr. Joseph Katz and his associates. In this study, the results of the numerical simulations will be compared with qualitative observations from the experiments, as well as certain quantitative data collected with regard to the mixing length thickness in the case of the shear flow, and the maximum impingement depth in the case of the jet flow study. The results of these simulations indicate logical trends for the size and distribution of the fluid droplets formed, as well as good agreement between the DFE model and the results of the experiments detailed above.

Acknowledgements

I would like to extend my appreciation and my thanks to all those who contributed to the completion of this work. First, I would like to thank my committee members, Dr. John Kuhlman and Dr. Nigel Clark, whose instructive comments and assistance is greatly appreciated. I would also like to acknowledge the support of engineers and naval architects at the Naval Surface Warfare Center - Carderock Division (NSWC-CD) in Bethesda, Maryland, namely Dr. Peter Chang and Brian Hill. The assistance and experimental data provided by Xiongjun Wu and Peter Friedman, who work under the direction of Dr. Joe Katz at Johns Hopkins University, is also greatly appreciated.

To the other members of the CFD group at West Virginia University, I thank you for your friendship and wish you luck in your respective endeavors. A special thanks is given to Matthew Umbel, who provided much of the groundwork for this project, and whose assistance has been invaluable.

A special thanks is also extended to my advisor, Dr. Ismail Celik, without whose guidance and instruction this present work could not have been accomplished. He has proven to be a competent researcher and advisor, showing both an extensive knowledge of the subject matter and a willingness to provide whatever aid is required.

Finally, I wish to thank my wife, Christy, whose patience and understanding has been sorely tested at times, but whose love has withstood this long and intensive process.

Table of Contents

	Page
ABSTRACT.....	ii
Acknowledgements	iv
Table of Contents	v
List of Tables.....	viii
List of Figures	ix
Nomenclature	xiv
1.0 INTRODUCTION	1
1.1 Background Information.....	1
1.2 Objectives	11
1.3 Overview	12
2.0 REVIEW OF THE LITERATURE	15
2.1 Introductory Definitions and Comments.....	15
2.2 Review of Literature for Stratified Shear Flows	22
2.3 Review of Literature for Vertical Buoyant Jet Flows	30
2.4 Review of Literature for Droplet Formation and Breakage	35
3.0 DESCRIPTION OF VARIOUS MATHEMATICAL MODELS	41
3.1 SFST Model Formulation for Immiscible Fluids	41
3.2 k- ϵ Turbulence Model for Buoyant Flows	47
3.3 Empirical Correlation for the Slip Velocity.....	49
4.0 MASS CONSERVATION IN THE SFST MODEL	53
4.1 Validation and Case Specific Issues.....	53

4.2 Summary and Conclusions.....	65
5.0 DERIVATION OF DROPLET FORMATION/ENTRAINMENT MODEL	67
5.1 Description of Flow Regimes.....	68
5.2 Flow Regime Boundaries.....	70
5.3 Model Equations	72
5.4 Verification of the DFE Model	81
6.0 SFST MODEL PREDICTIONS FOR STRATIFIED SHEAR FLOWS	93
6.1 Experimental Conditions Simulated.....	93
6.2 Computational Details	95
6.3 Results and Discussion.....	99
7.0 SFST MODEL PREDICTIONS FOR VERTICAL BUOYANT JET FLOWS	143
7.1 Experimental Conditions Simulated.....	143
7.2 Computational Details	145
7.3 Results and Discussion.....	148
8.0 CONCLUSIONS.....	157
8.1 Summary	157
8.2 Recommendations for Future Work.....	160
BIBLIOGRAPHY	166
APPENDIX A: DERIVATION AND EQUATIONS FOR THE SFST MODEL.....	170
A.1: Complete Set of Equations for the SFST Model.....	170
A.2: New Formulation for Solution of the Volume Fraction.....	172
A.3: Alternative Empirical Correlation for the Slip Velocity	176
APPENDIX B: DOCUMENTATION FOR THE SFST MODEL	177

B.1 Introduction	177
B.2 Overview	177
B.3 Configuring the CFX Files for the SFST Model.....	178
B.3.1 The Geometry File	178
B.3.2 The Command File	179
B.3.3 User FORTRAN implementation of the SFST and DFE Models	183
Appendix C: Details on Shear Flow Data Reduction Program.....	212

List of Tables

	Page
Table 5.1 - Flow Regime Boundaries for DFE Model.....	72
Table 5.2 - DFE Model Equations for Different Flow Regimes.....	79
Table 5.3 - General Model Expressions for the Droplet Diameter	80
Table 6.1 – Boundary Conditions and Overall Parameters for CFX model.....	98
Table 6.2 – Model Coefficients in Calibrated DFE Model.....	126
Table 7.1 – Inlet Parameters for Impinging Jet Experiments	148

List of Figures

	Page
Figure 1.1 - Geometry of typical compensated fuel ballast tank (CFBT).	2
Figure 1.2 - Volume fraction and velocity vectors (manhole - two-compartment tank) at time = 15.0 seconds (HMP).	6
Figure 1.3 - Volume fraction and velocity vectors (manhole - two-compartment tank) at time = 15.0 Seconds (SFST).	6
Figure 4.1 - Schematic of two-dimensional test case geometry.	54
Figure 4.2 – Comparison of predicted fuel volume using upwind and MIN-MOD schemes.	57
Figure 4.3 – Errors in predicted fuel volume using upwind and MIN-MOD schemes. ...	58
Figure 4.4 – Comparison of variations in predicted fuel volume with time (laminar flow case).	59
Figure 4.5 – Errors in predicted fuel volume as a function of time (laminar flow case)..	60
Figure 4.6 – Comparison of variations in predicted fuel volume with time (turbulent flow case).	61
Figure 4.7 – Errors in predicted fuel volume as a function of time (turbulent flow case).	62
Figure 4.8 – Wireframe sketch of two-compartment geometry.	63
Figure 4.9 – Predicted variations in fuel volume with time (3-D turbulent flow case). ...	64
Figure 4.10 – Errors in predicted fuel volume vs. time (3-D turbulent flow case).	65
Figure 5.1 - Wireframe sketch of two-compartment tank geometry.	81
Figure 5.2 - Volume fraction (inlet - front view) at t = 15.0 sec.	84
Figure 5.3 - Velocity vectors (inlet - front view) at t = 15.0 sec.	84

Figure 5.4 - Droplet diameter (inlet - front view) - large scale at $t = 15.0$ sec.	85
Figure 5.5 - Droplet diameter (inlet - front view) - small scale at $t = 15.0$ sec.	85
Figure 5.6 - Volume fraction (manhole - front view) at $t = 15.0$ sec.	86
Figure 5.7 - Velocity vectors (manhole - front view) at $t = 15.0$ sec.	86
Figure 5.8 - Droplet diameter (manhole - front view) - large scale at $t = 15.0$ sec.	87
Figure 5.9 - Droplet diameter (manhole - front view) - small scale at $t = 15.0$ sec.	87
Figure 5.10 - Volume fraction (exit - front view) at $t = 15.0$ sec.	88
Figure 5.11 - Velocity vectors (exit - front view) at $t = 15.0$ sec.	88
Figure 5.12 - Droplet diameter (exit - front view) - large scale at $t = 15.0$ sec.	89
Figure 5.13 - Droplet diameter (exit - front view) - small scale at $t = 15.0$ sec.	89
Figure 5.14 - Volume fraction (top view - $y = H/2$) at $t = 15.0$ sec.	90
Figure 5.15 - Velocity vectors (top view - $y = H/2$) at $t = 15.0$ sec.	90
Figure 5.16 - Droplet diameter (top view - $y = H/2$) - large scale at $t = 15.0$ sec.	91
Figure 5.17 - Droplet diameter (top view - $y = H/2$) - small scale at $t = 15.0$ sec.	91
Figure 6.1 – Johns Hopkins shear flow experimental setup.	94
Figure 6.2 – Johns Hopkins shear flow geometry used in CFX.	96
Figure 6.3 – Comparison of south cell face source term with boundedness checks; $Ri^*=0.7, d_p=2mm$	102
Figure 6.4 – Comparison of north cell face source term with boundedness checks; $Ri^*=0.7, d_p=2mm$	103
Figure 6.5 – Volume fraction contours; $Ri^* = 0.7, d_p = 6mm$	105
Figure 6.6 – Streamlines and volume fraction contours; $Ri^* = 0.7, d_p = 6mm$	106
Figure 6.7 – Volume fraction contours; $Ri^* = 0.7, d_p = 2mm$	107

Figure 6.8 – Streamlines and volume fraction contours; $Ri^* = 0.7$, $d_p = 2\text{mm}$	108
Figure 6.9 – Volume fraction contours; $Ri^* = 0.32$, $d_p = 6\text{mm}$	109
Figure 6.10 – Streamlines and volume fraction contours; $Ri^* = 0.32$, $d_p = 6\text{mm}$	110
Figure 6.11 – Volume fraction contours; $Ri^* = 0.32$, $d_p = 2\text{mm}$	111
Figure 6.12 – Streamlines and volume fraction contours; $Ri^* = 0.32$, $d_p = 2\text{mm}$	112
Figure 6.13 – Mixed fluid thickness vs. normalized downstream distance for varying droplet diameter; $Ri^*=0.7$	113
Figure 6.14 – Mixed fluid thickness vs. normalized downstream distance for varying droplet size; $Ri^* = 0.32$	114
Figure 6.15 – Mixed fluid thickness vs. normalized downstream distance; $Ri^*=0.7$, $d_p =$ 4mm (influence of σ_ϕ).	116
Figure 6.16 – Mixed fluid thickness vs. normalized downstream distance; $Ri^*=0.32$, $d_p=4\text{mm}$ (influence of σ_ϕ).	117
Figure 6.17 – Mixed fluid thickness vs. normalized downstream distance; $Ri^*=0.7$ (influence of grid refinement).	120
Figure 6.18 – Mixed fluid thickness vs. normalized downstream distance; $Ri^*=0.32$ (influence of grid refinement).	121
Figure 6.19 – Instantaneous mixing layer near water inlet; After Wu and Katz [38].	122
Figure 6.20 – Instantaneous mixing layer near central section; After Wu and Katz [38].	123
Figure 6.21 – Instantaneous mixing layer near fuel inlet diffuser; After Wu and Katz [38].	124

Figure 6.22 – Volume fraction contours; $Ri^* = 0.7$, $d_p = \text{variable}$	127
Figure 6.23 – Volume fraction contours and streamlines; $Ri^* = 0.7$, $d_p = \text{variable}$	128
Figure 6.24 – Normalized droplet diameter with volume fraction; $Ri^* = 0.7$, $x/L = 0.25$	129
Figure 6.25 – Normalized droplet diameter with volume fraction; $Ri^* = 0.7$, $x/L = 0.5$	130
Figure 6.26 – Normalized droplet diameter with volume fraction; $Ri^* = 0.7$, $x/L = 0.75$	131
Figure 6.27 – Volume fraction contours; $Ri^* = 0.32$, $d_p = \text{variable}$	133
Figure 6.28 – Volume fraction contours and streamlines; $Ri^* = 0.32$, $d_p = \text{variable}$	134
Figure 6.29 – Normalized droplet diameter with volume fraction; $Ri^*=0.32$, $x/L = 0.25$	135
Figure 6.30 – Normalized droplet diameter with volume fraction; $Ri^* = 0.32$, $x/L = 0.5$	136
Figure 6.31- Gradient Richardson number profiles; $Ri^* = 0.7$, $d_p = \text{variable}$	138
Figure 6.32 – Gradient Richardson number profiles; $Ri^* = 0.32$, $d_p = \text{variable}$	139
Figure 6.33 – Mixed fluid thickness vs. normalized downstream distance; $Ri^* = 0.7$, $d_p =$ variable.....	140
Figure 6.34 – Mixed fluid thickness vs. normalized downstream distance; $Ri^*=0.32$, $d_p =$ variable.....	141
Figure 7.1 - Fuel impingement experimental test facility, after Friedman & Katz [17].	144

Figure 7.2 - Schematic of computational geometry used to model the impinging jet facility.	145
Figure 7.3 – Comparison of results for normalized maximum vertical penetration as a function of the interface Richardson number.....	150
Figure 7.4 – Volume fraction contours; $Ri^* = 0.21$, $d_p = \text{variable}$	151
Figure 7.5 – Instantaneous image of impinging jet facility for $Ri^* = 0.21$; after Friedman and Katz [17].....	152
Figure 7.6 – Comparison of predicted aspect ratio with experimental results [17]......	153
Figure 7.7 – Droplet diameter contours; $Ri^* = 0.21$	155
Figure 8.1 – Typical Kelvin-Helmholtz shear layer instability.	161

Nomenclature

English

d	Droplet diameter
d_p	Droplet diameter
D	Jet diameter
D_c	Critical droplet diameter
F	Densimetric Froude number
g	Acceleration due to gravity
h	Concentration boundary layer thickness
h	Mean mixed layer depth
h_s	Maximum velocity gradient thickness
k	Specific turbulent kinetic energy
Pe	Peclet number
Pr	Prandtl number
r	Volume fraction
R	Ratio of unmixed phase densities (i.e. ρ_α/ρ_β)
R_{noz}	Nozzle radius
Ri_f	Flow Richardson number
Ri_g	Gradient Richardson number
Ri_i	Interface Richardson number
Ri_L	Layer Richardson number
Ri_s	Mean shear Richardson number

Ri_u	Richardson number (based on mean velocity of mixed layer)
u_i	Mean interface velocity
u_s	Slip velocity
U	Mean jet velocity
V_s	Slip velocity
z_m	Maximum vertical penetration depth

Greek Symbols

α	Dimensionless wavenumber
α_d	Dispersed phase void fraction
δ	Interface thickness (instantaneous)
\bar{d}	Mean interface thickness
δ_b	Buoyancy interface thickness
δ_m	Mixed fluid thickness
δ_ρ	Maximum density gradient thickness
δ_s	Shear layer thickness
δ_v	Maximum velocity gradient thickness
δ_w	Wave amplitude at interfacial layer
$\Delta\rho$	Difference in the densities of the unmixed fluids (i.e. $\rho_\beta - \rho_\alpha$)
ΔU	Difference in the free stream velocities of the two fluid layers
ε	Dispersed phase hold-up (i.e. volume fraction)
ε	Dissipation of turbulent kinetic energy

Γ	Scalar diffusivity
λ_{KH}	Wavelength of Kelvin-Helmholtz instabilities at interface
μ	Molecular viscosity
μ_t	Turbulent eddy viscosity
ρ	Density
$\bar{\rho}$	Mean density
σ_ϕ	Turbulent Prandtl-Schmidt number for scalar equation

Subscripts

α	Alpha phase (denotes lighter fluid)
β	Beta phase (denotes heavier fluid)
c	Continuous phase
d	Dispersed phase
i	Interface quantity
m	Mixture quantity
0	Denotes lower layer in density stratified shear flows
1	Denotes upper layer in density stratified shear flows

1.0 INTRODUCTION

1.1 Background Information

Compensated fuel/ballast tanks (CFBT's) are used in US Navy ships for stability and ease of operation. The tanks, which are located in the bottom of the ships, are linked together in groups of 2-5 tanks. As the fuel is consumed during operation, seawater is allowed to enter the tank to retain ballast, and to provide a stable center of gravity for the ship. The typical tank is broken up into a series of compartments that are connected by manholes and limberholes. Each tank may hold anywhere from 30,000 to 120,000 liters (8,000 to 32,000 gallons) of fuel, with each set of tanks holding approximately 260,000 liters (70,000 gallons). As fuel is drawn off the top, seawater is allowed to enter the bottom of the tanks, and when empty, a tank typically has a 0.08 m (3 in) layer of fuel on the top. During re-fueling, fuel enters near the top of the tank, through an upward inlet pipe, at flow rates between 60 to 95 liters/sec (950 to 1,500 gal/min.). The compensating water is forced out of the bottom of the tank through an outlet, located in the last tank. The density of the fuel is about 850 kg/m^3 , compared to the density of the seawater, which is approximately $1,000 \text{ kg/m}^3$. Though buoyancy forces compete to keep the fluids separated, the turbulence that develops because of the relatively high shear rates causes some of the fuel to become entrained in the seawater that is discharged overboard. This is a concern not only because of the wasted fuel, but also primarily because of environmental considerations, as some of the fuel may be forced out of the tank during refueling. Another problem typically encountered in these tanks is that of water hideout, where seawater is trapped at the bottom of a compartment, which may constitute a

significant portion of the tank volume and is an obvious inefficiency [9]. A sketch of a generic CFBT is shown in Figure 1.1 below.

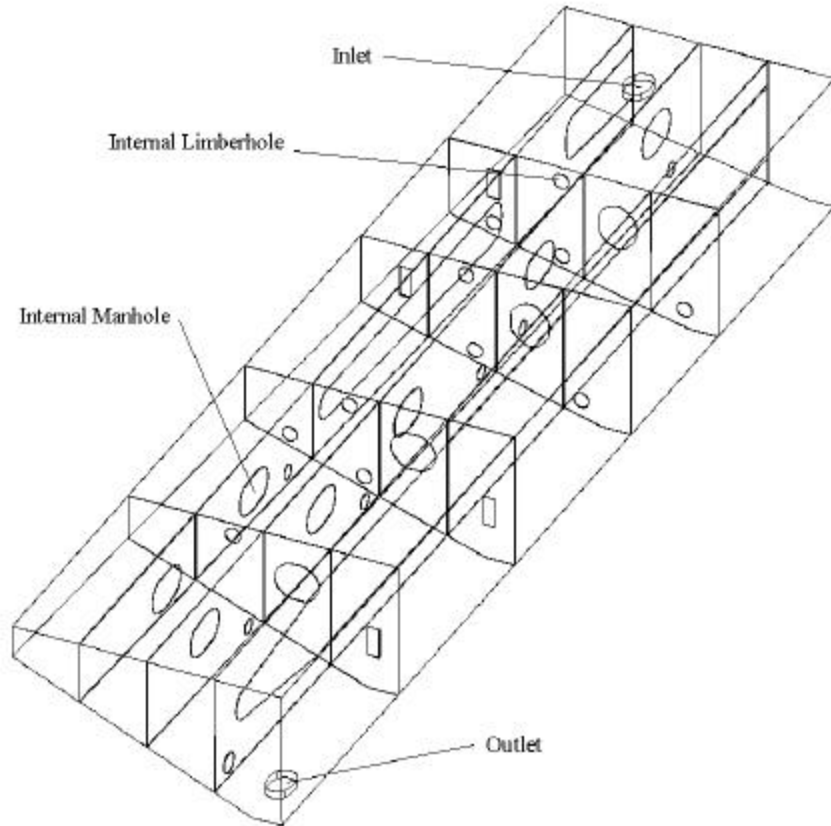


Figure 1.1 - Geometry of typical compensated fuel ballast tank (CFBT).

The US Navy has undertaken an extensive research effort to analyze the flow that develops during the refueling of these tanks, and to assess the current performance characteristics and develop design improvements that may be implemented in future ship construction. Computational fluid dynamics (CFD) analyses have focused on the Arleigh Burke (DDG-51) class of US Navy guided missile destroyers. The current design of the DDG-51 class CFBT has a number of internal structures that promote mixing of the two fluid phases and cause fuel to be entrained in the compensating water. This is especially

evidenced by buoyant flow events that occur when the fuel is forced from one compartment into the next via manholes, limberholes, or rectangular openings between the two compartments. As the fuel enters the second compartment, buoyancy forces force the fuel towards the ceiling of the second tank. The buoyant jet that develops causes large shear forces at the interface between the two fluids, thus leading to mixing of the fuel and water. Increased mixing within the tank is a major concern regarding the amount of fuel that may be discharged overboard as the compensating water is forced out of the tank during refueling.

There are a number of different phenomena that occur during the refueling process of a compensated fuel/ballast tank. As the fuel is pumped into the tank, a buoyant jet issues from the vertical inlet pipe. A similar buoyant jet event occurs when the fuel is forced from one compartment into the next through several different types of openings, and a shear layer region develops in the interior portions of the compartment between these openings. Another issue concerns the breakup of the fuel into small droplets due to the competition of buoyancy, inertia, and shear forces. In light of the discussion by Sullivan and List [33] and Fernando *et al* [16], we may also break up the flow into several different regimes based on the primary mixing mechanism, which may be due to local turbulence effects, or Kelvin-Helmholtz type instabilities that occur at the interface between the two fluids. All of these can effect the overall mixing that occurs within the tanks, and the difficulty of the problem is compounded by the complexity of the geometry and the turbulent nature of the flow.

Work is currently being performed at West Virginia University to analyze the general flow characteristics, and to predict when and where mixing occurs within these tanks. Turbulent multiphase sub-models are being developed to characterize the flow of the two fluids and to predict fuel entrainment in light of results from the literature and experiments. While true multiphase analysis of this type of flow may involve the modeling of each fluid as a separate phase, a single fluid, scalar transport (SFST) model is currently being used, which is a variant of the drift flux model suggested by Ishii [22]. The homogeneous multiphase (HMP) model, which is a default model in CFX-4, was not used because a comparison demonstrated the advantages of the SFST model in terms of accuracy and computational efficiency. The HMP model showed an overtly large amount of mixing, which also causes the fuel to reach the outlet prematurely. The reason for this is believed to be the lack of any mechanism for fuel separation, in addition to the numerical diffusion present in the volume fraction equation [8]. For larger, more complex geometries, the HMP model was also limited in that a turbulence model could not be included because of extreme convergence difficulties. Were the turbulence model present, however, an even greater amount of diffusion would occur, as the buoyant production/dissipation terms, which have the effect of damping the turbulence, would not be present [8].

In light of the convergence difficulties for more complex tank configurations, a comparison was made between the two models using a simplified two-compartment tank geometry [8]. This simplified geometry consists of two rectangular compartments separated by a manhole. The fuel enters the first compartment through a vertical inlet

pipe, flows through the manhole, and exits through a vertical exit pipe located in the second compartment. While being a simpler geometry, this configuration still exhibits many of the flow characteristics of compensated fuel/ballast tanks. Figures 1.2 and 1.3 show the volume fraction contours and velocity vectors within the two-compartment tank using the HMP model and SFST model respectively. In Figure 1.2, the Reynolds number through the manhole is approximately $Re = 100,000$, and the overall Richardson number, Ri^* is approximately $Ri^* = 1.4$, where the overall Richardson number is given by

$$Ri^* = \frac{gH(\mathbf{r}_{water} - \mathbf{r}_{fuel})}{\mathbf{r}_{fuel}(U_{water} - U_{fuel})^2} \quad (1.1)$$

Here H is the total height of the two layers, and U is the average velocity of the fuel and water layers. In Figure 1.3, the Reynolds number through the manhole is approximately $Re = 87,000$, and the overall Richardson number is approximately $Ri^* = 2.0$. As the HMP model causes the fuel to reach the outlet prematurely, the increase in the Reynolds number is not surprising. Nor is the decreased Richardson number, as the HMP model predicts a large increase in mixing owing to increased shear. As the Richardson number is inversely proportional to the shear, this causes a decreased Richardson number in the case of the HMP model, which is indicative of more turbulent flow.

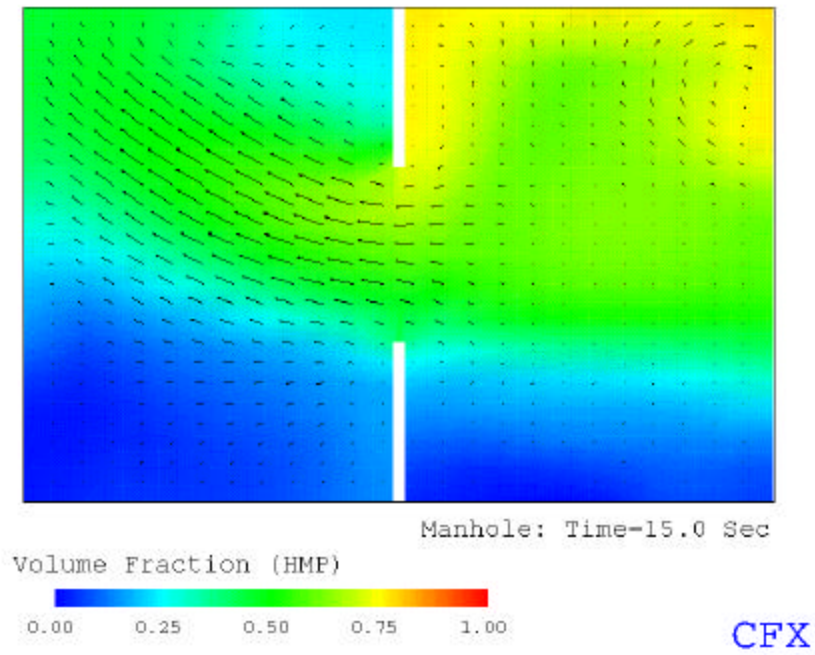


Figure 1.2 - Volume fraction and velocity vectors (manhole - two-compartment tank) at time = 15.0 seconds (HMP).

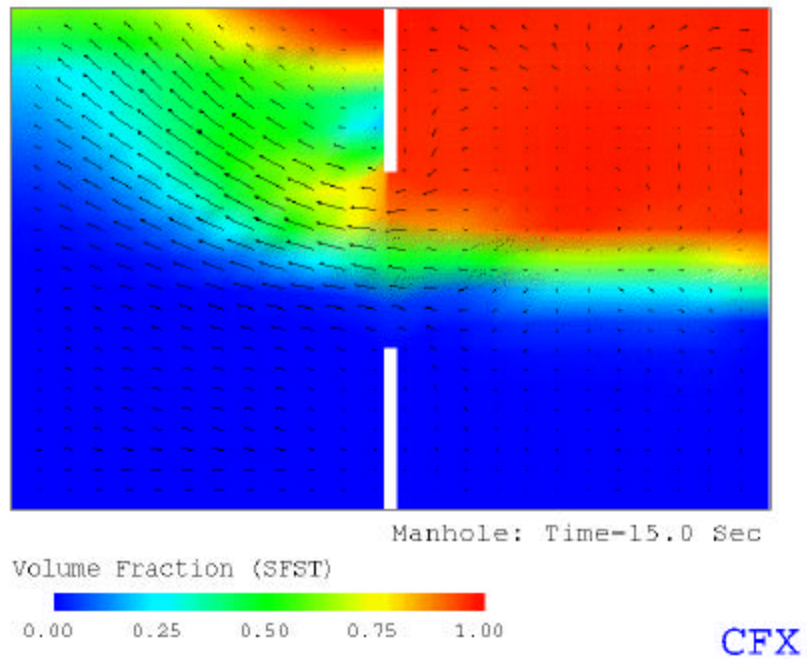


Figure 1.3 - Volume fraction and velocity vectors (manhole - two-compartment tank) at time = 15.0 Seconds (SFST).

The results from Figures 1.2 and 1.3 above demonstrate the overly diffusive nature of the HMP model, indicated by the significant increase in the amount of mixed fluid. This becomes an important issue regarding the accuracy of the calculations, as a large amount of numerical diffusion is introduced in the volume fraction equations. Another important issue regarding the comparison of these two models is that of computational time. Simulations of the two-compartment geometry, for the same amount of elapsed time and using the same convergence criteria, demonstrated that the SFST model requires approximately 30% less time [8]. The savings from the SFST model would increase significantly as the number of cells increased, especially for realistic tank geometries.

Due to the turbulent nature of the flow, requiring a turbulence model, and in light of increased computational efficiency, a single fluid, scalar transport (SFST) model was used to predict the bulk fluid motion and regions of mixing. In general, the SFST model assumes that the two-fluid mixture can be considered as a whole, rather than as two separate phases. Mixture quantities are used to discretize the conservation equations, which are formed by summing the individual phase equations. This results in a mixture continuity equation, and a set of momentum equations similar to the single-phase Navier-Stokes equations, which includes an additional source term to account for the relative slip between the two phases. While there are many different relationships which could be used to describe the slip velocity (see e.g. [26], [27]), here we have used an empirical relation to model the relative or slip velocity as being predominately given by the terminal rise velocity of a fluid droplet, while also accounting for multi-particle effects. The second continuity equation is then put into a form where it can be used to determine

the concentration or volume fraction of one of the phases, the other volume fraction being given by the algebraic constraint that the two must sum to unity. A modified form of the standard k - ϵ model is used to describe the turbulence, including turbulent production/dissipation resulting from the effects of buoyancy. The complete set of equations for the SFST model is given in Appendix A.1.

To analyze the shear regions that develop in the interior portions of the fuel/ballast tanks, the transport of a scalar at a turbulent sheared density interface was studied in light of the experiments by Sullivan and List [33]. Here the primary concern was the interfacial mixing or entrainment of one fluid into the other. The flow was characterized by a Richardson number, defining the relative influence of buoyancy and shear forces. Results showed that the numerical model is reliable in predicting the resulting interface location and free stream velocities, and was reasonably accurate in predicting the shear layer thickness and concentration boundary layers that develop at the interface [7].

A similar study was performed in light of experiments being conducted at Johns Hopkins University. Comparison with preliminary experimental observations and results indicate that the simulations produce reasonable results with regard to the overall flowfield, prediction of recirculation zones, and the development of the mixed-fluid layer, using an assumed average droplet diameter which is also reasonably close to the observed average droplet size [6,36]. By comparison between the simulation results and measurements, it was shown that the model predicts the growth of the shear layer with reasonable accuracy. This type of flow is very similar to that which would develop in the interior

portions of a tank compartment. The results of the simulations demonstrate the effectiveness of the use of the single fluid, scalar transport (SFST) model to predict the general characteristics of the flow, including the development of the shear layer and recirculation zones.

Another flow phenomenon that occurs in compensated fuel/ballast tanks, and is important for overall mixing, is that of the buoyant jet. This occurs both when the fuel enters the tank through the vertical inlet pipe, and when the fuel is forced from one tank compartment into the next via a manhole or other opening. Because the density of the fuel is less than that of the compensating water, buoyancy forces compete with gravitational and inertial forces to separate the two fluids and draw the fuel towards the tank ceiling. This produces a large amount of shear at the interface between the two fluids and promotes mixing. Simulations of this type of flow have been performed in light of experiments being conducted at Johns Hopkins University to study the mixing mechanisms in such flows [38].

Another important issue regarding the inlet jet is that of impingement on the tank ceiling, which may cause the fuel jet to break up into small droplets. This breakup phenomenon also becomes important for buoyant jet events, which occur when fuel is forced through compartment openings, as well as in the shear regions in the interior portions of the tank. In light of this, a droplet formation/entrainment (DFE) model is currently being developed to predict the size of the dispersed phase (i.e. fuel) droplets based on local flow parameters [6]. These would include local turbulence quantities, appropriate length

and velocity scales, and dimensionless parameters such as the Reynolds number and Richardson number. The effects of surface tension may also be included through the use of a critical Weber number, which may determine the amount of shear necessary for breakage to occur. The modeling of the relative motion or slip between the two fluids in the SFST model also necessitates the use of a locally determined droplet diameter for accurate simulations of the actual flow phenomena.

CFD simulations of a full-scale model tank geometry indicate that the SFST model is very effective in predicting the bulk fluid motion of the fuel and water, and in predicting regions where fuel/water mixing and water hideout are likely to occur [6,8]. Buoyant jet events are observed from the transient calculations in the regions occupied by the inlet jet, and in regions of flow through the manholes. Mixing events are also observed in regions of mixed-fluid, where droplet breakup is also likely to occur. Water hideout near the bottom of the tank compartments can also be observed [6,8].

The numerical models used in all of these cases require validation based on experimental results. To this end, observations and quantitative data from the experiments being conducted at Johns Hopkins University are used to validate the single fluid, scalar transport (SFST) model and droplet formation/entrainment (DFE) model in simulating these types of flows. Future scale model experiments of an actual CFBT may also be used to verify the predictions of the numerical models with regard to the bulk fluid motion, and prediction of fuel/water mixing and water hideout in compensated fuel/ballast tanks. These simulations may also then be used to develop full-scale testing

techniques and predict scale-up difficulties, as well as to analyze the effects of geometric modifications.

1.2 Objectives

The overall goal of the research effort at West Virginia University, of which the present study is an integral part, is to develop numerical models that can be used to predict fuel/water mixing and water hideout in compensated fuel/ballast tanks. The development and application of the droplet formation/entrainment model in conjunction with the numerical models already in place is vital to the accurate prediction of mixing phenomena and general flow characteristics. Therefore, the present study focuses on the implementation of the DFE model and the assessment of its performance in the prediction of experimental parameters in certain canonical flows that will also be important in the large-scale flow configuration of a typical CFBT.

The objectives of the present study are primarily concerned with the development and validation of the droplet formation/entrainment model, while also examining certain case specific issues related to the shear flow and impinging jet experiments currently being conducted at Johns Hopkins University. The first objective is the development and verification of the DFE model based on shear flow experiments, which would represent typical flow behaviors expected in the interior portions of the large-scale tank compartments. The second objective involves validation of the DFE model in predictions of experimental observations concerning the impingement of a negatively buoyant

vertical jet into a quiescent environment as an independent case study. This would represent phenomena that typically occur during the initial stages of refueling of a CFBT, as compensating water would be forced into the remaining fuel layer at the top of the tank. Analyses from these simulations will also be important in assessing trends which would occur during the later refueling stages of a typical CFBT, as the lighter fluid (diesel fuel) would be forced into a more dense water layer.

In all of these predictions, the primary objective is to assess the performance of the SFST and DFE models based on experimental observations and quantitative data available in the literature. This assessment will provide validation for the use of these sub-models in future simulations of small-scale and full-scale geometries of the DDG-51 CFBT and other scale model tests.

1.3 Overview

First, a review of the literature concerning density stratified shear flows, vertical buoyant jets, and droplet formation and entrainment phenomenon will be examined. This will provide information regarding the parameters of interest in each of these areas. This review will include issues related to numerical and turbulence modeling, and will also provide experimental results and reviews as they relate to each of these phenomena.

Following the literature review, an explanation of all of the numerical models will be given, including a detailed description of the SFST model for immiscible fluids. This

section will also examine algebraic expressions for the slip velocity and modifications to the standard k - ϵ turbulence model for buoyant flows. The proceeding chapter will discuss problems with mass conservation (i.e. conservation of the fuel volume) with the previous version of the SFST model. In this section a new formulation for calculating the volume fraction will be discussed in light of this problem, and results will be presented detailing the improvements made through this new formulation.

Following this, a complete description and derivation of the current version of the droplet formation/entrainment model will be presented, with reference to its origins in various literature sources. Results from verification studies performed on a two-compartment tank will demonstrate that the values predicted for the droplet sizes are reasonable both in magnitude and physical distribution.

The next section will provide results from simulations concerning the density stratified shear flow experiments being conducted at Johns Hopkins University in which the implementation of the DFE model will be examined and evaluated. Some comparison will also be made between predictions from the model and actual experimental measurements for the variation in the mixed fluid thickness as a function of downstream distance.

Following the simulations of the shear flow experiments, the droplet formation/entrainment model will be examined in light of experiments involving the impingement of a negatively buoyant vertical jet into a quiescent reservoir. Here again,

comparisons will be made between numerical predictions and experimental measurements. Modifications to the DFE model for this flow scenario and specific computational issues will also be discussed.

Finally, some overall conclusions regarding the use of the SFST model in conjunction with the droplet formation/entrainment model will be presented. Suggestions for future studies and improvements to the numerical sub-models will also be given.

2.0 REVIEW OF THE LITERATURE

2.1 Introductory Definitions and Comments

While the focus of the present study is divided between several different flow phenomena, including stratified shear flows, buoyant jet flows, and droplet formation and entrainment, there are several parameters that will become important in describing all of these. First, we will discuss the relevant length scales that become important in characterizing each of these types of flows, followed by a discussion of the relevant dimensionless parameters. Then, a review of the literature for stratified, shear flows, buoyant jet flows, and droplet formation studies will be presented.

Characteristic Length Scales:

Sullivan and List [33] performed experimental measurements of tracer dye concentrations in a density stratified, shear flow generated in a water channel apparatus. In these experiments a layer of aqueous ethanol solution acts as the lighter fluid, and flows over a layer of aqueous saline (the heavier fluid). They define a concentration boundary layer thickness, h , as the distance from the mean interface location, \bar{h} , to the location (either above or below the interface) where the probability is 0.02 of finding fluid whose concentration differs from the local mean by $0.01C_0$. Here C_0 is the unmixed dye concentration in the lower layer. Physically, this gives some measure of the level to which the turbulent motions are able to transport the scalar in the vertical direction.

While this definition applies to a tracer dye concentration in this particular case, it is easily applied to any transported scalar variable.

Another important length scale based on the concentration profile is that of the interfacial thickness, δ . Sullivan and List [33] define δ according to

$$\mathbf{d} = y(C \geq 0.9) - y(C \leq 0.1) \quad (2.1.1)$$

where C again represents the tracer dye concentration. In describing the velocity profile near the interface, they further define a maximum velocity gradient thickness, h_s , given by

$$h_s = \frac{\Delta U}{(\partial u / \partial y)_{\max}} \quad (2.1.2)$$

where ΔU is a characteristic velocity which usually represents the difference in the free stream velocities of the two unmixed layers in a stratified shear flow, and $(\partial u / \partial y)_{\max}$ represents the maximum mean velocity gradient at the interface in the vertical direction. The maximum velocity gradient thickness is also used by Atsavapranee and Gharib [1], though it is given by the notation δ_v .

Atsavapranee and Gharib [1] define a similar parameter with regards to the density profile. They define a maximum density gradient thickness, δ_ρ , as

$$\mathbf{d}_r = \frac{\Delta \rho}{(\partial \rho / \partial y)_{\max}} \quad (2.1.3)$$

where $\Delta \rho$ is the difference in the densities of the two unmixed layers, and $(\partial \rho / \partial y)_{\max}$ is the maximum density gradient that occurs at the interface in the vertical direction. Here

the maximum density gradient thickness has been defined similarly to the maximum velocity gradient thickness, but in terms of the density profile, rather than the velocity profile.

Another important length scale is the mixed fluid thickness, which is defined as the vertical length over which a mixed concentration (or density) layer exists, defined similarly to a displacement thickness [1]. Here, the mixed fluid thickness is defined similarly to Eq. (2.1.1) as

$$\mathbf{d} = y(C \geq 0.99) - y(C \leq 0.01) \quad (2.1.4)$$

This length scale is related to the maximum density gradient thickness by

$$\mathbf{d}_r \approx 2\mathbf{d}_m \quad (2.1.5)$$

where δ_ρ is defined by Eq. (2.1.3) above.

The relevant streamwise length scale that characterizes mixing phenomena and wave motion at the interface is the Kelvin-Helmholtz instability wavelength, λ_{KH} [1]. This parameter can also be related to the maximum density gradient thickness at the interface through the use of a dimensionless wavenumber, α , given by

$$\mathbf{a} \equiv \frac{2\mathbf{p}\mathbf{d}_r}{l_{KH}} \quad (2.1.6)$$

where λ_{KH} is the wavelength of the Kelvin-Helmholtz vortices. The K-H wavelength, along with the mixed fluid thickness, will be of importance later during the discussion of the various mixing regimes as they relate to the formulation of the droplet entrainment model expressions in the present study.

Dimensionless Parameters:

As the major forces that are responsible for interface mixing appear to be the buoyancy and inertial forces, the most appropriate dimensionless parameter for characterizing the types of flows in the current study is the Richardson number, which describes the relative influence of these two forces. Here, a large Richardson number represents a large buoyancy force, with very little shear or turbulence, while a small Richardson number represents a large shear force, with little influence from buoyancy. One common problem in the literature, however, is in how the Richardson number should be defined. In light of this, several different expressions for the Richardson number will be presented in this section. To avoid confusion, the notation used in the present study may not necessarily coincide with that used in the literature.

In characterizing the stratified shear flow of two fluid layers with different densities flowing over one another, Sullivan and List [33] use a layer Richardson number in describing the relative influence of buoyancy and inertia within a given layer. This layer Richardson number, Ri_L , is given by

$$Ri_L = \frac{\Delta b h}{(U - u_i)^2} \quad (2.1.7)$$

where h is the boundary layer thickness of the layer, U represents the free stream velocity of the layer in question, and u_i denotes the mean interface velocity. The buoyancy jump across the interface, Δb , is given by

$$\Delta b = \frac{g \Delta \mathbf{r}}{\mathbf{r}_1} \quad (2.1.8)$$

where $\Delta\rho = \rho_0 - \rho_1$ is the difference in the densities of the two layers, and ρ_1 denotes the density of the lighter phase. This term essentially represents the buoyancy force per unit mass. The layer Richardson number is important in characterizing the flow of a given turbulent layer in a density stratified shear flow.

Narimousa and Fernando [31] employ a similar expression in characterizing interfacial mixing events by assuming that the governing velocity scale is given by the mean interface velocity, \bar{u} . In their experiments, a mixed fluid layer was driven over a denser fluid layer, and the mixed fluid layer thickness and entrainment were examined. Further, they assume the relevant length scale to be determined by the average depth of the mixed layer, h , resulting in a Richardson number of the form

$$Ri_u = \frac{\Delta b h}{\bar{u}^2} \quad (2.1.9)$$

To characterize the relative effects of the two fluid layers in the region of the interface, Sullivan and List [33] also define a mean shear Richardson number, Ri_s , given by

$$Ri_s = \frac{\Delta b h_s}{(U_0 - U_1)^2} \quad (2.1.10)$$

where U_1 and U_0 represent the free stream velocities of the upper (i.e. lighter fluid) layer and lower (i.e. heavier fluid) layer, respectively, and h_s is the maximum velocity gradient thickness at the interface, as given by Eq. (2.1.2).

To allow for a more general characterization of the flow of two turbulent shear layers, sometimes an overall Richardson number is used, where the relevant length scale encompasses both fluid layers [14]. The overall Richardson number is defined by

$$Ri^* = \frac{H\Delta b}{(U_{ch})^2} \quad (2.1.11)$$

where H is the total depth of both fluid layers, and U_{ch} is some characteristic velocity scale that is often taken equal to the difference between the free stream velocities of the two layers. This parameter becomes important for characterizing general flow characteristics, and is also a convenient way of comparing different flow scenarios by using appropriate length and velocity scales.

A similar expression can be used for buoyant jet flows, using the jet radius as the integral length scale. The densimetric Froude number can be written as [40]

$$F = \frac{V_0}{\sqrt{\frac{\Delta \rho}{\rho_0} g R_{noz}}} \quad (2.1.12)$$

where $\Delta \rho = \rho_0 - \rho_a$ is the difference between the discharge fluid density of the jet and the ambient fluid density, R_{noz} is the radius of the source (e.g. nozzle), and V_0 is the mean exit velocity from the source. This parameter is very similar to a Richardson number in that it also characterizes the relative influence of buoyancy and inertial forces. It will become important in the examination of vertical buoyant jet flows, as the densimetric Froude number will be used to describe the amount of mixing, as well as the penetration depth of the jet.

Atsavaprane and Gharib [1] characterize interfacial instabilities through the comparison of the maximum density and velocity gradient thicknesses, which gives some measure of the relative influence of buoyancy and shear forces. To this end, they define a flow Richardson number given by

$$Ri_f = \frac{g\Delta r d_r}{\bar{r}(\Delta U)^2 Q^2} \quad (2.1.13)$$

where \bar{r} denotes the mean density, ΔU is again a characteristic velocity scale representing the difference in the free stream velocities, and Q is the ratio of δ_p to δ_v .

Many of the preceding definitions of the Richardson number have been based on average length and velocity scales relative to the entire fluid layer. As a numerical simulation would require solution at all points within the domain, it may be more appropriate to examine a Richardson number based on local parameters. The gradient Richardson number, Ri_g , is defined according to [33]

$$Ri_g = \frac{-(g/r) \cdot \partial r / \partial y}{(\partial u / \partial y)^2} \quad (2.1.14)$$

and allows for characterization of the flow in a particular local region, rather than based on large-scale integral parameters. For much of the numerical implementation of the SFST model, the gradient Richardson number will be used, as it can be calculated at a given point based on local flow parameters. This will also become important in the formulation of the droplet entrainment model for determining the local droplet diameter.

Another parameter that is useful in characterizing viscous flows is the Prandtl number, which represents a measure of the influence of viscosity and diffusion forces. Here, the Prandtl number is defined according to

$$\text{Pr} = \frac{\boldsymbol{n}}{D} \quad (2.1.15)$$

where \boldsymbol{n} is the kinematic viscosity, and D is the diffusivity.

Another parameter is the Peclet number, which also gives some measure of the influence of molecular diffusion. It can be defined by [15]

$$\text{Pe} = \frac{h(\Delta U)_{ch}}{D} \quad (2.1.16)$$

where h is the boundary layer thickness, and $(\Delta U)_{ch}$ is a characteristic velocity scale. For the present work the velocity scale may be well represented by the interface velocity.

2.2 Review of Literature for Stratified Shear Flows

Narimousa and Fernando [31] studied interfacial phenomena during entrainment processes of two fluid layers subjected to interfacial velocity shear. In their experiments a saltwater layer was driven over a quiescent fresh water layer (unstable stratification) by means of a disc pump. Tracer dye was released into the flow, and the dispersions of the dye particles in space and time were studied through photographic techniques. These photographs were then used to measure the changes in the mean velocity profile, and the thicknesses of the shear layer and momentum diffusive layer. Their experiments were

characterized by a Richardson number, Ri_u , which was defined in terms of interfacial parameters as [31]

$$Ri_u = \frac{\Delta b h}{\bar{u}^2} \quad (2.2.1)$$

where Δb is the buoyancy jump across the interface (Eq. 2.1.7), h is the average depth of the mixed fluid layer, and \bar{u} is the mean velocity of the mixed-fluid layer. The results of these experiments showed a sharp interfacial layer whose thickness, δ , increased linearly with the mixed-layer depth h , independent of the Richardson number, as $\mathbf{d} \approx 0.07h$. The shear layer thickness, δ_s , was found to be independent of the Richardson number, and was approximately given by $\mathbf{d}_s \approx 0.20h$. Variations in the wave amplitude, however, showed a Richardson number dependence. The wave amplitude, δ_w , normalized by the mixed-layer depth, was found to follow a power-law relationship

$$\frac{\mathbf{d}_w}{h} \cong 0.232 Ri_u^{-0.61} \quad (2.2.2)$$

This relationship, along with the variations in the other characteristic length scales, will become important in the derivation of the model expressions for the droplet formation/entrainment model (see Section 5).

Narimousa and Fernando [31] also observed large-scale coherent structures, appearing as regularly spaced billows with thin braids of fluid connecting them. These interfacial instabilities were observed at relatively low values of the Richardson number ($Ri_u < 5$).

As the Richardson number was increased, the frequency with which these structures appeared decreased, and mixing appeared to be caused by wave-breaking phenomena.

These wave-breaking events were observed over a wide range of Richardson numbers, with decreasing occurrences as the Richardson number increased. At moderately high Richardson numbers, Narimousa and Fernando also observed the occurrence of large-amplitude solitary waves, which traveled through the interfacial layer without breaking. At very large Richardson numbers, molecular diffusion processes became dominant in the entrainment mechanism.

Fernando [15] provides some general review of the relevant mixing phenomena and flow regimes involved in flows of stratified fluids. With regard to the different mixing regimes that develop, a similar development is postulated by which mixing is dominated either by the direct influence of turbulent eddies, or by local instabilities that develop at the interface of the two fluids. These two phenomena can be delineated by an appropriately defined Richardson number, with the latter occurring at relatively large values of the Richardson number. Other governing parameters for these types of flows include the ratio of the buoyancy and velocity interfacial layer thicknesses, δ_b/δ_v , and the normalized interfacial displacement, $2d/\delta_v$. Here d represents the vertical distance between the interfaces of the buoyancy and velocity interfacial layers. It is conjectured that when $\delta_v < 2\delta_b$, $d=0$ (i.e. the interfaces coincide), and the gradient Richardson number, Ri_g , is less than some critical value, then the shear layer becomes unstable and wavenumber-dependent Kelvin-Helmholtz type vortices develop at the interface [15]. Here the critical value of the gradient Richardson number is usually assumed to be approximately 1/4.

Fernando [15] also discusses the processes of wave-breaking and diffusion-dominated entrainment. The wave-breaking phenomenon requires that the rate at which energy is supplied to the waves be greater than the rate at which energy is dissipated by internal viscous forces. If both of these are of the same order, then the waves will decay without breaking. It was also found that wave breaking will not occur at low values of the Peclet number (i.e. when $Pe < 200$). Entrainment by molecular diffusion processes was found to occur at large values of the Richardson number, at which time wave breaking no longer occurs. A critical value for the Richardson number defining this transition was found to be given by

$$Ri_c = 1.25 Pr Pe^{-1/2} \quad (2.2.3)$$

where Pr is the Prandtl number, and Pe is the Peclet number (see Eq. 2.1.15 and Eq. 2.1.16).

Sullivan and List [33] examined mixing and transport at the interface of a density stratified shear flow. Their experiments consisted of measurements of tracer dye concentration in a laboratory water channel that was 5 m long and 10 cm wide. Laser-induced fluorescence (LIF) was used to measure the concentration of the tracer dye. These experiments were conducted for a range of layer Richardson numbers between 1.0 and 10.0, where the layer Richardson number is given by Eq. (2.1.5). This also corresponds to a range of approximately 0.2 to 2.0 for the mean shear Richardson number (Eq. 2.1.9). This range of Richardson numbers corresponded to two distinct flow regimes, which the authors define as a Kelvin-Helmholtz (K-H) instabilities regime, and a shear-driven wave-breaking regime. The K-H instabilities regime was observed for

mean shear Richardson numbers, Ri_s , up to approximately 0.4 - 0.45. The wave-breaking regime was observed for somewhat larger Richardson numbers. In both cases, the authors found that vertical transport of the mixed fluid was accomplished through eddy scouring, in which the turbulent eddies impinged on the interface and carry fluid away from its outer edges.

Sullivan and List [33] also discuss two other mixing regimes. These are the turbulent interface regime, which occurs for very low values of the Richardson number, and the diffusion-dominated regime at very large Richardson numbers. According to Sullivan and List [33], at very low Richardson numbers, interfacial disturbances are not present, and only small-scale turbulence exists at the interface, where adjacent fluid is engulfed in the interface. At larger Richardson numbers, K-H type instabilities are observed and the scale of the turbulence at the interface decreases. As the Richardson number is further increased, the interfacial mixing is dominated by waves that become potentially unstable and are sheared off by turbulent eddies. At very large Richardson numbers, the interfacial waves are suppressed and mixing is dominated by molecular diffusion. This implies a Peclet number dependence as well. This is a similar development of the relevant mixing phenomena as reported by Narimousa and Fernando [31] above. Figure 12 of the paper by Sullivan and List shows the different flow regimes as a function of the layer Richardson number [33]. This will become the basis for delineating the flow regimes in the droplet formation/entrainment model in Section 5.0.

Atsavapranee and Gharib [1] also examined two-dimensional mixing layer behavior by studying the temporal evolution of the layer in a stratified tilting tank. Here the two fluid layers were of different densities, but similar indexes of refraction. The two-dimensional density field was measured using laser-induced fluorescence (LIF). In their experiments, an enclosed rectangular tank is half filled with fresh water or ethanol-water solution, then epsom-salt-water solution is introduced into the tank slowly through openings at the bottom of the tank. To maintain a sharp interface, deflector plates were installed just above the openings. At the interface, a density-gradient layer is formed whose thickness can be controlled by the time allowed for diffusion processes to occur. The tank is then tilted about an axis, allowing for the two layers to accelerate in opposite directions, resulting in a shear flow at the interface. After a certain time has elapsed, the tank is moved back into the horizontal position providing a steady flow, during which the development of Kelvin-Helmholtz type instabilities occurs.

In these experiments, the shear layer is characterized by two vertical length scales: the maximum velocity gradient thickness (Eq. 2.1.2), δ_v , and the maximum density gradient thickness (Eq. 2.1.3), δ_ρ . The flow is also characterized by a Richardson number, given by Eq. (2.1.13). Observations showed that increased stratification caused a decrease in mixing due to the reduction of the entrainment of fluid into Kelvin-Helmholtz type vortices, a reduction in vortex pairing, and a large decrease in the turbulence of the flow due to restratification. Several secondary features were also observed including gravitational instability within the cores, vortex pairing, and the appearance of Holmboe type instabilities.

The density thickness of the diffusive interface layer was determined by calculating an equivalent mixed-fluid thickness, δ_m , defined in a similar manner to the displacement thickness. Atsavapranee and Gharib found that the maximum density gradient thickness, δ_ρ , was approximately twice δ_m . It was also found that the dimensionless wavenumber (Eq. 2.1.5), α , of the K-H type instabilities, was independent of the Richardson number, with an average value of approximately 0.4. The height of the Kelvin-Helmholtz waves, normalized by the wavelength, α , was measured as a function of the Richardson number, and is given in Fig. 10 of their text. These measurements show that with increasing stratification (i.e. with increasing Richardson number) the K-H vortices entrain less fluid into increasingly smaller cores. This in turn causes a decrease in the level of turbulence, and a decreased amount of mixing [1]. This observation was also confirmed by measurements of the mixed-fluid thickness as a function of the Richardson number. These results are given graphically in Fig. 17 of the original paper, where the mixed-fluid thickness is normalized by the maximum velocity gradient thickness, δ_v [1].

A power-law curve fit of the data in the present study resulted in the following relationship

$$\frac{d_m}{d_v} \cong 0.017 Ri^{-3/2} \quad (2.2.4)$$

This relationship will be used in the derivation of the model expressions for the droplet formation/entrainment model (Section 5). On a general note, the authors also provide several images detailing the evolution of the flow, including the development of the

Kelvin-Helmholtz type vortices, roll-up and pairing, and the destruction of these waves through shear-driven wave-breaking events.

Wu and Katz [38] conducted experiments involving a stratified shear layer flow of diesel fuel and water. Of primary interest in these experiments was identifying certain mixing mechanisms that develop, as well as some examination of the onset of droplet formation. Two different flow structures were identified, including finger-like structures and large-scale Kelvin-Helmholtz type vortices. Digital images showing the formation and evolution of these structures (see Figs. 6.19-6.21 of this work) are given for a range of inlet parameters, primarily based on changes in the inlet velocities of the two fluids. The results of these experiments showed an increase in the mixed-fluid layer with decreasing Richardson number [38]. The mixed-fluid layer also reached a maximum just after the rollup of the large-scale vortices, then decreased with time until the rollup of the next vortices. The presence of vortex pairing was identified for cases involving large inlet velocities [38]. The formation of fluid droplets was observed due to the rollup of large-scale vortices, and the shearing off of finger-like structures. Some subsequent breakage of these droplets into smaller droplets was also observed, and the characteristic droplet size decreased with increased velocity [38].

2.3 Review of Literature for Vertical Buoyant Jet Flows

Fernando *et al* [16] conducted experiments involving a planar turbulent buoyant jet impinging on a stable density interface. This phenomenon is similar to the buoyant jet events that occur in compensated fuel/ballast tanks (CFBT's) as fuel is forced horizontally from one tank compartment into the next, and buoyancy causes the jet to flow vertically towards the ceiling of the tank. In the experiments by Fernando *et al* [16] the jet was injected horizontally into a homogeneous lower layer, where the top fluid layer was separated from the homogeneous layer by a density jump. Measurements were made for the entrainment velocity, time evolution of the vertical density profiles, and the interfacial layer thickness. In these experiments, the lower layer consisted of salt dissolved in tap water, and the top layer consisted only of water. The discharge temperature of the jet was manipulated to allow for highly buoyant, slightly buoyant, or neutrally buoyant cases. Flow visualization was performed using fluorescent dye particles and dye lines, which were then illuminated by a vertical laser sheet for still photographs and video recording.

In the case of the neutrally buoyant jet, mixing occurs due to shear instabilities, where high shear at the interface causes Kelvin-Helmholtz type vortices in the region near the jet impingement. Farther downstream from the jet impingement region turbulent mixing is greatly decreased [16]. In the case of the slightly buoyant jet, the interface becomes patchy in the region of the jet impingement, and mixing takes place within the intermittent patches. As the patches merge with the rest of the mixed layer, the mixed-layer thickness increases [16]. Here, the mixed layer is assumed to be the bottom layer,

which has constant density, ρ_m . In the highly buoyant case, the vertical velocity of the jet is considerably higher, causing an elevation of the interface in the form of a cap. This causes sloshing of the fluid into the mixed layer [16].

Zhang and Baddour examined the maximum vertical penetration of both round [40] and plane [39] densely buoyant jets. With respect to the present study, the information for round vertical jets is more applicable. These experiments involved the discharge of saltwater into a quiescent tank filled with freshwater, for a range of three different sizes of round nozzles. The temperature of both the fresh water and salt water was maintained at a constant value to avoid thermal effects. A series of experiments was conducted by which the Froude number of the jet was varied, while maintaining turbulent flow conditions at the exit of the nozzle. It was determined that the jet penetration and mixing increased with increasing Froude number, where the Froude number of the jet was given by Eq. (2.1.12).

The results of the experiments by Zhang and Baddour [40] for round vertical jets showed two empirical relationships for the maximum vertical penetration of the jet depending on the value of the Froude number. For large Froude number ($F > 7$), the maximum penetration z_m was given by

$$\frac{z_m}{R_{noz}} = 3.06F \quad (2.3.1)$$

where R_{noz} is the radius of the nozzle, and F is the Froude number. For small Froude numbers ($F < 7$), the empirical relationship for the maximum penetration was given by

$$\frac{z_m}{L_m} = 1.7F^{0.3} \quad (2.3.2)$$

where L_m is a characteristic length scale related to the momentum flux and buoyancy flux of the jet [40]. All of the numerical simulations in the present study are within the small Froude number regime.

Friedman and Katz [17] examined the impingement of a liquid/liquid interface by a densely buoyant vertical jet (see Fig. 7.1 of the present work). This study is of practical significance in analyzing the flow phenomena that occur during the refueling process in compensated fuel/ballast tanks (CFBT's) using in U.S. Navy surface ships. At the start of the refueling process, there is a thin residual layer of fuel at the top of the tanks. As the fuel begins to enter the upstream tanks, the later tanks in the series experience a vertical jet consisting of compensating water from the upstream tanks. This vertical jet impacts the residual fuel layer that remains at the tank ceiling. In the experiments conducted by Friedman and Katz, a densely buoyant water jet issuing from a nozzle impacts a quiescent fuel layer, a similar phenomenon to that which occurs during refueling of CFBT's. The experiments conducted also allowed for the height of the inlet nozzle to be varied such that the distance between the nozzle exit and the fuel/water interface could be varied.

A dimensional analysis showed that the relevant parameters for this type of flow include the Richardson number, which measures the relative influence of buoyancy and inertial forces, the Reynolds number, and the Weber number. It was found, however, that for the

experimental conditions under consideration the surface tension forces, and hence the Weber number, had very little influence on the dynamics of the flow [17].

According to Turner [36], a negatively buoyant jet which is directed upward will collapse and fall around a rising central core. A similar phenomenon was observed during the experiments by Friedman and Katz [17], where it was found that the penetration depth of the core increased with increasing exit velocity. Several different mixing regimes were identified, where the dominant mixing mechanism differs in each case. Flow regime 1 was observed at large values of the Richardson number ($Ri_i > 10$). Here the Richardson number is defined in terms of interface parameters by

$$Ri_i = \frac{g\Delta\rho}{\rho_w} \cdot \frac{D_i}{U_i^2} \quad (2.3.3)$$

where $\Delta\rho$ is the density difference between the two fluids, and D_i and U_i represent the diameter and velocity of the jet at the interface, respectively. In regime 1 a smooth stable deformation forms at the interface, and fluid exiting the deformation remains attached along the liquid/liquid interface. No mixing was observed in this regime [17]. Regime 2 occurs for moderate values of the Richardson number ($10 > Ri_i > 1$). As the jet velocity increases, the height of the deformation at the interface increases. The sides of the deformation become increasingly steeper until a separation develops at the edge of the deformed interface. When the downward velocity of the falling water is large enough, a portion of the fuel layer is drawn down below the fuel/water interface. Mixing occurs when the fuel that is drawn down is broken into droplets, this being further promoted as the velocity of the jet is increased [17].

Flow regime 3 occurs for relatively small values of the Richardson number ($Ri_i < 1$) and the velocity of the jet is significantly higher. In this regime large droplets are formed, and may either return immediately to the fuel layer or break into smaller droplets. This regime is characterized by extensive mixing. A secondary mechanism was also observed by which the upward velocity of fuel droplets returning to the fuel layer was sometimes great enough as to drag some of the water upward into the fuel layer. This is the only observed mechanism by which water droplets are formed in the fuel layer [17]. Regime 4 occurs at even smaller Richardson numbers where the jet velocity is sufficient to impact the impingement plate. In this regime there is extensive mixing, and upon impacting the impingement plate, the water jet causes a splattering of very fine droplets in a radial pattern, creating an extensive cloud of water droplets in the fuel layer. While the small size of the droplets formed make measurements difficult, it is believed that the droplet diameter decreases with increased jet velocity [17].

Friedman and Katz [17] also present results for the onset of droplet formation as a function of the interface Richardson number and the Reynolds number. In all cases, the onset of droplet formation was distinct and repeatable. Measurements were also made for the ratio of the jet penetration height to the interface jet diameter (aspect ratio). This parameter was found to be a function of the interface Richardson number [17]. This observation inspired us to formulate Eq. 8.2.7. Comparison will be made between the measurements of the aspect ratio and the results of the numerical simulations (Section 7).

2.4 Review of Literature for Droplet Formation and Breakage

One of the earlier works involved with droplet formation was that performed by Hayworth and Treybal [19], who studied drop formation of a liquid dispersion from simple nozzles of one liquid into another immiscible liquid. The relevant governing parameters were assumed to be the densities and viscosities of the dispersed and continuous phases, interfacial tension, velocity of the dispersed phase through the nozzle, the nature of the flow of the continuous phase, which phase (light or heavy) became dispersed, and integral parameters including the geometry of the nozzle. Experiments were conducted using different size nozzles, and various liquid/liquid pairs, for injection into a stationary continuous phase. Their results indicated that drop size was increased by increased interfacial tension, decreased density difference between the two phases, increased viscosity of the continuous phase, and increased nozzle diameter [19]. It was also found that drop size was independent of which fluid was dispersed and showed negligible influence of the dispersed phase viscosity [19].

In order to determine a method for predicting drop sizes exiting the nozzle, Hayworth and Treybel [19] utilized a force balance on the droplet. The important forces acting on the droplet were assumed to be due to buoyancy, F_B , interfacial tension, F_σ , and the kinetic energy of the jet fluid entering the droplet, F_K . From these forces, several partial volumes were obtained, each of which was assumed to contribute either to the growth or destruction of the fluid droplet. Then, the volume of the fluid droplet was given by the sum of these partial volumes, including (1) the volume necessary to overcome interfacial tension forces, (2) the volume necessary to produce a rising velocity of the droplet at least

equal to the exit velocity of the nozzle, and (3) the volume of the kinetic energy supplied by the exiting fluid. This eventually led to an empirical relationship for the droplet diameter in terms of fluid and integral parameters given by [19]

$$Q_F + (4.11 \times 10^{-4}) \cdot Q_F^{2/3} \left(\frac{r_d V^2}{\Delta r} \right) = 21 \times 10^{-4} \left(\frac{s d_N}{\Delta r} \right) + 1.069 \times 10^{-2} \left[\frac{d_N^{0.747} V^{0.365} m_c^{0.186}}{\Delta r} \right]^{3/2} \quad (2.4.1)$$

which could be solved for the fluid droplet volume, Q_F , and in turn yield the droplet diameter. Here, V is the exit velocity from the nozzle, d_N is the nozzle diameter, and the subscripts c and d refer to the continuous and dispersed phase, respectively. While this is a useful relationship in examining the general effects of certain parameters on the droplet size, it also involves certain integral parameters that are specific to a given geometry and flow type, and therefore it can not be used for comparison with our computational results.

In another earlier work involving droplet formation and breakup, Hinze [21] examined the conditions necessary for droplet breakage to occur, as well as the different types of droplet deformation. This analysis was primarily based on a balance of the important forces, including surface tension, pressure forces, inertial forces, and viscous stresses. This force budget leads to several dimensionless groups, whose magnitudes are examined in light of the conditions required for the droplet to break. These include a Weber number, given by

$$We = \frac{tD}{s} = \frac{rU^2 D}{s} \quad (2.4.2)$$

and a dimensionless group involving viscosity, given by

$$N_{vi} = \frac{m_d}{\sqrt{r_d s D}} \quad (2.4.3)$$

where τ is the surface force per unit area, D is the diameter of the fluid droplet, σ is the interfacial tension, and the subscript d denotes the dispersed phase. As the Weber number increases, the ratio of the external surface force to the restoring force due to surface tension increases until some critical value $(We)_{crit}$ is attained whereby the droplet breaks. In general, $(We)_{crit}$ will be a function of N_{vi} , yielding the following relationship [21]

$$(We)_{crit} = C[1 + j(N_{vi})] \quad (2.4.4)$$

where the function j decreases to zero as N_{vi} approaches zero, and C is the value of the critical Weber number when the effects of viscosity are negligible.

Hinze [21] also examines the dispersion of one liquid in another. It is assumed that turbulent fluctuations are responsible for the breakup of the droplets, and that these fluctuations increase with increasing wavelength.

This yields

$$(We)_{crit} = \frac{\mathbf{r}_c \overline{u^2} D_{max}}{\mathbf{s}} \quad (2.4.5)$$

where $\overline{u^2}$ is the average value of the squares of the velocity differences over a distance D_{max} . For the case of isotropic, homogeneous turbulence, the main contribution to the kinetic energy is made by fluctuations where the wavelength is within the range valid for the Kolmogorov energy distribution law. With this assumption, the turbulence pattern will be solely determined by the dissipation rate of turbulent kinetic energy, ε . It can be shown for this region that

$$\overline{u^2} = C_1 (\mathbf{e} \cdot D)^{2/3} \quad (2.4.6)$$

where C_1 is approximately 2.0. The same power-law relationship was also determined by Kuboi *et al* [25] (see also Tennekes and Lumley [34]).

Martinez-Bazan *et al* examined the size particle distribution function (PDF) [29] and the break-up frequency [28] of an air bubble injected into a fully developed turbulent flow. While this analysis involves gas-liquid interaction, it is assumed that some of their discussion and results will also hold true for liquid-liquid systems. While we have chosen to use phenomenological models for the droplet size in the present study, the statistical aspects of their experiments will not be discussed in detail; however, the authors also present a model for the critical droplet size, which will be used for comparison with the numerical simulations.

In their experiments, air bubbles were injected into a high Reynolds number, vertical water jet at a prescribed distance along its centerline corresponding to fully developed turbulent flow. The Reynolds number of the jet was varied from 2.5×10^4 to 9×10^4 . The downstream location of the injection point of the air bubbles was also varied in the streamwise direction from 10 to 50 jet diameters, allowing for variations in the turbulent kinetic energy of the underlying turbulence. The size of the injected air bubbles was also varied by changing the flowrate of the air through the injection needle. Digital imaging techniques were then used to track the evolution of the droplet size distribution as a function of downstream distance.

Martinez-Bazan et al [28] developed a model for the break-up frequency of the injected air bubbles. While we are not interested in the statistical aspects of this model, an important relationship results from their analysis describing the critical droplet diameter, D_c , as a function of surface tension forces and the turbulent dissipation rate, ϵ . Here, the critical droplet diameter represents the largest bubble (droplet) diameter that will be stable and not break. According to their analysis, for a bubble to break, the deformation forces caused by turbulent stresses in the surrounding water must be greater than the surface restoring pressure. The minimum energy required to deform a bubble of size D is

$$E_s(D) = \rho \sigma D^2 \quad (2.4.7)$$

where σ is the interfacial tension. The corresponding surface restoring pressure is

$$t_s(D) = \frac{6E_s(D)}{\rho D^3} = \frac{6\sigma}{D} \quad (2.4.8)$$

The average deformation for per unit surface produced by turbulent stresses due to velocity fluctuations existing in the liquid at two points separated by a distance D is approximated by [28]

$$t_t(D) = \frac{1}{2} \rho \overline{\Delta u^2}(D) \quad (2.4.9)$$

where ρ is the density of the water. If the deformation force is greater than the surface restoring force, then the bubble will break. By setting the two equal to each other, a critical droplet diameter is defined such that droplets of smaller diameters will always be stable and will not break. Following Kolmogorov's theory, and assuming homogeneous isotropic turbulence, the mean value of the velocity fluctuations between two points separated by a distance D can be approximated by

$$\overline{\Delta u^2(D)} = \overline{|u(x+D, t) - u(x, t)|^2} = \mathbf{b}(\mathbf{e}D)^{2/3} \quad (2.4.10)$$

where β is a constant, approximately equal to 8.2 [3]. This is a different statement of Eq. (2.4.6). Substituting Eq. (2.4.9) into Eq. (2.4.8), and equating it with Eq. (2.4.7) yields the following expression for the critical droplet diameter

$$D_c = \left(\frac{12\mathbf{s}}{\mathbf{br}} \right)^{3/5} \mathbf{e}^{-2/5} \quad (2.4.11)$$

Although not directly applicable to the present study as these analyses were done for a gas-liquid system, this is a good example of a similar type of phenomenological model for determining the fluid droplet size based on certain flow parameters.

3.0 DESCRIPTION OF VARIOUS MATHEMATICAL MODELS

In this section we will describe the different mathematical models used and derive some of the model expressions. First, a description of the SFST model will be given, along with the form of the k- ϵ turbulence model used, including extra terms to account for buoyant production/destruction, and the correlation used for the slip velocity. The model expressions for the droplet formation/entrainment (DFE) model will be derived and presented in Section 5.0. For further information regarding the derivation of other model equations the reader is directed to Appendix A.

3.1 SFST Model Formulation for Immiscible Fluids

For the numerical predictions in this study, the multiphase model that was used was a mixture model, where only one set of momentum equations was solved for the given two-fluid system. Specifically, the model that was used was, to some extent, a simplified variation of the drift flux model as given by Ishii [22]. Essentially, the present study adopts the definitions for the mixture quantities and the form of the individual phase mass and momentum equations as given by Ishii [22]. From these definitions and equations, a model is developed for turbulent flows where two liquids mix and the relative velocity between the liquids is non-zero as is typical for buoyant flow of immiscible fluids. This model is described as being a single fluid, scalar transport (SFST) model.

The primary assumptions that are used in formulating the SFST model are: (i) the individual phases are incompressible, (ii) the flow is isothermal, (iii) the density difference between the phases is small compared to the density of the mixture. These assumptions allow certain terms to be neglected in the model equations for turbulent flows. Another important assumption involves the use of a gradient diffusion model for the average turbulent stresses in the momentum equations. The SFST model is described in the following sections, and the equations presented are written in terms of time-averaged variables.

As with any mixture model, the basic concept is to consider the two-phase mixture as a whole, rather than as two separate phases. The mixture variables are defined as:

the center of mass velocity (or mixture velocity)

$$u_m = \frac{(u_a r_a \mathbf{r}_a + u_b r_b \mathbf{r}_b)}{\mathbf{r}_m} \quad (3.1.1)$$

mixture density

$$\mathbf{r}_m = \mathbf{r}_a r_a + \mathbf{r}_b r_b \quad (3.1.2)$$

and mixture viscosity

$$\mathbf{m}_m = \mathbf{m}_a r_a + \mathbf{m}_b r_b \quad (3.1.3)$$

where the unmixed phase quantities are denoted by the subscripts α and β (e.g. u_α is the velocity of phase alpha) and r is the phase volume fraction. In light of these definitions, the current model expresses the conservation of mass and momentum for the two-phase mixture by summing the individual phase equations to form a single equation. Here the

momentum inter-phase transfer terms, as would be found in a two-fluid model, cancel each other in the addition. The resulting equations are then put into a form similar to the single-phase Navier-Stokes equations where the variables of interest are the mixture variables. Since the flowfield is turbulent, the model equations are modified to account for turbulent stresses and turbulent diffusion. The additional terms that appear in the equations because of time averaging are modeled using an eddy viscosity model. The mixture density fluctuations in the multiphase equations do present some complications in the derivation of the model equations. Though these fluctuations in the density do exist, for cases where the density of either phase is large compared to the density difference, they may be neglected in the continuity and momentum equations. Fortunately for the cases under consideration in this study, the assumption concerning the density difference being small is valid.

The conservation of mass equation is given by

$$\frac{\partial(\rho_m)}{\partial t} + \frac{\partial(\rho_m u_{m,i})}{\partial x_i} = 0 \quad (3.1.4)$$

which is derived from the addition of the individual phase continuity equations. The assumption that the density fluctuations in the mixture density may be neglected allows the time-averaged mixture continuity equation to be given by the same form as the instantaneous mixture continuity equation.

The individual phase momentum equations are added and the resulting equation is put into a form that is similar to the single-phase Navier-Stokes equations for Newtonian fluids with variable properties (see Umbel [37]).

The resulting momentum equations for a turbulent flow are then given by

$$\begin{aligned} \frac{\mathcal{I}}{\mathcal{I}t} [\mathbf{r}_m u_{m,i}] + \frac{\mathcal{I}}{\mathcal{I}x_j} [\mathbf{r}_m u_{m,i} u_{m,j}] = & - \frac{\mathcal{I}}{\mathcal{I}x_j} \left[\frac{r_a \mathbf{r}_a r_b \mathbf{r}_b}{\mathbf{r}_m} (u_{S,i} u_{S,j}) \right] \\ & - \frac{\mathcal{I}P}{\mathcal{I}x_i} + \frac{\mathcal{I}}{\mathcal{I}x_j} \left((\mathbf{m}_m + \mathbf{m}_l) \frac{\mathcal{I}u_{m,i}}{\mathcal{I}x_j} \right) + \mathbf{r}_m g_i \end{aligned} \quad (3.1.5)$$

where the respective phases are denoted by α and β , and indicial notation is used where repeated indices indicate summation. The slip (or relative) velocity in Eq. (3.1.5) is given by

$$u_{S,i} = (u_{a,i} - u_{b,i}) \quad (3.1.6)$$

In the mixture momentum equation, an additional flux due to the relative motion between the phases appears as the second term on the right hand side of equation (3.1.5). This extra term is sometimes referred to as the drift flux term, and originates from using the mixture velocity definition in the convective terms. It accounts for the macroscopic flux of momentum due to the relative velocity between the phases and is written on the right hand side of the equation as a fictitious stress term. This is somewhat analogous to the microscopic transport of momentum due to the molecular transport that produces viscosity.

The primary assumption of the mixture model is that the dynamics of the two phases can be expressed by the preceding mixture momentum equation and some algebraic equation for the slip velocity between the phases. In general, the model assumes an empirical slip velocity relation of the form

$$u_S = f(r_a, \mathbf{r}_m, u_m, g, \dots) \quad (3.1.7)$$

This assumption is justified if the motion of the two phases is strongly coupled. Since the freedom of using one of the phase momentum equations is still available, it can be used to aid in determining the slip velocity equation. An equation for the slip velocity can be determined by assuming that the slip velocity is a function of the terminal velocity of an average size droplet. For flows in which more extensive relationships are needed, experiments can be used to aid in determining equations for the slip velocity. These assumptions reduce the two individual phase momentum equations into a single momentum equation with one extra term that is a function of the slip velocity. The form of the slip velocity used in the present study will be discussed in Section 3.3.

The volume fractions are solved from one of the individual phase continuity equations and from the algebraic constraint that the individual phase volume fractions must sum to unity (i.e. $r_\alpha + r_\beta = 1$). It should be noted that the turbulent fluctuations in the volume fraction must be maintained in the formulation; hence, to account for turbulent diffusion of the volume fraction (i.e. turbulent flux terms $-\overline{r'_a u'_m}$), the turbulent transport terms are modeled using an eddy diffusivity model. In the present study, the α -phase continuity equation is put into the form of a scalar transport equation, with a source term that is a function of the slip velocity. The time-averaged form of the modeled transport equation in the SFST model is given by (See Appendix A.2 for a detailed derivation):

$$\frac{\partial}{\partial t} [r_m \mathbf{f}] + \frac{\partial}{\partial x_i} [r_m u_{m,i} \mathbf{f}] = - \frac{\partial}{\partial x_i} \left[\frac{r_a \mathbf{f} (1 - \mathbf{f}) u_s}{\mathbf{f} + R(1 - \mathbf{f})} \right] + \frac{\partial}{\partial x_i} \left[\Gamma \left(\frac{\partial \mathbf{f}}{\partial x_i} \right) \right] \quad (3.1.8)$$

where $R = \rho_\alpha/\rho_\beta$ represents the ratio of the two fluid densities, and Γ represents the effective diffusivity. Here the slip velocity, u_s , appears in an additional convective term (treated as a source term), and the equation is solved for the scalar variable, ϕ .

From this, then, the volume fraction of the lighter phase (i.e. the fuel) is solved from the following algebraic relation:

$$r_a = \frac{f}{f + R(1-f)} \quad (3.1.9)$$

The volume fraction of the heavier phase is then solved from the algebraic constraint that the two must sum to unity. This solution of the volume fraction is particularly appealing since it is not directly dependent on the solution of the mixture density, which in turn depends on the solution of the volume fraction (see Eq. (3.1.2)), requiring an iterative procedure. It should be noted that this methodology for the solution of the volume fraction differs from that used in the previous version of the SFST model [8,37] in that it requires no simplifying assumptions concerning the density variations. A full derivation of Eq. (3.1.8) and Eq. (3.1.9) is given in Appendix A.2.

In summary, Eqs. (3.1.4), (3.1.5), (3.1.7), and (3.1.8) represent four coupled equations which can be solved for the mixture velocity, pressure, phase volume fractions, and relative velocity between the phases. This model maintains the provision of reducing to a set of single-fluid equations with variable properties and some additional source terms, which may be easily added in any single-phase code. Hence, the name single fluid, scalar transport (SFST) model is based on the model's close ties to its corresponding single-

phase equations. It should be noted that in light of this fact, the SFST model does provide for the expected density variation in the continuity and momentum equations and also provides for relative velocity effects between the phases. These capabilities are important features of the model, making it attractive in any extensive computational effort for predicting immiscible multiphase flows.

3.2 k-e Turbulence Model for Buoyant Flows

While most turbulence is generated as a function of shear, in flows with appreciable density gradients the turbulent eddies may receive or lose energy due to the effects of buoyancy. For flows with density gradients, it can be shown that the specific turbulent kinetic energy equation is given by (see e.g. [32])

$$\begin{aligned} \frac{\overline{\rho k}}{\overline{\rho}} + \frac{\overline{\rho}}{\overline{\rho}} \left(\overline{\rho u_j k} \right) = \overline{\rho} \frac{\overline{u_i}}{\overline{\rho}} - \overline{\rho} \frac{\overline{u_i' u_i'}}{\overline{\rho}} + \overline{u_i' \rho' g} + \\ \frac{\overline{\rho}}{\overline{\rho}} \left(\overline{\rho} \frac{\overline{k}}{\overline{\rho}} - \frac{1}{2} \overline{\rho u_i' u_i' u_j'} - \overline{\rho' u_j'} \right) \end{aligned} \quad (3.2.1)$$

where the density fluctuations in the inertial terms have been neglected. Here $\overline{()}$ denotes a fluctuating component. Each of the terms in Eq. (3.2.1) are accounted for in the original modeled k -equation, except for the extra term represented by

$$G_k = \overline{u_i' \rho' g} \quad (3.2.2)$$

which is referred to as buoyant production and represents the rate of work done against buoyancy forces by the turbulent motion. This is essentially a transfer of either potential energy to turbulent kinetic energy, as would be the case in an unstably stratified flow, or a transfer of turbulent kinetic energy to potential energy, as would be the case in the

mixing of a heavy fluid with a lighter fluid against the action of gravity (stably stratified flow).

The buoyancy production term is usually modeled as [32]

$$G_k = -\sigma_p \overline{u_i' r'} = \sigma_p \frac{\overline{u_i' r}}{\overline{u_i' x_i}} \quad (3.2.3)$$

Here σ_p is a kind of turbulent Prandtl number that is usually taken equal to 1.0. A negative density gradient corresponds to a stably stratified flow and the term acts as a sink on turbulent kinetic energy. The correlation between the fluctuating vertical velocity component and fluctuating density tends to be positive. For positive density gradients an unstable stratification exists and the term acts as a source for k ; this corresponds to the negative correlation between the fluctuating vertical velocity component and fluctuating density.

The epsilon equation is modified by adding the source term given by

$$G_e = \frac{C_{e1} \epsilon}{k} C_{e3} \max(G_k, 0) \quad (3.2.4)$$

where C_{e3} is a constant [32]. This term increases ϵ for unstable stratification and gives no change in ϵ for stable stratification. In CFX, G_k and G_e are included using the thermal expansion coefficient; for isothermal flows, when a generic scalar transport equation is solved, they must be added via user FORTRAN.

With the modeled equations defined as above, the k - ϵ turbulence model for buoyant flows in a Cartesian coordinate system is given by:

the k -equation:

$$\frac{\overline{rk}}{\overline{t}} + \frac{\overline{ru_j k}}{\overline{x_j}} = t_{ij} \frac{\overline{u_i}}{\overline{x_j}} - r\mathbf{e} + \frac{\overline{r}}{\overline{x_j}} \left(\left(m + \frac{m_t}{s_k} \right) \frac{\overline{r k}}{\overline{x_j}} \right) + g \frac{m_t}{r s_r} \frac{\overline{r}}{\overline{y}} \quad (3.2.5)$$

and the ε -equation:

$$\frac{\overline{r\mathbf{e}}}{\overline{t}} + \frac{\overline{ru_j \mathbf{e}}}{\overline{x_j}} = C_{e1} \left(\frac{\mathbf{e}}{k} t_{ij} \frac{\overline{u_i}}{\overline{x_j}} + \frac{\mathbf{e}}{k} C_{e3} \max(G_k, 0) \right) - C_{e2} r \frac{\mathbf{e}^2}{k} + \frac{\overline{r}}{\overline{x_j}} \left(\left(m + \frac{m_t}{s_e} \right) \frac{\overline{r\mathbf{e}}}{\overline{x_j}} \right) \quad (3.2.6)$$

where

$$m_t = \frac{r C_m k^2}{\mathbf{e}} \quad (3.2.7)$$

$$\Gamma_t = \frac{m_t}{s_r} \quad (3.2.8)$$

$$t_{ij} = -\overline{ru'_i u'_j} = m_t \left(\frac{\overline{u_i}}{\overline{x_j}} + \frac{\overline{u_j}}{\overline{x_i}} \right) - \frac{2}{3} r k d_{ij} \quad (3.2.9)$$

with the closure coefficients given by

$$C_{e1} = 1.44, \quad C_{e2} = 1.92, \quad C_{e3} = 1.0, \quad C_\mu = 0.09, \quad \sigma_k = 1.0, \quad \sigma_\varepsilon = 1.3,$$

$$\sigma_r = 1.0, \quad \sigma_\rho = 1.0$$

In Eqs. (3.2.5) - (3.2.9) ρ represents the mixture density ρ_m .

3.3 Empirical Correlation for the Slip Velocity

The correlation used for the slip velocity in the present form of the SFST model assumes that the relative velocity between the two phases is proportional to the terminal velocity of a single particle in an infinite medium. The effects of multiple droplets are then

included via a function of the volume fraction of the continuous phase, with the condition that the slip velocity must approach the terminal velocity in the dilute limit (i.e. when the volume fraction of the dispersed phase approaches zero).

According to Ishii and Zuber [24], the terminal velocity of a single solid particle in an infinite medium, $V_{r\infty}$, is given by

$$V_{r\infty}|V_{r\infty}| = \frac{8}{3} \frac{r_d}{C_{D\infty} \mathbf{r}_c} (\mathbf{r}_c - \mathbf{r}_d) g \quad (3.3.1)$$

where $C_{D\infty}$ represents the drag coefficient for a single particle in an infinite medium, r_d is the radius of the particle or droplet, and the subscripts c and d denote the continuous and dispersed phase, respectively. Writing Eq. (3.3.1) in terms of the droplet diameter yields

$$V_{r\infty}|V_{r\infty}| = \frac{4}{3} \frac{d_p}{C_{D\infty} \mathbf{r}_c} (\mathbf{r}_c - \mathbf{r}_d) g \quad (3.3.2)$$

For a multiple particle system, the relative velocity between the two phases is given by [24]

$$V_r|V_r| = \frac{8}{3} \frac{r_d}{C_D \mathbf{r}_c} (\mathbf{r}_c - \mathbf{r}_d) g (1 - \mathbf{a}_d) \quad (3.3.3)$$

where \mathbf{a}_d represents the dispersed phase void fraction. Next we assume that in Allen's regime, the drag coefficient for the single particle system displays a direct similarity to that for the multiple particle system. Allen's regime is typically defined for particle Reynolds numbers between 1 and 1000, where the particle Reynolds number, Re_p , is defined according to

$$\text{Re}_p = \frac{\mathbf{r}_c V_r d_p}{\mathbf{m}_c} \quad (3.3.4)$$

The form of the drag coefficient, C_D , in this flow regime is given by [24]

$$C_D = \frac{24}{\text{Re}_p} \left(1 + 0.1 \text{Re}_p^{0.75} \right) \quad (3.3.5)$$

Here, we make a slight simplification by assuming a power-law curve fit of Eq. (3.3.5) given by [37]

$$C_D = \frac{18}{\text{Re}_p^{0.6}} \quad (3.3.6)$$

This is done to avoid costly iteration in the numerical algorithm. Substituting for Eq. (3.3.6) and Eq. (3.3.4) in Eq. (3.3.3) yields

$$V_r^2 = \frac{4gd_p \Delta \mathbf{r} (1 - \mathbf{a}_d)}{3(18)\mathbf{r}_c} \left[\frac{\mathbf{r}_c V_r d_p}{\mathbf{m}_c} \right]^{0.6} \quad (3.3.7)$$

which becomes

$$V_r = \left[\left(\frac{4gd_p^{1.6}}{54\mathbf{m}_c^{0.6}} \right) \left(\frac{\mathbf{r}_c - \mathbf{r}_d}{\mathbf{r}_c^{0.4}} \right) \right]^{5/7} (1 - \mathbf{a}_d)^{5/7} \quad (3.3.8)$$

It can then be shown that by simply solving for the terminal velocity for a single particle system yields the bracketed term on the right hand side of Eq. (3.3.8). Therefore, the relative or slip velocity for a multiple particle system can be written as a function of the dispersed phase volume fraction multiplied by the terminal velocity for a single particle.

The general form of this expression then is given by [24]

$$u_s = (1 - \mathbf{a}_d)^m u_{s\infty} \quad (3.3.9)$$

where $u_{s\infty}$ represents the terminal velocity for a single particle in an infinite medium, and the exponent “m” will be investigated in later chapters. This empirical correlation is a

rather simple one. For more advanced relationships, an alternative slip velocity correlation is given in Appendix A.3.

4.0 MASS CONSERVATION IN THE SFST MODEL

Due to questions regarding fuel mass (volume) conservation in the previous version of the SFST model, a new algorithm has been formulated for determining the volume fraction of the light phase (i.e. the fuel). These problems arose when it was found that the previous version of the SFST model did not conserve the fuel volume in the domain within a reasonable error. It is important to keep in mind that the present study is an element of a larger project, which is constantly undergoing modification. In this section, the new formulation for the solution of the volume fraction will be given, along with results detailing the improvement in the conservation of the fuel volume as compared with results from the previous model. Further details concerning the previous version of the SFST model can be found in Celik *et al* [8], and Umbel [37].

4.1 Validation and Case Specific Issues

To validate the new formulation for the solution of the volume fraction in the SFST model, and for comparison with previous results, a two-dimensional test case was developed involving a shear layer flow within a filling process. A schematic of the geometry used is given in Figure 4.1. The overall dimensions of the center compartment were 40 cm long by 20 cm high by 20 cm wide. For the two-dimensional simulation, however, the z-direction is ignored, using only one cell length in the direction of the tank width. The dimensions of the inlet and outlet compartments each measured 10 cm long

by 10 cm high. A uniform grid was employed such that each computational cell measured 5 mm long by 5 mm high, with a volume of $5.0 \times 10^{-6} \text{ m}^3$. While this computational mesh was somewhat coarse, it was used for economy of computational time so that several different parameters could be investigated.

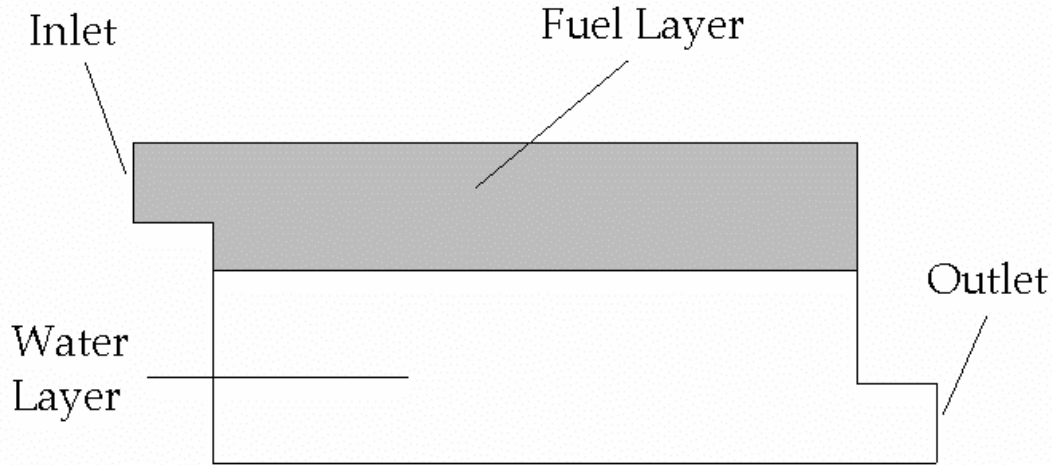


Figure 4.1 - Schematic of two-dimensional test case geometry.

The tank was initially filled with water, having a density of 1000.0 kg/m^3 in the lower portion of the tank, and fuel, having a density of 850.0 kg/m^3 , in the upper portion. The initial condition was prescribed in this manner so that only one fluid would be present at the inlet and outlet and the boundary conditions could be examined. The inlet consisted of specified values of the velocity and volume fraction. Here the inlet velocity was specified as 0.01 m/s , corresponding to a Reynolds number of 1,000, and 0.2353 m/s , corresponding to a Reynolds number of 10,000, for a laminar and turbulent flow case, respectively.

For the turbulent flow cases, the values of the turbulence quantities, k and ε , were specified at the inlet according to [12]

$$k_{inl} = c_{p1} U_{inl}^2 \quad (4.1.1)$$

and

$$\varepsilon_{inl} = \frac{k_{inl}^{1.5}}{c_{p2} D_H} \quad (4.1.2)$$

where D_H is the hydraulic diameter, and c_{p1} and c_{p2} are empirical constants with values of 0.002 and 0.3, respectively. Hence, Dirichlet boundary conditions were set on all variables at the inlet, except for the pressure, which was extrapolated from downstream. The outlet was modeled by setting a zero-derivative condition on all transported variables.

Of primary interest in these simulations was the comparison of the predicted fuel volume within the tank with the theoretical value that was expected if mass (volume) were conserved. Here, the theoretical value of the fuel volume was determined from the following relation

$$V_f^{new} = V_f^{old} + [(Q_f)_{in} - (Q_f)_{out}] \cdot \Delta t \quad (4.1.3)$$

where V_f is the total fuel volume contained in the tank, Q_f is the volumetric flowrate of the fuel, Δt is the time step, and the superscripts represent the corresponding time step. In cases with constant fuel flow at the inlet, and where there is no fuel exiting the domain, this expression reduces to the product of the inlet flowrate and the elapsed time, given by

$$V_f = (Q_f)_{in} t \quad (4.1.4)$$

The predicted value of the total fuel volume in the tank was determined using integral methods across the entire domain. In order to accomplish this integration, a rectangular (mid-point) rule was employed, where the volume of fuel contained in each computational cell was summed over the entire domain at each time step. While a more accurate integration scheme such as Simpson's rule could have been employed, it was found that the much simpler mid-point rule was sufficient for the present task. It should also be noted that Simpson's rule does not perform well for cases involving sharp gradients. This would be the case for the laminar flow cases studied, as the fuel/water interface would remain sharp in the absence of mixing. In order for an independent comparison to be made between the two formulations for the solution of the volume fraction, then, the mid-point rule was applied in all cases.

All numerical simulations were performed as transient, two-dimensional flows, where time marching was accomplished using Euler's method. A total elapsed time of 20.0 seconds was used for each run, as this was expected to be a reasonable amount of time to investigate the changes in the fuel volume within the tank. For the turbulent flow cases, where the inlet velocity was much higher, this elapsed time also allowed for some of the fuel to exit the domain, so that the boundary conditions at the exit could be examined.

The velocity components were discretized using the higher-order upwind scheme, while the turbulence quantities used the HYBRID scheme, and the Poisson equation for the pressure was discretized using central differencing. During the course of our investigations, it was determined that some improvement could be achieved by using a

flux limiting scheme for the solution of the volume fraction, rather than the first-order upwind scheme as recommended by the CFX User's Manual [12]. Here we have chosen to use a MUSCL scheme, namely the MIN-MOD scheme. In order to illustrate this improvement, results are presented below for a laminar flow case using the geometry described previously. Figure 4.2 shows the predicted variations in the fuel volume compared with the theoretical value, using both upwinding and MIN-MOD.

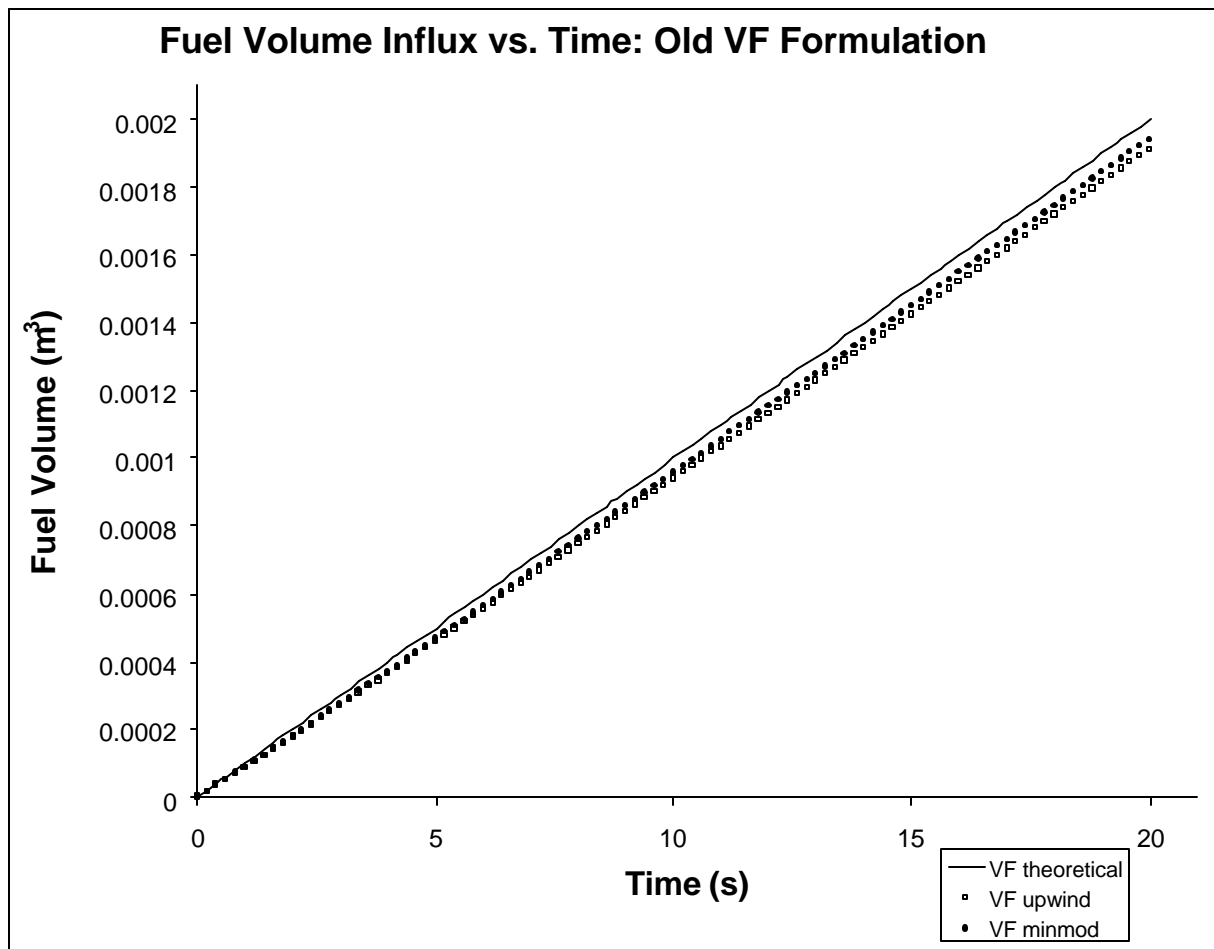


Figure 4.2 – Comparison of predicted fuel volume using upwind and MIN-MOD schemes.

It is seen in Fig. 4.2, the predictions of the fuel volume using the MIN-MOD scheme more closely match the theoretical values. The errors in these predictions are given in Fig. 4.3 below and serve to better clarify this point.

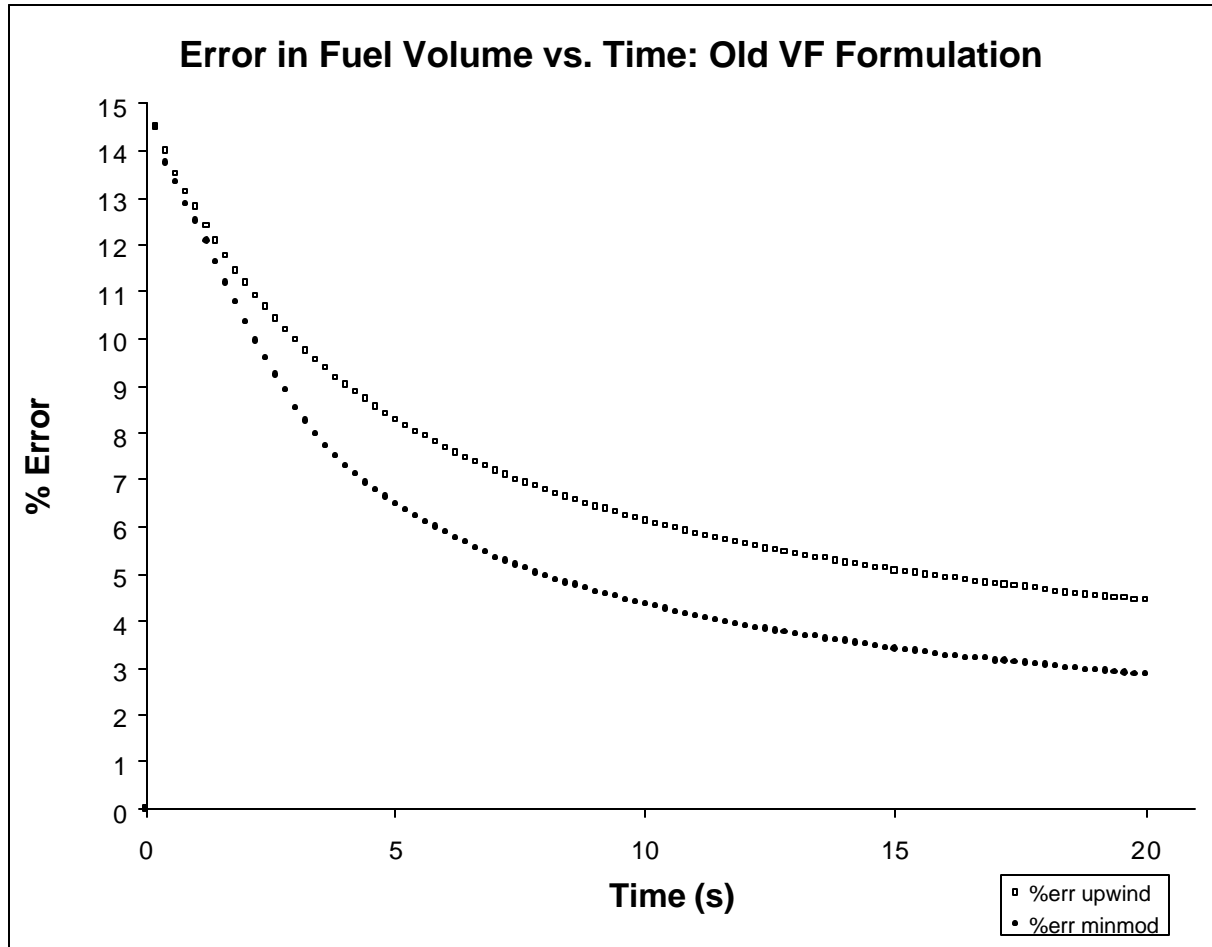


Figure 4.3 – Errors in predicted fuel volume using upwind and MIN-MOD schemes.

Figure 4.3 above provides a much clearer picture concerning the predictions of the variation in the fuel volume using these two schemes. After an elapsed time of 20.0 seconds, the predictions of the fuel volume using first-order upwinding differ from the theoretical value by approximately 4.5%, while those using the MIN-MOD scheme are in error by slightly less than 3%. In a typical simulation with a large number of

computational cells, this can become a considerable error. It should be noted that this result differs from the recommendation in the CFX User's Manual [12], which suggests that first-order upwinding be used for user-defined scalar variables.

Having illustrated the improvement in using the MIN-MOD scheme, we will now present results in which comparison will be made between the new formulation for the solution of the volume fraction and that used in the previous version of the SFST model. Figures 4.4 and 4.5 below show the predicted fuel volume using both formulations and the errors in those predictions, respectively, for the laminar flow case.

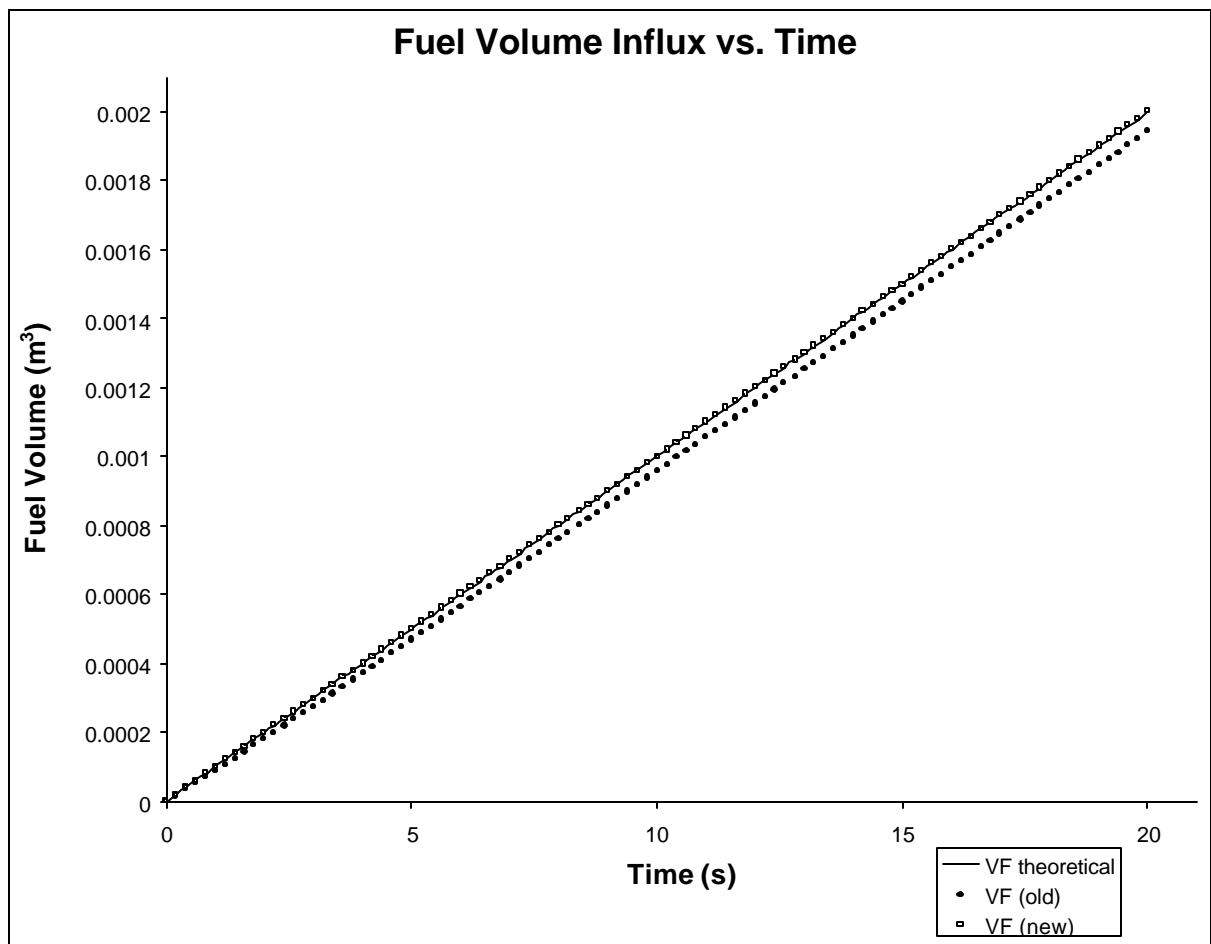


Figure 4.4 – Comparison of variations in predicted fuel volume with time (laminar flow case).

As can be seen in Fig. 4.4 above, the new formulation for the volume fraction predicts the fuel volume in the tank nearly exactly, while there is some error in the predictions using the previous formulation. This result was expected, as certain simplifying assumptions were made in the previous version of the SFST model, while the new formulation involves no assumptions except those involved in the turbulence modeling. Figure 4.5 below depicts the errors in the predicted fuel volume and shows that the error in the new formulation is very nearly zero (to at least 7 decimal places), while the predictions using the previous formulation show a significant error.

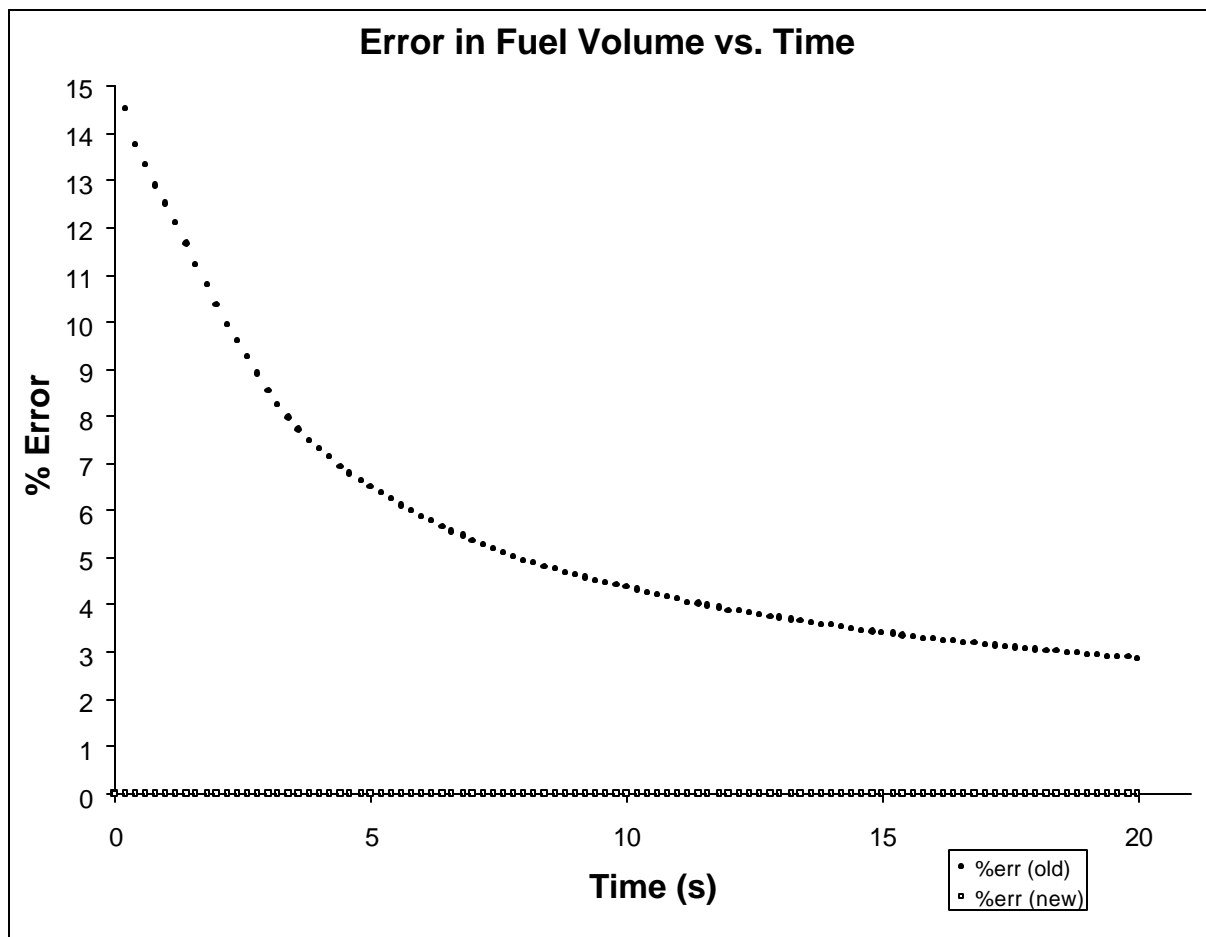


Figure 4.5 – Errors in predicted fuel volume as a function of time (laminar flow case).

In order to ensure that the new formulation of the volume fraction is indeed conservative for all flow scenarios, we will next present results for the turbulent flow case as described previously. Similar profiles for the variation in the fuel volume and the errors upon comparison with the theoretical values are given in Figures 4.6 and 4.7, respectively.

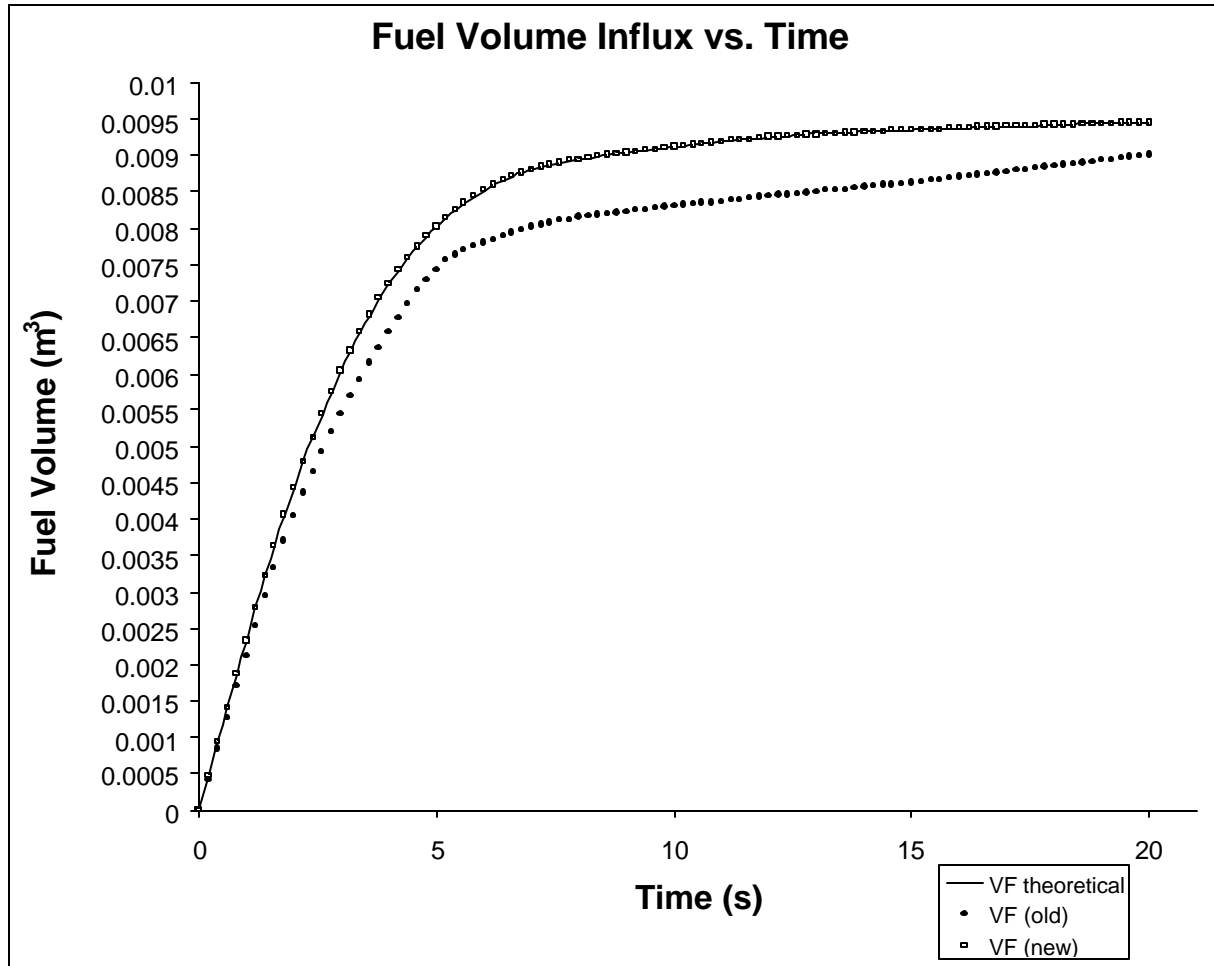


Figure 4.6 – Comparison of variations in predicted fuel volume with time (turbulent flow case).

Again we can see that the new formulation for the solution of the volume fraction predicts the fuel volume within the tank with very little error. This is further

demonstrated by the errors in the predicted fuel volume when compared with the theoretical value depicted in Fig. 4.7 below.

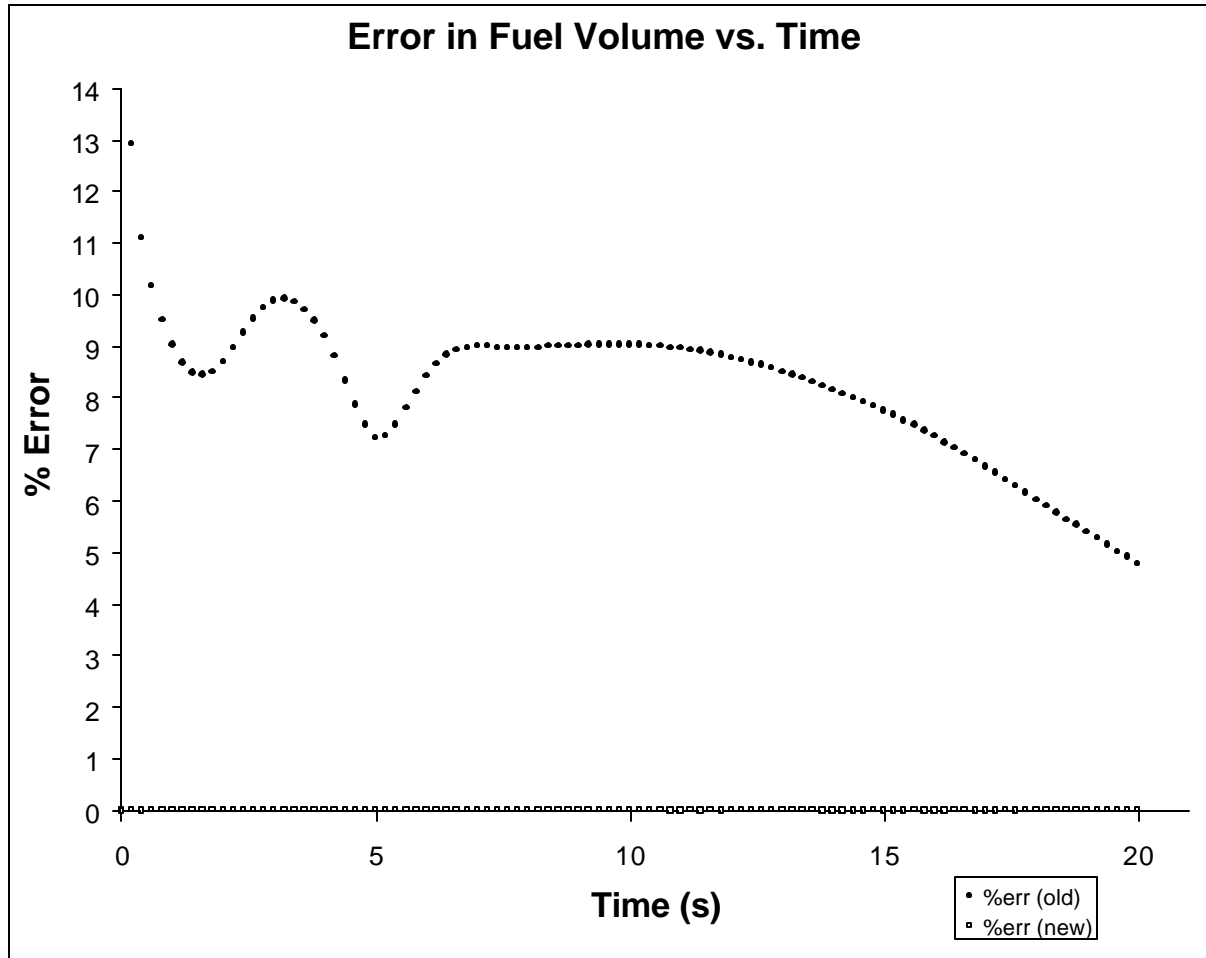


Figure 4.7 – Errors in predicted fuel volume as a function of time (turbulent flow case).

The new volume fraction formulation was next applied to a fully turbulent, three-dimensional flow case. A wireframe sketch of the two-compartment geometry used for these simulations is given in Fig. 4.8. The overall dimensions of the tank were 1.2 m long by 1.2 m wide by 0.8 m high. The relatively course uniform grid used was 24x24x16, for a total of approximately 9,200 cells, each with a volume of $1.25 \times 10^{-4} \text{ m}^3$.

As in the two-dimensional case, we have chosen to use a coarse grid for economy of computational time, while allowing that this may cause some numerical errors.

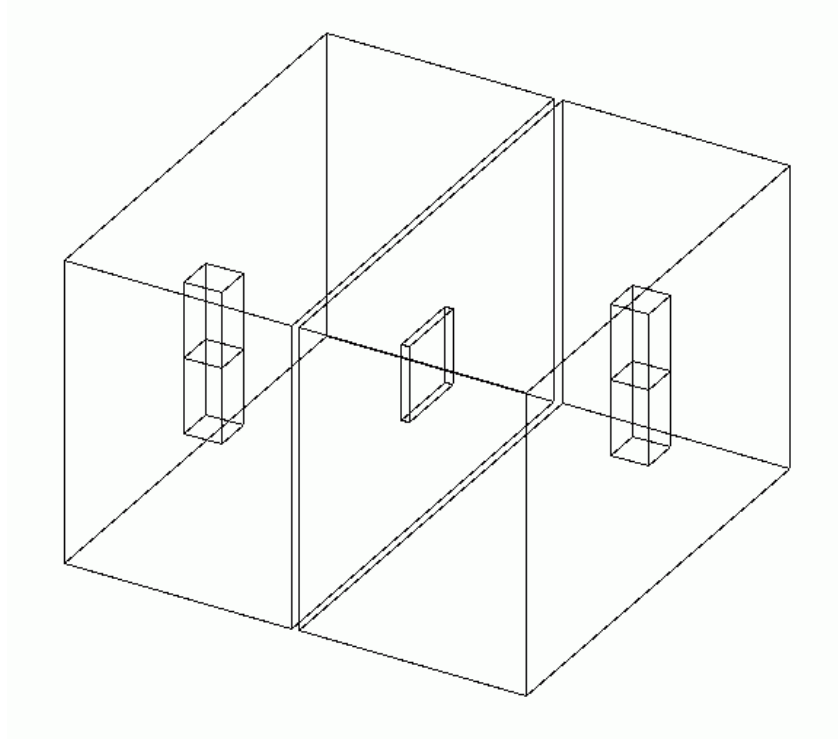


Figure 4.8 – Wireframe sketch of two-compartment geometry.

The inlet velocity was specified as 1.0 m/s, resulting in a Reynolds number of approximately 85,000 based on the inlet parameters. The same differencing schemes as were used for the two-dimensional case were used for all variables. A total elapsed time of 20.0 seconds was simulated using the geometry given above. This case allowed for a fully turbulent, three-dimensional flow scenario to be simulated using the new formulation for the volume fraction, and to study the conservation of the fuel volume.

The variations in the fuel volume and errors when compared with the theoretical values are given in Figures 4.9 and 4.10, respectively. Again, we have shown that the solution

of the fuel volume as a function of time is extremely accurate. In this case, the error does not exceed 0.18 % after an elapsed time of 20.0 seconds.

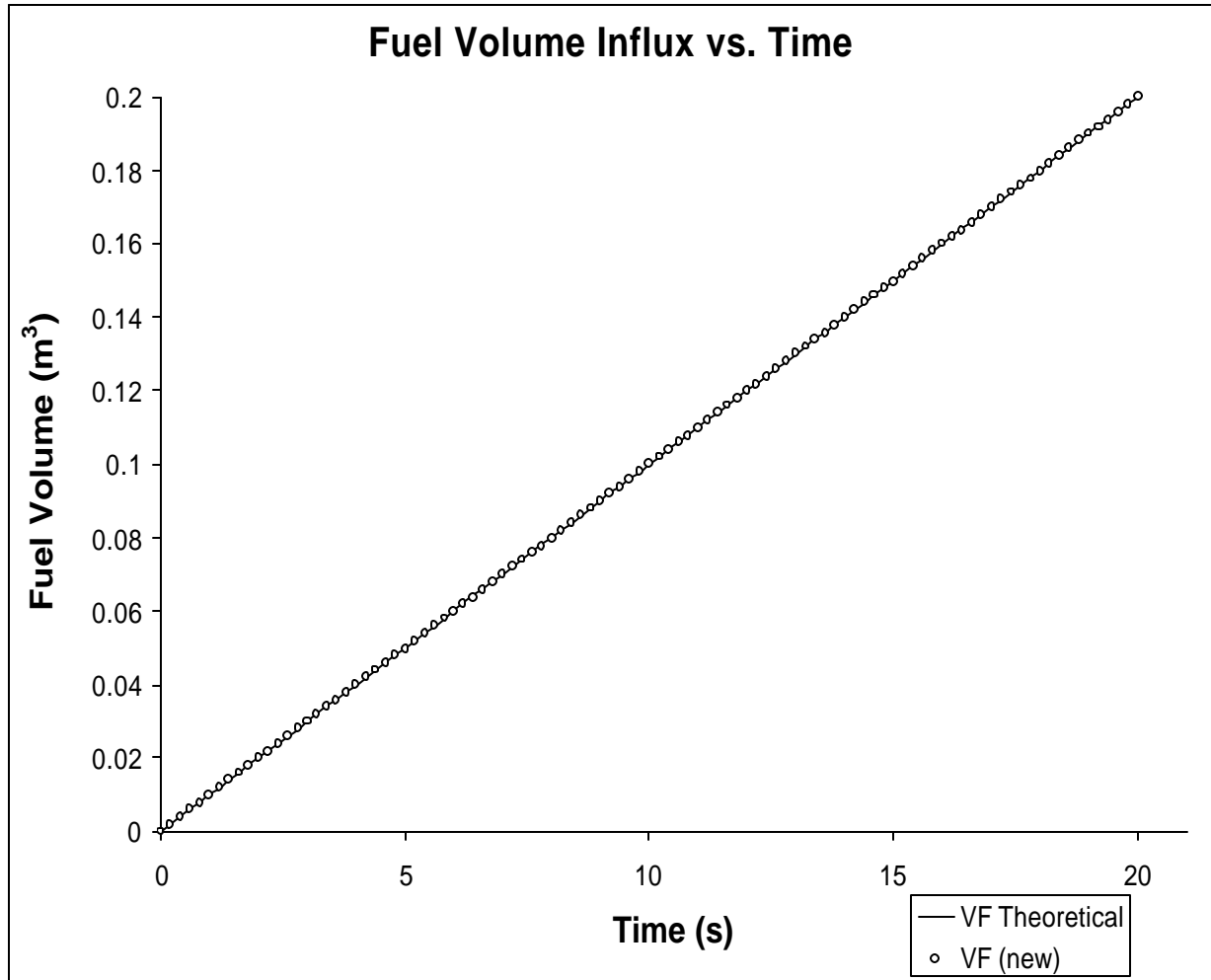


Figure 4.9 – Predicted variations in fuel volume with time (3-D turbulent flow case).

The errors shown in Fig. 4.10 below further demonstrate the accuracy in predictions of the fuel volume using the new formulation for the solution of the volume fraction equation.

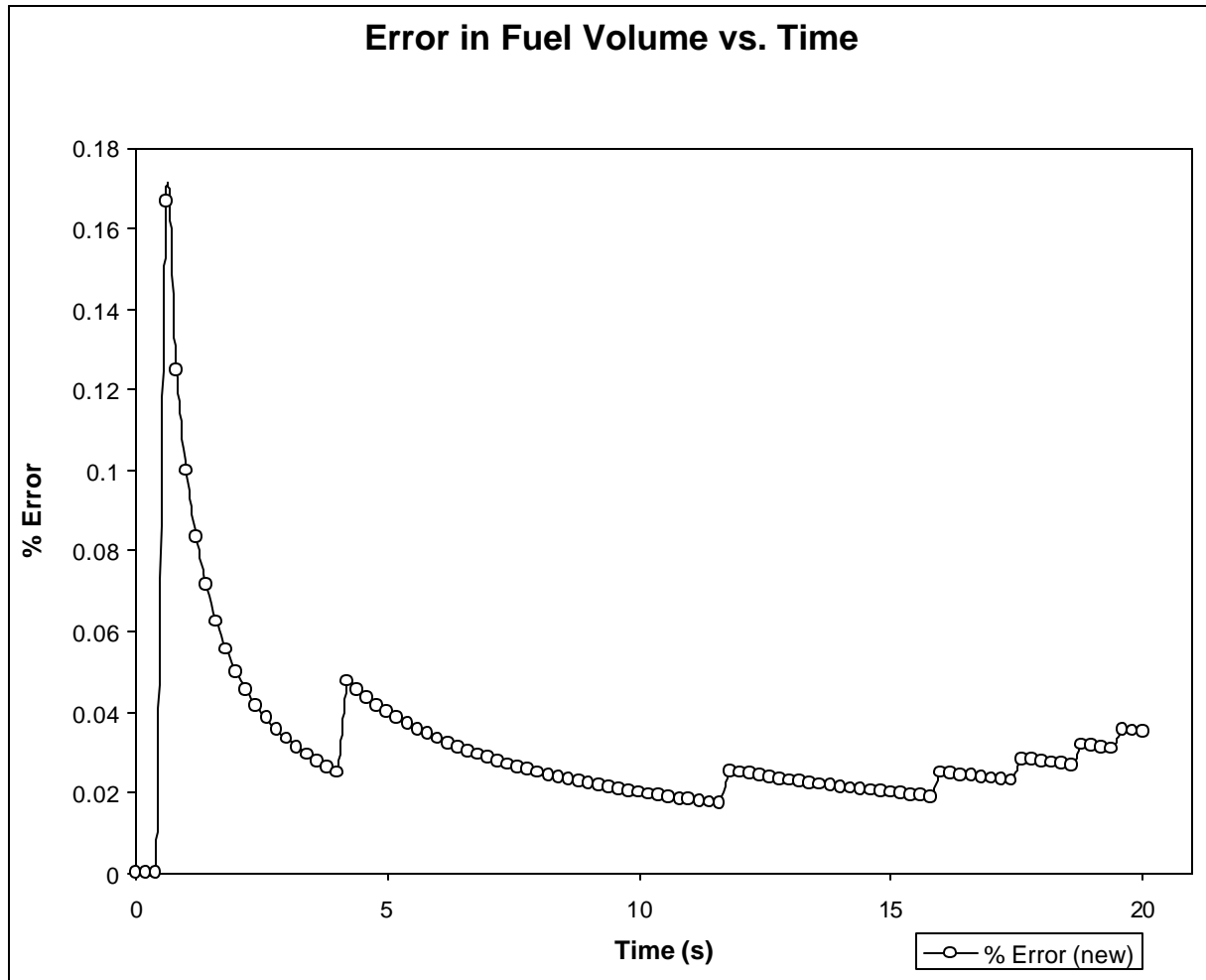


Figure 4.10 – Errors in predicted fuel volume vs. time (3-D turbulent flow case).

4.2 Summary and Conclusions

Due to questions regarding the conservation of mass (volume) in the SFST model, a new formulation for the solution of the volume fraction was developed. To validate the new model, an extensive series of tests was conducted, using both a two-dimensional and three-dimensional geometry, for both laminar and turbulent flow scenarios. During the course of the investigations, it was found that the differencing scheme used to discretize

the volume fraction equation, namely first-order upwind, was not a good choice. In light of this, a flux-limiting scheme, namely MIN-MOD, was used as it provided boundedness in the solution of the volume fraction. Following this careful analysis, it has been demonstrated that the new formulation for the volume fraction shows a high degree of accuracy in the prediction of the fuel volume for a variety of flow conditions and geometries.

5.0 DERIVATION OF DROPLET FORMATION/ENTRAINMENT MODEL

A mathematical model is currently being developed to predict the local size of any dispersed phase (i.e. fuel) droplets, which are formed as a result of instabilities at the fluid interface. The current form of the model follows the discussion by Sullivan & List [33] in dividing the flow into several different regimes. According to Figure 12 [33], these flow regimes include a turbulent interface regime, Kelvin-Helmholtz (K-H) regime, a wave-breaking regime, and a molecular-diffusion-dominated regime. Each of these regimes can be delineated by an appropriately defined Richardson number, in this case the layer Richardson number which is defined according to

$$Ri_L = \frac{g\Delta\rho h}{\rho_1(\Delta U)^2} \quad (5.0.1)$$

where $\Delta\rho$ is the difference in the two unmixed fluid densities, h is the boundary-layer thickness, ρ_1 is the density of the lighter phase, and ΔU is the difference in the free stream velocities of the two fluid layers.

Since in both the K-H regime and the wave-breaking regime the interface mixing mechanism involves Kelvin-Helmholtz type waves, we have chosen to combine these two into one, referred to as the Kelvin-Helmholtz vortices regime. The present form of the model does not include the molecular-diffusion-dominated regime, which occurs at very large values of the Richardson number, as we expect that this regime will not occur often in our application. At a later time this regime may be included by utilizing a newly

formed length scale based on the mixture kinematic viscosity. This will be discussed later.

5.1 Description of Flow Regimes

For our simulations, we have chosen to consider the two flow regimes that we believe will occur most often in our application. These include the turbulent interface regime for very low values of the Richardson number, and the K-H vortices regime for moderate values of the Richardson number. The latter was composed of the K-H regime and the wave-breaking regime as described by Sullivan & List [33]. Descriptions of the various flow regimes are given below.

Turbulent Interface Regime

This regime occurs at very low values of the Richardson number. As the Richardson number is a measure of the relative influence of buoyancy and shear forces, this would correspond to areas where the effects of shear forces are dominant. We will assume that for this regime, the size of any droplets formed is directly controlled by the local turbulence quantities k and ε (e.g. see Eq. 2.4.12).

K-H Vortices Regime

The second regime that we have considered in the present droplet model is that of the Kelvin-Helmholtz vortices regime, which occurs for moderate values of the Richardson number. In this regime, the fluid interface becomes unstable and waves develop. The

mixture mechanism is dominated by the roll-up and pairing of K-H type vortices, which scour fluid away from the mixed fluid region. Depending on the value of the Richardson number these waves will either grow and collapse cyclically, or, if buoyancy forces are great enough (i.e. the Richardson number is large enough), then the waves will become too large, leading to gravitational instability, and will break. We assume that in this regime the size of any droplets formed is proportional to the height of these K-H type waves, which develop as a result of instabilities at the interface. Through our analysis of some of the results from the literature for two-dimensional stratified shear flow, we have related this wave height to an appropriately defined length scale and to the Richardson number. The length scale determination will be discussed later.

Molecular-Diffusion Regime

This regime occurs for relatively large values of the Richardson number, where the effects of shear are very small compared to buoyancy. Because of this, very few or no instabilities occur at the interface, and the mixing is dominated by molecular diffusion. At the present time we are ignoring this regime, as we expect that it will not occur often in our application. In the future, this regime may be included by making use of a characteristic length scale $l_d = \nu/V$, where ν is the kinematic viscosity and V is the vertical velocity. This length scale can then be substituted into the expression for the droplet diameter in the K-H vortices regime, and it may also account for the changing Richardson number, which will be much higher in this regime. (See section 5.3)

5.2 Flow Regime Boundaries

As stated above, we have divided the flow into several different regimes, each of which is delineated by an appropriately defined Richardson number. The discussion by Sullivan & List [33] used the layer Richardson number; however, for our simulations we have chosen to use the gradient Richardson number given by Eq. (2.1.14) because it is a *local* quantity measuring the relative influence of shear forces and buoyancy.

The next step then is to relate the gradient Richardson number to the layer Richardson number so that appropriate limiting values can be determined separating the different flow regimes. The gradient Richardson number can be approximated as follows:

$$Ri_g = \frac{-(g/\mathbf{r}) \cdot (\partial \mathbf{r} / \partial y)}{(\partial u / \partial y)^2} \approx \frac{g \cdot \Delta \mathbf{r}}{r_1 (\Delta U)^2} \cdot \frac{d_v^2}{d_m} \quad (5.2.1)$$

This is done by simply approximating the partial derivatives as differences, and assuming that Δy scales as δ_m in the case of the density gradient and δ_v in the case of the velocity gradient. Here δ_m is the mixed-fluid, or interface, thickness (see Eq. 2.1.4) and δ_v is the maximum velocity gradient thickness, as defined by Eq. (2.1.2). By inspection, we can relate the approximate expression for the gradient Richardson number with the definition of the layer Richardson number if we also assume that the boundary layer thickness, h , scales as the velocity layer thickness δ_v . This yields

$$Ri_g = Ri_L \cdot \left(\frac{d_v}{d_m} \right) \quad (5.2.2)$$

From Figure 17 of Atsavapranee & Gharib [1], the ratio of the mixed-fluid thickness to the velocity gradient thickness can be approximated by a curve fit, given by

$$\frac{d_m}{d_v} \cong 0.017 \cdot Ri^{-3/2} \quad (5.2.3)$$

where Ri is a kind of Richardson number defined by

$$Ri = \frac{g \cdot \Delta r \cdot d_v^2}{\bar{r} \cdot d_r} \quad (5.2.4)$$

Here \bar{r} is the mean density and δ_ρ is the maximum density gradient thickness, given by Eq. (2.1.3), which is approximately equal to twice the mixed fluid thickness, δ_m , as given by Eq. (2.1.5). By substituting Eq. (2.1.5) into Eq. (5.2.4) we obtain

$$Ri = \frac{g \cdot \Delta r \cdot d_v^2}{2 \cdot \bar{r} \cdot d_m} \quad (5.2.5)$$

By examination of Eq. (5.2.5) and Eq. (5.2.1) we can then relate Ri to the gradient Richardson number by

$$Ri = \frac{1}{2} Ri_g \quad (5.2.6)$$

and by substituting Eq. (5.2.6) into Eq. (5.2.3) we find

$$\frac{d_m}{d_v} \cong 0.0481 \cdot Ri_g^{-3/2} \quad (5.2.7)$$

With this expression we can now relate the gradient Richardson number to the layer Richardson number. This yields

$$Ri_g \cong 0.2 \cdot Ri_L^{1.22} \quad (5.2.8)$$

which will in turn allow us to determine the flow regime boundaries in terms of the gradient Richardson number, which can be determined locally in the CFX model.

According to Figure 12 of Sullivan & List [33], the different flow regimes are delineated by the value of the layer Richardson number; however, as we are using a locally defined gradient Richardson number, we have converted the flow regime boundaries. Table 5.1 below describes the different values used to separate these flow regimes. It should be noted that we have combined the Kelvin-Helmholtz regime and the wave-breaking regime into a single K-H vortices regime.

Table 5.1 - Flow Regime Boundaries for DFE Model

FLOW REGIME	RICHARDSON NUMBER
Turbulent Interface Regime	$Ri_L < 1$ $Ri_g < 0.2$
K-H Vortices Regime	$1.0 < Ri_L < 20$ $0.2 < Ri_g < 7.5$
Molecular Diffusion Regime	$Ri_L > 20$ $Ri_g > 7.5$

5.3 Model Equations

In this section we will develop the model equations implemented in the SFST model for the different flow regimes described above. First we will examine the turbulent interface regime, which occurs for values of the gradient Richardson number less than approximately 0.2, and the K-H vortices regime for intermediate values of the gradient Richardson number (between approximately 0.2 and 7.5).

Turbulent Interface Regime

From the discussion by Hinze [21], the product of the droplet diameter and the turbulent dissipation, raised to the 2/3 power, is proportional to the square of the fluctuating vertical velocity component. The constant of proportionality is found to be approximately 2.0. This yields

$$u'^2 \cong 2.0 \cdot (\mathbf{e} \cdot \mathbf{d})^{2/3} \quad (5.3.1)$$

This expression was also determined by Kuboi *et al* [25] from the analysis of experimental results for stirred tanks and turbulent pipe flow. From the definition of the turbulent kinetic energy, k ,

$$k = \frac{1}{2} (u'^2 + v'^2 + w'^2) \quad (5.3.2)$$

and assuming isotropic turbulence we obtain

$$k = \frac{1}{2} (3u'^2) \quad (5.3.3)$$

If we then substitute for u'^2 into Eq. (5.3.1) we find

$$\frac{2}{3} k \cong 2.0 \cdot (\mathbf{e} \cdot \mathbf{d})^{2/3}$$

which can be solved for the droplet diameter in terms of k and \mathbf{e}

$$d_p \cong 0.1925 \cdot \left(\frac{k^{3/2}}{\mathbf{e}} \right) \quad (5.3.4)$$

For the CFX model, we will next include a function of the volume fraction to account for the fact that there should be no droplets formed in regions where only one phase is present and where that phase forms the continuum.

This yields, with a constant of proportionality C_1 ,

$$d \cong C_1 \cdot (r_a)^m \cdot (1 - r_a)^n \cdot \left(\frac{k^{3/2}}{\mathbf{e}} \right) \quad (5.3.5)$$

where r_α is the volume fraction of the dispersed phase (i.e. the fuel), and $(1-r_\alpha)$ is the volume fraction of the continuous phase (i.e. water). This is the model expression for the droplet diameter in the turbulent interface regime (i.e. where $Ri_g < 0.2$). The model coefficient C_1 was set to approximately 0.2, and the exponents m and n were arbitrarily set to 2 in both cases. This causes the droplet diameter to become very small as r_α approaches 1 (i.e. approaching a continuous fuel layer where we expect no droplets) or 0 (i.e. continuous water layer). Equation (2.4.11) indicates that this coefficient should be a function of the Weber number.

In Eq. (5.3.5), $k^{3/2}/\mathbf{e}$ is a length scale that is a measure of the size of the turbulent eddies at a given location within the domain. This is the integral turbulence length scale used by most two-equation turbulence models.

K-H Vortices Regime

As stated previously, in this regime we will assume that the size of any dispersed phase droplets formed is proportional to the height of the K-H type waves that form at the fluid interface. From Figure 15 of Narimousa & Fernando [31], the wave amplitude δ_w normalized by the mixed-layer depth, h , can be expressed as

$$\frac{d_w}{h} \cong 0.232 \cdot Ri_u^{-0.61} \quad (5.3.6)$$

where the Richardson number Ri_u is defined as

$$Ri_u = \frac{g \cdot \Delta \mathbf{r} \cdot h}{\bar{u}^2} \quad (5.3.7)$$

and \bar{u} is the mean velocity of the mixed-fluid layer. The mixed-layer depth h can be related to the shear layer thickness δ_s by [31]

$$\frac{d_s}{h} \cong 0.2$$

By substitution for h into Eq. (5.3.6) we find

$$\frac{d_w}{d_s} \cong 1.16 \cdot Ri_u^{-0.61} \quad (5.3.8)$$

Again we face the problem of converting the Richardson number into a gradient Richardson number for use in the CFX model. By examination of Eq. (5.3.7) and Eq. (5.2.1), and assuming that the flow is characterized by the mean interface velocity \bar{u} , we find that this is a simple relation

$$Ri_u = 1.5 \cdot Ri_g \quad (5.3.9)$$

If we now substitute for Ri_u into Eq. (5.3.8), and assume that the shear layer thickness δ_s scales as the maximum velocity gradient thickness δ_v , we find

$$d_w \cong 0.905 \cdot d_v \cdot Ri_g^{-0.61} \quad (5.3.10)$$

Multiplying and dividing the right hand side of Eq. (5.3.10) by the mixed-fluid thickness, δ_m , yields

$$d_w \cong 0.905 \cdot d_m \cdot \left(\frac{d_v}{d_m} \right) \cdot Ri_g^{-0.61}$$

We have already determined the relationship between the ratio of the mixed-fluid thickness to the maximum velocity gradient thickness and the gradient Richardson number in Eq. (5.2.10). Substituting for this expression yields

$$\mathbf{d}_w \cong 18.8 \cdot \mathbf{d}_m \cdot Ri_g^{0.89} \quad (5.3.11)$$

As stated previously, in this regime we assume that the droplet diameter is proportional to the wave height. Here we will assume that the constant of proportionality is approximately 1/4. This seems reasonable in that it assumes that during a wave-breaking event the wave breaks up into approximately four droplets ($d_p \cong 0.25\mathbf{d}_w$). With this assumption, the droplet diameter is given by

$$d_p \cong 4.7 \cdot \mathbf{d}_m \cdot Ri_g^{0.89} \quad (5.3.12)$$

More generally we can express Eq. (5.3.12) in terms of some appropriate length scale l_{ch} and with some constant C_2 by

$$d_p \cong C_2 \cdot l_{ch} \cdot Ri_g^{0.89} \quad (5.3.13)$$

This was done so that the length scale included in the model expression could account both for regions where the flow acts like a stratified flow, as well as regions that are occupied by either the inlet jet or the buoyant jet that occurs through the manholes of the different tank geometries. This will be explained in greater detail later.

Again we choose to include a function of the volume fraction as we did in the turbulent interface regime to account for regions where only the lighter phase is present. This yields the model expression for the K-H vortices regime:

$$d_p \cong C_2 \cdot (r_a)^m \cdot (1 - r_a)^n \cdot l_{ch} \cdot Ri_g^{0.89} \quad (5.3.14)$$

where C_2 is a model constant on the order of 5.0, and m and n are again set to 2.

Determination of Length Scales

As we have seen from the model expression derived above, there can be several different length scales which characterize the flow in a given flow regime. These will be discussed in this section.

For the turbulent interface regime, we assume that the characteristic length scale is that of the turbulent eddy size given by

$$l_{te} = \frac{k^{3/2}}{\epsilon} \quad (5.3.15)$$

For the K-H vortices regime there are several different length scales that might be used to characterize the flow. The derivation of the model expression based on the results from the literature on two-dimensional stratified shear flows yielded a length scale based on the mixed-fluid thickness. This length scale is determined from the volume fraction profile as the distance over which the dispersed phase volume fraction changes from 0.01 to 0.99. The limitation of this, however, is that it is derived from two-dimensional shear flow experiments, which do not include three-dimensional effects. Also, for the geometries used in our CFX models, this would not account for regions of the flow in which an impinging jet occurs, nor would it include regions of buoyant jet phenomena. To account for all of these we have included a much more general length scale expression in the model equation for this flow regime. We will assume that the size of any droplets

formed will be determined by the smallest, locally determined, characteristic length scale, as given by

$$l_{ch} = \text{Min}(\mathbf{d}_{mx}, \mathbf{d}_{my}, \mathbf{d}_{mz}, l_{te}, \mathbf{d}_{wall}) \quad (5.3.16)$$

where δ_{mx} , δ_{my} , and δ_{mz} represent the mixed-fluid thickness in each of the three coordinate directions. l_{te} is the turbulent eddy length scale defined by Eq. (5.3.15), and δ_{wall} is the distance from the cell node to the nearest wall, which limits the size of the droplets by their proximity to a solid boundary, where l_{te} changes approximately as $0.4y_n$, y_n being the normal distance from the wall. For the calculation of the three mixed-fluid thicknesses, we employ a method based on the volume fraction profile by which we sweep the domain in each coordinate direction to determine a mixed fluid thickness. The wall distance term in Eq. (5.3.16) is included to account for the fact that near solid boundaries the size of a given droplet must be bounded in a physical sense by the distance to the nearest wall, which determines the local turbulent length scale near a wall. Our implementation of the CFX model calculates all of these length scales locally at each grid node and determines the smallest one to include in the model expression for this flow regime.

In the molecular diffusion regime we have already conjectured that we may include a new length scale based on the local kinematic viscosity and include it in the model expression for the K-H vortices regime using a higher Richardson number. This length scale is given by

$$l_{ch} = \frac{\mathbf{n}}{V} \quad (5.3.17)$$

where the kinematic viscosity ν and the vertical velocity V are determined locally at each grid node. The vertical velocity component was chosen as we expect that any diffusion that occurs will be dominated by the vertical component.

Summary of Model Expression for Various Flow Regimes

In the previous sections we have derived expressions to predict the dispersed phase droplet diameter based on local flow quantities. A summary of these expressions for each corresponding flow regime as they are implemented in the CFX code is given in Table 5.2 below.

Table 5.2 - DFE Model Equations for Different Flow Regimes

Flow Regime	Model Expression	Richardson numbers
Turbulent Interface	$d_p \cong 0.2 \cdot (r_a)^2 (1 - r_a)^2 \left(\frac{k^{3/2}}{e} \right)$	$Ri_L < 1.0$ $Ri_g < 0.2$
K-H Vortices	$d_p \cong 5.0 \cdot (r_a)^2 (1 - r_a)^2 \cdot l_{ch} \cdot Ri_g^{0.89}$ where $l_{ch} = \text{MIN}(\delta_{mx}, \delta_{my}, \delta_{mz}, l_{te}, \delta_{wall})$	$1.0 < Ri_L < 20$ $0.2 < Ri_g < 7.5$
Molecular Diffusion	$d_p \cong 5.0 \cdot (r_a)^2 (1 - r_a)^2 \cdot \left(\frac{\nu}{V} \right) \cdot Ri_g^{0.89}$	$Ri_L > 20$ $Ri_g > 7.5$

General Expressions

It is important to keep in mind that the expressions for the droplet diameter were derived from the analysis of results in the literature for two-dimensional stratified shear flows involving miscible fluids. The actual flow scenario may involve a much more complex three-dimensional mixing of immiscible liquids (e.g. vertical buoyant jet flow). In light of this, we can rewrite the droplet model expressions for the three different flow regimes in a more general form. Table 5.3 below shows the general form of the model equations.

Table 5.3 - General Model Expressions for the Droplet Diameter

Flow Regime	Model Expression	Richardson numbers
Turbulent Interface	$d_p \cong C_1 \cdot (r_a)^m (1 - r_a)^n \left(\frac{k^{3/2}}{e} \right)$	$Ri_L < K_1$ $Ri_g < k_1$
K-H Vortices	$d_p \cong C_2 \cdot (r_a)^m (1 - r_a)^n \cdot l_{ch} \cdot Ri_g^{0.89}$ where $l_{ch} = \text{Min}(\delta_{mx}, \delta_{my}, \delta_{mz}, l_{te}, \delta_{wall})$	$K_1 < Ri_L < K_2$ $k_1 < Ri_g < k_2$
Molecular Diffusion	$d_p \cong C_3 \cdot (r_a)^m (1 - r_a)^n \cdot \left(\frac{n}{V} \right) \cdot Ri_g^{0.89}$	$Ri_L > K_2$ $Ri_g > k_2$

In the above generalized expressions, the model coefficients C_1 , C_2 , and C_3 , the exponents m and n , and the flow regime boundary limits on the Richardson number, K_1 , k_1 , K_2 , and k_2 , would need to be determined from experimental results.

5.4 Verification of the DFE Model

To verify the droplet formation/entrainment model, a two-compartment geometry was used in conjunction with the SFST model and the model expressions for the DFE model as described above. It should be noted that these verification studies were done prior to the modifications made to the solution of the volume fraction as described in the previous chapter. A wireframe sketch of the geometry used is given in Fig. 5.1 below.

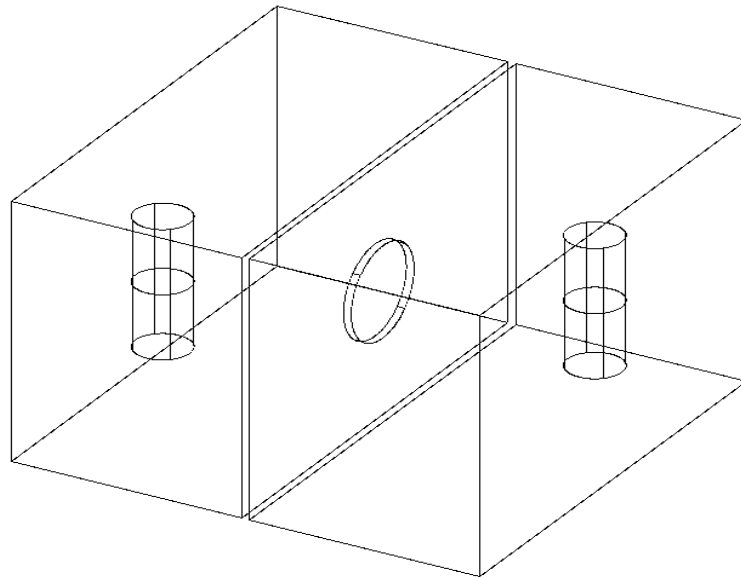


Figure 5.1 - Wireframe sketch of two-compartment tank geometry.

The physical dimensions of the tank are 1.2 meters long by 1.2 meters wide by 0.8 meters high. The uniform grid used is $60 \times 24 \times 24$, for a total of approximately 35,000 cells, and an average cell volume of $3.33 \times 10^{-5} \text{ m}^3$. The inlet was modeled as a mass flow boundary with specified flux of 8.0 kg/s , corresponding to an inlet velocity of approximately 6.7 ft/s and an inlet volumetric flowrate of approximately 150 gal/min ; the

exit was modeled as a pressure boundary. The advection scheme used was second order upwind, while the k and ε equations were discretized using the hybrid scheme. The volume fraction used upwinding, and the time discretization used backward Euler differencing.

The model equations for the droplet diameter in each of the different flow regimes were implemented for the above geometry, using the SFST model, including the buoyancy terms in the k - ε equations. The results of these simulations are discussed in the next section.

Results are given for the volume fraction, and the droplet diameter solved for as a passive scalar. That is, the locally calculated diameter was not included in the slip velocity expression dynamically. With regard to the droplet diameter contour plots there are two figures included. The first shows the larger scale fuel droplets, and the second is used to show the smaller droplets by altering the scale of the contour plot. Due to the color interpolation performed by the CFX post-processor, CFX-Visualize, this was necessary since the smaller scale droplets would not appear on the contours without altering the scale. Any values larger than the upper limit of the display scale are shown as the high value (i.e. red in a color plot). Velocity vector plots representing the flow field for each time value are also included in the results presented below.

In the following sections, several different views are presented for the variables in question. Three vertical planes corresponding to the z -value of the inlet pipe, manhole,

and exit pipe (the z -direction being the dimension into the page), and one horizontal plane at a height of $H/2$ (H being the total height of the tank), are shown at time equal to 15.0 seconds. It is important to be mindful of the scale shown for each figure, as they are not always the same, except in the case of the small scale contours for the droplet diameter, which all have an upper limit of 0.0005 m (0.5 mm).

Observations made concerning the results given indicate that the droplet model seems to predict reasonable values for the dispersed phase diameter. The values range from extremely small droplets up to larger droplets whose diameters are on the order of 1-2 cm. Based on the qualitative observations of the shear flow experiments conducted at Johns Hopkins University this range appears to be quite reasonable. Also, with regard to geometric trends, there are no droplets predicted in regions where only one phase is present, and the majority of the droplets predicted by the model appear in regions at or near the interface of the two fluids. The larger the droplets, the closer they are to the mean interface of the two fluids.

Inlet Plane at Time = 15.0 seconds

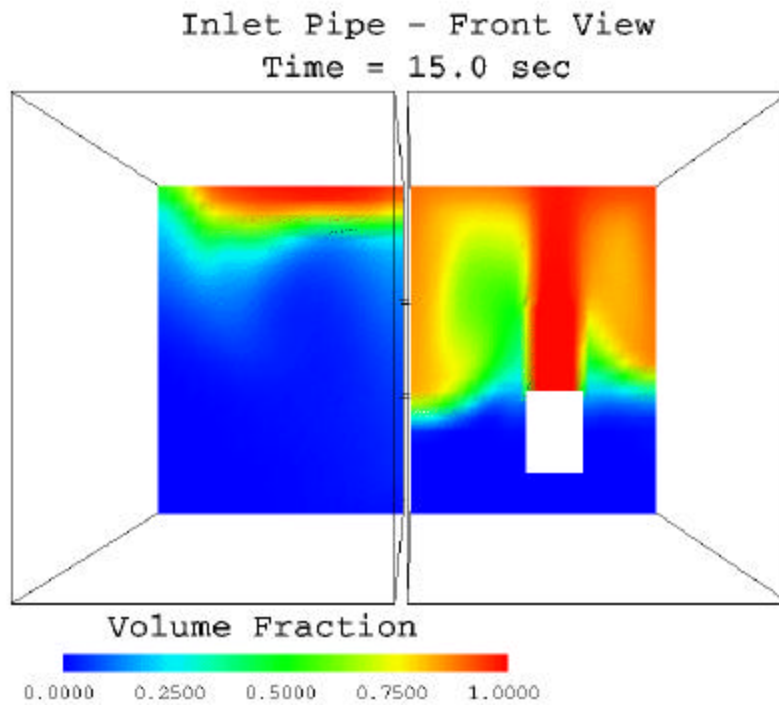


Figure 5.2 - Volume fraction (inlet - front view) at t = 15.0 sec.

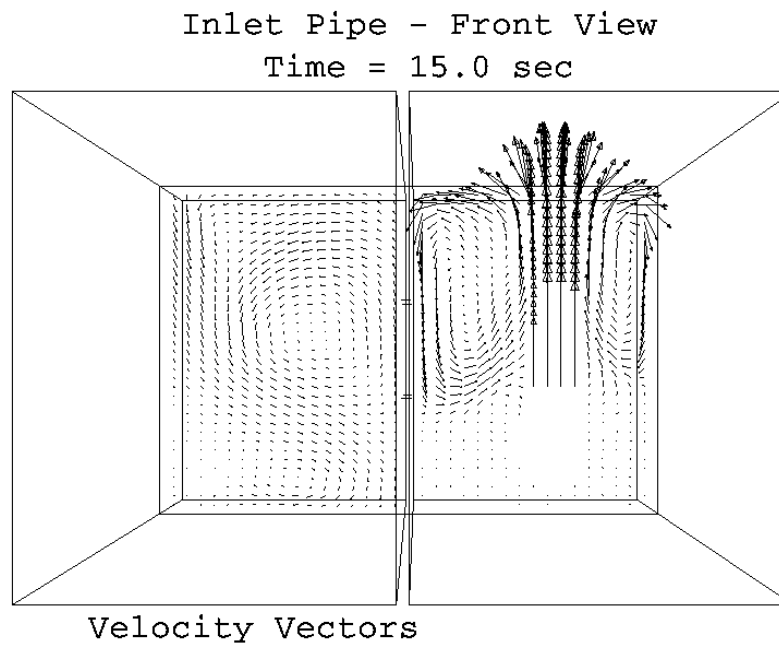


Figure 5.3 - Velocity vectors (inlet - front view) at t = 15.0 sec.

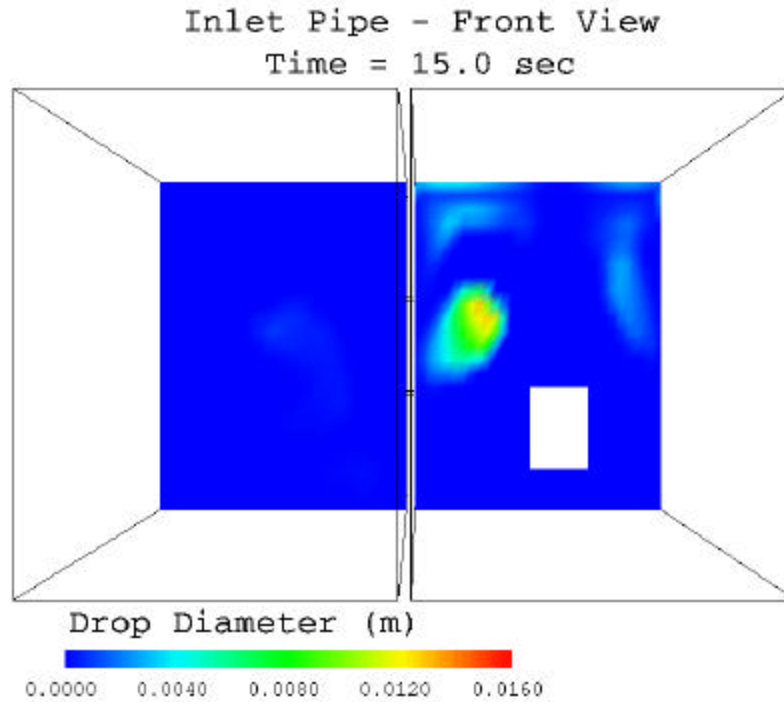


Figure 5.4 - Droplet diameter (inlet - front view) - large scale at t = 15.0 sec.

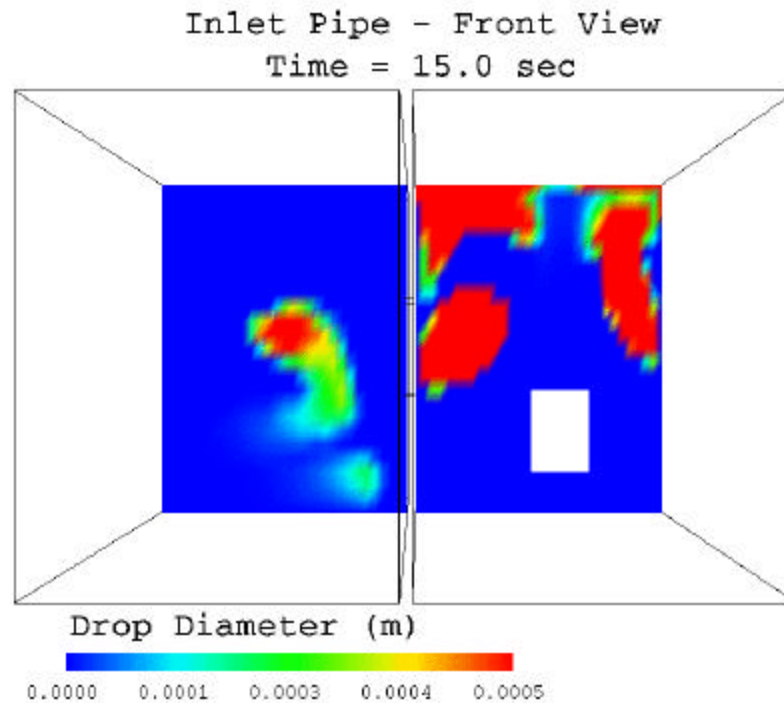


Figure 5.5 - Droplet diameter (inlet - front view) - small scale at t = 15.0 sec.

Manhole at Time = 15.0 seconds

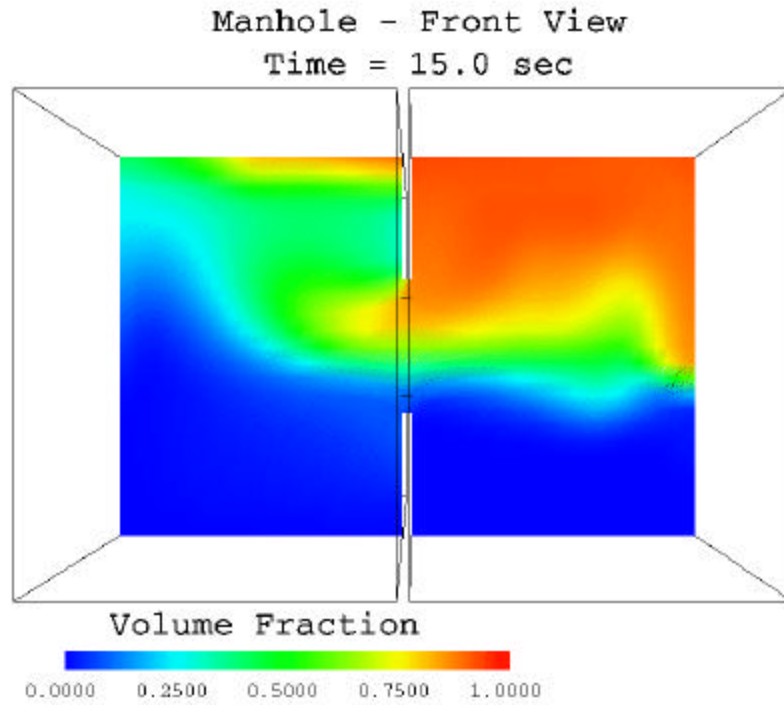


Figure 5.6 - Volume fraction (manhole - front view) at $t = 15.0$ sec.

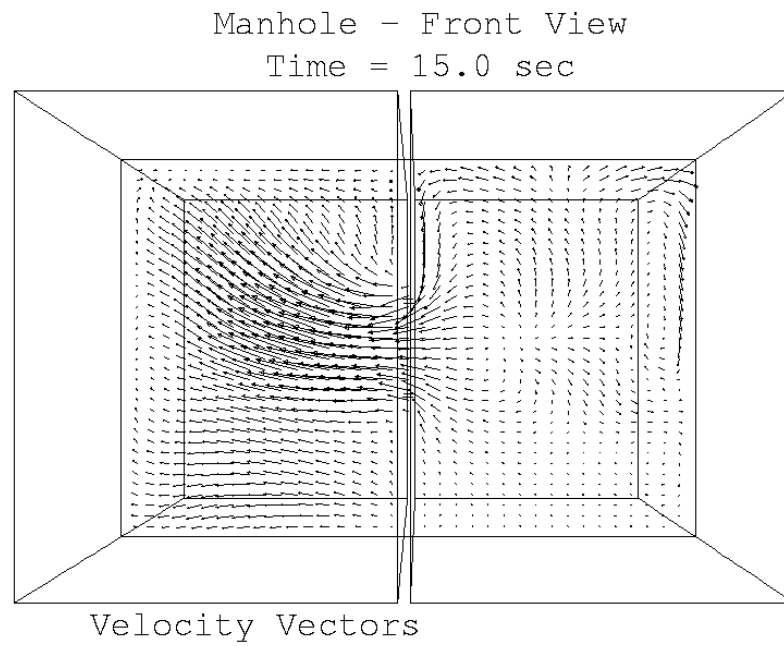


Figure 5.7 - Velocity vectors (manhole - front view) at $t = 15.0$ sec.

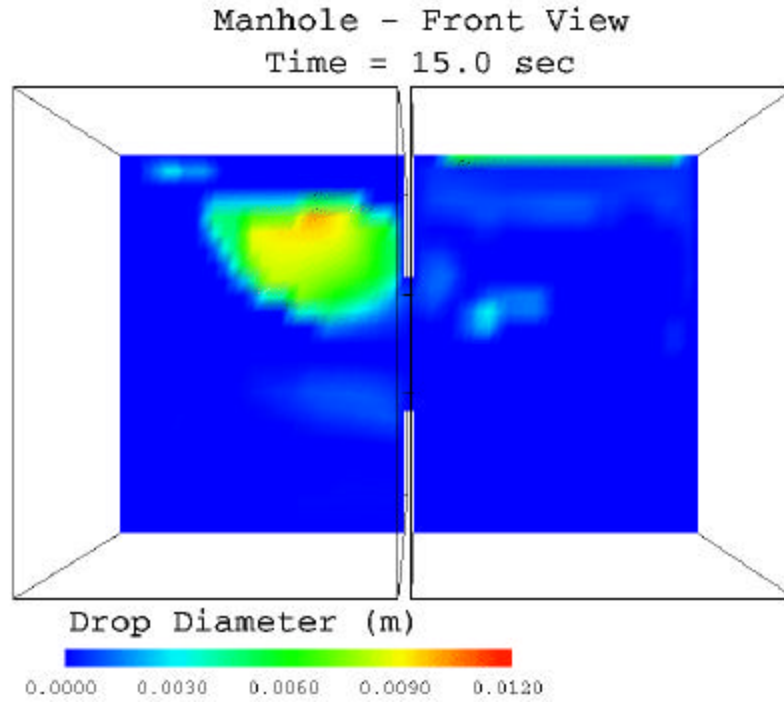


Figure 5.8 - Droplet diameter (manhole - front view) - large scale at t = 15.0 sec.

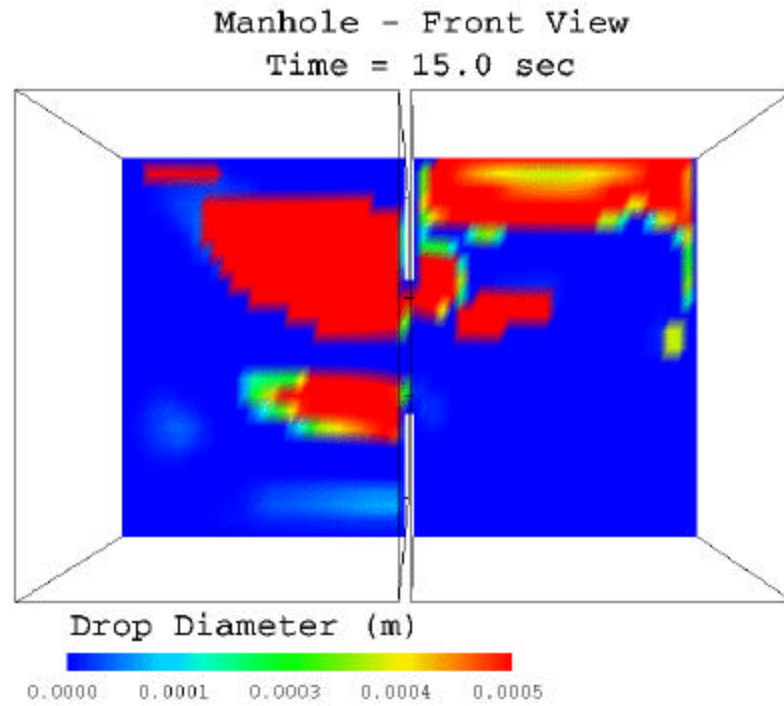


Figure 5.9 - Droplet diameter (manhole - front view) - small scale at t = 15.0 sec.

Exit Plane at Time = 15.0 seconds

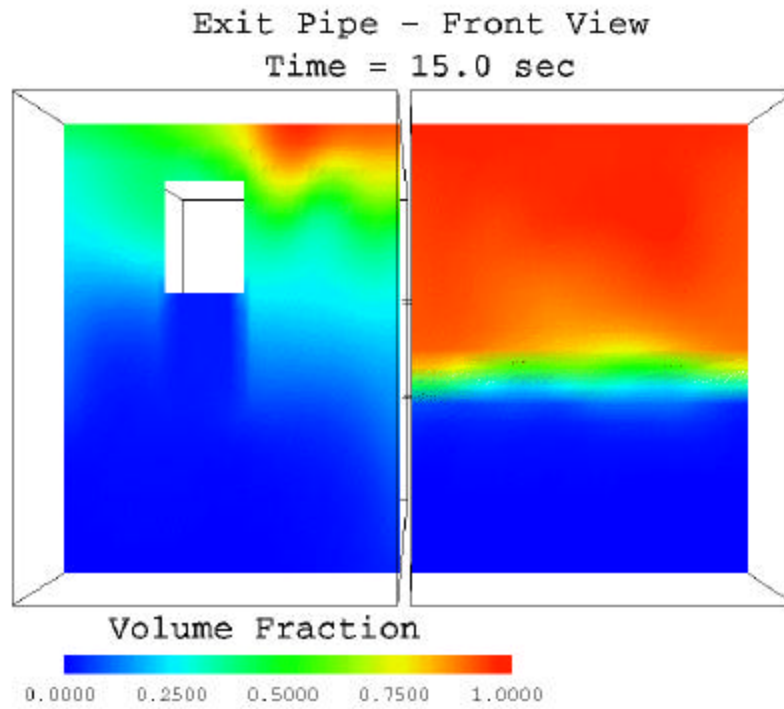


Figure 5.10 - Volume fraction (exit - front view) at $t = 15.0$ sec.

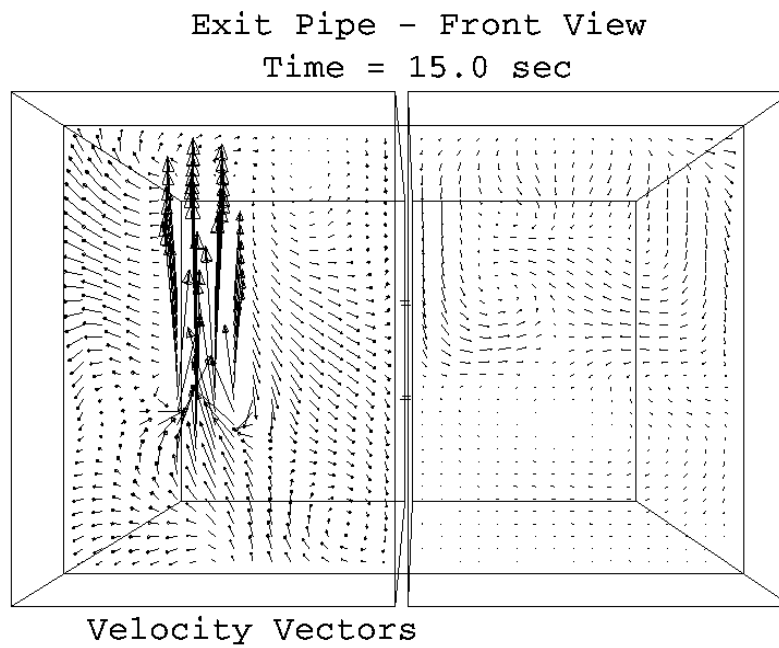


Figure 5.11 - Velocity vectors (exit - front view) at $t = 15.0$ sec.

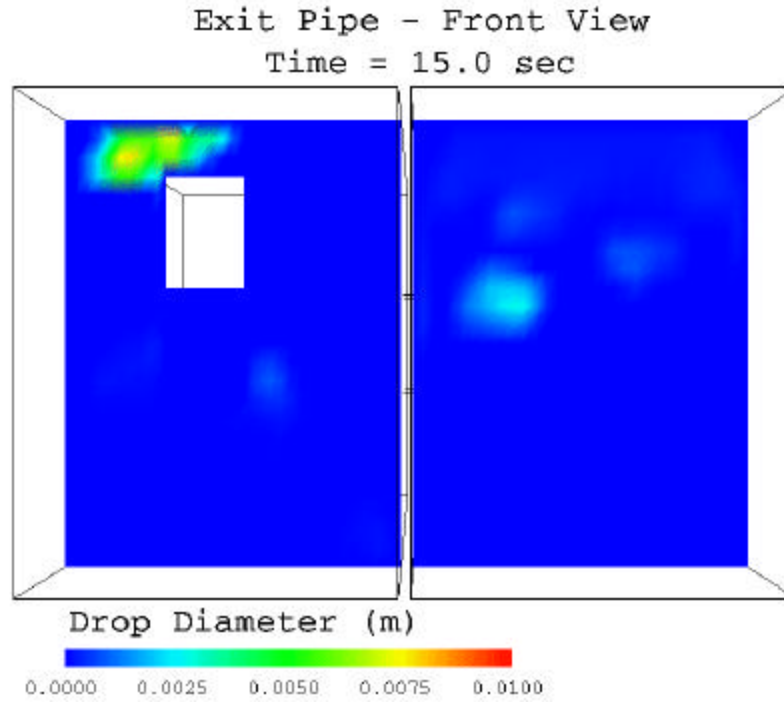


Figure 5.12 - Droplet diameter (exit - front view) - large scale at t = 15.0 sec.

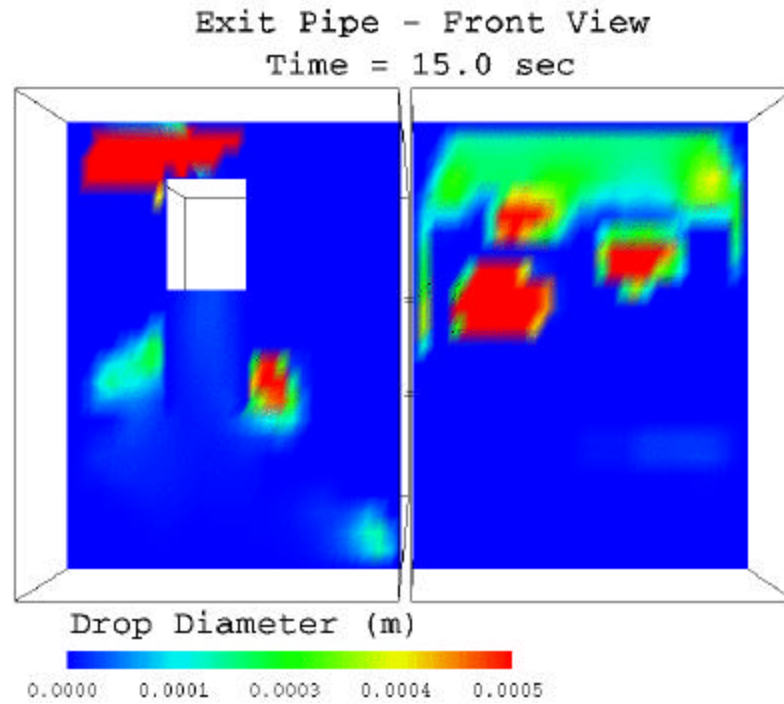


Figure 5.13 - Droplet diameter (exit - front view) - small scale at t = 15.0 sec.

Top View ($y = H/2$) at Time = 15.0 seconds

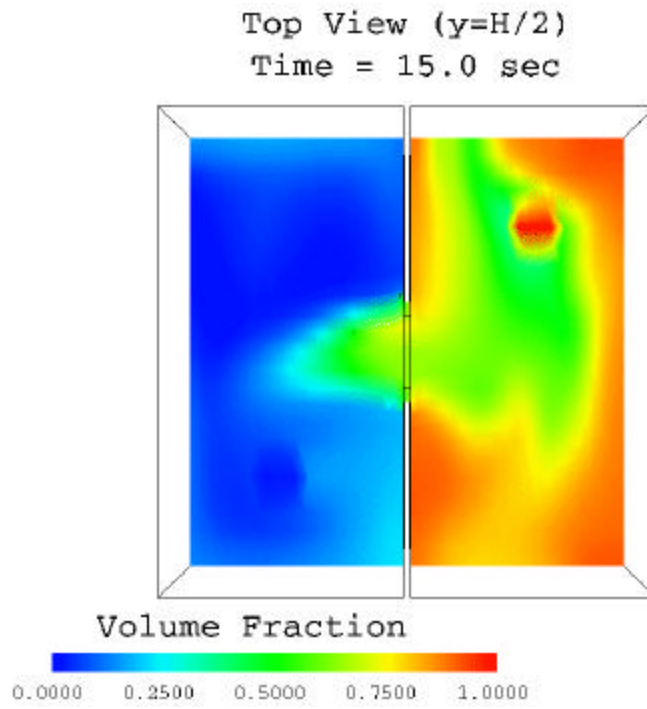


Figure 5.14 - Volume fraction (top view - $y = H/2$) at $t = 15.0$ sec.

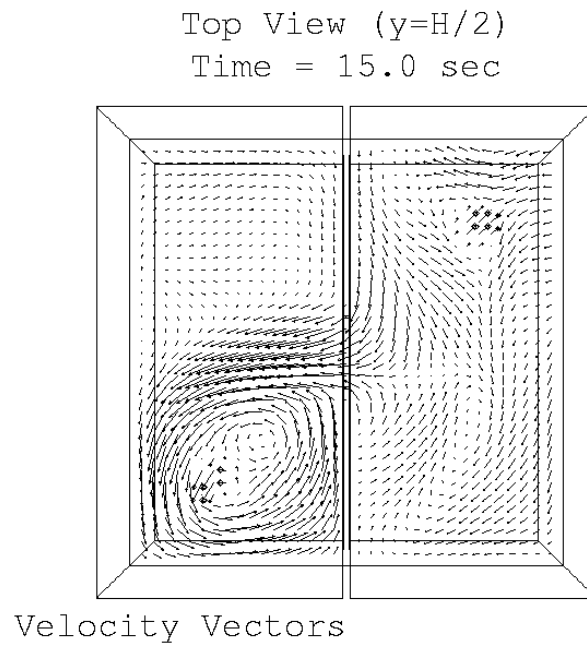


Figure 5.15 - Velocity vectors (top view - $y = H/2$) at $t = 15.0$ sec.

Top View ($y=H/2$)
Time = 15.0 sec

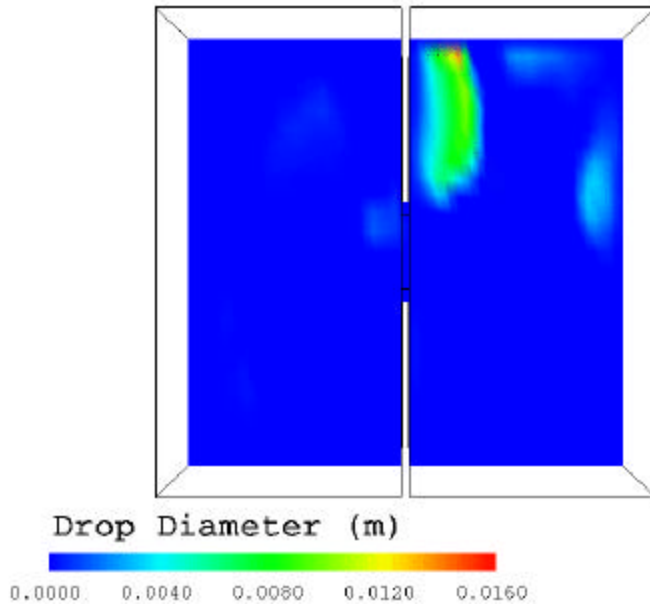


Figure 5.16 - Droplet diameter (top view - $y = H/2$) - large scale at $t = 15.0$ sec.

Top View ($y=H/2$)
Time = 15.0 sec

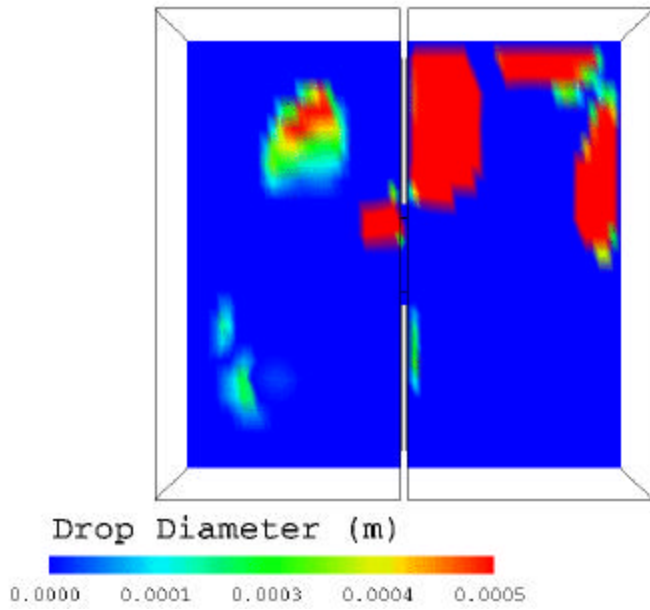


Figure 5.17 - Droplet diameter (top view - $y = H/2$) - small scale at $t = 15.0$ sec.

From the figures given above, it can be seen that the droplet formation/entrainment model produces reasonable values of the dispersed phase droplet diameter. The typical range of droplet sizes extend to approximately 2 cm at the maximum value. This seems quite reasonable by comparison with results from the experiments being performed at Johns Hopkins University for stratified shear flows. As we expected, there are no droplets predicted in regions where only one phase is present (i.e. where the volume fraction is either zero or one), and the majority of the fluid droplets are formed at or near the interface of the two fluids.

6.0 SFST MODEL PREDICTIONS FOR STRATIFIED SHEAR FLOWS

The SFST model, as described previously, was applied to the simulations of an experimental facility at Johns Hopkins University [38] to investigate certain mixing phenomena in stratified shear flows. The droplet formation/entrainment (DFE) model was also used in conjunction with this model for verification purposes and to investigate the droplet size distributions predicted by the numerical models. Of primary interest in these simulations were the predictions of the overall flowfield, as well as the prediction of the mixed fluid thickness as a function of downstream distance. Wherever possible, comparisons will be made between the results of the numerical simulations and the experimental measurements.

6.1 Experimental Conditions Simulated

The experimental setup consisted of a laboratory channel apparatus in which two stratified, immiscible fluids flow opposite to each other. A sketch of the apparatus is given in Fig. 6.1. The overall dimensions are approximately 150.0 cm long by 32.0 cm high by 7.5 cm wide, and both the water and fuel inlets span a vertical distance of approximately 11.0 cm. In the experiments, fuel with a density of 850.0 kg/m^3 entered the tank through the upper left inlet, while water, with a density of 1000.0 kg/m^3 and flowing at a much higher velocity than the fuel, entered the tank through the lower right inlet. The incoming fuel and water layers were separated at the left and right walls by thin splitter plates, and the fuel layer was smoothly transitioned into the oncoming water

by means of the inlet diffuser shown. Here, the angle between the inlet diffuser and the left splitter plate could be varied for different flow conditions, but remained fixed for a given experimental trial. As the purpose of the inlet diffuser is to prevent any of the water from being entrained in the fuel layer and being drawn above the left splitter plate, the angle of the inlet diffuser needed to be changed depending on the inlet velocity of the water layer. Some of the fuel exited the tank through the upper right outlet and returned to the fuel reservoir, while the majority of the fuel was entrained in the water and exited via the lower left outlet. The outlet weir located below the inlet diffuser acted to direct the flow of water along the fuel/water interface.

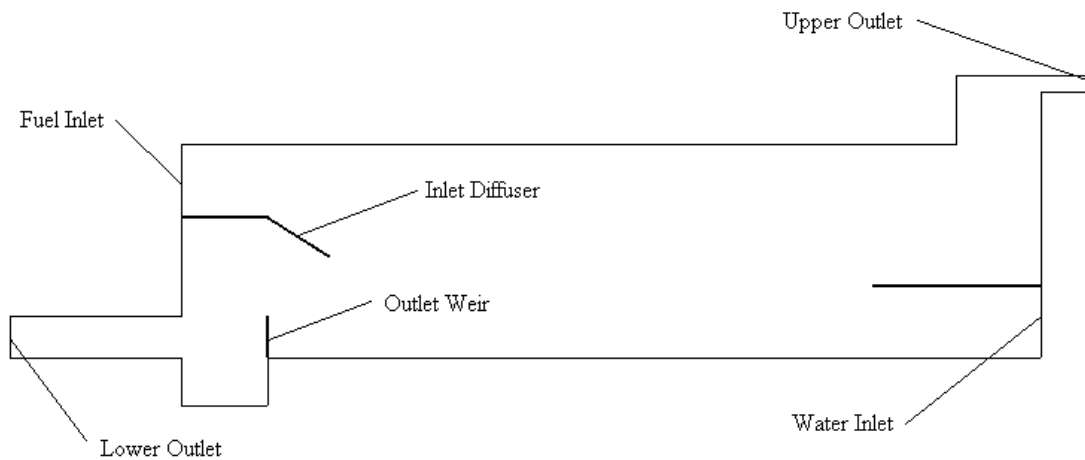


Figure 6.1 – Johns Hopkins shear flow experimental setup.

The main shear region, which is located between the inlet diffuser and the splitter plate above the water inlet, was approximately 0.8 m in length. Typical inlet flow rates for the fuel were approximately $9.464 \times 10^{-4} \text{ m}^3/\text{s}$ (15.0 gal/min), corresponding to an inlet velocity of approximately 0.15 m/s. Inlet flow rates for the water ranged from 0.00505

m^3/s to $0.00757 \text{ m}^3/\text{s}$ (or 80 gal/min to 120 gal/min), corresponding to mean inlet velocities of 0.8345 m/s to 1.2517 m/s. The overall Richardson number, as given by Eq. (2.1.11), was used to characterize each of the different cases simulated. Here the characteristic velocity scale was taken as the difference between the mean inlet velocities of the fuel and water inlets.

6.2 Computational Details

To simulate the experimental setup, a two-dimensional model was configured using CFX-4. Here, the SFST model, as was described in Section 3.1, was used. The effects of turbulence were modeled using the modified k - ϵ model, described in Section 3.2, including the additional terms to account for buoyant production/destruction. The constitutive equation for the relative motion between the phases was given by the slip velocity relation described in Section 3.3.

Several different flow scenarios were simulated, encompassing two different overall Richardson numbers, defined in terms of inlet parameters. For each value of the Richardson number, three numerical runs were performed, where two assumed a constant, average droplet diameter, and the third utilized the droplet formation/entrainment (DFE) model. For cases involving the DFE model, the droplet diameter that was calculated during the course of the simulation was dynamically implemented in the slip velocity relationship at all points in the domain.

A 20-block geometry was configured using CFX-Meshbuild to simulate the experimental setup. A sketch of this configuration is given in Fig. 6.2, where all block structures and dimensions are shown as they were modeled in CFX. Lines inside the domain represent inter-block boundaries, and shaded regions denote boundary patches. The dimensions of this model followed those used in the experiments at Johns Hopkins University [38].

The grid used for the simulations consisted of approximately 29,175 cells. In the main shear region, between the splitter plates, 150 cells were used in the longitudinal (streamwise) direction, and 104 cells were used in the vertical direction. In this region, the mesh was concentrated towards the lower wall and center of the model using a geometric progression factor of 1.02. This gave the smallest cell at or near the interface dimensions of approximately 5.0 mm long by 1.0 mm high.

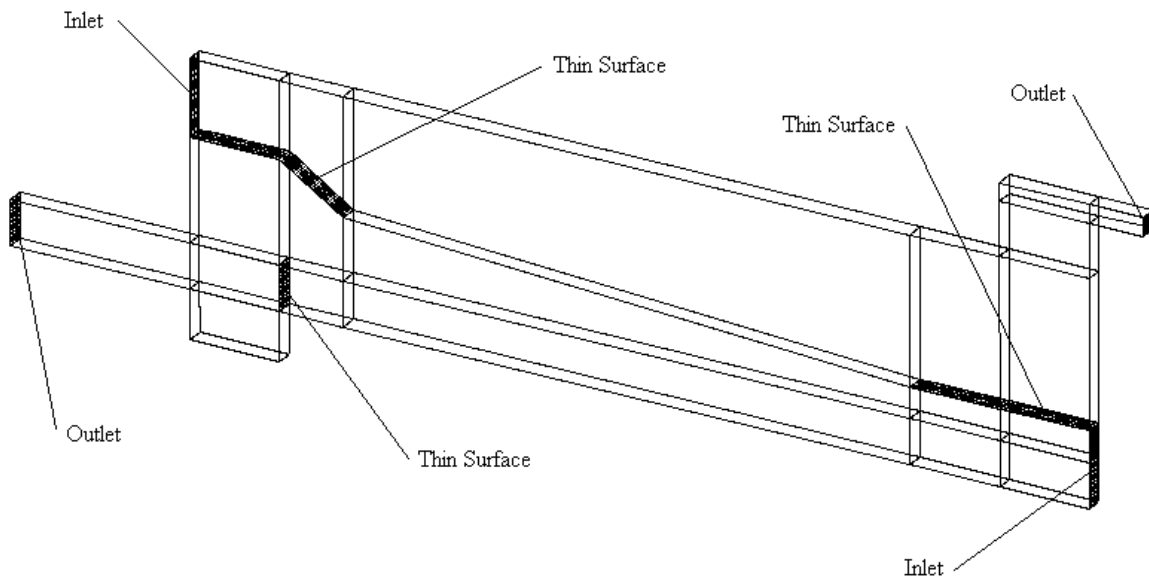


Figure 6.2 – Johns Hopkins shear flow geometry used in CFX.

Boundary conditions for the inlets were modeled by setting a fixed velocity such that the overall Richardson numbers matched those in the experiments based on the inlet flow rates used. The volume fraction was also specified at the inlets, corresponding to the pure, unmixed fluid values. The turbulence quantities, k and ϵ , were estimated at the inlets using Eq. (4.1.1) and (4.1.2), and pressure at the inlets was extrapolated from downstream. Therefore, Dirichlet boundary conditions were specified at the inlets on all quantities except the pressure.

Boundary conditions at the outlets were set as if the fluid were exiting the domain with a free surface at the top of the outlet boundary in the longitudinal direction, with atmospheric conditions at the top of the boundary. For stratified flows exiting the domain perpendicular to the gravity vector, the discretized pressure for this condition is set according to

$$P_j = P_{j+1} + \int_j^{j+1} (\rho_m - \rho_{ref}) (g) dy \quad (6.2.1)$$

where the gravitational acceleration acts downward, and the j index indicates the vertical direction. Here ρ_{ref} is a reference density, which was set equal to the average of the unmixed phase densities. In addition to the hydrostatic distribution, constant pressures of approximately 2,600.0 Pa and 5,300.0 Pa were set at the upper right outlet for the lower and higher Richardson number cases, respectively, corresponding to pressure differences of approximately 0.375 psi and 0.75 psi between the upper and lower outlets. This was done since the fuel outlet tank on the right of the apparatus was typically pressurized

during the experiments. Boundary conditions for all other quantities at the outlets were modeled by setting a zero-derivative condition.

Six different cases were simulated, encompassing two different values for the overall Richardson number, with variations in the droplet diameter, d_p . For each value of the overall Richardson number, two cases were simulated using two different values for the droplet diameter as a constant, average value. A third case was also simulated, implementing the droplet formation/entrainment model, and dynamically updating the droplet diameter value used in the slip velocity relation. Table 6.1 below illustrates the boundary conditions and overall parameters for each case.

Table 6.1 – Boundary Conditions and Overall Parameters for CFX model

<u>Water Inlet Parameters</u>					<u>Overall Parameters</u>	
Case	u (cm/s)	ρ (kg/m ³)	k (cm ² /s ²)	ε (cm ² /s ³)	dp (mm)	Ri*
1	73.72	1000.0	10.87	15.68	2.00	0.7
2	73.72	1000.0	10.87	15.68	6.00	0.7
3	73.72	1000.0	10.87	15.68	variable	0.7
4	84.37	1000.0	14.23	20.04	2.00	0.32
5	84.37	1000.0	14.23	20.04	6.00	0.32
6	84.37	1000.0	14.23	20.04	variable	0.32

<u>Fuel Inlet Parameters</u>				
Case	u (cm/s)	ρ (kg/m ³)	k (cm ² /s ²)	ε (cm ² /s ³)
1	0.1467	850.0	0.4304	0.12044
2	0.1467	850.0	0.4304	0.12044
3	0.1467	850.0	0.4304	0.12044
4	0.1467	850.0	0.4304	0.12044
5	0.1467	850.0	0.4304	0.12044
6	0.1467	850.0	0.4304	0.12044

A second order upwind scheme was used to discretize the velocity components, and central differencing was used for the pressure. As was discussed in Section 4.1, it was

found that a flux-limiting scheme performed better in discretizing the volume fraction equation; therefore, the MIN-MOD scheme was used. The turbulence quantities were calculated using the Hybrid scheme.

All simulations were performed using transient marching to steady state. Typically, 50 to 75 outer iterations were performed for a total elapsed time of 20.0 seconds, where a constant time step of 0.1 seconds was used throughout. The total elapsed time corresponded to approximately 2 flow-through times for the fuel, and approximately 10 to 15 flow-through times for the water. At this time the outlet flow rates and vertical profiles of all quantities remained essentially constant, and the solution was taken as the steady state.

6.3 Results and Discussion

In this section, results will be presented for the different simulations outlined above. Wherever possible, comparison will be made with experimental measurements, particularly in relation to the streamwise variation in the mixed fluid thickness, δ_M , for each case. Also in this section will be discussion of the calibration of various parameters involved in the SFST and DFE models by using the comparison of the predicted values for δ_M . Following this, the final predictions from the calibrated models will be presented.

The first important parameter in the SFST model that required calibration was the exponent used in the slip velocity relationship. Recall, that the slip velocity was related to the terminal velocity of a single particle by

$$u_s = (1 - r_a)^m u_\infty$$

Ishii and Zuber [24] recommended a value for the exponent m of $5/7$. After several simulations where the exponent was varied while maintaining all other parameters, it was found that this was an appropriate value to use in the slip velocity equation.

The difficulty that arises in determining the proper expression for the slip velocity lies in the interaction of the source term in the volume fraction equation with certain boundedness checks, which are designed to ensure that the volume fraction does not go below 0.0 or above 1.0. The boundedness checks essentially only enforce physical limitations to the amount of scalar that can be transported from one cell to another, in a similar manner to the donor-acceptor method. They allow that a given cell cannot donate more fuel to an adjacent cell than it has available, and it cannot accept more fuel than the amount of water available in it to be displaced. The extent to which this is allowed to occur is determined by the constant β , which must be a value between 0 and 1.0. This term then, represents the percentage of the available fuel volume that the current cell will allow to be donated to an adjacent cell. In the present study, β is given a value of 0.9 (i.e. 90% of the available fuel volume may be displaced).

During the solution of the volume fraction equation, the magnitudes of the source term at the north and south cell faces are compared with the corresponding boundedness terms, and the minimum is taken in each case according to

$$\text{UNSRC} = \text{MIN}(\text{USLN1}, \text{USLN2}, \text{USLN3}) \quad (6.3.1)$$

$$\text{USSRC} = \text{MIN}(\text{USLS1}, \text{USLS2}, \text{USLS3}) \quad (6.3.2)$$

where USLS1 and USLN1 represent the source term calculated at the north and south cell face in terms of the slip velocity, and USLS2, USLS3, USLN2, and USLN3 represent the two boundedness checks each at the north and south faces, respectively. For more information on the boundedness parameters, see Appendix B.3.3, which details the FORTRAN implementation of the various models.

The difficulty that arises, then, is in the fact that if the calculated source term is too large, then the algorithm will always take one of the boundedness checks to determine the source term in the volume fraction equation. This is good for ensuring a physical (viable) solution, but in effect this will damp the effect of the droplet size on the relative velocity. This in turn will influence the amount of separation (segregation) that occurs following unstable density stratification and will alter the solution of the volume fraction field.

So, to determine the appropriate value to be used for the exponent in the slip velocity expression, was one of the important tasks. Several different numerical simulations were performed, where the exponent was varied while keeping all the other parameters constant, and the source term and boundedness parameters were printed as a function of vertical position for several different streamwise locations. It was found that the value of $5/7$ given by Ishii and Zuber [24] was the most appropriate choice. Figures 6.4 and 6.5 below show a comparison of these terms at approximately halfway between the right splitter plate and the inlet diffuser (i.e. at $x/L = 0.5$). The volume fraction is also plotted

to show the location of the interface. The case plotted here corresponds to $Ri^* = 0.7$ and droplet diameter $d_p = 2\text{mm}$. As it is seen from these figures, the source term calculated in terms of the slip velocity (USLS1 and USLN1) is at all points either less than the boundedness checks, or very close. For regions away from the fuel/water interface, the relative magnitudes of the three terms is either zero, in the case of an unmixed fluid layer (i.e. where $r_\alpha = 0$ or 1), or so small that the differences are negligible.

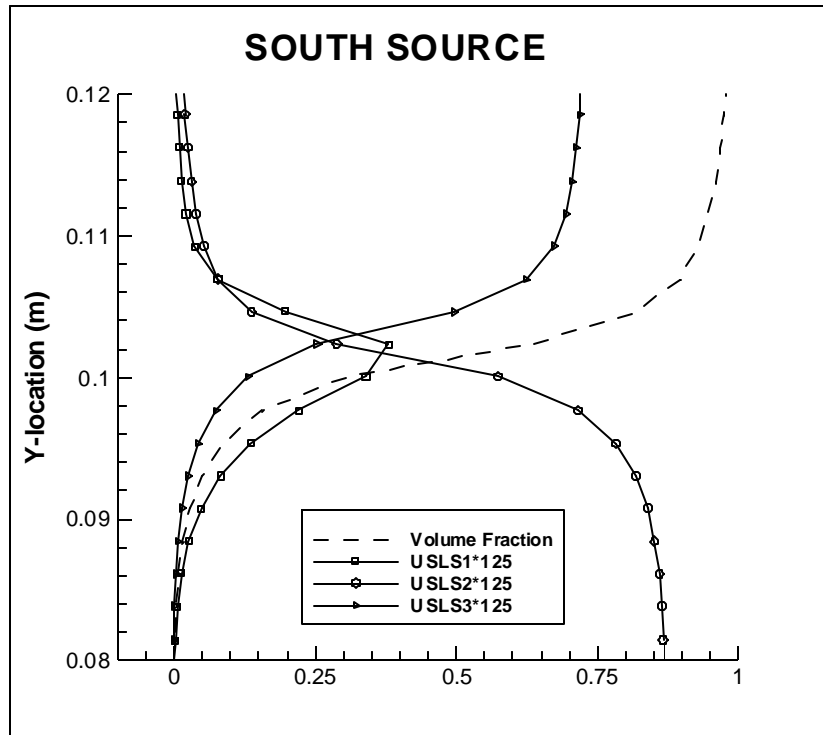


Figure 6.3 – Comparison of south cell face source term with boundedness checks; $Ri^*=0.7$, $d_p=2\text{mm}$.

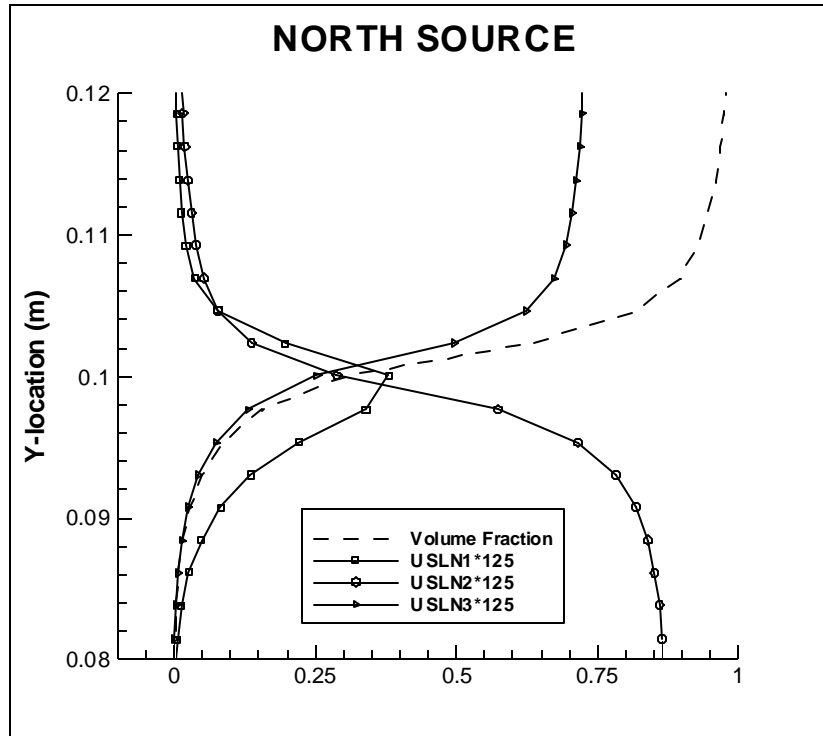


Figure 6.4 – Comparison of north cell face source term with boundedness checks; $Ri^*=0.7$, $d_p=2\text{mm}$.

After having determined the exponent to use in the slip velocity, simulations were performed to investigate the influence of the droplet diameter for both values of the overall Richardson number, $Ri^* = 0.7$ and $Ri^* = 0.32$. The results of these simulations are given below. The figures that depict the streamlines (Figs. 6.6 and 6.8) reflect the complex nature of the flow, and the development of several recirculation zones throughout the test apparatus. The presence of these recirculation zones, particularly in the region near the inlet diffuser, was confirmed by experimental observation at Johns Hopkins University.

An important conclusion from the figures given below is that the mixed fluid thickness decreases with increasing droplet size. This of course makes sense as a larger fluid

droplet will have a larger terminal velocity and will tend to move towards the fluid interface at a faster rate than a smaller droplet. This then also increases the rate at which settling, or separation, occurs by which fluid droplets will tend to return to their original fluid layer, and the system moves towards a stable density stratification. As the mixed fluid thickness is a measure of the amount of fluid at the interface that has not returned to a continuous fluid layer, an increase in the rate of separation would cause δ_M to decrease.

It can also be seen by comparing corresponding figures for both values of the overall Richardson number (e.g. Fig. 6.7 and Fig. 6.11), that δ_M increases as Ri^* decreases. Again, this makes sense because since Ri^* is a measure of the ratio of buoyancy to shear forces, a decrease in the Richardson number indicates an increase in turbulence, and hence increased mixing.

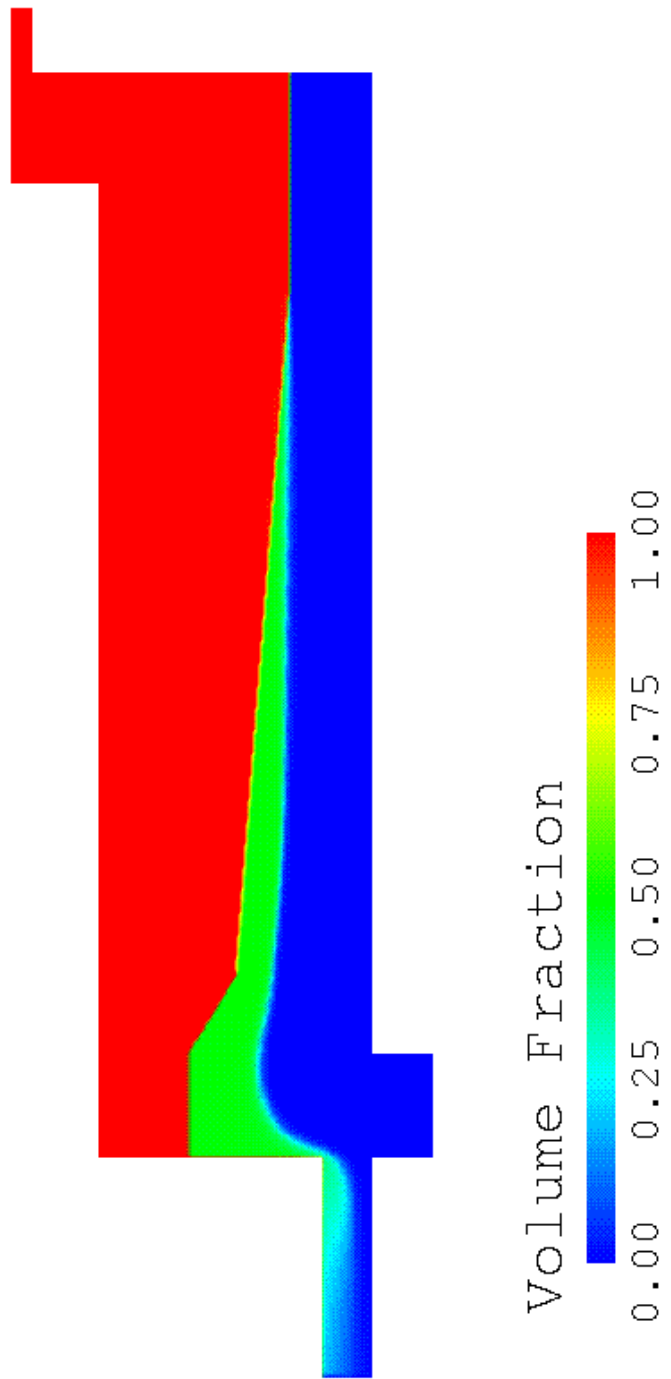


Figure 6.5 – Volume fraction contours; $Ri^* = 0.7$, $d_p = 6\text{mm}$.

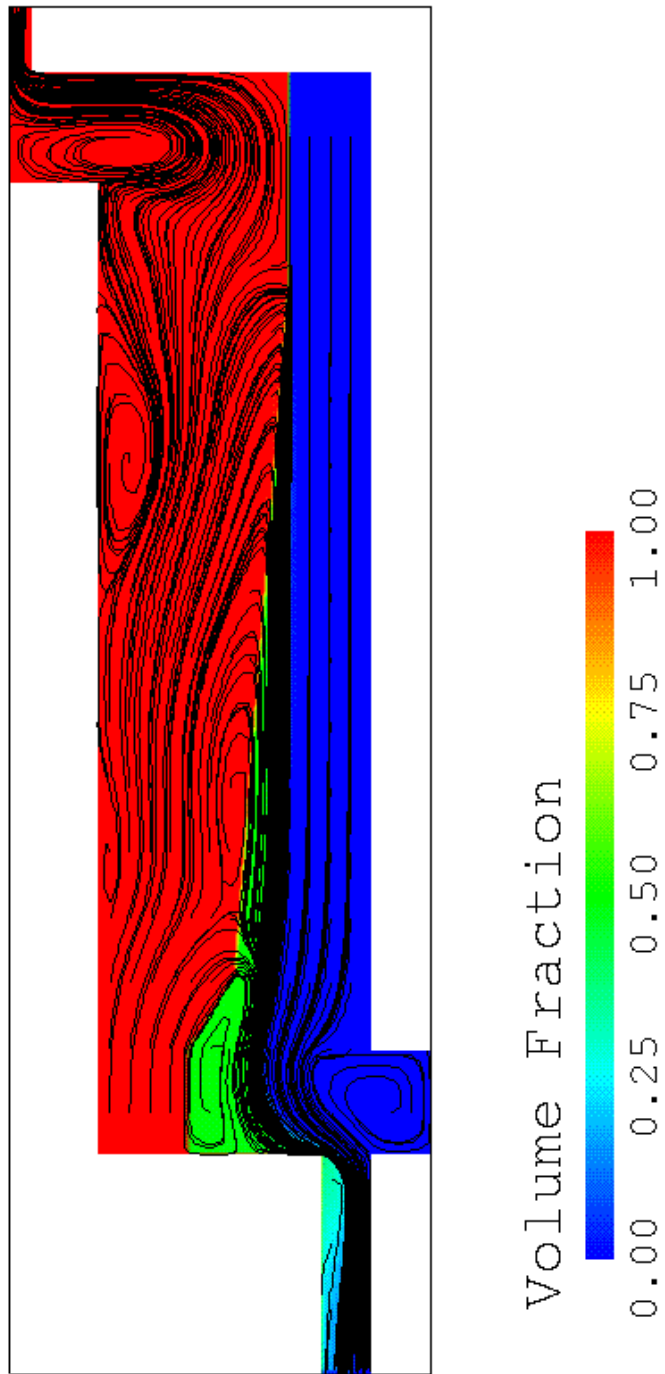


Figure 6.6 – Streamlines and volume fraction contours; $Ri^* = 0.7$, $d_p = 6\text{mm}$.

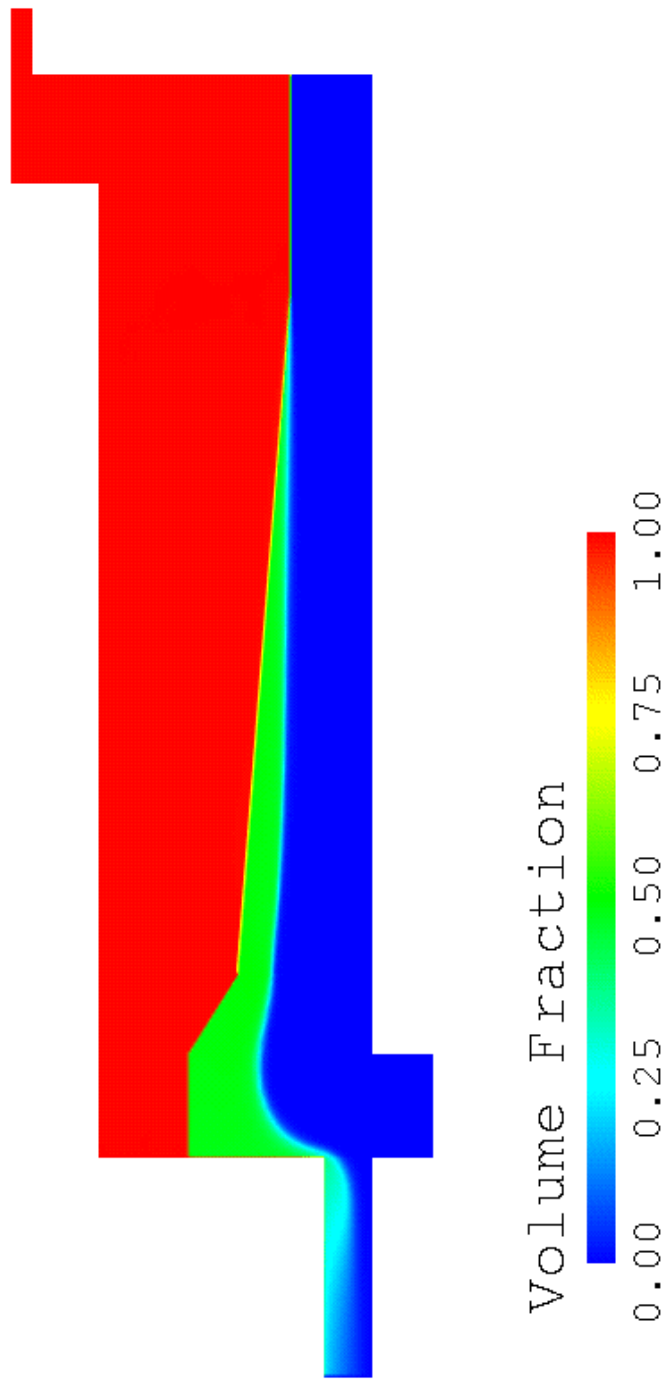


Figure 6.7 – Volume fraction contours; $Ri^* = 0.7$, $d_p = 2\text{mm}$.

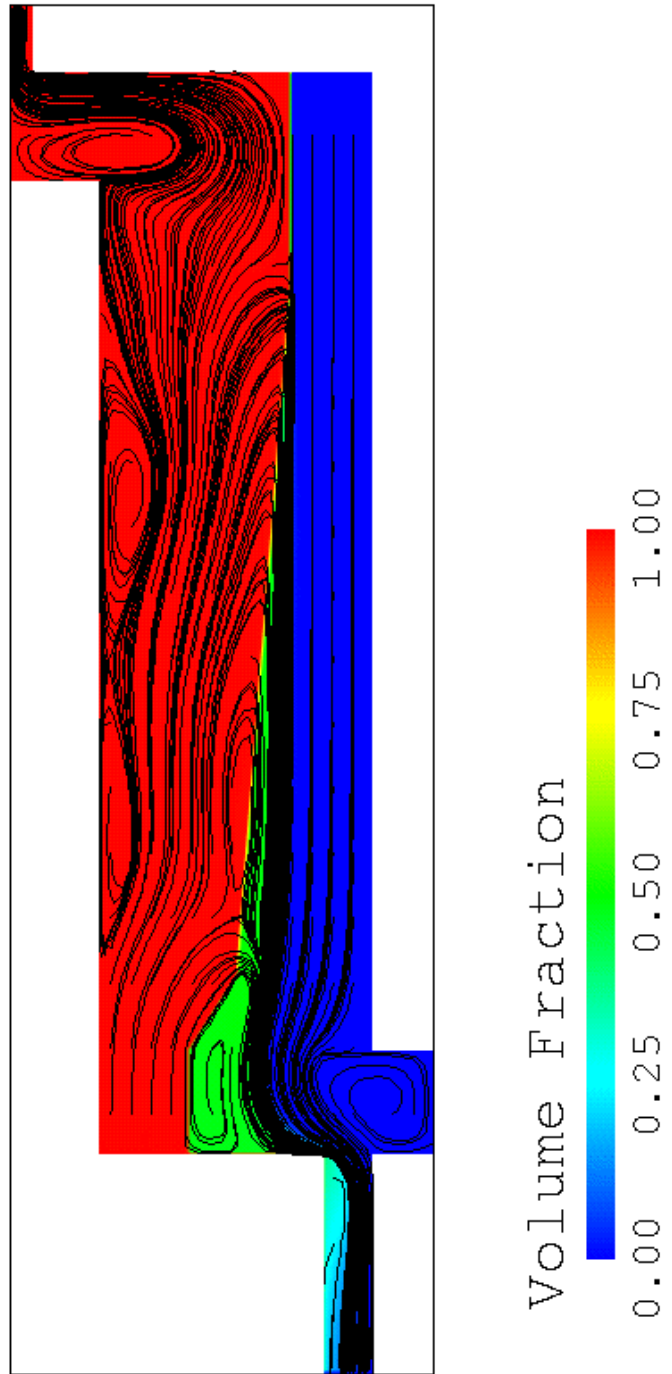


Figure 6.8 – Streamlines and volume fraction contours; $Ri^* = 0.7$, $d_p = 2\text{mm}$.

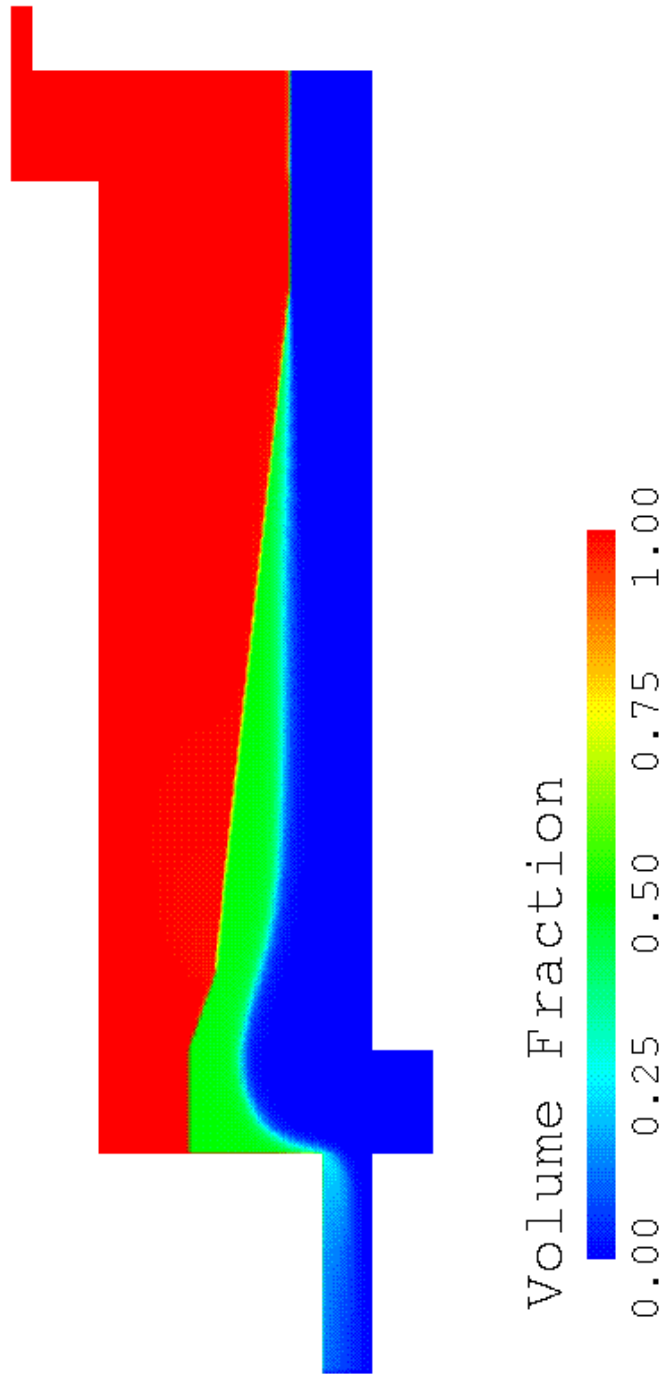


Figure 6.9 – Volume fraction contours; $Ri^* = 0.32$, $d_p = 6\text{mm}$.

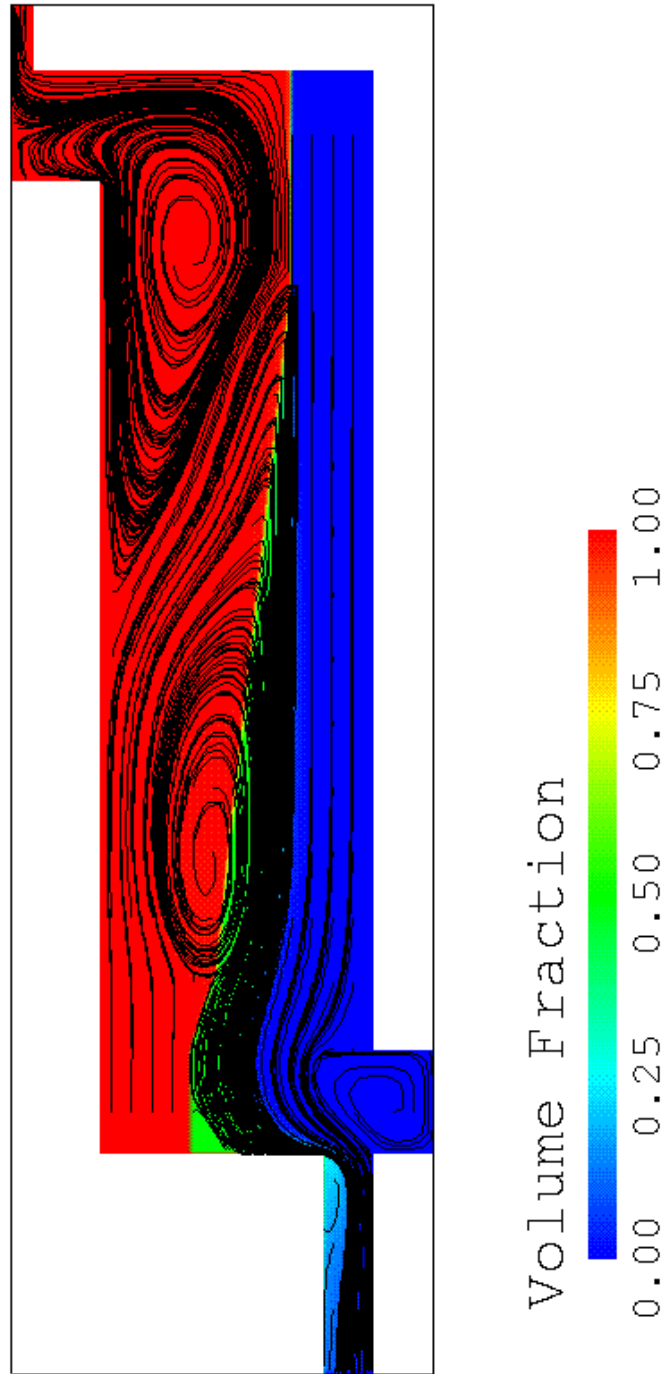


Figure 6.10 – Streamlines and volume fraction contours; $Ri^* = 0.32$, $d_p = 6\text{mm}$.

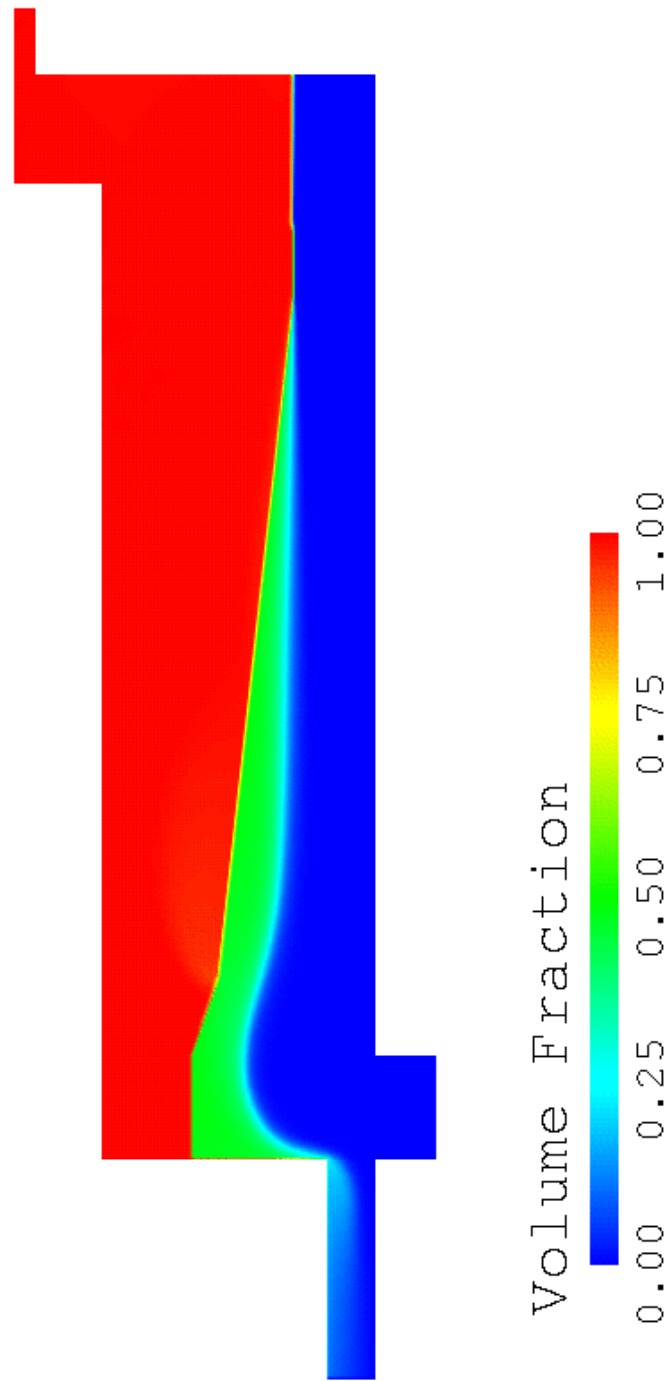


Figure 6.11 – Volume fraction contours; $Ri^* = 0.32$, $d_p = 2\text{mm}$.

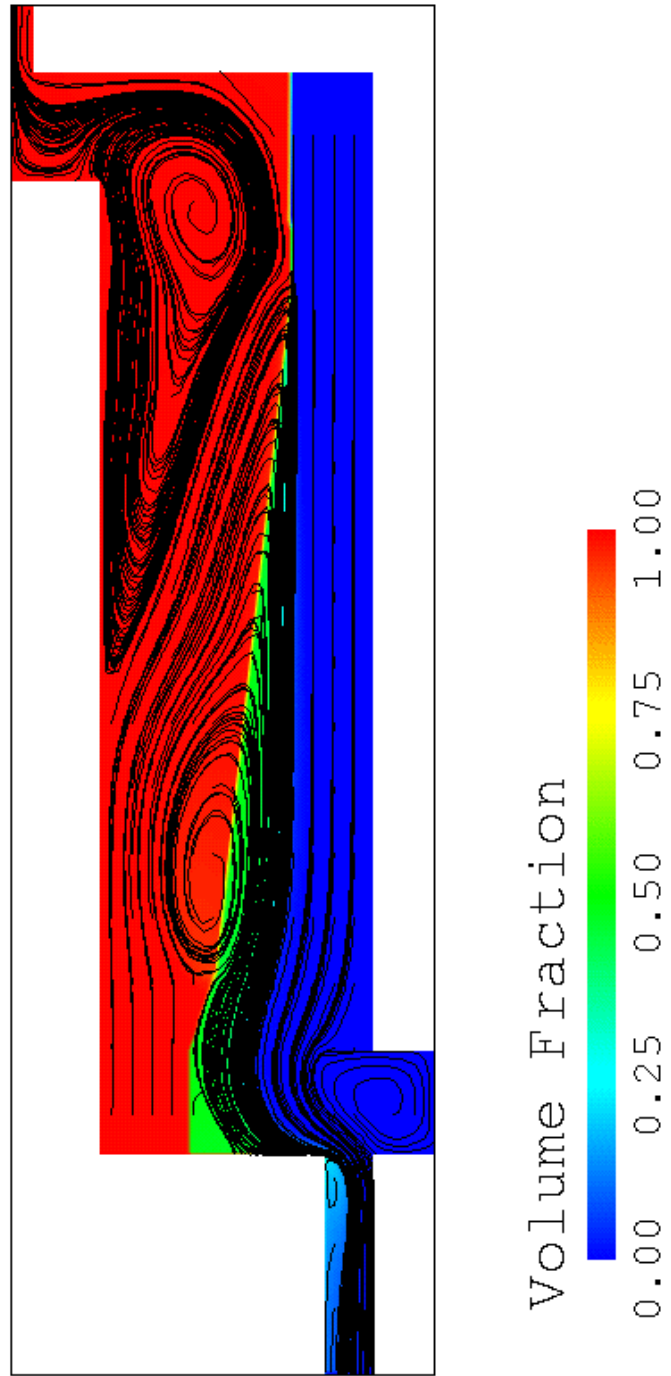


Figure 6.12 – Streamlines and volume fraction contours; $Ri^* = 0.32$, $d_p = 2\text{mm}$.

The decrease in the mixed fluid thickness, however, is really only noticeable far downstream from the right splitter plate, near the fuel inlet diffuser. Here there is a noticeable change in the amount of mixed fluid, by comparison of Fig 6.5 and Fig. 6.7. In the region near the right splitter plate, there appears to be very little change as a result of the increased droplet size. Figure 6.13 below shows the mixed fluid thickness plotted as a function of downstream distance x , normalized by the total streamwise distance L between the right splitter plate and the inlet diffuser, for both values of the droplet diameter. The above-mentioned conclusions regarding the influence of the droplet diameter can be much more clearly seen in this figure.

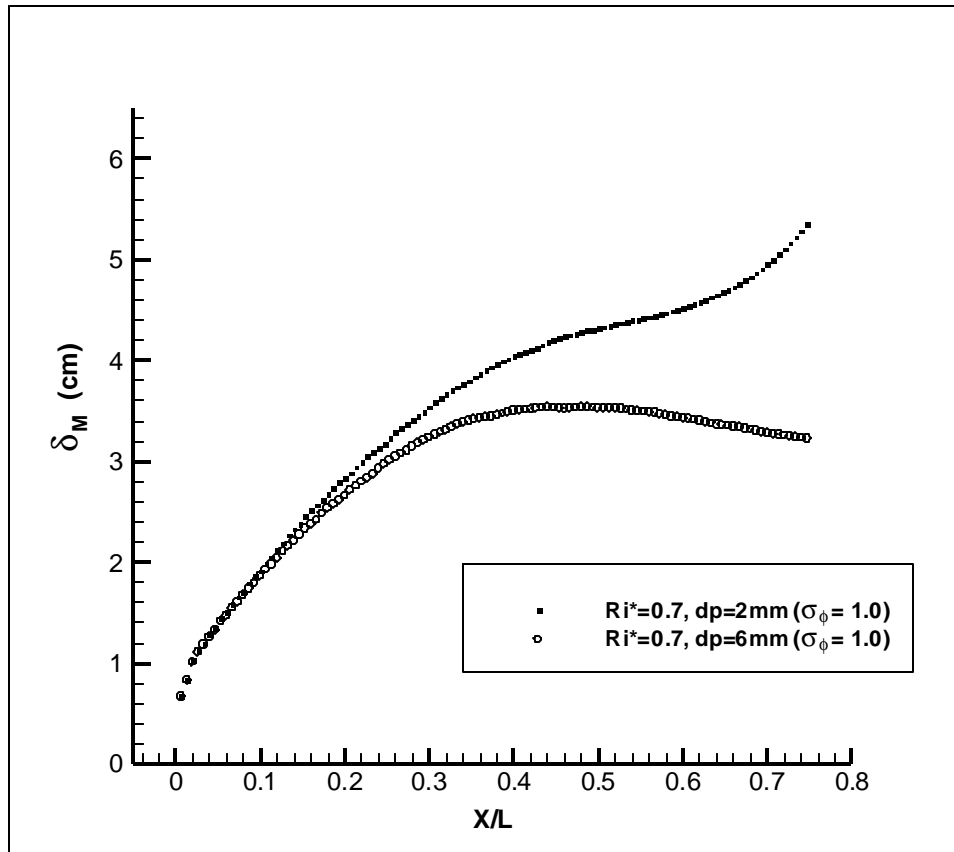


Figure 6.13 – Mixed fluid thickness vs. normalized downstream distance for varying droplet diameter; $Ri^*=0.7$.

An investigation of the influence of the droplet size for the case of $Ri^* = 0.32$ yielded similar results. The mixed fluid thickness variations as a function of downstream distance for $Ri^* = 0.32$ are given in Fig. 6.14 below. The results indicate a similar trend with respect to the decrease in the mixed fluid thickness with increasing droplet diameter, as well as an increase in the mixed fluid thickness in the streamwise direction from the right splitter plate towards the inlet diffuser.

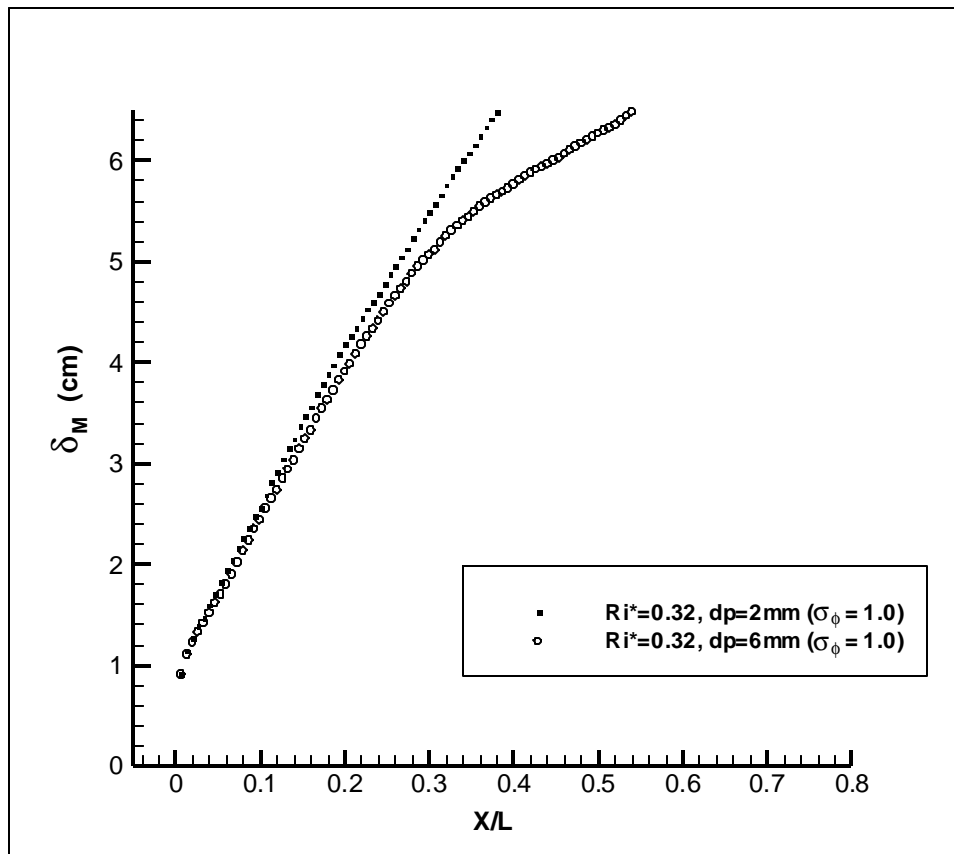


Figure 6.14 – Mixed fluid thickness vs. normalized downstream distance for varying droplet size; $Ri^* = 0.32$.

After having shown the influence of the droplet diameter, an investigation was also performed for the influence of the turbulent Prandtl number, σ_ϕ , for the scalar equation. Recall that the scalar transport equation used to solve for the volume fraction was altered from the previous version of the SFST model by changing the source term. This would in turn cause a change in the value of σ_ϕ compared to σ_α . The diffusion term here is given by

$$\frac{\partial}{\partial x_i} \left[\Gamma_{eff} \left(\frac{\partial \mathbf{f}}{\partial x_i} \right) \right] = \frac{\partial}{\partial x_i} \left[\left(\Gamma_f + \frac{\mu_t}{\sigma_\phi} \right) \frac{\partial \mathbf{f}}{\partial x_i} \right] \quad (6.3.3)$$

where Γ_f represents the molecular diffusivity, and μ_t and σ_ϕ represent the eddy viscosity and turbulent Prandtl-Schmidt number, respectively. As it is not known *a priori* what the value of σ_ϕ should be used for the new variable $\mathbf{f} = r_a \mathbf{r}_a / r_m$ (see Eqs. A.2.11, A.2.17), simulations were performed to investigate the influence of changing σ_ϕ . For these simulations, a characteristic droplet diameter of 4mm was chosen as a good approximation for the average droplet size, as per discussion with the researchers conducting the experiments. The variation in the mixed fluid thickness as a function of downstream distance for $\sigma_\phi = 1.0$ and $\sigma_\phi = 1.5$ is given in Figs. 6.15 and 6.16 below.

These results are also plotted along with the data from the experiments so that a comparison can be made.

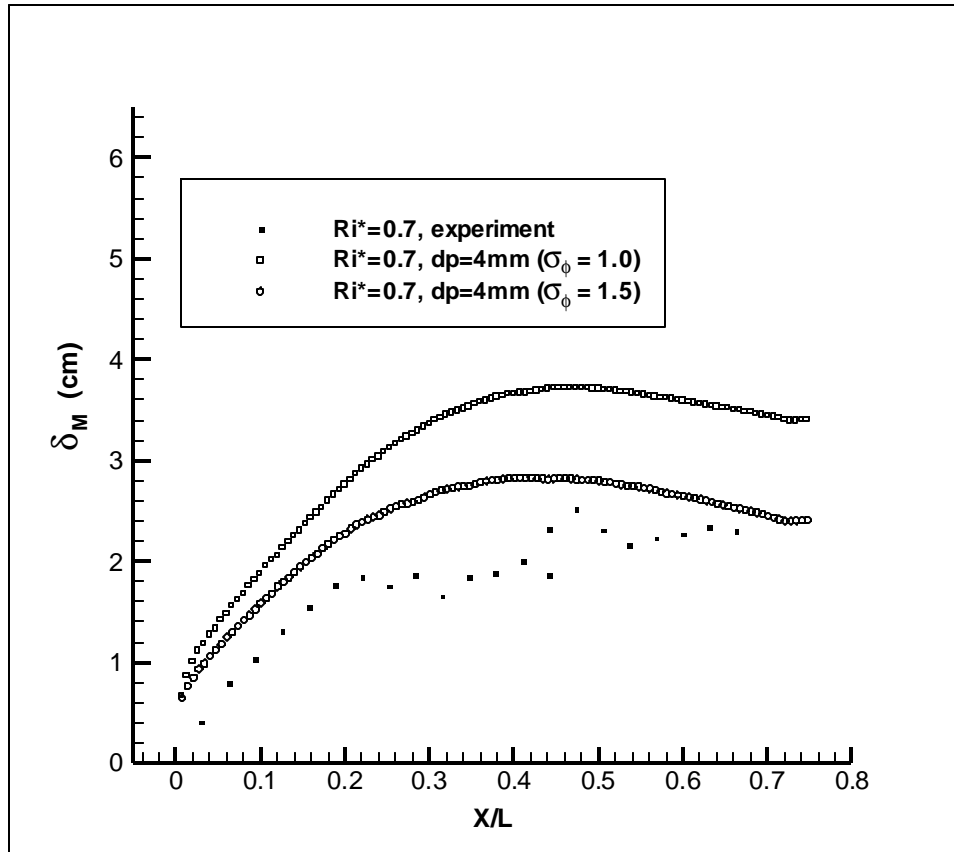


Figure 6.15 – Mixed fluid thickness vs. normalized downstream distance; $Ri^*=0.7$, $d_p = 4\text{mm}$ (influence of σ_ϕ).

As expected, the mixed fluid thickness decreases with increasing turbulent Prandtl number, σ_ϕ (Fig. 6.15). An increase in the turbulent Prandtl number for the scalar causes a decrease in the diffusion term present in the scalar transport equation used to solve for the volume fraction. This would in turn cause the thickness of the mixed fluid regions to decrease. Similar results for $Ri^* = 0.32$ are given in Fig. 6.16 below.

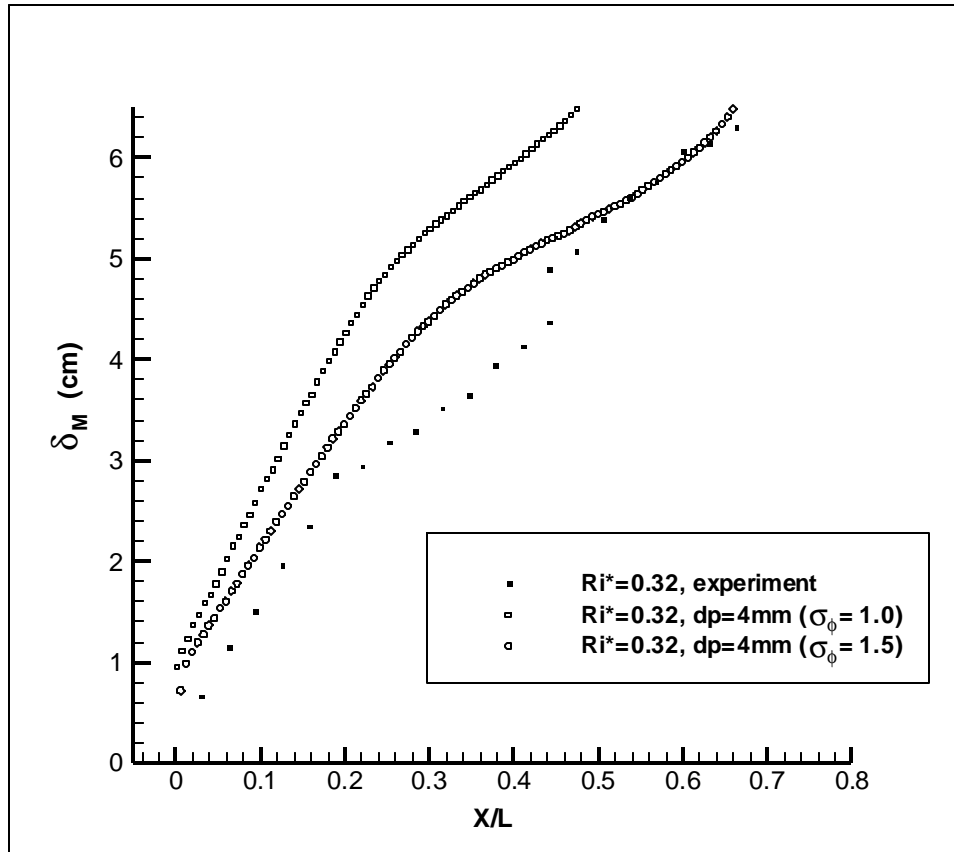


Figure 6.16 – Mixed fluid thickness vs. normalized downstream distance; $Ri^*=0.32$, $d_p=4\text{mm}$ (influence of σ_ϕ).

Results for the mixed fluid thickness variation with downstream distance show good agreement with the experimental results with regard to trends, as well as in magnitude for the case of $\sigma_\phi=1.5$. By comparing Fig. 6.15 and Fig. 6.16 above, it appears that this agreement is better in the case of $Ri^*=0.32$. The reason for this is most probably due to the fact that the characteristic droplet size should increase as the overall Richardson number increases; therefore, while good agreement was found for $Ri^*=0.32$, the same should not be true for a higher Ri^* using the same characteristic droplet size.

One comment should be made here with regard to the errors in the experimental data. In measuring the mixed fluid thickness, a series of high-speed photographs were taken, and the mixed fluid thickness at each downstream location was then averaged over time. While the error in the data has not yet been fully analyzed, by comparison of several different measurements at different times for the same location, it would appear that the error is on the order of approximately ± 0.25 cm. After accounting for this error, the agreement between the experiments and the numerical predictions is quite good.

One cause for concern in Fig. 6.15 and Fig. 6.16 above is in regard to the slope of the predicted values of δ_M very near the right splitter plate (i.e. for x/L approaching 0). As shown in the above figures, the rate at which the predicted values for δ_M change near the left hand side of the figure is much greater than that observed in the experiments. One possible explanation for this was thought to be that the computational mesh needed to be refined further in the vertical direction near the location of the interface, as well as in the streamwise direction near the right splitter plate. To investigate the effects of this mesh refinement, a finer grid was constructed such that 250 cells would be used in the streamwise direction in the mixing region (there were 150 cells in the previous mesh), and 150 cells in the vertical direction (there were 104 cell in the previous mesh). To demonstrate the influence of this refinement, a value of 2mm was used for the droplet diameter in simulating both the $Ri^*=0.7$ and $Ri^*=0.32$ cases, as the smaller diameter produces more mixing, and so any changes would be more apparent.

The results for the variation in δ_M with x/L are given below in Fig. 6.17 and Fig. 6.18, and are plotted along with the results from the courser mesh described in Section 6.2. As can be seen in both cases, there is some improvement in the region near the right splitter plate in that the slope has been decreased, but this is only a minor improvement. It is believed, then, that for the cases simulated in the present study that the results are nearly grid independent with regard to the mixed fluid thickness. It is further believed that much of this discrepancy with regard to the slope near the right splitter plate is most probably due to the turbulence model, and possibly the corresponding inlet conditions, used. It would be beneficial to investigate the use of a low-Reynolds number model, which would more accurately describe the turbulence levels in those regions just above the splitter plate in the fuel layer, which are probably essentially laminar. It may also be that a more accurate solution of the turbulence quantities through the use of a second moment closure model, or algebraic stress model may be necessary.

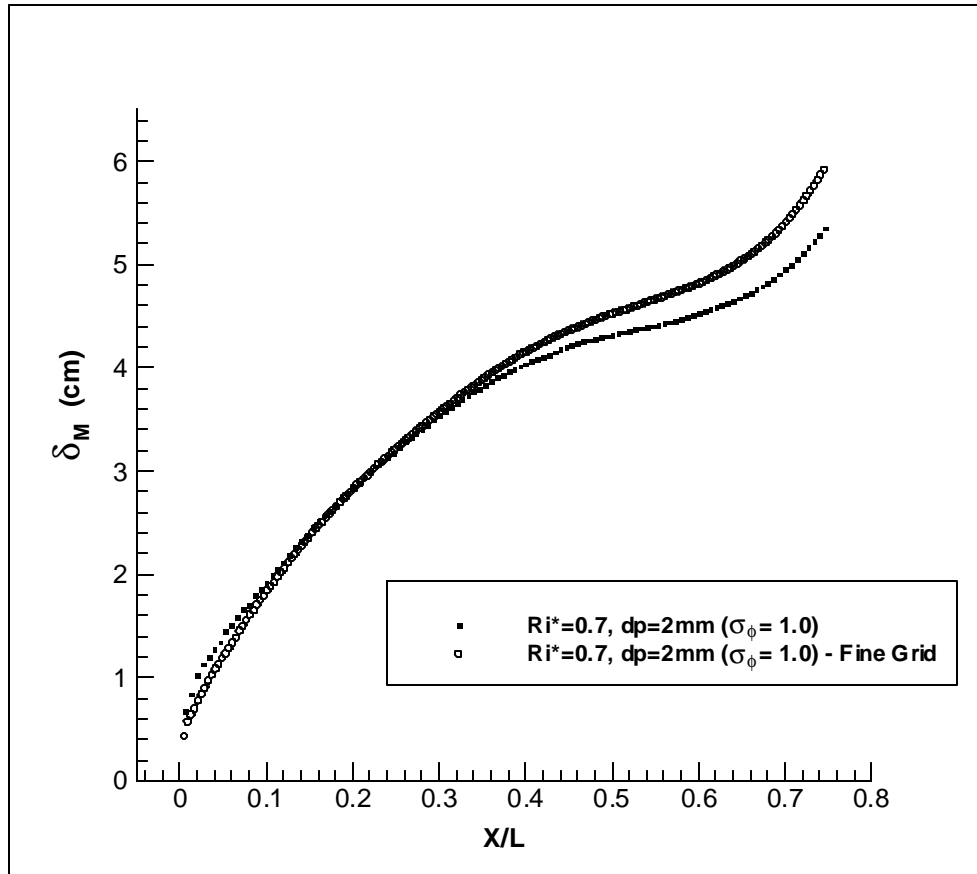


Figure 6.17 – Mixed fluid thickness vs. normalized downstream distance; $Ri^*=0.7$ (influence of grid refinement).

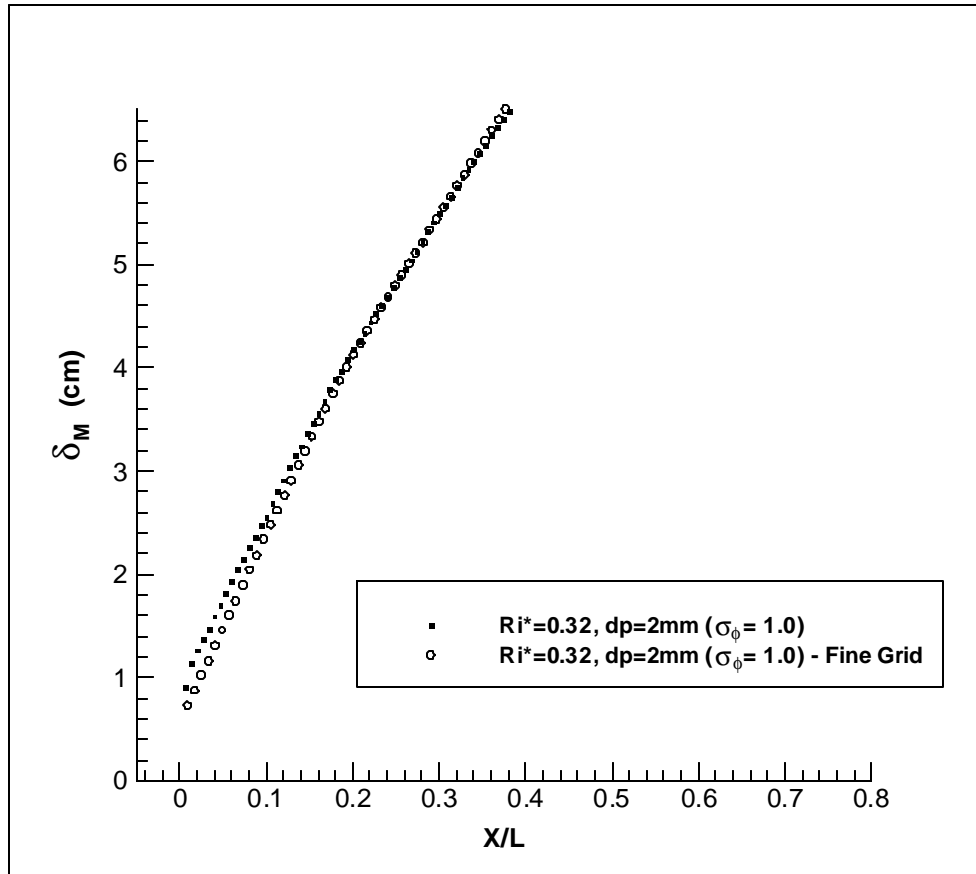


Figure 6.18 – Mixed fluid thickness vs. normalized downstream distance; $Ri^*=0.32$ (influence of grid refinement).

Several digital images were taken [38] during the actual experiments at three different locations in the streamwise direction. They are given below in Figures 6.19-6.21. They depict the downstream development of the mixture layer for the case of an inlet water flowrate of 120 gal/min, which corresponds to $Ri^* = 0.32$. Some comparison can be made between these photographs and the results of the simulations, although it is important to remember that these are instantaneous images, whereas the simulations provide a time-averaged solution.

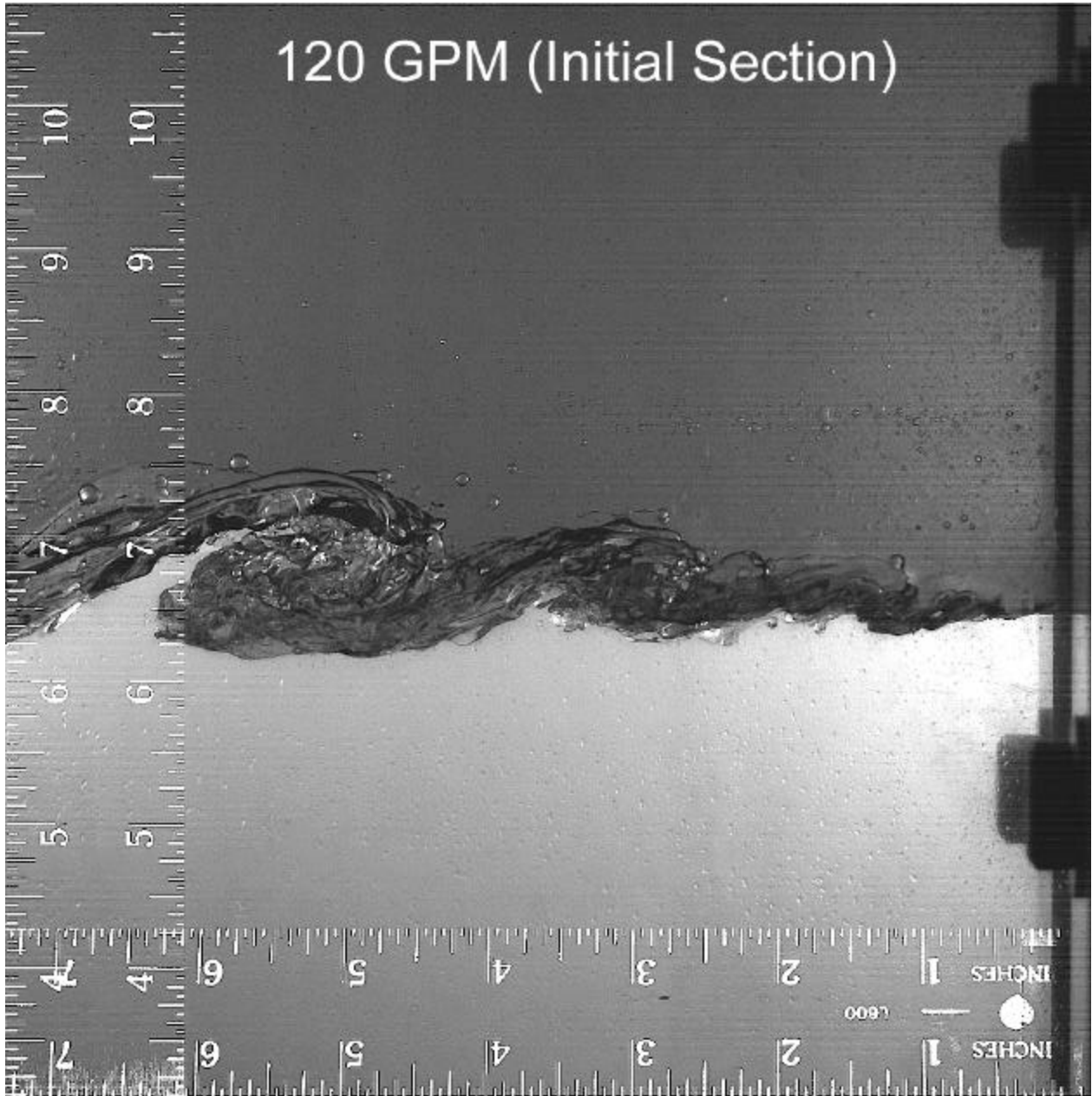


Figure 6.19 – Instantaneous mixing layer near water inlet; After Wu and Katz [38].

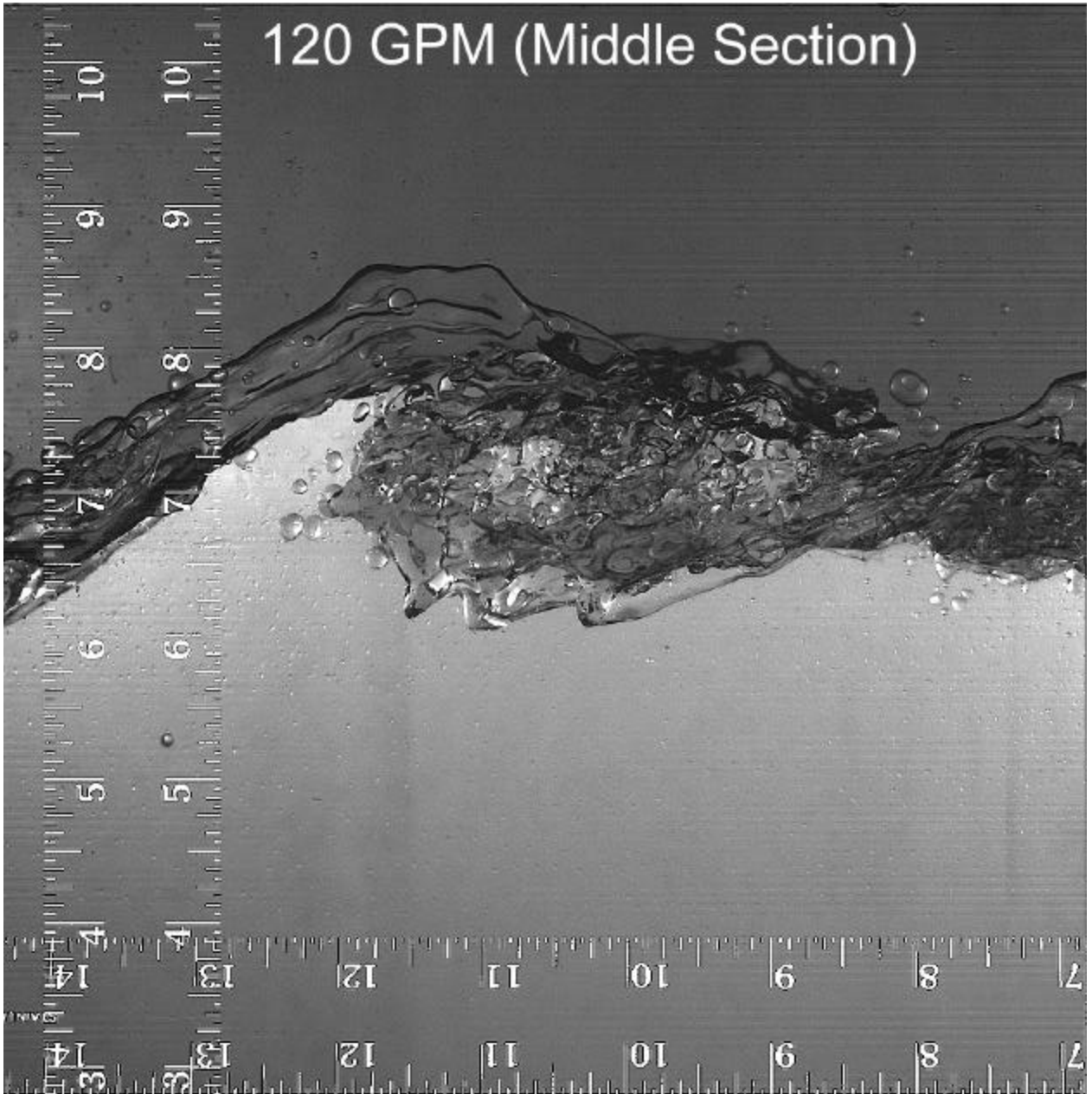


Figure 6.20 – Instantaneous mixing layer near central section; After Wu and Katz [38].

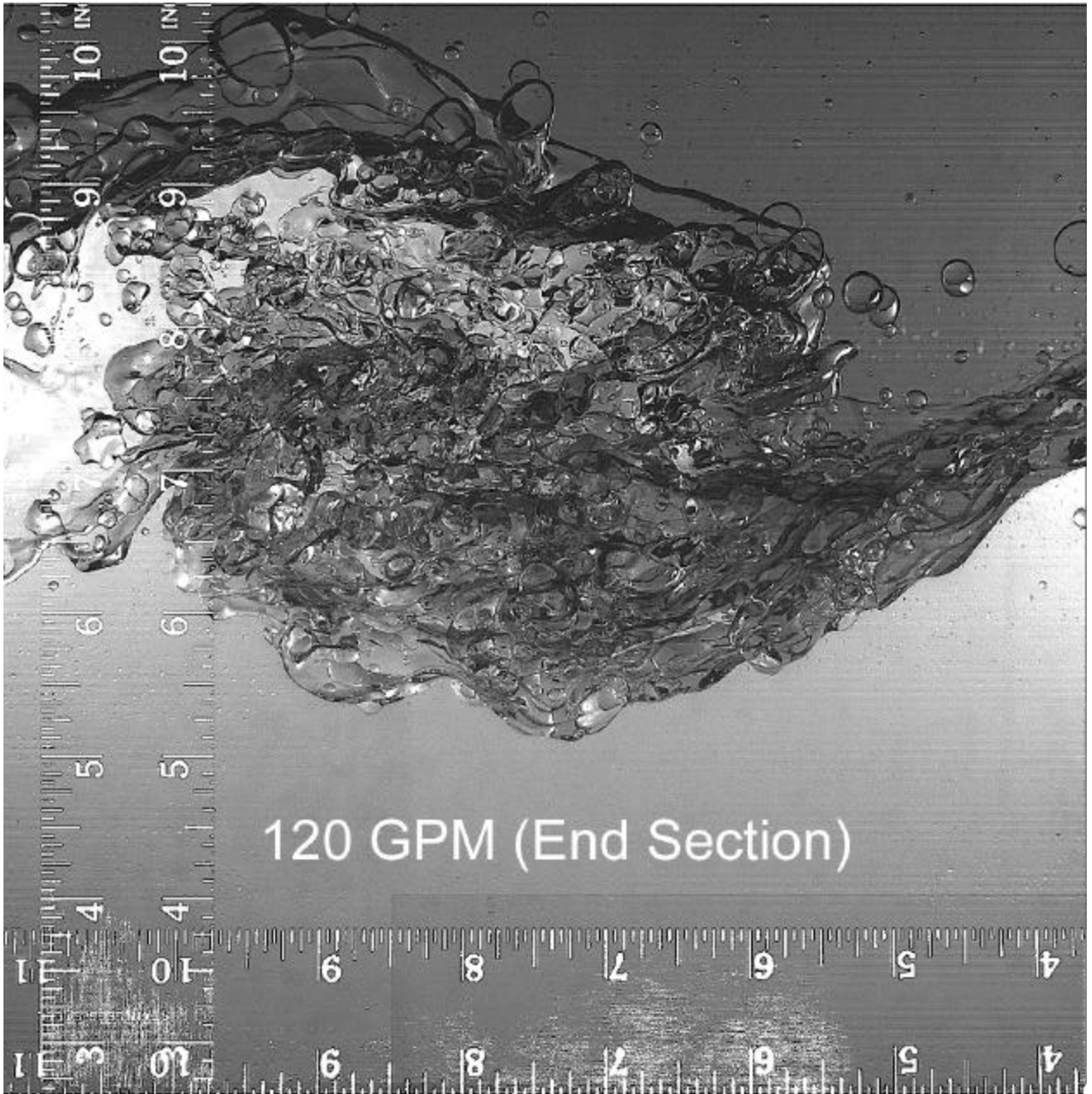


Figure 6.21 – Instantaneous mixing layer near fuel inlet diffuser; After Wu and Katz [38].

Figures 6.19-6.21 indicate that the thickness of the mixture layer increases with downstream distance, as more of the outlying fuel is entrained into the water layer. This trend is confirmed by the numerical simulations detailed previously. It is also interesting to note the Kelvin-Helmholtz (K-H) type waves that develop as the flow progresses downstream. Roll-up and pairing phenomena have also been observed experimentally. The presence of these types of waves further lends some credibility to the numerical model for predicting the droplet size, as the model expressions were derived from analyses of K-H instabilities. It is also important to note here that the numerical predictions in this study utilize time-averaged quantities. The numerical models cannot account for the types of transient phenomena evidenced in Figs. 6.19-6.21, such as the roll-up and pairing of K-H vortices, and the interface fluctuations.

In the next section, results will be presented from the predictions of the simulations in which the SFST model was used in conjunction with the DFE model, and the locally calculated droplet size was implemented in the slip velocity relationship for each individual fluid cell. Here, it was decided that a value of 1.3 was an appropriate value for the turbulent Prandtl number in the scalar equation, σ_ϕ , based on the previous investigation of its influence in the simulations performed with a constant, average droplet size.

In order to properly use the dynamic DFE model, the model expressions given in Table 5.2 were abandoned in favor of the general model expressions given in Table 5.3. The two constants C_1 and C_2 , and the exponents m and n were then calibrated based on

predictions for the variations in the mixed fluid thickness in the streamwise direction, as well as the average droplet size in the vertical direction. Results are given below for the predictions from simulations in which the calibrated model was used. The final values of the two exponents and two constants after having completed the calibration procedures are given in Table 6.2 below.

Table 6.2 – Model Coefficients in Calibrated DFE Model

EXPONENTS		CONSTANTS	
m	n	C ₁	C ₂
0	0.1	4.0	15.0

In order to apply some physical limitations to the droplet sizes predicted, the droplet diameter was limited by half of the mixed fluid thickness in the vertical direction, based on observations from the experiments, as well as the distance to the nearest wall. Results for the droplet diameter and gradient Richardson number profiles will be presented later.

The volume fraction contour and fluid streamlines are given in Fig. 6.22 and Fig. 6.23 for the simulations using the dynamic DFE model for the case of $Ri^* = 0.7$. As can be seen from examining these figures, there is not a large change in the volume fraction profiles as compared with the results from simulations using a constant, average droplet size. This demonstrates that the use of the dynamic DFE model does not cause drastic changes in the flowfield, and maintains reasonable results for the volume fraction field. Results for the droplet diameter and gradient Richardson number profiles are given at several different downstream locations following these figures.

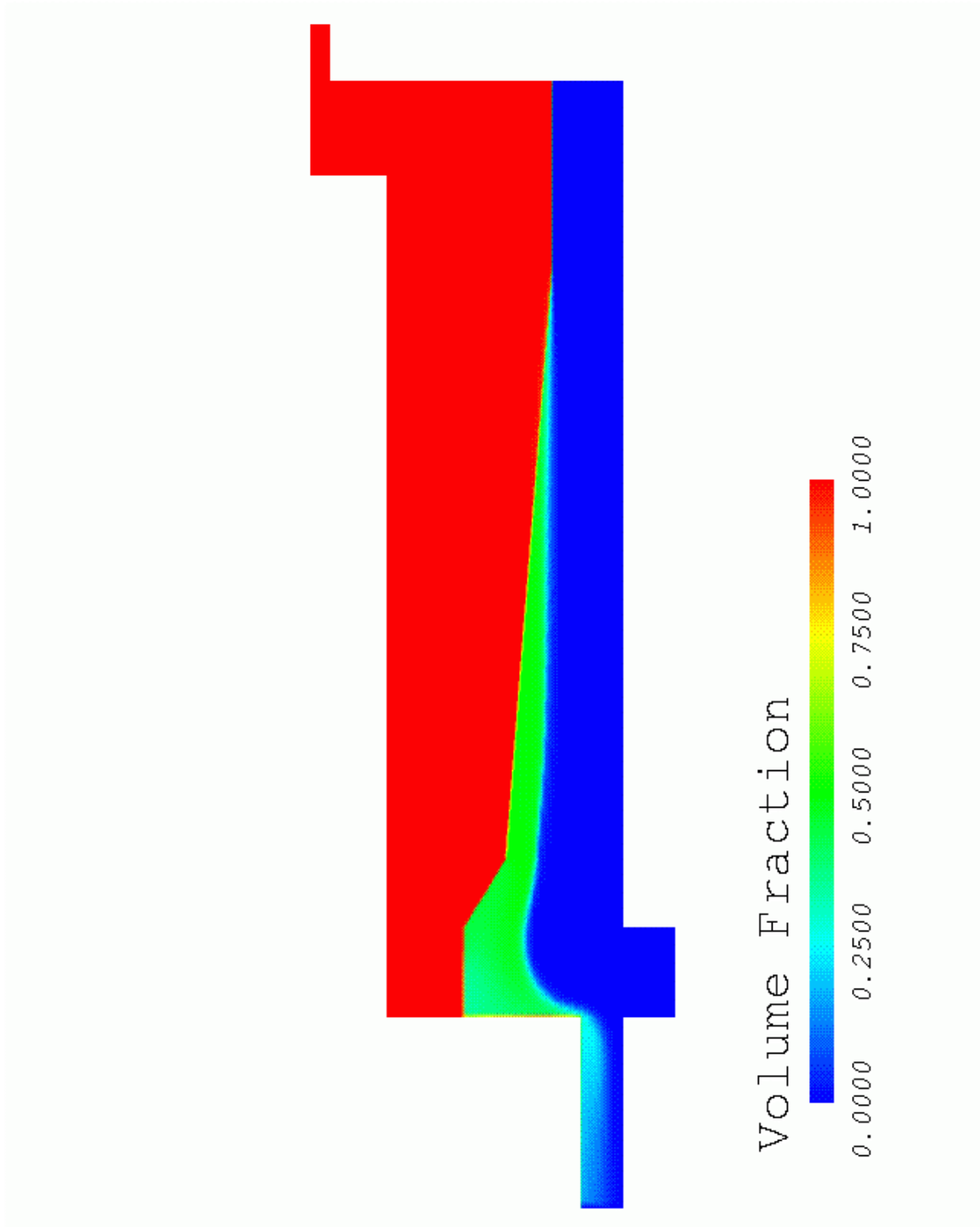


Figure 6.22 – Volume fraction contours; $Ri^* = 0.7$, $d_p = \text{variable}$.

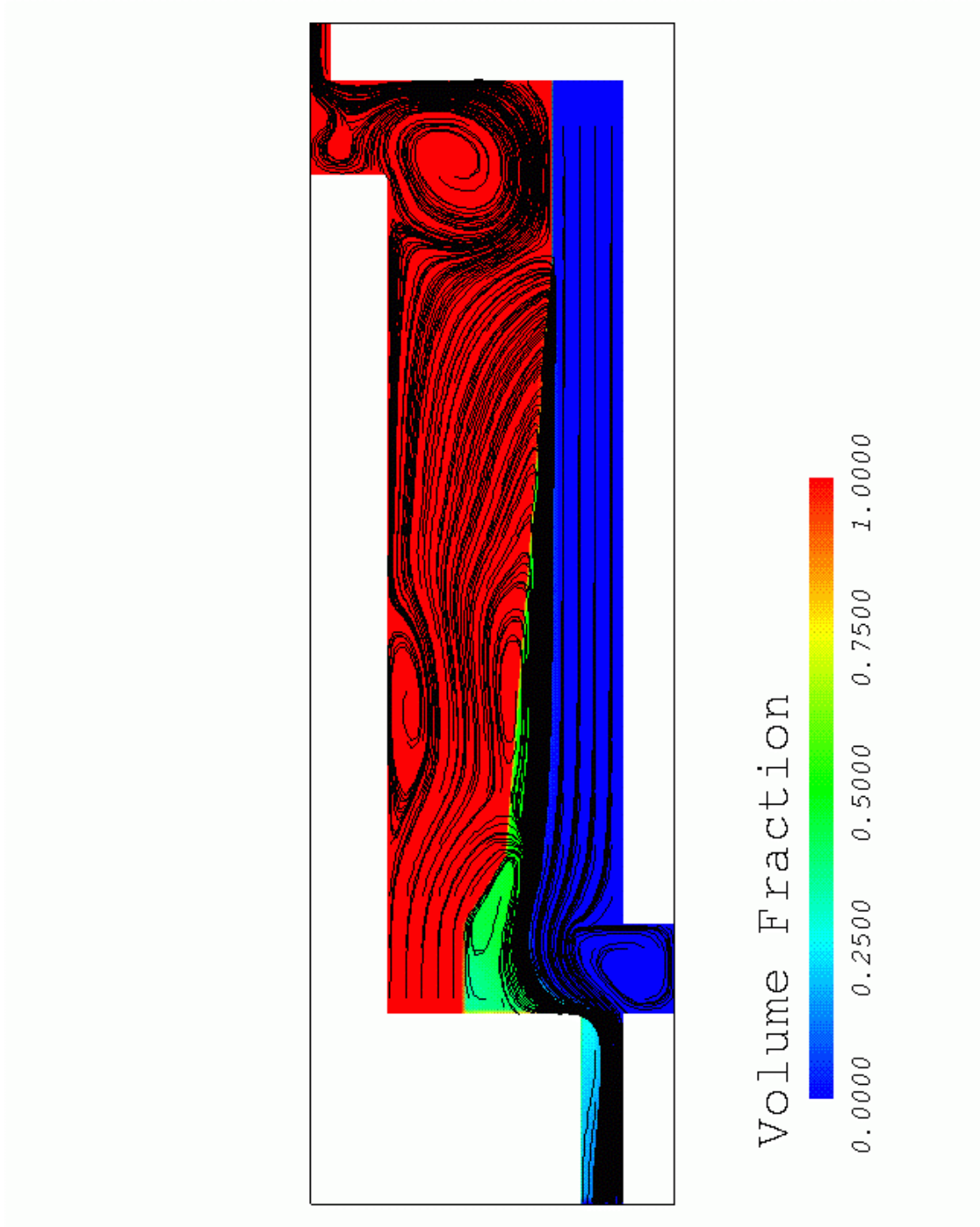


Figure 6.23 – Volume fraction contours and streamlines; $Ri^* = 0.7$, $d_p = \text{variable}$.

Next, we will examine the droplet diameter profiles using the dynamic DFE model for the case of $Ri^* = 0.7$. The predicted droplet sizes are plotted along with the volume fraction profile as a function of vertical position at downstream locations of $x/L = 0.25$, 0.5, and 0.75 in Figures 6.24 – 6.26 below. Here the droplet diameter is normalized by the maximum value across the shear layer of 2.0 cm.

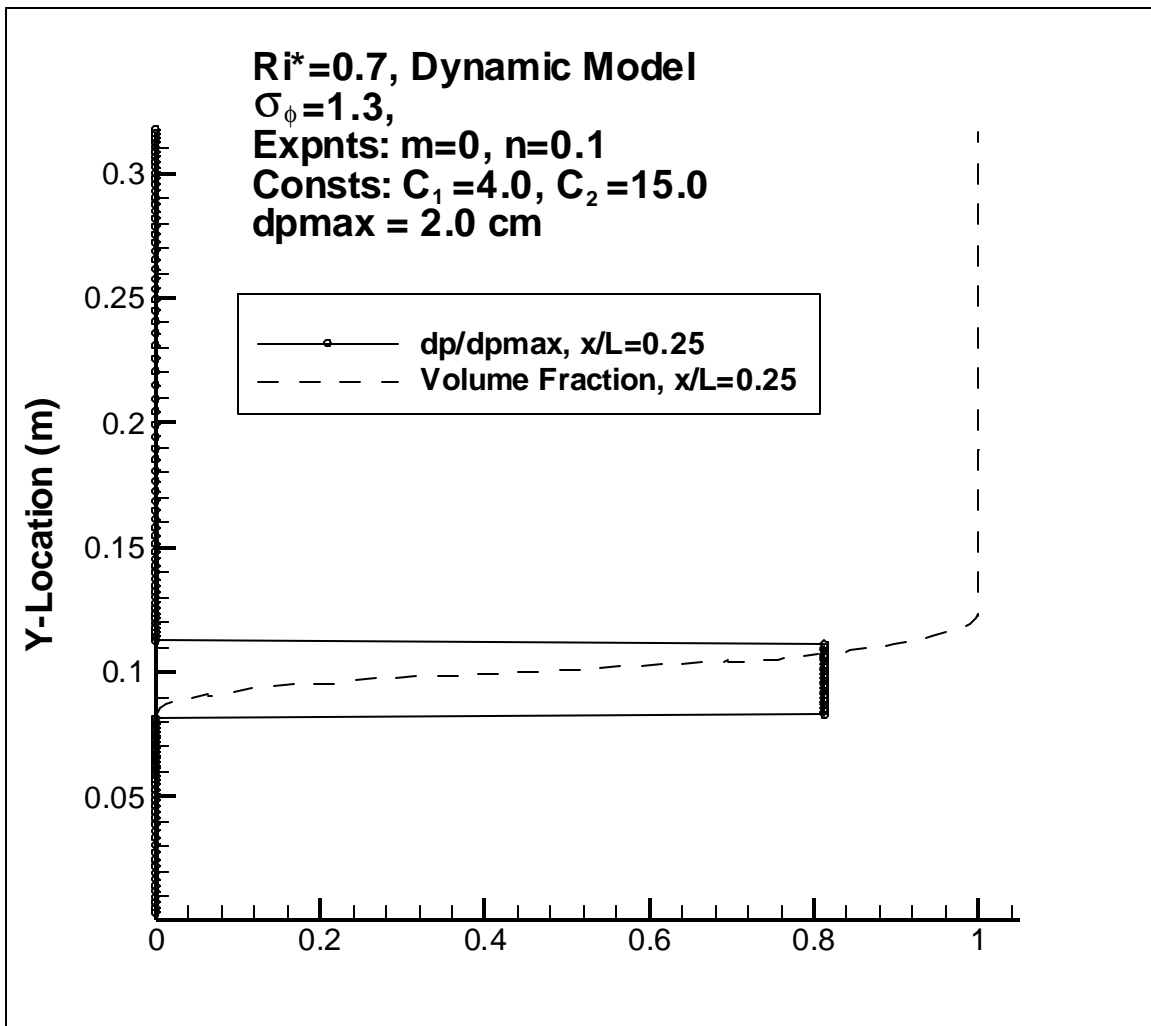


Figure 6.24 – Normalized droplet diameter with volume fraction; $Ri^* = 0.7$, $x/L = 0.25$.

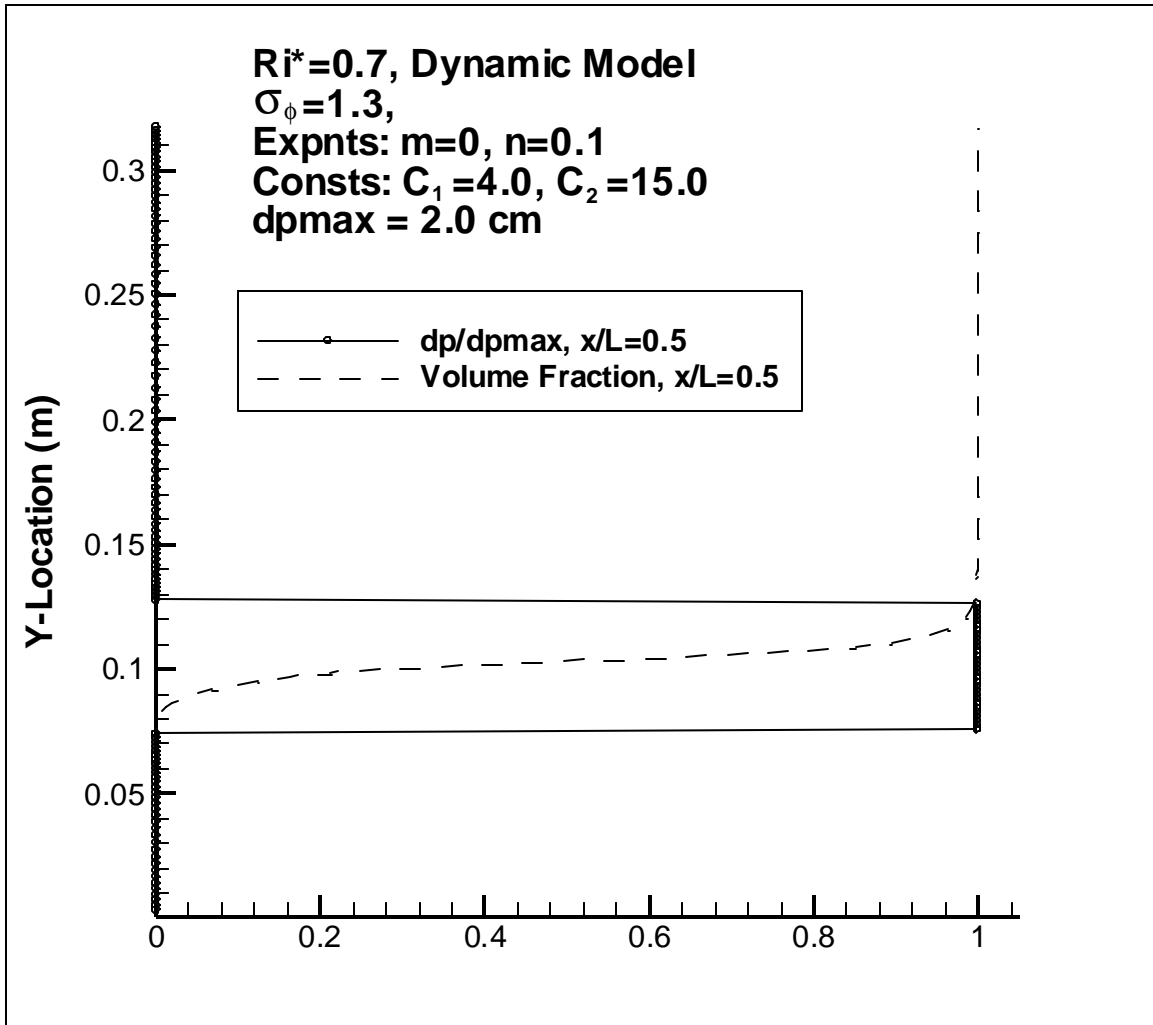


Figure 6.25 – Normalized droplet diameter with volume fraction; $Ri^* = 0.7$, $x/L = 0.5$.

As can be seen by examining Figs. 6.24 – 6.26, the droplet diameter profile is not unreasonable, both in magnitude and location. There are no droplets predicted in the regions where the volume fraction approaches 0.0 or 1.0, and the maximum value is not unreasonable based on experimental observations. It is also interesting to note that the droplet diameter first increases and then decreases in the streamwise direction, and also that the vertical distance over which droplets are generated follows the same progression.

This is indicative of the manner in which the mixed fluid thickness first increases and then decreases, as was observed in the experiments for these conditions.

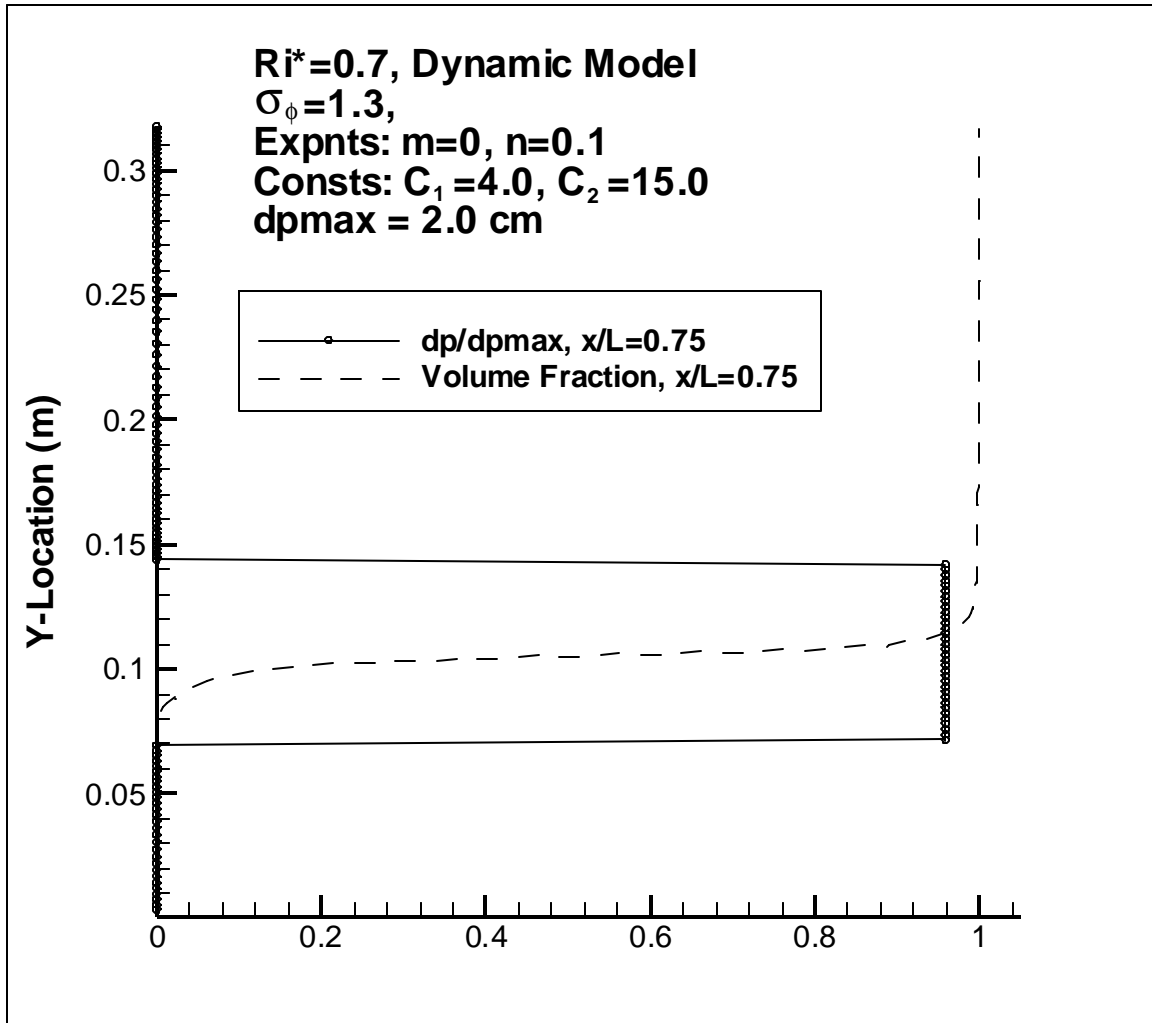


Figure 6.26 – Normalized droplet diameter with volume fraction; $Ri^* = 0.7$, $x/L = 0.75$.

Similar studies have also been performed for the cases of $Ri^* = 0.32$, which corresponds approximately to an inlet water velocity of 1.2 m/s in the experiments at Johns Hopkins University [38]. Here, the model coefficients were already set through the calibration

studies performed for the $Ri^* = 0.7$ case, and these simulations were performed to assess any Richardson number effects.

The volume fraction contours and streamlines are presented in Fig. 6.27 and Fig. 6.28. Here again, we can infer from the volume fraction contours that the DFE model produces reasonable results with regard to gross parameters, and that no striking changes have occurred by comparison with the predictions using a constant, average droplet size. Of note here is the slightly mixed region in the fuel layer, owing to the recirculation zone near the inlet diffuser, a feature that was observed during the experiments. This recirculation zone is clearly evident in Fig. 6.28.

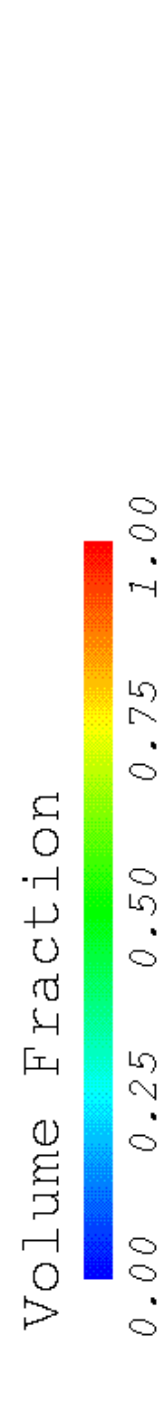


Figure 6.27 – Volume fraction contours; $Ri^* = 0.32$, $d_p = \text{variable}$.

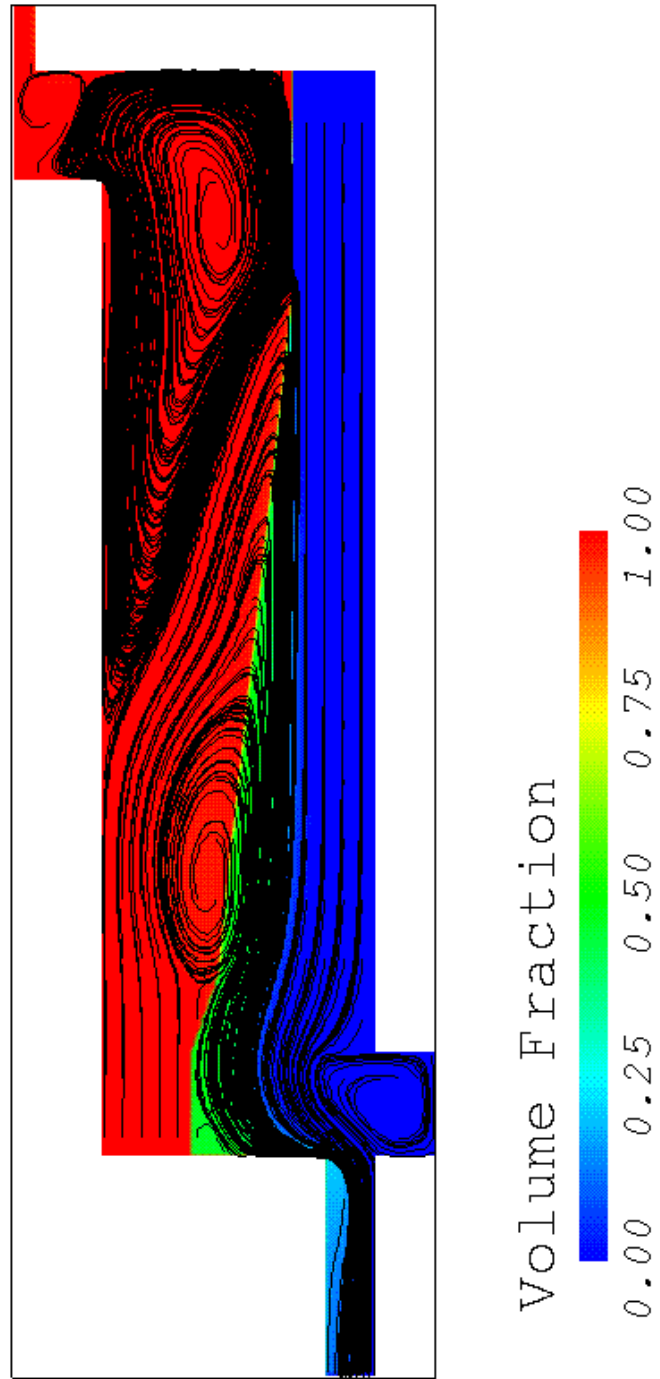


Figure 6.28 – Volume fraction contours and streamlines; $Ri^* = 0.32$, $d_p = \text{variable}$.

Next, we will examine the predictions of the fuel droplet size for the case of $Ri^* = 0.32$. The vertical droplet diameter and volume fraction profiles are presented in Fig. 6.29 and Fig. 6.30 for $x/L = 0.25$ and 0.5 , respectively. Here, we have chosen not to present profiles for further downstream, as these results would be influenced by the presence of the recirculation zone near the inlet diffuser. Again, the droplet diameter is normalized with respect to the maximum droplet size that occurs across the entire shear layer, in this case 3.2 cm .

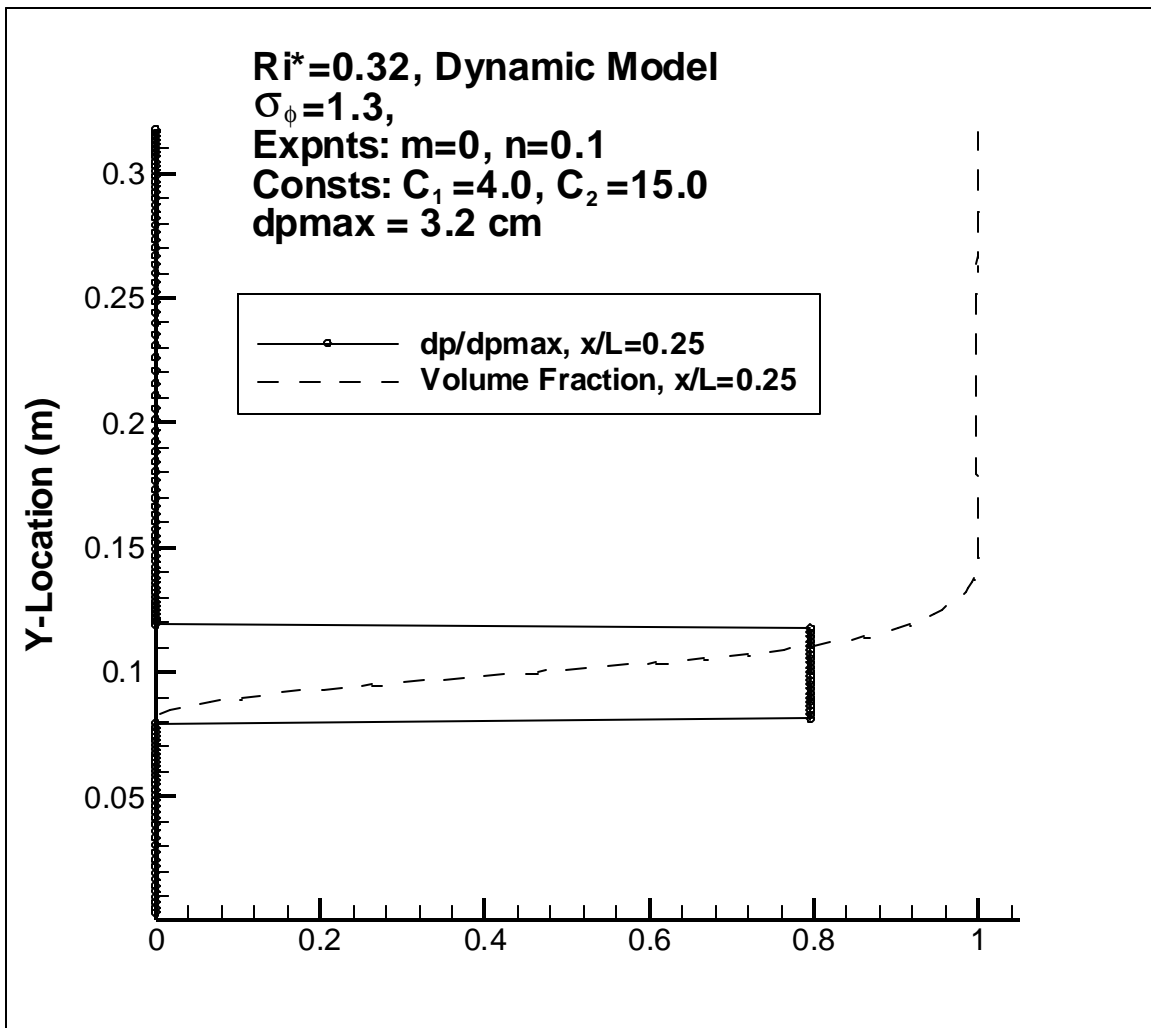


Figure 6.29 – Normalized droplet diameter with volume fraction; $Ri^*=0.32$, $x/L = 0.25$.

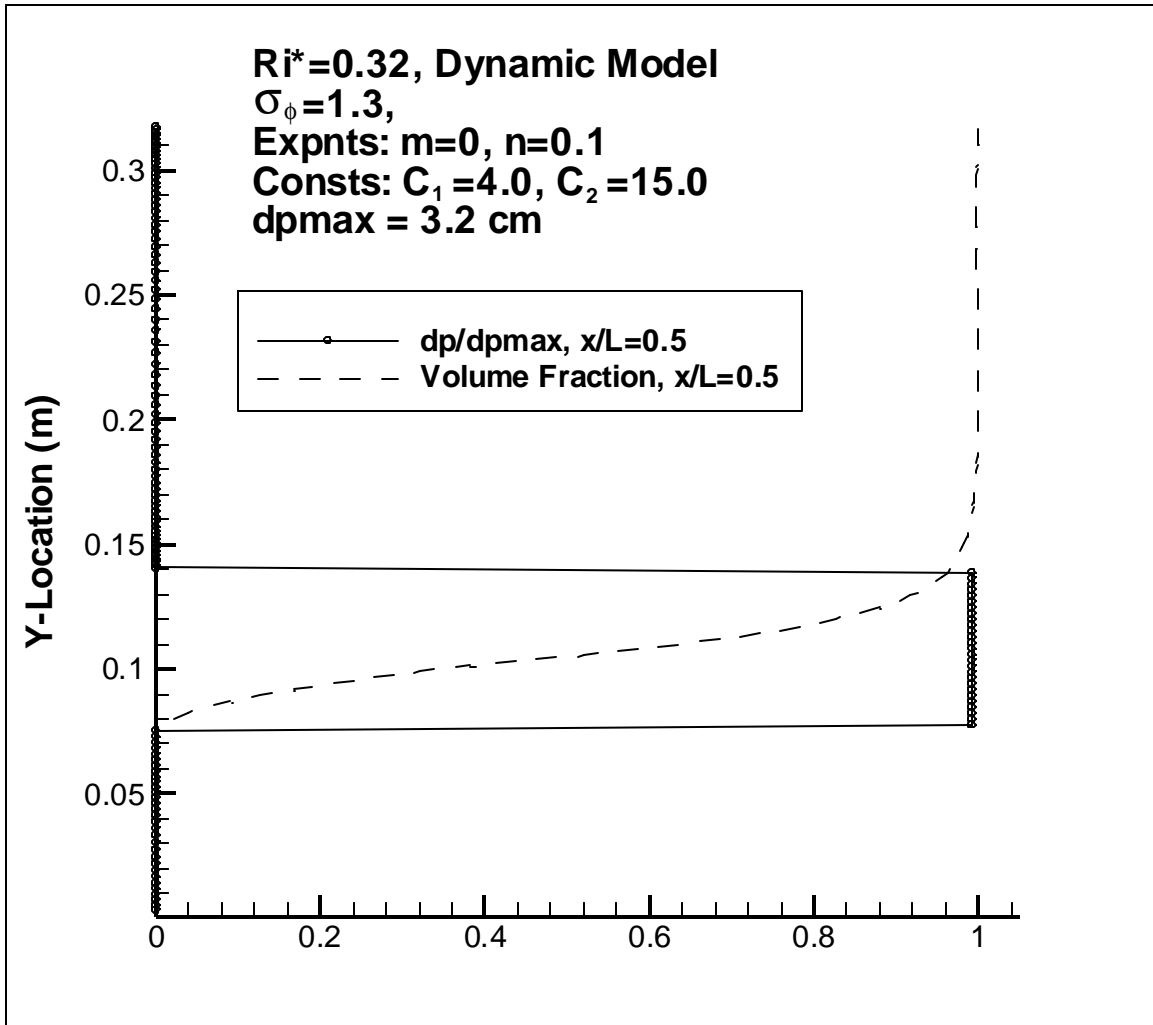


Figure 6.30 – Normalized droplet diameter with volume fraction; $Ri^* = 0.32$, $x/L = 0.5$.

The results presented in Figs. 6.29 and 6.30 above confirm the observations made concerning the $Ri^* = 0.7$ case. Here again we can see that the droplet size and vertical range over which droplets are generated increases with downstream distance, owing to the increase in the size of the mixture layer as we proceed downstream. The size of the predicted fuel droplets is very reasonable by comparison with experimental observations, and we find no droplets are predicted in regions where only one phase is present. It is also interesting to note from Fig. 6.30 that the predicted droplets show some bias towards

the water layer near the bottom of the test section. This makes sense, since we are only concerned with the prediction of lighter phase (i.e. fuel) droplets, which should not be present in the fuel layer. The water layer, on the other hand, should contain small fuel droplets that are generated at the interface.

Now that we have shown some reasonable results with regard to the predictions of the droplet size using the DFE model, we will next examine the gradient Richardson number profiles for the two different cases. Figures 6.31 and 6.32 depict the gradient Richardson number profile at different downstream locations for $Ri^* = 0.7$ and $Ri^* = 0.32$, respectively. Here again, we have limited the range over which results are presented for the case of $Ri^* = 0.32$ to avoid the influence of the recirculation zone near the inlet diffuser.

An important observation from these figures is that in the region near the interface Ri_g generally increases with downstream location. This is a result of the velocity layer spreading, as well as the fact that $(\partial u / \partial y)^2$ decreases more rapidly than the density gradient. Tennekes and Lumley [34] comment that for $Ri_g < 0.2$ turbulence will persist at the interface in typical shear flows. According to Miles [30], for unbounded parallel shear flows, if $Ri_g > 0.25$, then no turbulent instabilities will be present, owing to damping of the turbulence by buoyancy forces. However, for bounded shear flows, the criterion for this transition can be much lower [15].

In light of these findings, it seems reasonable to estimate from Fig. 6.32 that the interface was probably fully turbulent for the case of $Ri^* = 0.32$, while for the case of $Ri^* = 0.7$ the interface was probably characterized partially by Kelvin-Helmholtz vortices. These observations are also in good agreement with the flow regime boundaries for the DFE model (see Section 5.2). In formulating the DFE model it was found that the critical gradient Richardson number for transition from the fully turbulent interface regime to the Kelvin-Helmholtz vortices regime is approximately 0.2.

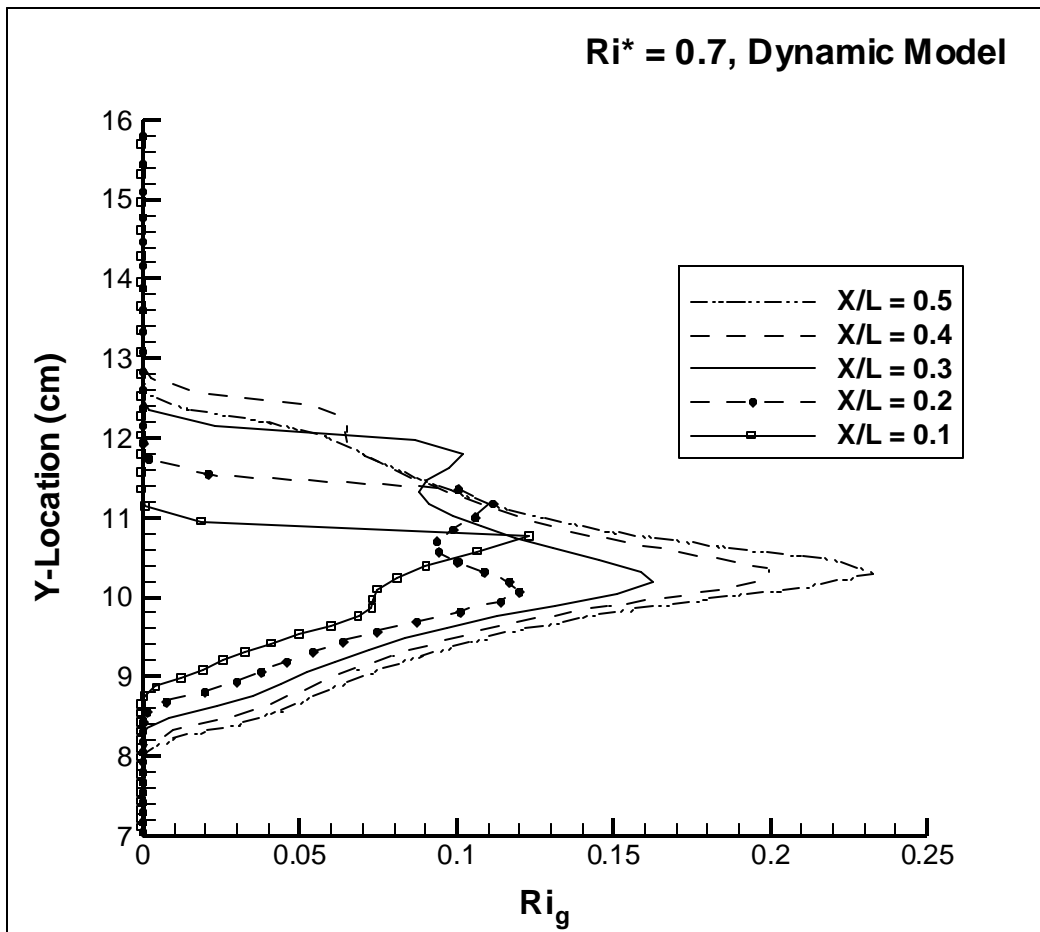


Figure 6.31- Gradient Richardson number profiles; $Ri^* = 0.7$, $d_p = \text{variable}$.

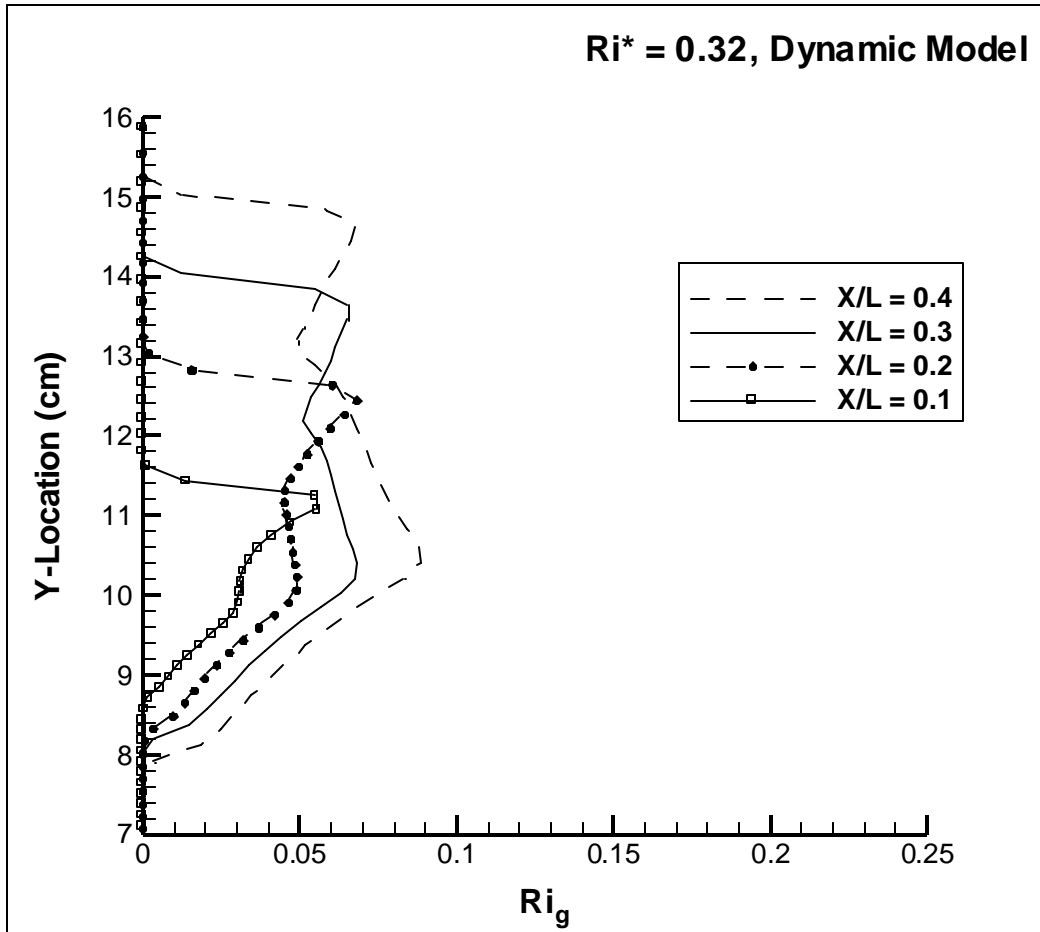


Figure 6.32 – Gradient Richardson number profiles; $Ri^* = 0.32$, $d_p = \text{variable}$.

Next, we will examine the variations in the predicted mixed fluid thickness profile for the case of $Ri^* = 0.7$ using the dynamic DFE model. Results for the vertical mixed fluid thickness profile is given in Fig. 6.33 below. As can be seen from this figure, the dynamic DFE model performs reasonably well in predicting the mixed fluid thickness. While the magnitudes are somewhat large, the trend in the downstream direction is well represented. Discrepancies between the predicted and measured magnitudes of the mixed layer thickness reflect the need for further calibration of the model coefficients; however,

as shown in Fig. 6.33, the variable droplet size allows for a more accurate representation of the flow dynamics.

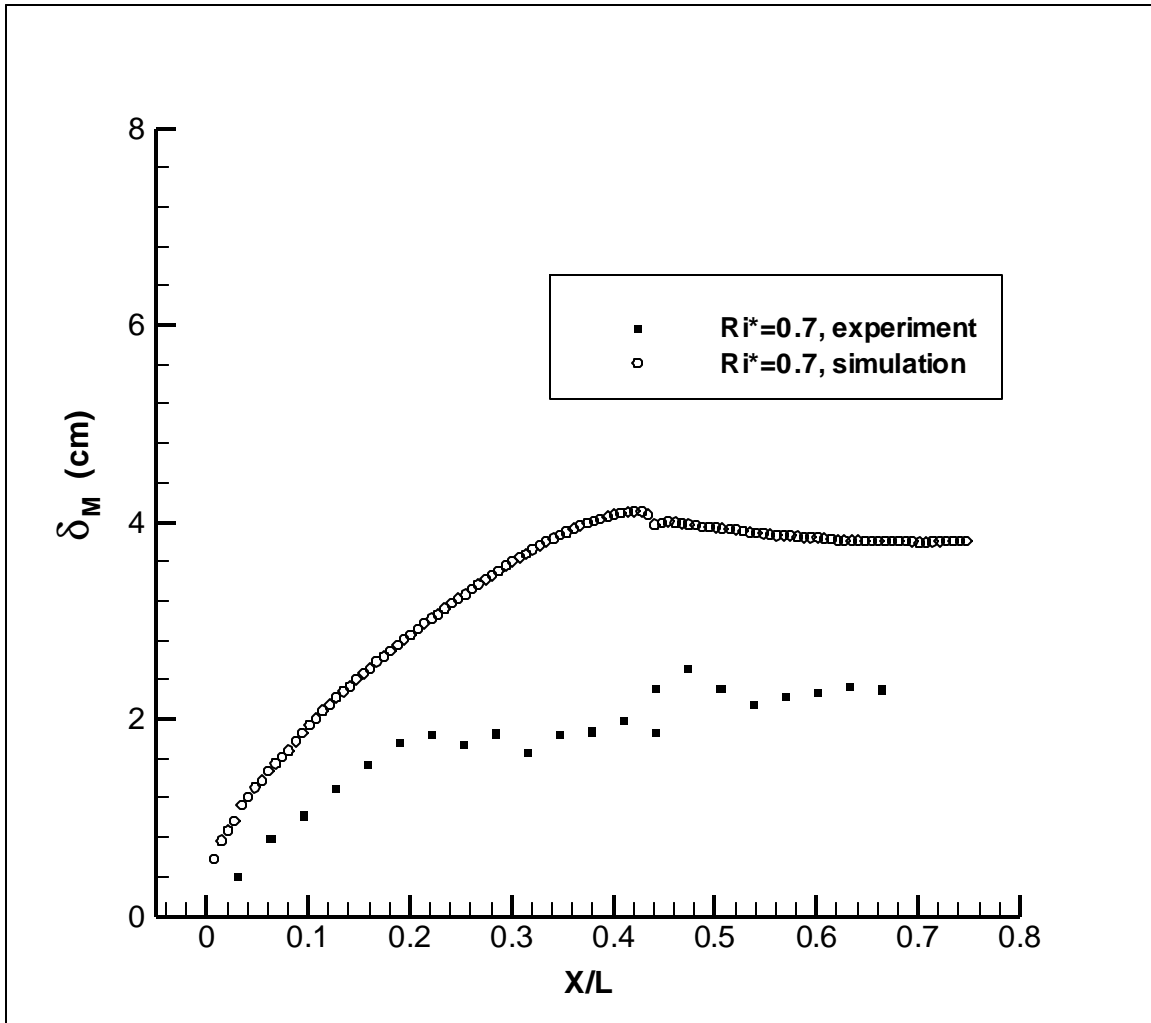


Figure 6.33 – Mixed fluid thickness vs. normalized downstream distance; $Ri^* = 0.7$, $d_p = \text{variable}$.

The same simulations were also performed for the case of $Ri^* = 0.32$, using the same parameters and the same coefficients in the DFE model. The mixed fluid thickness profile is shown in Fig. 6.34. Here again only about half of the mixture layer is shown, as

results at larger x/L values would be influenced by the recirculation zone near the inlet diffuser.

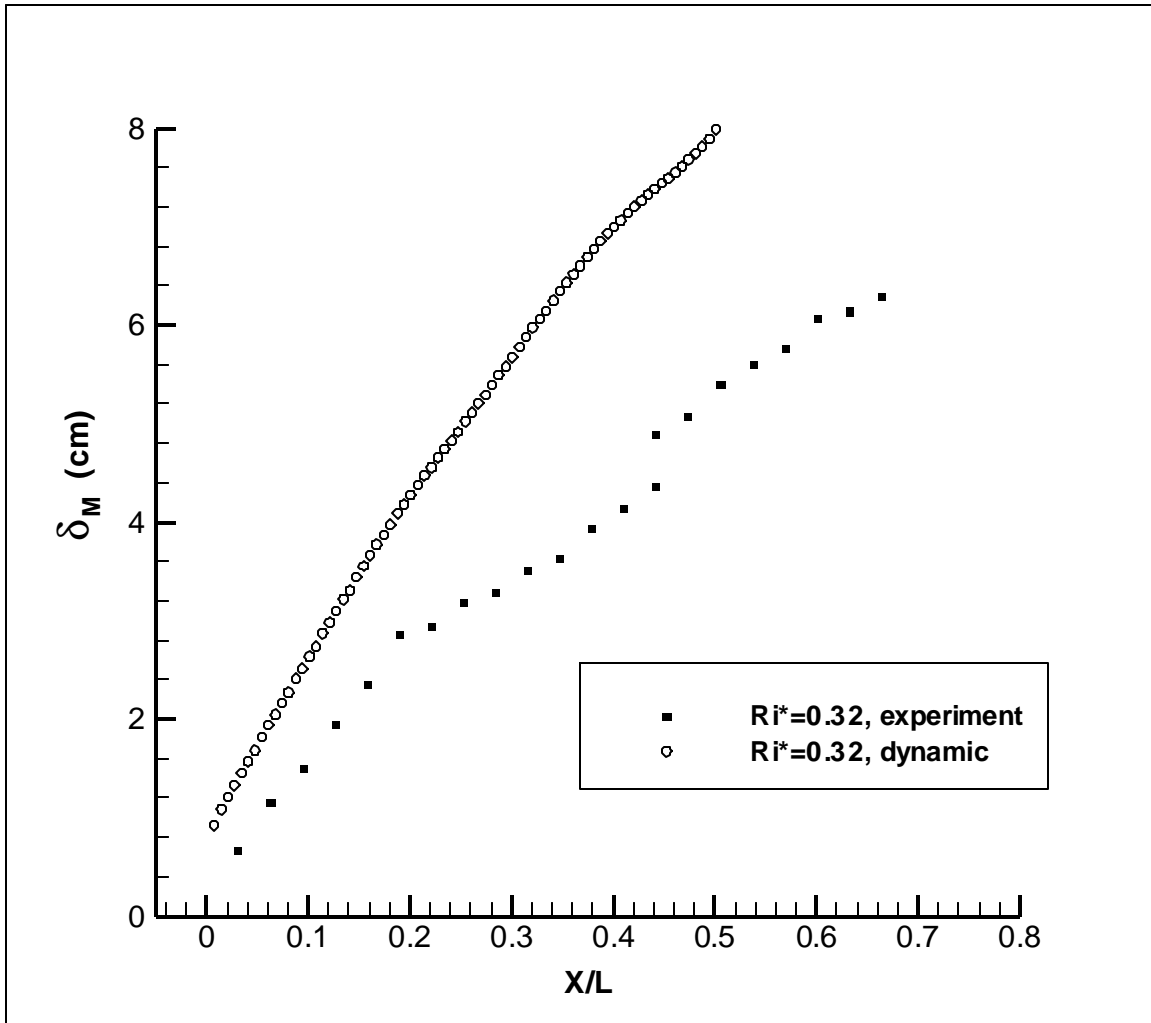


Figure 6.34 – Mixed fluid thickness vs. normalized downstream distance; $Ri^*=0.32$, d_p = variable.

The existence of the different flow regimes is evident in Figs. 6.33 and 6.34 in the manner in which the mixed fluid thickness changes as a function of downstream distance. For the case of $Ri^* = 0.32$, interface mixing is entirely dominated by turbulence effects,

as evidenced by the fact that the gradient Richardson number remains small throughout the mixing layer (see Fig. 6.32). Because of this, the slope of the mixed fluid thickness remains approximately constant. In the case of $Ri^* = 0.7$, however, this is not the case. Initially, the interface is likely to be dominated by turbulence effects, and so the mixed fluid thickness increases steadily. At further downstream locations, however, the turbulence becomes damped by buoyancy forces, and the slope decreases towards a value of zero and the mixed layer stabilizes. As we continue further downstream, the influence of the droplet size becomes more important, as was shown previously. Here, the slip velocity becomes more dominant, and has the influence of separating the two fluid layers, thus causing the mixed fluid thickness to decrease. These trends in the mixed fluid thickness were also confirmed in the experiments at Johns Hopkins University [38].

In general, we have shown that the SFST model, with constant droplet size, performs quite well and accurately represents the flow dynamics. Results from the DFE model indicate that improvements have been made in the accuracy of the solution of the flow, as evidenced by improvements in matching the trends in the mixed fluid thickness profiles. Discrepancies between the predicted values and the experimental measurements can most likely be accounted for by further calibration of the model coefficients. It is also possible that three-dimensional effects in the experiments need to be explored.

7.0 SFST MODEL PREDICTIONS FOR VERTICAL BUOYANT JET FLOWS

The SFST model, as described in Section 3.0, was used in conjunction with a computational grid modeled after the experimental facility being used at Johns Hopkins University [17] to study the impingement of a water jet on a fuel/water interface. Of primary interest in these simulations were the predictions of the overall flowfield as compared with experimental observations, as well as verification of the droplet formation/entrainment model with regard to trends in the prediction of the fuel droplet sizes, and the prediction of the maximum penetration depth of the jet. Here, comparisons will be made between the numerical predictions of the jet penetration depth with results from the literature [40] and experimental results from the actual flow facility [17].

7.1 Experimental Conditions Simulated

As mentioned above, the numerical simulations were modeled after the experimental facility being used at Johns Hopkins University. Here, a vertical water jet impinges on an initially quiescent layer of fuel. A schematic of the actual flow facility being used is given in Fig. 7.1. The fuel layer is contained in the upper center portion of the tank by two fuel weirs, and the water enters the tank through the vertical inlet pipe. As the water penetrates the fuel layer, mixing will occur if the shear forces are great enough compared with the buoyancy, or gravity, forces (i.e. if the Richardson number is small enough). As the water becomes entrained in the fuel layer, the excess water is forced to the sides of the tank and exits through the drains located in the upper left and right compartments. If

no mixing occurs, then the excess fuel will be forced over the fuel weir where it can return to the fuel supply. An impingement plate is located in the center of the tank above the inlet pipe. If the velocity of the incoming water is great enough, then the jet will impinge on the plate. This will cause breakage of the inlet jet and the formation of fluid droplets, which will cascade back towards the fuel/water interface.

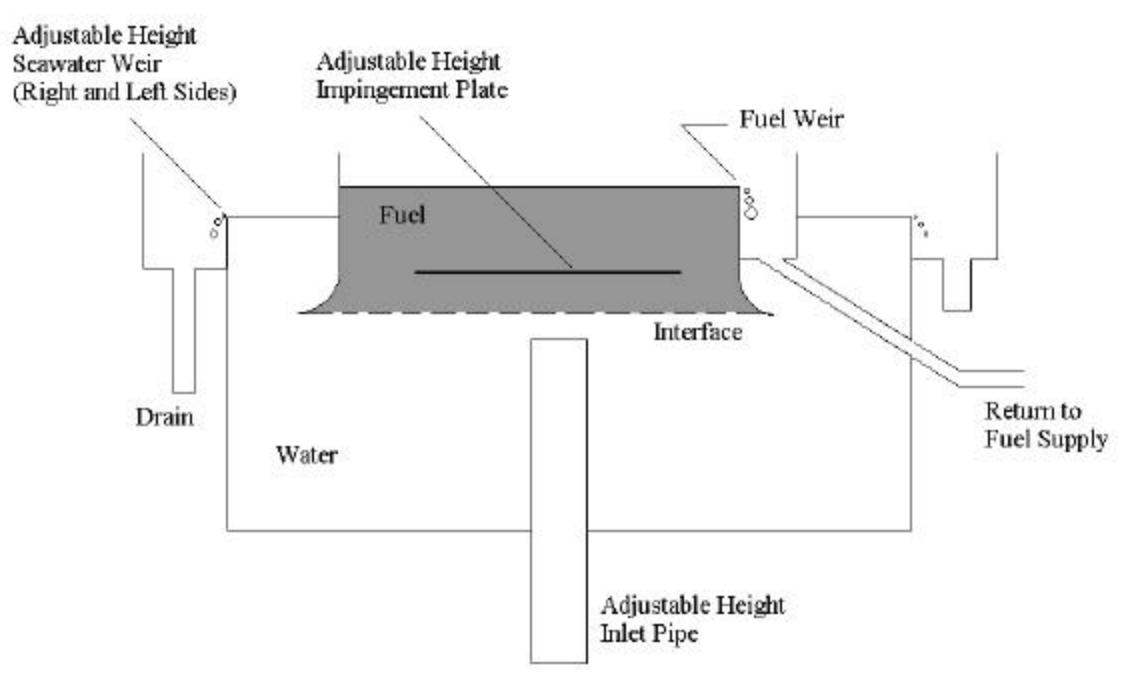


Figure 7.1 - Fuel impingement experimental test facility, after Friedman & Katz [17].

Due to the complexity of the geometry, and because we are mainly interested with phenomena near the interface and in the fuel layer, some simplifications were made in the computational geometry. First, the curved fuel weirs were assumed to be vertical walls to avoid skewness in the grid in these regions, and the drain pipes and fuel supply return pipe were neglected. The upper portion of the tank, which is vented to the atmosphere, was also neglected; here the upper interface was modeled using a plane of symmetry.

7.2 Computational Details

Having made the simplifications describe in the previous section, the computational geometry used in the simulations is given in Fig. 7.2 below.

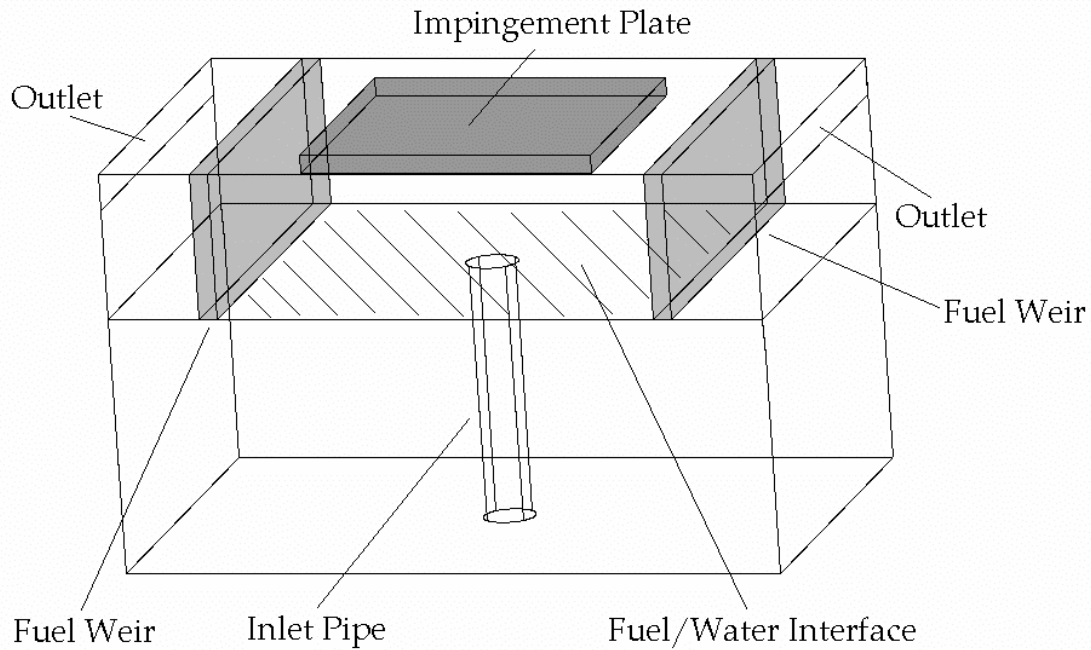


Figure 7.2 - Schematic of computational geometry used to model the impinging jet facility.

The overall dimensions of the tank are 0.9144 m (36 inches) long by 0.5588 m (22 inches) high by 0.6096 m (24 inches) wide, and matched the dimensions of the experimental facility after having neglected the upper portion of the tank that is vented to the atmosphere. The fuel weirs on either side of the fuel layer were modeled as internal solids that were 2.54 cm (1 inch) thick, and the impingement plate measured 40.64 cm (16 inches) square, and was also modeled as a solid with thickness of 2.54 cm. While the height and thickness of the inlet pipe were variable in the experiments, here we have used an inlet pipe that measured 5.08 cm (2 inches) in diameter, with the height extending to

the depth of the fuel/water interface. In the experiments, the height of the impingement plate was also variable; however, we have chosen to set the height of the impingement plate at 17.78 cm (7 inches) above the fuel/water interface, which corresponds to the maximum height used in the experiments.

The relatively fine grid that was used consisted of 72x46x24 cells, for a total of approximately 79,500 computational cells. A uniform mesh was used in the x-direction, while in the z-direction the cells were concentrated towards the center using a symmetric geometric progression (SGP) factor of 0.96. In the vertical direction, the cells were focused towards the exit of the inlet pipe, using several different geometric progression factors above and below the interface. This was done to provide a greater resolution in the region containing the exit of the inlet pipe and the fuel layer.

The SFST model was used, with the k- ϵ turbulence model including buoyant production/destruction for turbulent flow cases, as detailed in Sections 3.1 and 3.2, respectively, and the calibrated dynamically implemented DFE model described in the previous section. All simulations were performed as three-dimensional, transient flows. The velocity components were discretized using higher-order upwinding, while the HYBRID scheme was used for the turbulence quantities where appropriate. The first-order upwind scheme was used for the density, and the scalar, ϕ , was discretized using the MUSCL scheme, Min-Mod. Transient time marching was accomplished using backward differencing approaching steady state.

While several different mixing regimes were studied in the experiments, here only one case has been simulated, by setting the inlet velocity of the water jet to produce the same Richardson number. Here, the Richardson number is defined in terms of the interface jet width by

$$Ri_i = \frac{D_i \Delta \rho g}{r_b U_i^2} \quad (7.2.1)$$

where D_i is the diameter of the jet at the fuel/water interface, $\Delta \rho = \rho_\beta - \rho_\alpha$ is the density difference between the two fluids, and U_i is a characteristic velocity scale, which in this case corresponds to the interface velocity. Because the flow is characterized by parameters at the interface, the reason for setting the height of the inlet pipe at the fuel/water interface becomes apparent. By doing so, the interface jet diameter and velocity are easily represented by the diameter of the inlet pipe and the velocity of the water as it exits the pipe.

One case was simulated using CFX-4 with the SFST model as described previously and the k- ϵ turbulence model including the effects of buoyancy production/destruction. As reported by Friedman and Katz [17], there are several different mixing regimes which develop, each of which can be characterized by the value of the interface Richardson number given by Eq. (7.2.1). Regime 1 has not been considered in this study, as it is essentially a laminar flow with little to no mixing, and is therefore of little interest. Table 7.1 below illustrates the inlet parameters for each of the different regimes investigated in the experiments, including boundary conditions on the inlet velocity and turbulence

quantities, as well as the relevant dimensionless parameters. Here F is the densimetric Froude number based on the inlet quantities, given by Eq. (2.1.12).

Table 7.1 – Inlet Parameters for Impinging Jet Experiments

Regime	R_{ij}	V_{inlet} (m/s)	k_{inlet} (m^2/s^2)	ϵ_{inlet} (m^2/s^3)	Re_{inlet}	F
2	0.65	0.3391	2.30E-04	2.29E-04	17,226	1.754
3	0.21	0.5966	7.12E-04	1.25E-03	30,308	3.086
4	0.12	0.7893	1.25E-03	2.89E-03	40,096	4.083

In the above table, the regimes listed represent those as defined by Friedman and Katz [17], as was discussed in Section 2.3. While in the experiments, the pipe diameter can vary, Table 7.1 corresponds only to the case of a pipe diameter of 2.0 inches, which is used in this study. Regime 4 indicates the regime in which the momentum of the fluid jet was sufficient to impact the impingement plate. For the present study, only regime 3 will be studied, as this entails the majority of the mixing mechanisms, while avoiding other complicated phenomena resulting from the inlet jet impacting the tank ceiling.

7.3 Results and Discussion

In this section, results will be presented for the volume fraction and streamline profiles for the simulations performed related to the impinging jet experiments currently being conducted at Johns Hopkins University. Results are presented for simulations of flow regime 3 using the SFST model in conjunction with the droplet formation/entrainment

model, where the predicted droplet size was dynamically implemented in the slip velocity relation. Results with regard to the prediction of the maximum jet penetration depth will also be compared with experimental results as provided by Friedman and Katz [17].

Upon review of the literature on vertical, buoyant jet flows, an article was found by Zhang and Baddour [40], in which the authors investigated the maximum penetration depth for vertical, round dense jets. In this article, the authors make a distinction between the flow phenomena that occur in jet with small (<7.0) and large (>7.0) Froude numbers. Here, the Froude number is defined according to Eq. (2.1.12). It was determined that the conditions of the present study were such that it fell into the small Froude number regime (see Table 7.1). For this regime, the authors determine a relationship for the maximum penetration depth given by

$$\frac{z_m}{L_m} = 1.7F^{0.3} \quad (7.3.1)$$

where z_m is the maximum vertical penetration, r is the radius of the source (e.g. nozzle radius), F is the densimetric Froude number, and $L_m = rF$ is a characteristic length scale.

Substituting for L_m , Eq. (7.3.1) becomes

$$z_m = 1.7rF^{1.3} \quad (7.3.2)$$

This result was found to be in good agreement with the experimental results of Friedman and Katz [17]. The experimental results are reported in the form

$$AR = \frac{y_{\max}}{D_i} = f(Ri_i) \quad (7.3.3)$$

where AR is the ratio of the maximum vertical penetration and the diameter of the jet at the interface (which corresponds to the diameter of the nozzle for the case where the exit of the pipe was set at the same depth as the interface). In order for a comparison of the two authors' results to be made, the densimetric Froude number in Eq. (7.3.2) was rewritten in terms of the interface Richardson number reported by Friedman and Katz [17]. This yields

$$\frac{z_m}{D_i} = 1.3338 Ri_i^{-0.65} \quad (7.3.4)$$

Figure 7.3 below illustrates the comparison between the results reported by both sets of authors, and shows good agreement. Results from numerical simulations in the present study will also be compared with these results.

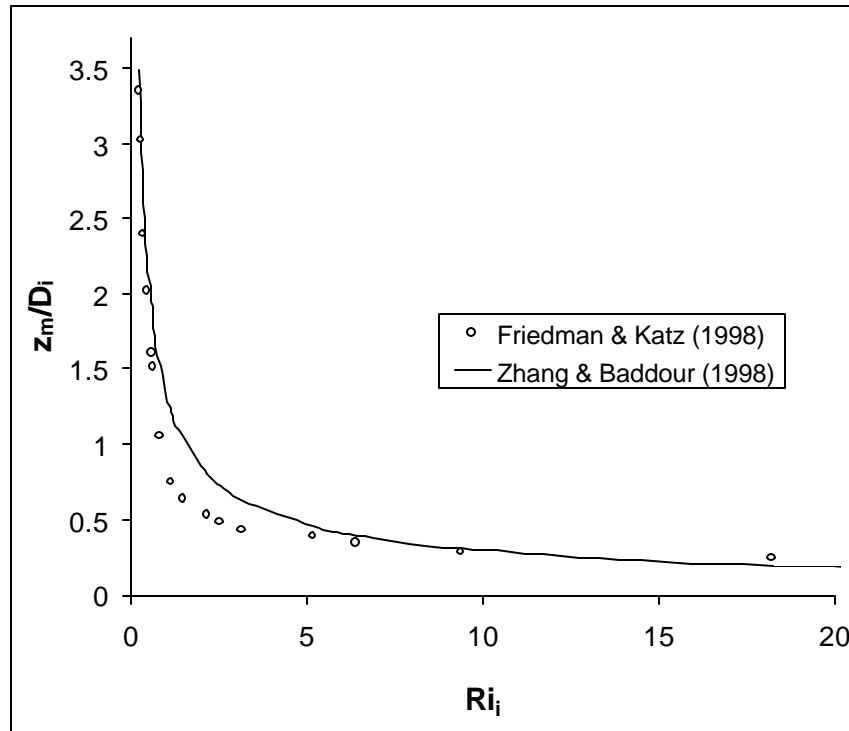


Figure 7.3 – Comparison of results for normalized maximum vertical penetration as a function of the interface Richardson number.

The steady-state volume fraction contours are shown in Fig. 7.4 for the case of $Ri^* = 0.21$. Here, blank areas indicate solid boundaries (e.g. impingement plate, fuel weirs, etc.). Again, it is important to remember that these simulations produce time-averaged solutions. They do not account for transient phenomena, in this case the fluctuation of the height of the inlet jet. For this case, the inlet jet is highly turbulent and the momentum of the jet is sufficient to extend through the majority of the fuel layer, but not enough to impact the impingement plate. For these flow conditions, the inlet jet is highly unstable and large falling blobs of water drag significant amounts of fuel down into the water layer. There is also significant fuel droplet generation below the interface, primarily caused by the shearing off of long finger-like structures [17].

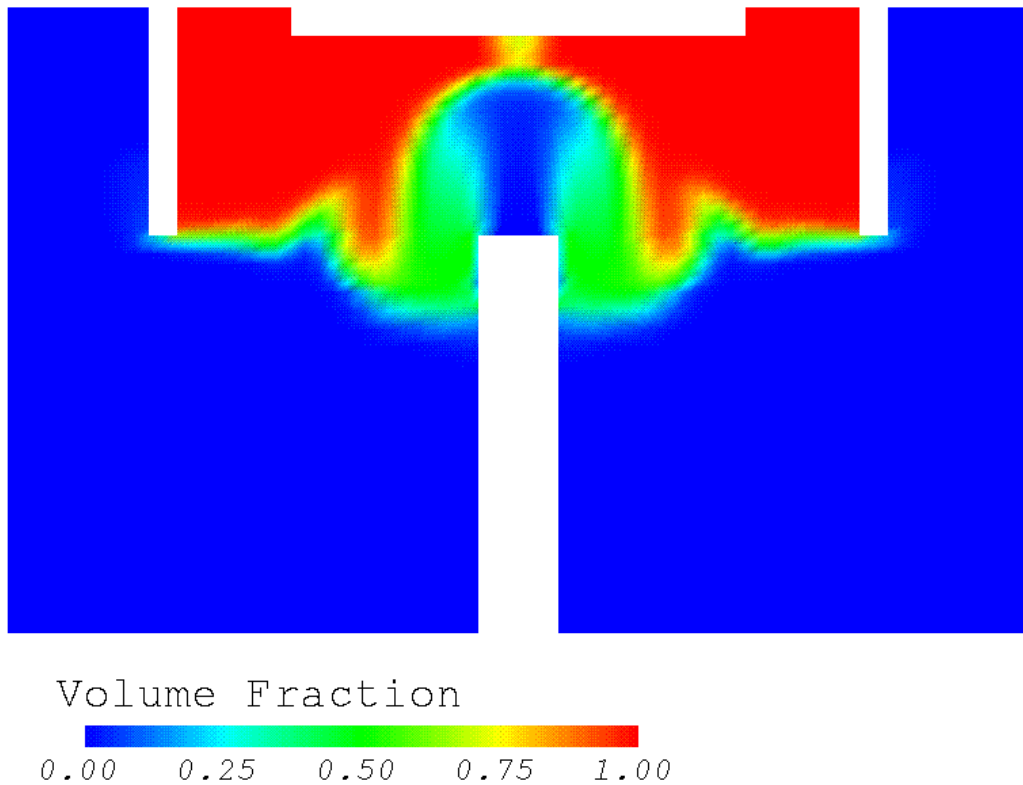


Figure 7.4 – Volume fraction contours; $Ri^* = 0.21$, $d_p = \text{variable}$.

Figure 7.5 shows a digital image taken from the experiments for these flow conditions. As you can see by comparison with the predicted volume fraction contours in Fig. 7.4, the numerical simulations seem to be accurately predicting the gross flow dynamics.

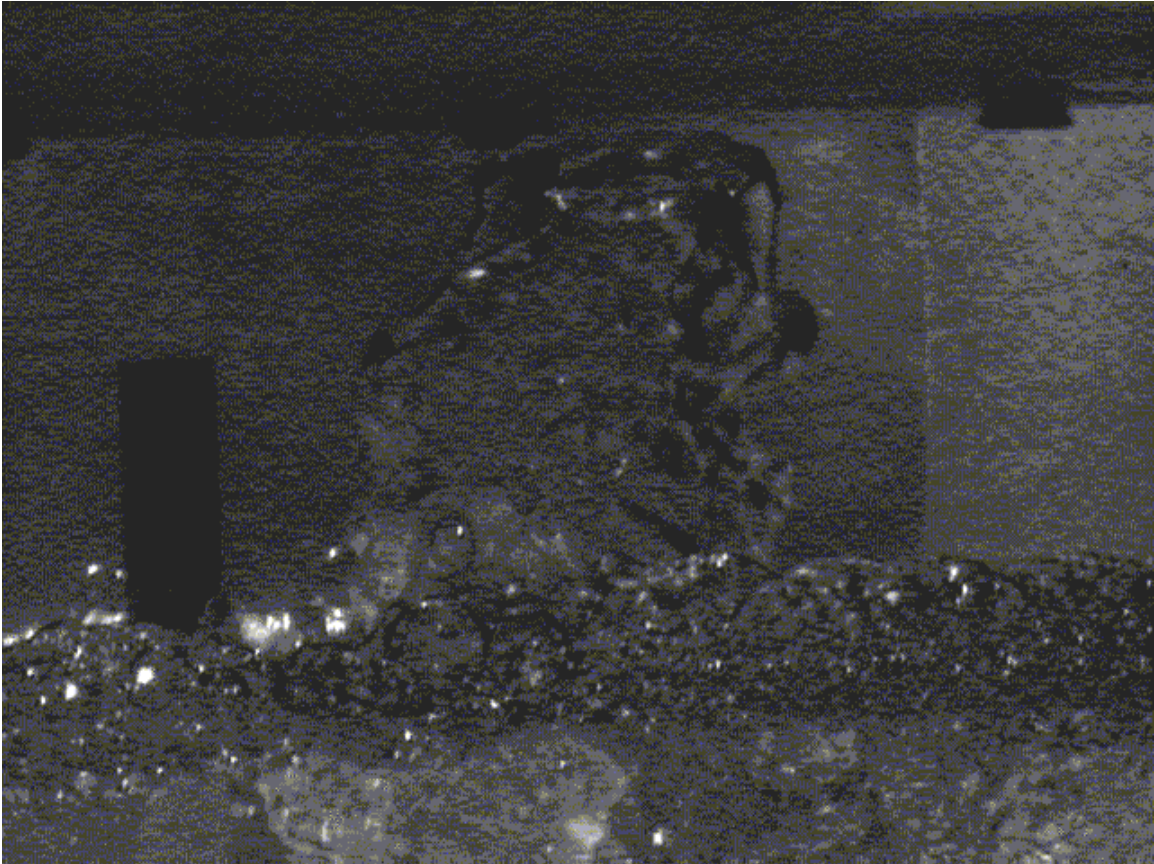


Figure 7.5 – Instantaneous image of impinging jet facility for $Ri^* = 0.21$; after Friedman and Katz [17].

One of the parameters investigated in these experiments is the maximum impingement depth as a function of interface Richardson number. Here, the maximum penetration depth is measured by the ratio of the maximum vertical penetration to the pipe diameter (see Eq. 7.3.3). The results from the experiments by Friedman and Katz [17], and the discussion by Zhang and Baddour [40] have already been discussed previously (see Fig.

7.3). During the simulations in this study, the maximum penetration depth was calculated from the volume fraction profile in the vertical direction above the center of the inlet pipe. Figure 7.6 shows the calculation for the case of $Ri^* = 0.21$, plotted along with the results from the experiments. As you can see, there is excellent agreement between the predicted value and the experimental measurements. This is expected, of course, as the maximum penetration depth should be primarily dependent on the momentum of the jet exiting the pipe, which should be primarily determined by the inlet conditions.

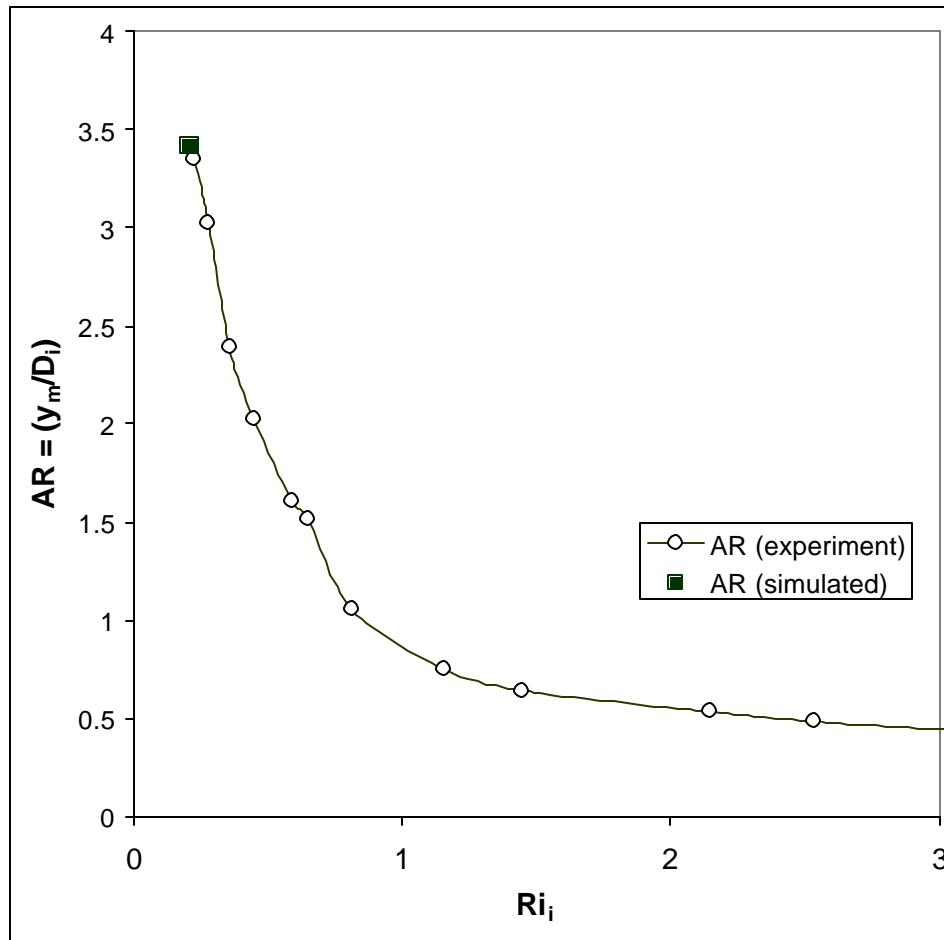


Figure 7.6 – Comparison of predicted aspect ratio with experimental results [17].

Next we will examine the predictions of the droplet size by the DFE model for this case. Figure 7.7 depicts the droplet diameter contour for the case of $Ri^*=0.21$. Here we can see that there is a large range of droplet sizes predicted. The larger sizes would represent the large blobs of fuel that are dragged down into the water layer by the falling pockets of water due to instabilities in the vertical jet. The smaller sizes would then represent the smaller discrete droplets that are generated at the interface or are broken off of the finger-like structures of fuel that penetrate the water layer. In Fig. 7.7 there are some droplets predicted in regions outside of the two fuel weirs. This is a product of the fact that the fuel weirs are not completely accurately represented (i.e. in the experiments they are curved, see above discussion). In any event, we are primarily interested in the regions in the proximity of the inlet pipe, which appears to be well represented by comparison with the experiments.

In Fig. 7.7 we can see that the predictions for the droplet diameter seem reasonable based on observations from the experiments. As yet there are not quantitative measurements of the spatial distribution of the droplet sizes; however, there are no droplets predicted in regions where only one phase is present, and the location and size of the droplets seems reasonable. The larger size blobs of fuel are shown in the region of the fuel/water interface on either side of the inlet pipe as expected, and the smaller droplets appear in the water layer below the interface, and at the edges of the vertical jet.

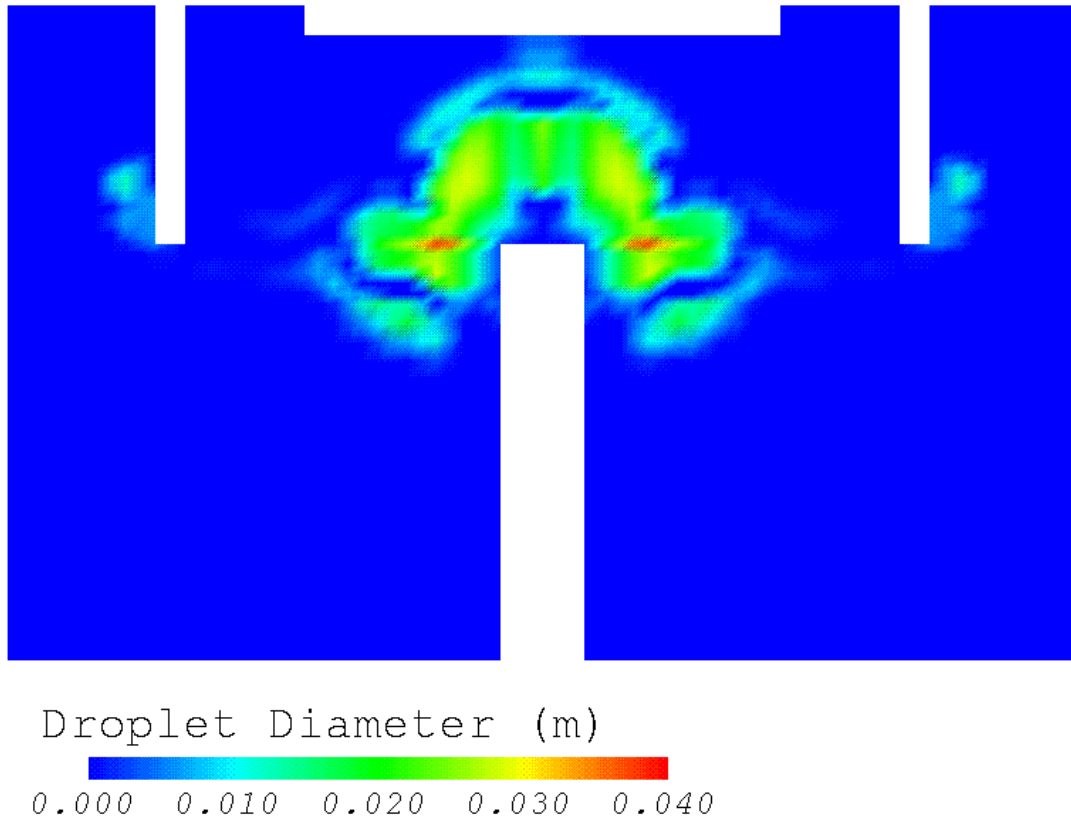


Figure 7.7 – Droplet diameter contours; $Ri^* = 0.21$.

In Fig. 7.7 we can also see regions where some pockets of fuel that have been dragged down into the water layer have become separated from the interface. This is indicative of the shearing off of the finger-like structures that penetrate the water layer, which is then broken into smaller droplets [15].

In general, it would appear that this independent test case for the DFE model shows reasonable results with regard to gross flow parameters, and that the predicted size and location of the fuel droplets makes sense based on observations from the experiments.

Further analysis of these results requires quantitative data from the experiments regarding the size and spatial distribution of the fuel droplets.

8.0 CONCLUSIONS

8.1 Summary

While true multiphase modeling requires that each phase be solved for independently, a simpler approach is to use a mixture model. Here the mixture is treated as a whole, solving only one set of momentum equations, having defined mixture quantities for the velocity, density, and viscosity. The volume fraction of each phase is then solved for separately. A key problem with this approach, however, lies in maintaining the conservative nature of the governing equations without increasing the complexity of the problem, while appropriately accounting for the slip between the two phases. To this end, a new formulation was derived for the solution of the volume fraction in which no simplifying assumptions were made, and which satisfies mass (volume) conservation of the individual phases. Results from simple two-dimensional and three-dimensional test cases, for both laminar and turbulent flows, showed that this new formulation is extremely accurate in the predictions of the individual phase volumes for a variety of different geometries and flow conditions. This is a significant improvement over the previous version of the SFST model [6,7,8,37].

A numerical model has also been developed to predict the dispersed phase droplet diameter in two-phase liquid-liquid flows. Here the droplet size is determined locally at each individual computational cell based on local flow parameters. These include certain length scales, as well as local turbulence quantities, and dimensionless parameters such as

the gradient Richardson number. The model was further divided into several different flow regimes based on results and discussion from certain shear flow literature, in which the primary mixing mechanism changes. Each of the different flow regimes can be delineated by an appropriately defined Richardson number. The DFE model allows for more accurate predictions of actual flow phenomena by correctly accounting for the changes in the relative velocity between the two phases as a function of the local droplet size.

Verification studies were performed for the droplet formation/entrainment model using a simple two-compartment tank, with a single inlet and outlet, and a manhole separating the two compartments. While much simpler, this configuration exhibits many of the flow phenomena observed in the full-scale compensated fuel/ballast tanks. Results from these studies showed that the DFE model produced logical trends with respect to the location and size of the dispersed phase droplets, in that no fluid droplets were formed in regions where only one phase was present, and the predicted sizes were reasonable in comparison with experimental observations.

Simulations were then performed for a developing shear layer of diesel fuel and water, based on the experimental configuration being used currently at Johns Hopkins University. Comparisons were made between the predictions for the streamwise variations in the mixed fluid thickness with the experimental measurements. These results were used to calibrate certain parameters in the slip velocity expression in the SFST model, as well as important constants in the DFE model.

After having calibrated the SFST and DFE models, simulations were performed to investigate the influence of the dispersed phase droplet diameter on the mixed fluid thickness. Here, the droplet size was specified by the user, and was assumed to be a constant, average value everywhere in the flow domain. It was found that, as expected, increasing the droplet size caused a decrease in the amount of mixing that occurred. Comparisons of predictions of the mixed fluid thickness showed good agreement with the experimental results.

Following these studies, simulations were performed in which the DFE model was used to predict the local size of any fuel droplets formed in each computational cell. The local predicted droplet size was then dynamically implemented in the slip velocity used in the source term in the volume fraction equation. The general form of the DFE model was used, and the model constants and exponents were then calibrated based on the predictions of the mixed fluid thickness profiles, as well as the average droplet diameter at each downstream location. With the calibrated model, predictions were made for both $Ri^* = 0.7$ and $Ri^* = 0.32$. Results from these predictions indicated good results with respect to the droplet diameter and gradient Richardson number profiles in the vertical direction, as well as the downstream variations in the mixed fluid thickness.

Finally, with the newly validated DFE model, simulations were performed for a densely buoyant vertical jet, where a heavier fluid impinged on a quiescent layer of lighter fluid. In this case, no changes were made to any of the model parameters. This served essentially as an independent check that the DFE and SFST models performed properly

for different flow configurations. The results of these simulations showed reasonable results with regard to the size and location of the predicted fuel droplets. Comparison of the volume fraction contours with digital images from the experiments indicated that the large-scale flow dynamics were well represented. This was also confirmed by good agreement between the predicted maximum penetration depth of the inlet jet with the experimental measurements. It was also found that certain characteristics of the droplet generation mechanisms were also predicted by the numerical simulations. Further analysis of these results requires quantitative experimental measurements concerning the size and spatial distribution of the fuel droplets.

8.2 Recommendations for Future Work

It is important to remember that this is a work in progress, and that much of the sub-model development has yet to be completed. One important phenomenon that has yet to be included in the DFE model is the effect of surface tension. This could be done through the use of some critical Weber number. The conditions under which droplets would break would then be determined through the competition of shear forces and surface tension forces. A typical K-H shear layer instability is shown in Fig. 8.1 below.

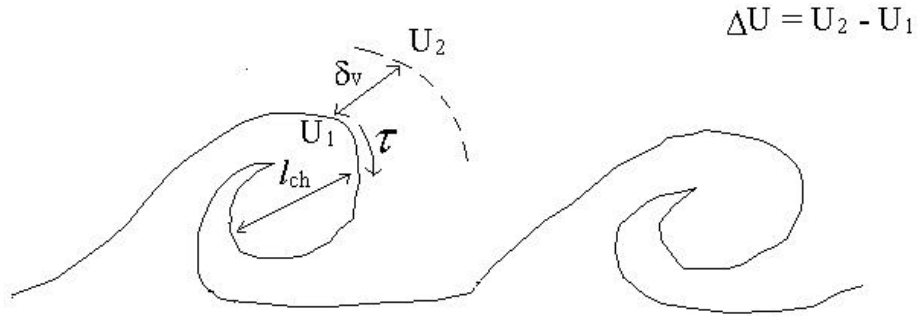


Figure 8.1 – Typical Kelvin-Helmholtz shear layer instability.

Here, a characteristic length scale l_{ch} is defined in terms of the width across the interfacial waves, and a characteristic velocity $\Delta U = U_2 - U_1$ is defined in terms of the difference between the velocity of the surface of the wave and ambient fluid. From these, we can then define certain dimensionless parameters, including a Reynolds number and a Weber number, given by

$$\text{Re} = \frac{\rho(\Delta U)l_{ch}}{\mu} \qquad \text{We} = \frac{\rho(\Delta U)^2 l_{ch}}{\sigma} \qquad (8.2.1)$$

where σ is the interfacial tension. The conditions for droplet breakage would then be determined by equating the shear force and the surface tension force.

$$F_{\text{shear}} = F_{\text{surface tension}} \qquad (8.2.2)$$

This yields

$$4\rho \left(\frac{l_{ch}}{2} \right)^2 \tau = \rho l_{ch}^2 \left(\mu \frac{\partial u}{\partial y} \right) = \sigma l_{ch} \qquad (8.2.3)$$

If we then divide both sides by $\mathbf{r}(\Delta U)^2 l_{ch}^2$ then

$$\frac{\mathbf{s}}{\mathbf{r}(\Delta U)^2 l_{ch}} = \frac{1}{We} = \frac{\mathbf{pm}(\partial u/\partial y)}{\mathbf{r}(\Delta U)^2} \approx \frac{\mathbf{pm}/\Delta y}{\mathbf{r}(\Delta U)} \quad (8.2.4)$$

If we then assume that Δy scales as the velocity layer thickness δ_v , then

$$\frac{1}{We} \approx \frac{\mathbf{pm}}{\mathbf{r}(\Delta U)\mathbf{d}_v} \quad (8.2.5)$$

or

$$(We)_{CR} \approx \frac{\mathbf{r}(\Delta U)\mathbf{d}_v}{\mathbf{pm}} \quad (8.2.6)$$

where we have replaced We by $(We)_{CR}$, since we know that when the two forces are equal defines the critical Weber number. Multiplying and dividing by l_{ch} yields

$$(We)_{CR} \approx \frac{1}{\mathbf{p}} \frac{\mathbf{r}(\Delta U)l_{ch}}{\mathbf{m}} \left(\frac{\mathbf{d}_v}{l_{ch}} \right) \approx C_1 \left(\frac{\mathbf{d}_v}{l_{ch}} \right) \text{Re} \quad (8.2.7)$$

The dispersed phase droplet diameter, normalized by the velocity layer thickness, could then be written in a form similar to

$$\frac{d_p}{\mathbf{d}_v} \approx \left\{ 1 - \left[\frac{(We)_{CR}}{We} \right]^N \right\} \quad (8.2.8)$$

If we further defined the quantity (\mathbf{d}_v/l_{ch}) in terms of a Richardson number, as was done for the model expressions in the current form of the DFE model, then the droplet diameter could be written as some function of the Reynolds number, Richardson number, and Weber number as

$$\frac{d_p}{\mathbf{d}_v} = f(\text{Re}, Ri, We) \quad (8.2.9)$$

Another improvement that could be made would be to determine a better length scale to use in the model expressions for the droplet size. At present, the characteristic length scale is determined as the smallest of either a turbulent length scale or a mixed fluid thickness defined in terms of the volume fraction profile. This method is, however, computationally expensive for determining the mixed fluid length scales. It would be much more efficient to define a new characteristic length scale, perhaps based on turbulence quantities, or some measure of the vorticity.

With regard to the simulations of the shear flow experiments, it would be helpful to perform some investigation into the effects of the turbulence model used. It might be beneficial to use a low-Reynolds number $k-\epsilon$ model, as much of the fuel layer at the top is probably laminar, even very close to the fluid interface. It may also be beneficial to refine the mesh near the interface further until a grid independent solution is attained. A finer grid near the interface would also improve predictions of the turbulence parameters, should a different turbulence model be used. The influence of three-dimensional effects for this facility may also need to be examined. The simulations in this study were performed as two-dimensional; however, the ratio of the test section width and height is not negligible (approximately 0.2). Velocity field measurements were unavailable to investigate any influence of the tank walls.

With regard to the new formulation used for the solution of the volume fraction, it was found that to maintain the same amount of diffusion, the turbulent Prandtl number for the scalar equation (i.e. the volume fraction), σ_ϕ , should be increased from 1.0 to

approximately 1.3. Some further investigation into the effects of this change would generate some improvement in the numerical predictions for the mixed fluid thickness, as was demonstrated in Section 6.3.

Finally, there are still some further calibration procedures that need to be performed on the dynamic DFE model. As seen in the results for the mixed fluid thickness profiles, some improvement still needs to be made so that the predicted magnitudes of δ_M more closely match the experimental results.

In light of recent findings, there are some improvements that could be made to the model expressions included in the DFE model. As the solution of the droplet diameter is a non-linear problem in relation to the mixed fluid thickness, it would seem that some measure of δ_M should be included in the model expression for the turbulent interface regime. In doing so, the need to limit the droplet diameter by 1/2 of δ_M would already be accounted for in the model expressions. This would then eliminate the truncation of the droplet size and allow for a continuous function in the vertical direction.

From recent analysis of the model coefficients, and the exponent used for the function of the volume fraction, it has been found that the calculated droplet sizes are too large, which are then truncated by the limiting function imposed. In light of this, and the need to included δ_M in the model expression for the turbulent interface regime, it has been conjectured that the model expressions should be changed to the following form:

$$d_p = C(1 - r_a)^n l_{ch} \quad (8.2.10)$$

where

$$l_{ch} = \begin{cases} \text{MIN}\left(\frac{\mathbf{d}_M}{2}, \frac{k^{3/2}}{\mathbf{e}}\right) & Ri_g < 0.2 \\ \text{MIN}\left(\frac{\mathbf{d}_M}{2} Ri_g^{0.89}, \mathbf{d}_{wall}, \frac{\mathbf{d}_M}{2}\right) & 0.2 < Ri_g < 7.5 \end{cases} \quad (8.2.11)$$

with

$$C \cong 1.5 \qquad m = 0.5 \quad (8.2.12)$$

The problem that remains, however, is that in allowing a more continuous function of the droplet size we have, in effect, reduced the characteristic droplet size for a given downstream location. This would, in turn cause the magnitudes of δ_M to increase. Other causes for the discrepancy in the predicted and measured values are currently being investigated.

BIBLIOGRAPHY

- [1] Atsavapranee, P. and Gharib, M. (1997) "Structures in Stratified Plane Mixing Layers and the Effects of Cross-Shear." *Journal of Fluid Mechanics*, 342: 53-86.
- [2] Barnea, E. and Mizrahi, J., (1973). "A generalized approach to the fluid dynamics of particulate systems: Part I - General Correlation for Fluidization and Sedimentation in Solid Multiparticle Systems," *Chem. Eng. J.* 5: 171.
- [3] Batchelor, G.K. (1956) *The Theory of Homogeneous Turbulence*. Cambridge at the University Press, Cambridge.
- [4] Bemporad, G.A. (1994) "Simulation of Round Buoyant Jet in Stratified Flowing Environment." *Journal of Hydraulic Engineering*, 120: 529-543.
- [5] Brauner, N. and Maron, D.M. (1992) "Flow Pattern Transitions in Two-Phase Liquid-Liquid Flow in Horizontal Tubes." *International Journal of Multiphase Flow*, 18: 123-140.
- [6] Celik, I. (1998). Sub-Model Development to Improve the Accuracy of CFD Simulations Of the Flow Inside Fuel-Ballast Tanks, Report No.: MAE-IC98-3, Interim Progress Report, 5/98 - 9/98. Submitted to Geo-Centers, Inc., West Mifflin, PA.
- [7] Celik, I. and Umbel, M. (1997). "CFD Simulations of a Scalar at a Sheared Density Interface." Proceedings of AEA Technology, International Users Conference '97, Chicago, Illinois, October 6-10, 1997.
- [8] Celik, I., Umbel, M., Wilson, W., Chang, P., and Hill, B. (1998) "Simulation of Transient Flow Inside an Experimental, Compensated Fuel/Ballast Tank Model Using Modified Two-Fluid Model." Proceedings of AEA Technology, Users Conference '98, Claymont, Delaware, September 28 - October 2, 1998.
- [9] Chang, P.A., Percival, S., and Hill, B. (1996a). "Computations of Two-Fluid Flows through Two Compartments of a Compensated Fuel/Ballast Tank." Report No.: CRDKNSWC/HD-1370-01, Hydromechanics Directorate Research and Development Report, October 1996.
- [10] Chang, P.A., Percival, S., and Hill, B. (1996b). "Transient, two fluid flow through two compartments of a compensated fuel-ballast tank." Proceedings of AEA Technology. The Third CFX International Users Conference, Chesham, Buckinghamshire, England, UK.

- [11] Chang, P.A. and Caplan, I. (1998). "Computational Fluid Dynamics Modeling of Compensated Fuel/Ballast Systems to Minimize Overboard Discharge of Fuel." Paper to be presented at the International Conference on Waste Water Treatment, Oldenburg, Germany, November 18-20, 1998.
- [12] *CFX-F3D Flow Solver User Guide*, Version 4.1. (1995) Computational Fluid Dynamics Services, Building 8.19, Harwell Laboratory, Oxfordshire OX11, ORA UK, October 1995.
- [13] Drew, D. (1983) "Mathematical Modeling of Two-Phase Flow." *Annual Review of Fluid Mechanics*. 15: 261- 291.
- [14] Ellison, T.H. and Turner, J.S. (1959) "Turbulent Entrainment in Stratified Flows." *Journal of Fluid Mechanics*, 6: 423-448.
- [15] Fernando, H.J.S. (1991) "Turbulent Mixing in Stratified Fluids." *Ann. Rev. Fluid Mech.* 23: 455-493.
- [16] Fernando, H.J.S., Johnstone, H., and Zangrando, F. (1991) "Interfacial Mixing Caused by Turbulent Buoyant Jets." *Journal of Hydraulic Engineering*, 117: 1-20.
- [17] Friedman, P. and Katz, J. (1998) "The Flow and Mixing Mechanisms Caused by Impingement of a Fuel-Water Interface with a Water Jet." Submitted to *Physics of Fluids*.
- [18] Gayler, R., Roberts, N.W., and Pratt, H.R.C. (1953). "Liquid-Liquid Extraction: Part IV - A Further Study of Hold-Up in Packed Columns," *Trans. Inst. Chem. Eng.* 31: 57.
- [19] Hayworth, C. and Treybal, R. (1950) "Drop Formation in Two-Liquid-Phase Systems." *Industrial and Engineering Chemistry*, 42: 1174-1181.
- [20] Hetsroni, Gad. (1982) *Handbook of Multiphase Systems*. New York: Hemisphere Publishing Company.
- [21] Hinze, J.O. (1955) "Fundamentals of the Hydrodynamic Mechanism of Splitting in Dispersion Processes." *AIChE Journal*, 1: 289-95.
- [22] Ishii, M. (1975) *Thermo-Fluid Dynamic Theory of Two-Phase Flow*. Paris: Eyrolles.
- [23] Ishii, M. (1977) "One-Dimensional Drift-Flux Model and Constitutive Equations for Relative Motion between Phases in Various Two-Phase Flow Regimes." Argonne National Laboratory Report, ANL-77-47.

- [24] Ishii, M. and Zuber, N. (1979) "Drag Coefficient and Relative Velocity in Bubbly, Droplet or Particulate Flows." *AIChE Journal*, 25: 843-855.
- [25] Kuboi, R., Komasa, I., and Otake, T. (1972) "Behavior of Dispersed Particles in Turbulent Liquid Flow." *Journal of Chemical Engineering of Japan*, 5: 349-355.
- [26] Kumar, A. and Hartland, S. (1985) "Gravity Settling in Liquid/Liquid Dispersions." *Canadian Journal of Chemical Engineering*, 63: 368-376.
- [27] Kumar, A. and Hartland, S. (1986) "Prediction of Drop Size in Rotating Disc Extractors." *Canadian Journal of Chemical Engineering*, 64: 915-923.
- [28] Martinez-Bazan, C., Montanes, J., and Lasheras, J. (1999) "On the Break up Frequency of an Air Bubble Injected Into a Fully Developed Turbulent Flow" Submitted to *Journal of Fluid Mechanics*.
- [29] Martinez-Bazan, C., Montanes, J., and Lasheras, J. (1999) "On the Size PDF Resulting From the Break Up of an Air Bubble Immersed Into a Turbulent Liquid Flow" Submitted to *Journal of Fluid Mechanics*.
- [30] Miles, J. (1984) "Richardson Number Criterion for Stability of Stratified Shear Flow." *Physics of Fluids*, 29: 3470-3471.
- [31] Narimousa, S. and Fernando, H.J.S. (1987) "On the Sheared Density Interface of an Entraining Stratified Fluid." *Journal of Fluid Mechanics*, 174: 1-22.
- [32] Rodi, W. (1980) "Turbulence Models and Their Application in Hydraulics: A State-of-the-Art Review." An IAHR (International Association of Hydraulic Research) Publication, Delft, The Netherlands.
- [33] Sullivan, G.D. and List, E.J. (1994) "On Mixing and Transport at a Sheared Density Interface." *Journal of Fluid Mechanics*, 273: 213-39.
- [34] Tennekes, H. and Lumley, J. (1972) *A First Course in Turbulence*. Cambridge: Massachusetts Institute of Technology Press.
- [35] Tsouris, C. and Tavlarides, L. (1994) "Breakage and Coalescence Models for Drops in Turbulent Dispersions." *AIChE Journal*, 40: 395-406.
- [36] Turner, J.S. (1966) "Jets and Plumes with Negative or Reversing Buoyancy." *Journal of Fluid Mechanics*, 26: 779-792.
- [37] Umbel, M. (1998) "Predictions of Turbulent Mixing at the Interface of Density Stratified, Shear Flows Using CFD." M.S. Thesis, West Virginia University.

- [38] Wu, X. and Katz, J. (1999) "On the Flow Structure and Mixing Phenomena in a Fuel-Water Stratified Shear Flow." Proceedings of the 3rd ASME/JSME Joint Fluids Engineering Conference, July 18-23, San Francisco, CA.
- [39] Zhang, H. and Baddour, R. (1997) "Maximum Vertical Penetration of Plane Turbulent Negatively Buoyant Jets." *Journal of Engineering Mechanics*, 123: 973-977.
- [40] Zhang, H. and Baddour, R. (1998) "Maximum Penetration of Vertical Round Dense Jets at Small and Large Froude Numbers." *Journal of Hydraulic Engineering*, 124: 550-553.

APPENDIX A: DERIVATION AND EQUATIONS FOR THE SFST MODEL

A.1: Complete Set of Equations for the SFST Model

Mixture Momentum:

$$\frac{\partial(\mathbf{r}u_i)}{\partial t} + \frac{\partial}{\partial x_i}(\mathbf{r}u_i u_i) = -\frac{\partial P_i}{\partial x_i} + \frac{\partial}{\partial x_i} \left(\mathbf{m}_j \frac{\partial u_i}{\partial x_j} \right) - \frac{\partial}{\partial x_i} \left[\frac{1}{\mathbf{r}} r_a r_b r_b (u_{s,i})^2 \right] + r g_i \quad (\text{A.1.1})$$

Mixture continuity:

$$\frac{\partial \mathbf{r}}{\partial t} + \frac{\partial}{\partial x_i}(\mathbf{r}u_i) = 0 \quad (\text{A.1.2})$$

Scalar transport equation:

$$\frac{\partial(\mathbf{r}f)}{\partial t} + \frac{\partial}{\partial x_i}(\mathbf{r}u_i f) = -\frac{\partial}{\partial y} \left[\frac{r_a f(1-f)u_s}{f + R(1-f)} \right] + \frac{\partial}{\partial x_i} \left[\Gamma \left(\frac{\partial f}{\partial x_i} \right) \right] \quad (\text{A.1.3})$$

Volume fraction:

$$r_a = \frac{f}{f + R(1-f)} \quad (\text{A.1.4})$$

k equation:

$$\mathbf{r} \frac{\partial k}{\partial t} + \mathbf{r}u_j \frac{\partial k}{\partial x_j} = \mathbf{t}_{ij} \frac{\partial u_i}{\partial x_j} - \mathbf{r}e + \frac{\partial}{\partial x_j} \left(\left(\mathbf{m} + \frac{\mathbf{m}_t}{\mathbf{s}_k} \right) \frac{\partial k}{\partial x_j} \right) + g \frac{\mathbf{m}_t}{\mathbf{r} \mathbf{s}_p} \frac{\partial \mathbf{r}}{\partial y} \quad (\text{A.1.5})$$

ϵ equation:

$$\mathbf{r} \frac{\partial e}{\partial t} + \mathbf{r}u_j \frac{\partial e}{\partial x_j} = \frac{\partial}{\partial x_j} \left(\left(\mathbf{m} + \frac{\mathbf{m}_t}{\mathbf{s}_e} \right) \frac{\partial e}{\partial x_j} \right) + C_1 \frac{e}{k} \mathbf{t}_{ij} \frac{\partial u_i}{\partial x_j} - C_2 \mathbf{r} \frac{e^2}{k} + C_1 \frac{e}{k} C_3 \max \left(g \frac{\mathbf{m}_t}{\mathbf{r} \mathbf{s}_r} \frac{\partial \mathbf{r}}{\partial y}, 0 \right) \quad (\text{A.1.6})$$

Auxiliary equations:

$$u = \frac{(u_a r_a \mathbf{r}_a + u_b r_b \mathbf{r}_b)}{\mathbf{r}} ; \quad \mathbf{r} = \mathbf{r}_a r_a + \mathbf{r}_b r_b ; \quad \mathbf{m} = \mathbf{m}_a r_a + \mathbf{m}_b r_b \quad (\text{A.1.7})$$

$$u_s = (1 - r_a)^m u_\infty \quad u_\infty = \left[\left(\frac{4gd_p^{1.6}}{54\mathbf{m}_t^{0.6}} \right) \left(\frac{\mathbf{r}_c - \mathbf{r}_d}{\mathbf{r}_c^{0.4}} \right) \right]^{5/7} \quad (\text{A.1.8})$$

$$C_D = \frac{18}{\text{Re}^{0.6}} \quad \text{where} \quad \text{Re} = \frac{\mathbf{r}_c V_s d}{\mathbf{m}_c} \quad (\text{A.1.9})$$

$$\mathbf{m} = \mathbf{m}_m + \mathbf{m}_t; \quad \mathbf{m}_t = \frac{\mathbf{r} C_m k^2}{\mathbf{e}} \quad (\text{A.1.10})$$

$$\mathbf{t}_{ij} = \mathbf{m}_t \left(\frac{\partial u_i}{\partial x_j} + \frac{\partial u_j}{\partial x_i} \right) - \frac{2}{3} \mathbf{r} k d_{ij} \quad (\text{A.1.11})$$

In the above equations ρ , u , and μ are taken to be the mixture quantities defined by Eqns. (A.7), and α and β represent the respective phases. Tensor notation is used, where repeated indices indicate summation.

A.2: New Formulation for Solution of the Volume Fraction

First, we start with the single-phase continuity equation for the α -phase, given by

$$\frac{\partial}{\partial t}(\mathbf{r}_a \mathbf{r}_a) + \frac{\partial}{\partial x_i}(\mathbf{r}_a \mathbf{r}_a u_{a,i}) = 0 \quad (\text{A.2.1})$$

From the definition of the mixture velocity, u_m ,

$$u_m = \frac{\mathbf{r}_a r_a u_a + \mathbf{r}_b r_b u_b}{\mathbf{r}_m} \quad (\text{A.2.2})$$

we can write

$$\mathbf{r}_m u_m = \mathbf{r}_a r_a u_a + \mathbf{r}_b r_b u_b \quad (\text{A.2.3})$$

But r_b is equal to $1-r_a$, from the algebraic constraint that the two must sum to unity.

Substituting for r_b in Eq. (A.2.3) yields

$$\mathbf{r}_m u_m = \mathbf{r}_a r_a u_a + \mathbf{r}_b (1 - r_a) u_b \quad (\text{A.2.4})$$

The slip velocity, u_s , is given by

$$u_s = u_a - u_b \quad (\text{A.2.5})$$

Rewriting in terms of u_b yields

$$u_b = u_a - u_s \quad (\text{A.2.6})$$

Substituting Eq. (A.2.6) into Eq. (A.2.4) yields

$$\mathbf{r}_m u_m = \mathbf{r}_a r_a u_a + \mathbf{r}_b (1 - r_a) [u_a - u_s]$$

which becomes

$$\mathbf{r}_m u_m = [\mathbf{r}_a r_a + \mathbf{r}_b (1 - r_a)] \cdot u_a - \mathbf{r}_b (1 - r_a) u_s \quad (\text{A.2.7})$$

The terms in the brackets, however, is simply the definition of the mixture density.

Substituting yields

$$\mathbf{r}_m u_m = \mathbf{r}_m u_a - \mathbf{r}_b (1 - r_a) u_s \quad (\text{A.2.8})$$

Next, we rewrite Eq. (A.2.1) by multiplying and dividing each term by the mixture density, ρ_m . This yields

$$\frac{\partial}{\partial t} \left(\frac{\mathbf{r}_a}{\mathbf{r}_m} r_a \mathbf{r}_m \right) + \frac{\partial}{\partial x_i} \left[\frac{\mathbf{r}_a}{\mathbf{r}_m} r_a \mathbf{r}_m u_{a,i} \right] = 0 \quad (\text{A.2.9})$$

Next, we substitute for $\rho_m u_\alpha$ from Eq. (A.2.8), which yields

$$\frac{\partial}{\partial t} \left[\mathbf{r}_m \left(\frac{\mathbf{r}_a}{\mathbf{r}_m} \right) r_a \right] + \frac{\partial}{\partial x_i} \left[\left[\mathbf{r}_m u_{m,i} + \mathbf{r}_b (1 - r_a) u_s \right] \frac{\mathbf{r}_a}{\mathbf{r}_m} r_a \right] = 0 \quad (\text{A.2.10})$$

If we make a variable substitution, say

$$\mathbf{f} = r_a \left(\frac{\mathbf{r}_a}{\mathbf{r}_m} \right) \quad (\text{A.2.11})$$

then we can rewrite Eq. (A.2.10) in terms of ϕ as

$$\frac{\partial}{\partial t} [\mathbf{r}_m \mathbf{f}] + \frac{\partial}{\partial x_i} [\mathbf{r}_m u_{m,i} \mathbf{f}] = - \frac{\partial}{\partial x_i} [\mathbf{r}_b (1 - r_a) u_s \mathbf{f}] \quad (\text{A.2.12})$$

By adding a diffusion term, we can rewrite Eq. (A.2.12) as a scalar transport equation with a source term based on the slip velocity by

$$\frac{\partial}{\partial t} [\mathbf{r}_m \mathbf{f}] + \frac{\partial}{\partial x_i} [\mathbf{r}_m u_{m,i} \mathbf{f}] = - \frac{\partial}{\partial x_i} [\mathbf{r}_b (1 - r_a) u_s \mathbf{f}] + \frac{\partial}{\partial x_i} \left[\Gamma \left(\frac{\partial \mathbf{f}}{\partial x_i} \right) \right] \quad (\text{A.2.13})$$

Equation (A.2.13) provides a generic scalar transport equation, which can be solved for the variable ϕ , from which we may solve for the volume fraction, r_α , from the algebraic expression given above (Eq. A.2.11). Equation (A.2.13) is particularly appealing because we have made no simplifying assumptions and are solving an exact equation. For laminar flow cases, where there is no mixing, the slip velocity will be zero, and hence,

the source term in Eq. (A.2.13) will be zero. For turbulent flow cases it will need to be included.

The solution of the volume fraction from the scalar variable, ϕ , can be performed as follows. We can rewrite Eq. (A.2.11) by using the definition of the mixture density as

$$r_a = \frac{[r_a \mathbf{r}_a + (1-r_a) \mathbf{r}_b] \cdot \mathbf{f}}{\mathbf{r}_a} \quad (\text{A.2.14})$$

Next, we multiply and divide the RHS of Eq. (A.2.14) by ρ_β , which yields

$$r_a = \frac{[r_a (\mathbf{r}_a / \mathbf{r}_b) + (1-r_a)] \cdot \mathbf{f}}{(\mathbf{r}_a / \mathbf{r}_b)} \quad (\text{A.2.15})$$

If we let $R = \rho_\alpha / \rho_\beta$, then Eq. (A.2.15) becomes

$$r_a = \frac{[r_a R + (1-r_a)] \cdot \mathbf{f}}{R} \quad (\text{A.2.16})$$

which can be rewritten as

$$R r_a = [R r_a + (1-r_a)] \mathbf{f}$$

or

$$R r_a (1-\mathbf{f}) = (1-r_a) \mathbf{f}$$

or

$$r_a [R(1-\mathbf{f}) + \mathbf{f}] = \mathbf{f}$$

which becomes

$$r_a = \frac{\mathbf{f}}{\mathbf{f} + R(1-\mathbf{f})} \quad (\text{A.2.17})$$

From Eq. (A.2.17), we can substitute for r_α in Eq. (A.2.13) so that it only involves ϕ .

This yields

$$\frac{\partial}{\partial t} [\mathbf{r}_m \mathbf{f}] + \frac{\partial}{\partial x_i} [\mathbf{r}_m u_{m,i} \mathbf{f}] = - \frac{\partial}{\partial x_i} \left[\mathbf{r}_b \left(1 - \frac{\mathbf{f}}{\mathbf{f} + R(1-\mathbf{f})} \right) u_{s,i} \mathbf{f} \right] + \frac{\partial}{\partial x_i} \left[\Gamma \left(\frac{\partial \mathbf{f}}{\partial x_i} \right) \right]$$

re-arranging yields

$$\frac{\partial}{\partial t}[\mathbf{r}_m \mathbf{f}] + \frac{\partial}{\partial x_i}[\mathbf{r}_m u_{m,i} \mathbf{f}] = -\frac{\partial}{\partial x_i} \left[\mathbf{r}_b \left(\frac{\mathbf{f} + R(1-\mathbf{f}) - \mathbf{f}}{\mathbf{f} + R(1-\mathbf{f})} \right) u_s \mathbf{f} \right] + \frac{\partial}{\partial x_i} \left[\Gamma \left(\frac{\partial \mathbf{f}}{\partial x_i} \right) \right]$$

or

$$\frac{\partial}{\partial t}[\mathbf{r}_m \mathbf{f}] + \frac{\partial}{\partial x_i}[\mathbf{r}_m u_{m,i} \mathbf{f}] = -\frac{\partial}{\partial x_i} \left[\mathbf{r}_b \left(\frac{R(1-\mathbf{f})}{\mathbf{f} + R(1-\mathbf{f})} \right) u_s \mathbf{f} \right] + \frac{\partial}{\partial x_i} \left[\Gamma \left(\frac{\partial \mathbf{f}}{\partial x_i} \right) \right] \quad (\text{A.2.18})$$

Using the definition of R, this can be simplified to

$$\frac{\partial}{\partial t}[\mathbf{r}_m \mathbf{f}] + \frac{\partial}{\partial x_i}[\mathbf{r}_m u_{m,i} \mathbf{f}] = -\frac{\partial}{\partial x_i} \left[\frac{\mathbf{r}_a \mathbf{f}(1-\mathbf{f}) u_s}{\mathbf{f} + R(1-\mathbf{f})} \right] + \frac{\partial}{\partial x_i} \left[\Gamma \left(\frac{\partial \mathbf{f}}{\partial x_i} \right) \right] \quad (\text{A.2.19})$$

In the numerical model in CFX, the scalar ϕ is solved from Eq. (A.2.19), and the volume fraction is then determined using Eq. (A.2.17). This is particularly appealing because the volume fraction is solely determined from an algebraic expression in which we have eliminated the mixture density. This in turn eliminates the need for an iterative procedure, as the mixture density requires the solution of the volume fraction.

A.3: Alternative Empirical Correlation for the Slip Velocity

One of the more extensive compilations of empirical data concerning the slip velocity has been performed by Kumar and Hartland [25,26]. Through the analysis of 998 published experiments for 29 liquid/liquid systems from 14 different data sources, they formulate a correlation for the slip velocity in terms of the drop diameter and physical properties given by

$$\frac{4dg\Delta r(1-e)}{3r_c V_s^2(1+ke^n)} = K_1 + \frac{24m_c}{r_c V_s d} \quad (\text{A.3.1})$$

Here d is the diameter of the dispersed phase fluid particle, ϵ is the hold-up ratio of the dispersed phase, V_s is the slip velocity, and the subscript c denotes the continuous phase.

The constants in the above equation are given by:

$$\begin{aligned} k &= 4.56 \\ K_1 &= 0.53 \\ n &= 0.73 \end{aligned} \quad (\text{A.3.2})$$

Equation (A.3.1) may be put into a similar form given by

$$\left(\frac{V_s}{V_{s,\infty}} \right)^2 = \frac{0.53 \text{Re} + 24(V_s/V_{s,\infty}) \left[\frac{1-e}{1+ke^n} \right]}{0.53 \text{Re} + 24} \quad (\text{A.3.3})$$

where $V_{s,\infty}$ is the terminal velocity of a single fluid droplet in an infinite continuous liquid, and Re is a Reynolds number given by

$$\text{Re} = \frac{r_c V_s d}{m_c} \quad (\text{A.3.4})$$

APPENDIX B: DOCUMENTATION FOR THE SFST MODEL

B.1 Introduction

This section is intended to provide a more detailed explanation of the requirements for the implementation of the SFST model in CFX. A numerical simulation in CFX-4 requires a geometry file, detailing all relevant grid information, a command file, which dictates certain command options, and a user FORTRAN file, which is used for modifications to the governing equations and for solution monitoring. While there are several different grid generation packages that can be used with CFX-4, CFX-Meshbuild was used in the present study. In this section, descriptions will be given for the relevant information needed in all three of these files as they relate to the SFST model. This will not include any general information as related to the CFX code, as this is left to the CFX Users Manual [12]. An explanation will also be given concerning modifications that can be made by the user to include different forms of the slip velocity, and for models to specify the droplet sizes.

B.2 Overview

The numerical algorithm used is a single fluid, scalar transport (SFST) model, which can be used for simulations of flows involving two immiscible fluids. The governing equations include one set of momentum equations and one scalar transport equation that is solved for a generic scalar variable, ϕ , from which the volume fraction of the dispersed phase is solved using an algebraic relation. An equation for solving for the mixture density in variable density flows may also be included. Additional terms may be added to the governing equations through the use of a user subroutine for adding source terms. For example, the convective flux that originates in the volume fraction equation because of the slip velocity is added through the subroutine, USRSRC. There are several different turbulence models that can be used for numerical simulations in CFX-4, including the standard k- ϵ model, low-Reynolds number model, and k- ω model. The current form of the SFST model employs the standard k- ϵ model with modifications to include a source term, which accounts for production/destruction of turbulent kinetic energy by buoyancy forces. For ease of implementation with different geometries and flow scenarios, the current form of the SFST model is designed in such a way that future changes can be made without large modifications to the source code. It can be used with any flow problem, provided that certain guidelines are followed concerning user modifications to the command file and FORTRAN file, as well as certain semantics in generating the computational grid.

B.3 Configuring the CFX Files for the SFST Model

As mentioned previously, a numerical simulation using CFX-4 requires three files: the geometry file, the command file, and the FORTRAN file. In this section, certain guidelines will be presented as the manner in which these files are used, as well as how modifications can be made to simulate different geometries and flow scenarios. Text that appears in the `Courier New` font indicates the actual syntax used in one of these files. It is important to keep in mind, also, that any specific values set in the following sections are given in SI units. It should also be noted that in some sections text is staggered between lines because of the page limits, whereas this text would not be staggered in the actual FORTRAN code.

B.3.1 The Geometry File

In generating the computational grid, the procedure is the same as for any other geometry using CFX-Meshbuild. For use with the SFST model, however, the following guidelines and conventions should be used.

1. It is important that all IJK coordinate systems in each individual block have the J index pointed in the opposite direction as the gravity vector in the global XYZ coordinate system. This is most easily accomplished by setting the J index in each block in the positive y-direction according to the global axes. Then the gravity vector is supplied in the command file as being -9.81 in the y-direction. It is also convenient to orient each individual block within a multi-block structure such that all coordinate axes are the same and match those of the global coordinate system. This eliminates a great deal of confusion, both in setting grid constraints within blocks, and also in determining cell locations for specifying parameters or acquiring output data.
2. In CFX-Meshbuild, block naming can be done in any convenient manner designated by the user; however, for use with the SFST model, a certain naming convention must be applied. The blocks should be numbered BLOCK-NUMBER-1 to BLOCK-NUMBER-N, where N is the total number of blocks, excluding any internal blocks used as child constraints.
3. Any internal solid blocks which are used as child constraints within larger active blocks should be named INTSOLID1 through INTSOLIDN. Here N would represent the total number of internal solid blocks used as child constraints.
4. There are five primary boundary patch types in CFX-Meshbuild. These are inlets, walls, pressure boundaries, mass-flow boundaries, and thin surfaces. These types of patches are the most common and should be used for specifying boundary conditions on a given geometry. It has also been found that pressure boundaries are far superior to mass-flow boundaries for specifying outlet conditions.

B.3.2 The Command File

In order to perform a simulation in CFX-4, a command file is required. The purpose of the command file is to specify constant boundary conditions, problem sizes, flow types (i.e. laminar, turbulent), grid types (e.g. body-fitted, unmatched), the equation solvers to be used, under-relaxation parameters, turbulence model parameters, scalar parameters, and time step and output options. Variable boundary conditions must be set in the user subroutine, USRBCS. In the following section, a detailed explanation will be given for all of the relevant parameters set in the command file, along with values used for the SFST model, and recommendations for modifications for use with different geometries or flow scenarios.

The first section of the command file is used to specify the workspace parameters used by the flow solver during a simulation. In a simulation where a geometry has been generated through the use of some pre-processor, then these workspace limits are not necessary. An example of this portion of the command file is given below, which was sufficient for many of the simulations performed in this study.

```
>>CFXF3D
  >>SET LIMITS
    TOTAL INTEGER WORK SPACE 18000000
    TOTAL CHARACTER WORK SPACE 50000
    TOTAL REAL WORK SPACE 35000000
```

The next portion of the command file specifies all of the different grid and flow options, including laminar or turbulent flow, coordinate systems, buoyancy and heat transfer options, and grid types. These parameters as set in the SFST model are given below

```
>>OPTIONS
  THREE DIMENSIONS
  BODY FITTED GRID
  CARTESIAN COORDINATES
  TURBULENT FLOW
  ISOTHERMAL FLOW
  COMPRESSIBLE FLOW
  BUOYANT FLOW
  TRANSIENT FLOW
  USER SCALAR EQUATIONS 9
```

Simulations may also be performed in two-dimensions and in cylindrical coordinates. The use of the COMPRESSIBLE FLOW option is done so that a variable density field can be specified through the use of a user subroutine. Under the compressibility options, the flow is specified as weakly compressible to allow for this changing density. If the incompressible flow option is specified, then the density field is given a constant value at all points in the domain. The TRANSIENT FLOW option allows for time-dependent solutions, as opposed to steady-state calculations. The final option is the number of user scalar equations that are specified for use in the FORTRAN.

In the SFST model, with the implementation of the droplet formation/entrainment model, scalar arrays are designated for the following variables:

```
>>VARIABLE NAMES
  USER SCALAR1 'SCALAR PHI '
  USER SCALAR2 'USRD DP '
  USER SCALAR3 'USRD CELLID '
  USER SCALAR4 'USRD UDMX '
  USER SCALAR5 'USRD UDMY '
  USER SCALAR6 'USRD UDMZ '
  USER SCALAR7 'USRD UDWALL '
  USER SCALAR8 'USRD VOLFR '
  USER SCALAR9 'USRD RICHARDS NMBR '
```

SCALAR PHI is the generic scalar variable, ϕ , solved for in the transport equation. From it, the volume fraction of the dispersed phase, r_α , is solved from an algebraic relationship. The values of r_α at each cell node for all time values are stored in the USRD VOLFR scalar array. USRD UDMX, USRD UDMY, and USRD UDMZ represent the scalar arrays used to store the three mixed-fluid thicknesses in the three coordinate directions, which are used in calculating the droplet diameter. USRD UDWALL is the array used to store the distance to the nearest wall at each cell node. The last scalar array is used for storing the values of the gradient Richardson number at each cell node. The use of the USRD option in the name of the scalar array indicates that the scalar transport equation will not be solved for that variable.

There are many user FORTRAN subroutines that can be utilized in a numerical simulation in CFX-4. The primary subroutines used in the SFST model are included below:

```
>>USER FORTRAN
  USRBCS
  USRDEN
  USRINT
  USRSRC
  USRTRN
```

USRINT and USRDEN are used to implement the initial conditions and for setting the mixture density equation, respectively. USRSRC is used to implement the source term in the scalar transport equation, and USRTRN is used for solution monitoring and acquiring output data. The subroutine USRBCS is used for implementing variable boundary conditions, while constant boundary conditions may be supplied simply through the use of the MODEL BOUNDARY CONDITIONS option in the command file.

There are also several options for the differencing schemes used for the different variables that are solved for during the course of a numerical simulation. The following set of schemes has been found to work well with the SFST model and DFE model. These may be adjusted by the user to suit different problems.

```

>>DIFFERENCING SCHEME
  U VELOCITY 'HIGHER UPWIND'
  V VELOCITY 'HIGHER UPWIND'
  W VELOCITY 'HIGHER UPWIND'
  PRESSURE 'CENTRAL'
  DENSITY 'UPWIND'
  K 'HYBRID'
  EPSILON 'HYBRID'
  SCALAR PHI 'MIN-MOD'

```

The use of the MUSCL scheme, Min-Mod, for the solution of the scalar, ϕ , was discussed in Section 4.0, where it was found that a significant improvement was made over the use of upwinding in the scalar transport equation. Again, this result does not agree with the recommendation in the CFX Users Manual [12], which suggests that upwinding be used for user scalar variables.

The PHYSICAL PROPERTIES command is used for setting buoyancy and compressibility parameters, as well as time marching information, turbulence parameters, and fluid properties. Under the sub-command BUOYANCY PARAMETERS, the gravity vector and buoyancy reference density is set. In this case, the gravity vector acts downward in the vertical direction, and the buoyancy reference density is set as the average of the two unmixed phase densities.

```

>>MODEL DATA
  >>PHYSICAL PROPERTIES
    >>BUOYANCY PARAMETERS
      GRAVITY VECTOR 0.0 -9.8 0.0
      BUOYANCY REFERENCE DENSITY 9.2500E+02
    >>COMPRESSIBILITY PARAMETERS
      WEAKLY COMPRESSIBLE
      UNIVERSAL GAS CONSTANT 1.0
      FLUID MOLECULAR WEIGHT 1.0
      REFERENCE PRESSURE 10000.0
    >>TRANSIENT PARAMETERS
      >>FIXED TIME STEPPING
        INITIAL TIME 0.0
        BACKWARD DIFFERENCE

```

The use of the WEAKLY COMPRESSIBLE option allows for a density equation to be set by the user in the subroutine USRDEN. This option instructs the code to solve the equations as if they were incompressible, but with a variable density field. The other parameters are included as the default density equation is the ideal gas law. However, these will only be used for the initialization of the density field, and the values will be overwritten using the user implemented density equation on the first outer iteration of the solver. Under TRANSIENT PARAMETERS, fixed time stepping is used, although adaptive time stepping may also be adopted, and backward differencing is used for the time discretization. The INITIAL TIME should always be set to 0.0 unless a restart is used from a previously generated dump file.

CFX-4 allows for several different equation solvers to be used. Again, while these may be adjusted by the user depending on the flow scenario, the following options were found to be adequate in the use of the SFST model.

```
>>SOLVER DATA
  >>EQUATION SOLVERS
    U VELOCITY 'AMG'
    V VELOCITY 'AMG'
    W VELOCITY 'AMG'
    PRESSURE 'ICCG'
    K 'STONE'
    EPSILON 'STONE'
    SCALAR PHI 'AMG'
```

A velocity field which satisfies conservation of mass is very important in not allowing for an unbounded value for the scalar, ϕ , or in turn the volume fraction. In order to facilitate this, the residual reduction factor for the pressure equation is set to a smaller value than the default value supplied. The value given under REDUCTION FACTORS by

```
>>SOLVER DATA
  >>REDUCTION FACTORS
    PRESSURE 0.05
```

has been used successfully. This ensures that the velocity field passed to the scalar transport equation, while not necessarily satisfying the momentum equations early in the outer iterations, will still satisfy continuity.

In order to use the droplet formation/entrainment (DFE) model, the following keywords must be set with regard to the USRD UDWALL variable, which stores the distances to the nearest wall at each cell center.

```
>>CREATE GRID
  >>GRID OPTIONS
    COMPUTE DISTANCES TO WALLS
```

This instructs the code to compute the distances from each cell node to the nearest wall patch at the beginning of the simulation. This information is then stored in the array DISWAL, which can be accessed from the USRINT subroutine.

B.3.3 User FORTRAN implementation of the SFST and DFE Models

In this section, details concerning the implementation of the SFST and DFE model will be provided. The user FORTRAN file used for the numerical simulations includes the subroutines UBCND, UGRDNT, USRINT, USRDEN, USRSRC, USRTRN, and LENGTH. Of these, USRINT, USRDEN, USRSRC, and USRTRN are CFX user subroutines, while the others are called from within the CFX subroutines. Further details regarding many of these will be presented in the following sections. The CFX subroutines USRBCS and USRTRN are used for implementing variable boundary conditions and solution monitoring, respectively, and will not be examined as these are problem specific issues.

General Notes:

Before presenting a detailed review of each of the user subroutines, some general notes concerning the FORTRAN code need to be addressed. Firstly, at the beginning of each CFX subroutine, the user subroutine UBCND needs to be called before attempting to prescribe any information. This ensures that the correct values for the fluid properties and geometric information are passed to the current subroutine. This will always appear at the beginning of USER AREA 5. Following this, the user scalar variable numbers need to be called and assigned variable strings. This is done using the GETSCA utility routine as follows:

```
C GET THE SCALAR NUMBERS CORRESPONDING TO THE APPROPRIATE VARIABLES
  CALL GETSCA('SCALAR PHI', ISCAL, CWORK)
  CALL GETSCA('USRD DP', ISCDP, CWORK)
  CALL GETSCA('USRD CELLID', ISCCI, CWORK)
  CALL GETSCA('USRD UDMX', ISCMX, CWORK)
  CALL GETSCA('USRD UDMY', ISCMY, CWORK)
  CALL GETSCA('USRD UDMZ', ISCMZ, CWORK)
  CALL GETSCA('USRD UDWALL', ISCDW, CWORK)
  CALL GETSCA('USRD VOLFR', ISCVF, CWORK)
  CALL GETSCA('USRD RICHARDS NMBR', ISCGR, CWORK)
```

The utility routine will then access the scalar number corresponding to the appropriate scalar variable array, and store it as the variable prescribed in the third option (e.g. ISCAL). This is done so that the scalar numbers can be accessed easily within the user subroutines, and also prevents any mistakes in accessing the correct array if scalar variables are removed from, or added to, the current problem.

If any information needs to be accessed or prescribed concerning a specific coordinate location, then the following options need to be set in USER AREA 3:

```
C VARIABLES TO BE USED FOR THE BLOCK NAMING
  CHARACTER SUBNAME*5, CHTIME*7
  CHARACTER*20 UBNAME(20)
  CHARACTER*20 UISNME(20)
  CHARACTER BASENAME*20, CH1*1, CH2*2
```

These commands reserve character workspace for the descriptions of the various blocks. The character space for UISNME need only be used for geometries containing internal solid blocks used as child constraints.

With these options set, the following must also be added in USER AREA 5, following the call of the UBCND subroutine, and accessing the user scalar variable numbers:

```

C*****
C***** INITIALIZE THE BASENAME MATRICES *****
C*****
C DETERMINE THE NUMBERS OF CHARACTERS IN BASENAME FOR BLOCKS
  BASENAME='BLOCK-NUMBER-'
  CALL LENGTH(BASENAME,20,NUMCHA)

C FILL THE UBNAME MATRIX WITH THE APPROPRIATE STRINGS OF BLOCK NUMBERS
  DO I=1,UNB
    IF(I.LE.9) THEN
      WRITE(CH1,'(I1)') I
      UBNAME(I)=(BASENAME(1:NUMCHA)//CH1)
    ELSE
      WRITE(CH2,'(I2)') I
      UBNAME(I)=(BASENAME(1:NUMCHA)//CH2)
    END IF
  END DO

C DETERMINE THE NUMBERS OF CHARACTERS IN BASENAME FOR INTERNAL SOLIDS
  BASENAME='INTSOLID'
  CALL LENGTH(BASENAME,20,NUMCHA)

C FILL THE UBNAME MATRIX WITH THE APPROPRIATE STRINGS OF BLOCK NUMBERS
  DO I=1,UNIS
    IF(I.LE.9) THEN
      WRITE(CH1,'(I1)') I
      UISNME(I)=(BASENAME(1:NUMCHA)//CH1)
    ELSE
      WRITE(CH2,'(I2)') I
      UISNME(I)=(BASENAME(1:NUMCHA)//CH2)
    END IF
  END DO

C*****

```

This portion of the code will fill the variable arrays UBNAME and UISNME with the appropriate value corresponding to a given block number. Again, UISNME would only be used for geometries containing internal solid blocks. This must be done before any information about a specific location can be accessed.

In order to return the correct block numbering information prescribed above, the utility routine IPREC is used, for example, in looping over all of the blocks:

```

C BEGIN THE LOOP OVER THE BLOCKS
  DO N=1,UNB

```

```

CALL LENGTH(UBNAME(N), 20, NUMCHA)
CALL IPREC(UBNAME(N)(1:NUMCHA), 'BLOCK', 'CENTERS', IPT, ILEN, JLEN,
&KLEN, CWORK, IWORK)

```

Here the user subroutine `LENGTH` determines the correct block number, from which the utility routine `IPREC` will return the number of subdivisions in each of the three coordinate directions (`ILEN`, `JLEN`, `KLEN`) within that specific block. The utility routine `IPALL` will serve the same function, but will return only a one-dimensional array. A given three-dimensional location is then determined using the utility routine `IP` as follows

```
INODE = IP(I,J,K)
```

The variable `INODE` can then be used in determining the coordinate space location of the given cell node, from which all other information can be accessed (e.g. `YP(INODE)` represents the y-location of the cell node).

Subroutine LENGTH:

The block number is returned from this subroutine and is used to fill the block name matrices. This subroutine is given below:

```

SUBROUTINE LENGTH(STRING, MAX, NUMCHA)

CHARACTER*(*) STRING

DO I=1, MAX
  IF(STRING(I:I).EQ.' ') GOTO 1
END DO

1  NUMCHA=(I-1)
   RETURN

END

```

Subroutine UBCND:

The purpose of this subroutine was to allow for different options to be set with regard to the SFST and DFE model without having to modify extensive portions of the FORTRAN code within the different subroutines. These include certain fluid properties for the two phases, flags to set the source terms in the scalar transport equation and turbulence equations, and options for setting a constant droplet diameter or allowing the DFE model to calculate the droplet size at each computational cell.

The first section is used to set the turbulent Prandtl number for k, which is used in setting the buoyant source terms in the turbulence equations. Here we use a value of 1.0.

```
C TURBULENCE SOURCE CONSTANTS
      UTPN = 1.0           !BUOYANT SOURCE PRANDTL NUMBER
```

The next section is for setting the fluid properties, and the average droplet diameter in the case where the DFE model is not used dynamically. The fluid properties include the unmixed densities of the two phases (in this case water and diesel fuel), as well as their molecular viscosities.

```
C FLUID PROPERTIES
      URHOW = 1000.0      !DENSITY OF HEAVY FLUID
      URHOF = 850.0      !DENSITY OF LIGHT FLUID
      UVISW = 0.001      !VISCOSITY OF HEAVY FLUID
      UVISF = 0.002      !VISCOSITY OF LIGHT FLUID
      UDIAP = 0.001      !AVERAGE PARTICLE (DROP) DIAMETER
```

Following this, the boundedness parameter for limiting the source term in the scalar transport equation is set. This term represents the percentage of the total fuel that can be donated from a given cell to its adjacent acceptor cell. Here the value is set to 0.75, though this may need to be adjusted to allow for more or less influence of the slip velocity. This will be explained in greater detail in the discussion of the USRSRC subroutine later. Here also, the exponent to be used for the function of the volume fraction in the slip velocity is set (see Section 3.3).

```
C SLIP VELOCITY
      USBND = 0.9         !SOURCE TERM BOUNDEDNESS PARAMETER
      UEXP1 = 0.71429     !EXPONENT TO BE USED IN SLIP VELOCITY
```

The geometric information that needs to be set includes the total number of active blocks, and the total number of internal solid blocks used as child constraints. The following values are those pertaining to the simulations of the impinging jet facility. If there are no internal solid blocks, then UNIS should be set to 0. This value is used for setting certain boundary conditions later in the code.

```
C SET GEOMETRIC INFORMATION
      UNB = 9             !NUMBER OF BLOCKS
      UNIS = 3            !NUMBER OF INTERNAL SOLIDS USED AS CHILD
                          CONSTRAINTS
```

In the case of the shear flow simulations, there are certain parameters that need to be set to control the output generated by CFX for use in plotting the various profiles as a function of streamwise distance (e.g. the mixed fluid thickness). The user must specify the *i*-location to begin the data dumps, as well as the final *i*-location, and the total number of dumps to be written to the output file and the final time of the simulation. During the final time step, then, CFX outputs the volume fraction, density, and streamwise velocity as a function of vertical position, for each streamwise location specified. From this data file, a reduction program is used to generate the data files necessary for plotting the

various profiles. A typical example of how these parameters were set for the present study are given below.

```
C DEFINE ON WHAT "X" LOCATION TO TAKE THE SHOTS AND WHEN
  UISHOT = 1          !INITIAL Y SHOT
  UFSHOT = 150       !FINAL Y SHOT
  USHOTI = 1         !SHOT INCREMENT
  UTIME = 20.0       !THE TIME TO WRITE THE DATA
```

This, then, would instruct the code to write out the appropriate data starting at $i=1$ and going to $i=150$ in the mixing layer region, in increments of 1, so that the data would be output at every cell in the streamwise direction.

Finally, the various flags for different run options need to be set. This is the primary purpose, and benefit, of using the UBCND subroutine. It allows for these different options to be changed for different simulations without major modifications to multiple sections of the code.

```
C SET SOLVER PARAMETERS
  USADD = 5          !OUTER ITERATION TO BEGIN SETTING SCALAR SOURCE
  UTADD = 5          !OUTER ITERATION TO BEGIN SETTING TURB SOURCE
                    TERMS
  USFST = 1         !FLAG TO INCLUDE SLIP SOURCE TERM IN SCALAR
                    TRANSPORT EQUATION
  UKEPS = 1         !FLAG TO INCLUDE BUOYANT K AND EPSILON SOURCE
                    TERMS
  UMNVF = 1         !FLAG TO MONITOR SCALAR PHI AND CORRECT
  UDYNM = 1         !FLAG TO USE DYNAMIC DROPLET MODEL
```

The terms USADD and UTADD represent an integer value for CFX to begin setting the scalar and buoyant source terms, respectively. The other terms are simply flags to turn certain options on (value = 1) or off (value = 0). This allows for several different cases to be simulated while only changing a few values in this subroutine. No other modifications need to be made in the remaining CFX subroutines.

Subroutine UGRDNT:

This is simply a subroutine that can be called to perform one-dimensional gradient calculations of different variables. It is used, for example, in calculating the density and velocity gradients used in determining the gradient Richardson number. The values that need to be passed to the subroutine are described below:

```
UPHI = VALUE OF VARIABLE AT CELL WHERE GRADIENT IS TO BE CALCULATED
UPHIP1 = VALUE OF VARIABLE AT HIGH CELL (J+1, K+1, ETC.)
UPHIM1 = VALUE OF VARIABLE AT LOW CELL (J-1, K-1, ETC.)
```

```

UX = COORDINATE AT CELL WHERE GRADIENT IS TO BE CALCULATED
UXP1 = COORDINATE AT HIGH CELL (J+1, K+1, ETC.)
UXM1 = COORDINATE AT LOW CELL (J-1, K-1, ETC.)
UWH = CFX WEIGHTING FACTOR AT HIGH FACE
UWL = CFX WEIGHTING FACTOR AT LOW FACE

```

Finally, UGRD is the variable name used for the returned value of the gradient calculation. The gradient is then calculated by linear interpolation between the high and low faces of the cell in question. In the case of a cell that is adjacent to a boundary, a one-sided difference should be used by setting

```

UPHI = UPHI1           for a high boundary
UPHI = UPHIM1         for a low boundary.

```

The one-dimensional gradient calculation is performed using the following algorithm:

```

SUBROUTINE UGRDNT(UPHI, UPHI1, UPHIM1, UX, UXP1, UXM1, UWH, UWL, UGRD)
C ***** CALCULATION OF GRADIENTS *****
      UXH = UX + UWH*(UXP1-UX)
      UXL = UX - UWL*(UX-UXM1)
      UPHIH = (1.0-UWH)*UPHI + (UWH)*UPHI1
      UPHIL = (1.0-UWL)*UPHI + (UWL)*UPHIM1
      UGRD = (UPHIH-UPHIL)/(UXH-UXL)

```

CFX Subroutine USRINT:

This is a CFX subroutine that is used for implementing any initial conditions within the domain. As these details will change with a given problem, a detailed description will not be given. Of note, however, is one option that needs to be set concerning the scalar array USRD UDWALL, which stores the wall distance information at each cell node. With the COMPUTE DISTANCES TO WALLS option set in the command file, at the beginning of the simulation CFX will determine the distance to the nearest wall at each cell node. This information is stored in the array DISWAL, which can be accessed in this subroutine. The following options need to be set when using the DFE model.

```

C SET DISTANCES TO NEAREST WALLS
  DO N=1, UNB
    CALL LENGTH(UBNAME(N), 20, NUMCHA)
    CALL IPREC(UBNAME(N)(1:NUMCHA), 'BLOCK', 'CENTERS', IPT, ILEN, JLEN,
&KLEN, CWORK, IWORK)

    DO I=1, ILEN
      DO J=1, JLEN
        DO K=1, KLEN

```

```

INODE=IP(I,J,K)
SCAL(INODE,1,ISCDW) = DISWAL(INODE)

END DO
END DO
END DO
END DO

```

Here, SCAL(INODE,1,ISCDW) represents the scalar array used to store the nearest wall distance in each computational cell. In the case of two-dimensional geometries, this value should be limited by the domain thickness in the third coordinate direction, say

```

SCAL(INODE,1,ISCDW) = MIN(DISWAL(INODE),0.0127)

```

CFX subroutine USRDEN:

In this subroutine the mixture density equation is set by the user. This, along with the option WEAKLY COMPRESSIBLE, allows for a variable density field to be set, while maintaining the incompressibility condition in the solution of the governing equations. Here, the mixture density is defined according to

$$\mathbf{r}_m = \mathbf{r}_a r'_a + \mathbf{r}_b r'_b$$

where the subscripts α and β represent the light and heavy phase, respectively, and r is the volume fraction. The density equation is prescribed as follows:

```

C***** AREA FOR MIXTURE DENSITY EQUATION*****
C SET THE NEW EQUATION OF STATE

CALL IPALL(' ',' ','BLOCK', 'CENTRES', IPT,NPT,CWORK,IWORK)
DO I=1,NPT
  INODE = IPT(I)

  DENN(INODE,1)=URHOF*SCAL(INODE,1,ISCVF)+
&      URHOW*(1-SCAL(INODE,1,ISCVF))

  DRHODP(INODE,1) = 0.0
END DO

CALL IPALL(' ',' ','PATCH', 'CENTRES', IPT,NPT,CWORK,IWORK)
DO I=1,NPT
  INODE = IPT(I)

  DENN(INODE,1)=URHOF*SCAL(INODE,1,ISCVF)+
&      URHOW*(1-SCAL(INODE,1,ISCVF))

  DRHODP(INODE,1) = 0.0
END DO
C*****

```

CFX Subroutine USRSRC:

This CFX subroutine is used for setting additional source terms in the governing equations. In the case of the SFST model and DFE model, this subroutine is used for setting the source terms in the scalar transport and turbulence equations, as well as for calculating the droplet diameter and determining the slip velocity.

Following the initialization of the name matrices (see General Notes above), the user scalar array USRD CELLID is filled with the appropriate values corresponding to different boundary cell specifiers. These values are used in determining certain boundary conditions when the active cell is adjacent to a boundary or patch. These calculations are only performed once, at the beginning of the simulation.

```
C*****
C*** SET THE CELL SPECIFIERS ACCORDING TO WHAT BOUNDARY PATCHES EXIST *
C*****

      IF (TIME.EQ.DT.AND.NITER.EQ.1) THEN
      CALL GETBCS ('USRSRC', 'INLET ', IILVEL, NIPTCH, NILBEL, NICV, IISTR)
      CALL GETBCS ('USRSRC', 'WALL  ', IWLVEL, NWPTCH, NWLBEL, NWCV, IWSTRT)
      CALL GETBCS ('USRSRC', 'PRESS ', IPLVEL, NPPTCH, NPLBEL, NPCV, IPSTRT)
      CALL GETBCS ('USRSRC', 'OUTLET', IMLVEL, NMPTCH, NMLBEL, NMCV, IMSTRT)

      !THE CELL INDICATORS
      !0 - INTERNAL SOLID CELL THAT IS PART OF A CHILD CONSTRAINT
      !1 - TYPICAL CELL
      !2 - HIGH WALL
      !3 - LOW WALL
      !4 - HIGH PRESSURE/MFB/INLET
      !5 - LOW PRESSURE/MFB/INLET

      DO N=1, UNB
      CALL LENGTH (UBNAME (N), 20, NUMCHA)
      CALL IPREC (UBNAME (N) (1:NUMCHA), 'BLOCK', 'CENTERS', IPT, ILEN, JLEN,
&KLEN, CWORK, IWORK)

      DO K = 1, KLEN
      DO J = 1, JLEN
      DO I = 1, ILEN

      INODE = IP (I, J, K)
      IFCES=IPFACN (INODE, 5)
      IFCEN=IPFACN (INODE, 2)

      C SET FLAG FOR NORMAL CELLS
      SCAL (INODE, 1, ISCCI)=1.0

      C SET FLAG FOR WALLS
      DO NW=IWSTRT, (IWSTRT+NWCV-1)
      IF (IFCEN.EQ.IPFACB (NW)) THEN
      SCAL (INODE, 1, ISCCI)=2.0
      END IF
      IF (IFCES.EQ.IPFACB (NW)) THEN
```

```

        SCAL(INODE,1,ISCCI)=3.0
    END IF
END DO

C SET FLAG FOR INLETS
DO NW=IISTR, (IISTR+NICV-1)
    IF (IFCEN.EQ.IPFACB(NW)) THEN
        SCAL(INODE,1,ISCCI)=4.0
    END IF
    IF (IFCES.EQ.IPFACB(NW)) THEN
        SCAL(INODE,1,ISCCI)=5.0
    END IF
END DO

C SET FLAG FOR PRESSURE PATCHES
DO NW=IPSTR, (IPSTR+NPCV-1)
    IF (IFCEN.EQ.IPFACB(NW)) THEN
        SCAL(INODE,1,ISCCI)=4.0
    END IF
    IF (IFCES.EQ.IPFACB(NW)) THEN
        SCAL(INODE,1,ISCCI)=5.0
    END IF
END DO

C SET FLAG FOR MASS FLOW BOUNDARIES
DO NW=IMSTR, (IMSTR+NMCV-1)
    IF (IFCEN.EQ.IPFACB(NW)) THEN
        SCAL(INODE,1,ISCCI)=4.0
    END IF
    IF (IFCES.EQ.IPFACB(NW)) THEN
        SCAL(INODE,1,ISCCI)=5.0
    END IF
END DO

C SET FLAG FOR INTERNAL SOLIDS
DO IS=1,UNISC
    IF(UISBLK(IS).EQ.INODE) THEN
        SCAL(INODE,1,ISCCI)=0.0
    END IF
END DO

END DO
END DO
END DO
END DO

END IF
C*****

```

Following this, the values of SCALAR PHI are monitored (if the appropriate flag, UMNVF, has been set) and corrected if the local value is less than zero or greater than one by at least 5.0×10^{-3} . The information concerning the times that these values are overwritten is stored in the two user text files shown. This process is performed at the

beginning of an outer iteration (as the solution starts with U VELOCITY), and is only performed if the number of iterations exceeds USADD. This was done for improved convergence, so that the first few values obtained were ignored.

```

C*****
C ***** MONITOR THE SCALAR PHI *****
C*****
      IF((UMNVF.EQ.1).AND.(CALIAS.EQ.'U VELOCITY')) THEN

C OPEN THE FILES TO MONITOR THE VOLUME FRACTION (SCALAR)
      OPEN(82,FILE='negvf.txt',STATUS='NEW')
      OPEN(83,FILE='posvf.txt',STATUS='NEW')

      DO N=1,UNB
      CALL LENGTH(UBNAME(N),20,NUMCHA)
      CALL IPREC(UBNAME(N)(1:NUMCHA),'BLOCK','CENTERS',IPT,ILEN,JLEN,
&KLEN,CWORK,IWORK)

      DO K = 1, KLEN
      DO J = 1, JLEN
      DO I = 1, ILEN

      INODE = IP(I,J,K)

      IF(SCAL(INODE,1,ISCAL).LT.0.0) THEN
      IF(ABS(SCAL(INODE,1,ISCAL)).GT.0.005.AND.NITER.GT.USADD) THEN
      WRITE(82,108)'VF= ',SCAL(INODE,1,ISCAL),'TIME= ',TIME,'NITER= ',
&NITER,' BLOCK= ',N,' J= ',J
      END IF
      SCAL(INODE,1,ISCAL)=0.0
      END IF

      IF(SCAL(INODE,1,ISCAL).GT.1.0) THEN
      IF(ABS(SCAL(INODE,1,ISCAL)).GT.1.005.AND.NITER.GT.USADD) THEN
      WRITE(83,108)'VF= ',SCAL(INODE,1,ISCAL),'TIME= ',TIME,'NITER= ',
&NITER,' BLOCK= ',N,' J= ',J
      END IF
      SCAL(INODE,1,ISCAL)=1.0
      END IF

      END DO
      END DO
      END DO
      END DO

      ENDIF

C*****

```

The next section of subroutine USRSRC is used for calculating the volume fraction from the scalar variable, ϕ . This was discussed in Section 4.0. As in the case of monitoring the scalar, this process is performed at the beginning of the outer iteration. Once the volume fraction is calculated for a given cell, the mixture density is immediately updated,

so that the current value of the mixture density will be used in the solution of the momentum equations.

```

C*****
C***** CALCULATE VOLUME FRACTION FROM PHI *****
C*****
      IF(CALIAS.EQ.'U VELOCITY') THEN

        DO N=1,UNB
          CALL LENGTH(UBNAME(N),20,NUMCHA)
          CALL IPREC(UBNAME(N)(1:NUMCHA),'BLOCK','CENTERS',IPT,ILEN,JLEN,
&KLEN,CWORK,IWORK)

          DO K = 1, KLEN
            DO J = 1, JLEN
              DO I = 1, ILEN
                INODE = IP(I,J,K)
                UPHI=SCAL(INODE,1,ISCAL)
                SCAL(INODE,1,ISCVF)= UPHI/(UPHI+(URHOF/URHOW)*(1-UPHI))

C UPDATE THE DENSITY FIELD WITH THE NEW VF DATA
                DEN(INODE,1)=URHOF*SCAL(INODE,1,ISCVF)+
& URHOW*(1-SCAL(INODE,1,ISCVF))

                END DO
              END DO
            END DO
          END DO

C SET VOLUME FRACTION IN ALL PATCHES

          CALL IPALL('*','*','PATCH','CENTRES',IPT,NPT,CWORK,IWORK)
          DO I=1,NPT
            INODE = IPT(I)

            UPHI=SCAL(INODE,1,ISCAL)
            SCAL(INODE,1,ISCVF)= UPHI/(UPHI+(URHOF/URHOW)*(1-UPHI))

C UPDATE THE DENSITY FIELD WITH THE NEW VF DATA
            DEN(INODE,1)=URHOF*SCAL(INODE,1,ISCVF)+
& URHOW*(1-SCAL(INODE,1,ISCVF))

            END DO

          ENDIF

C*****

```

The next portion of subroutine USRSRC is used for calculating the droplet diameter. This is only done if the proper flag (i.e. UDYNM) has been set. Here, the local volume fraction is checked, and if below some small value, then the droplet diameter is set to zero. This would correspond to regions that are occupied primarily by only the water phase. Next

the three mixed fluid thicknesses are calculated in each of the three coordinate directions, using a sweep method from the active cell, based on the volume fraction profile. From the active cell, the domain is swept in each direction and looks for either a solid boundary or a region where the volume fraction is relatively small (i.e. a cell filled mostly with water). This would define the edges of the mixed fluid thickness in that direction. This process is repeated along both the positive and negative axes for each of the three coordinate directions. The mixed fluid thickness is then determined by subtracting the two positions.

In the case of the shear layer simulations, and for any multi-block geometry where the interface may extend across inter-block boundaries, the sweep may need to extend through several blocks. In order to assure that the interface is captured, the sweeps performed in the horizontal and vertical directions are checked to make sure that either the extent of the mixed fluid thickness has been found or a solid boundary has been reached, else the process continues into the adjacent block. In this case, the problem is two-dimensional, and so the z-direction sweep is neglected. For a three-dimensional problem, this would be included in the same manner. The specific functions used for determining the adjacent block numbers must be determined by the user for a specific geometry. The implementation used for the shear flow geometry is given below.

```

C*****
C ***** CALCULATE THE DROPLET DIAMETER *****
C*****

C CHECK FOR FLAG TO USE DROPLET MODEL
      IF(UDYNM.EQ.1) THEN

C -- USE SWEEP METHOD TO DETERMINE LENGTH SCALES -----

      DO N=1,UNB
C GET THE THREE DIMENSIONAL ADDRESSES OF THE CELLS
      CALL LENGTH(UBNAME(N),20,NUMCHA)
      CALL IPREC(UBNAME(N)(1:NUMCHA),'BLOCK','CENTERS',IPT,ILEN,JLEN,
&KLEN,CWORK,IWORK)

      DO K=1,KLEN
      DO I=1,ILEN
      DO J=1,JLEN

      INODE=IP(I,J,K)

IF(SCAL(INODE,1,ISCVF).LT.(0.01).OR.SCAL(INODE,1,ISCVF).GT.(0.99)) THEN
      SCAL(INODE,1,ISCMX)=0.0
      SCAL(INODE,1,ISCMY)=0.0
      SCAL(INODE,1,ISCMZ)=0.0

      ELSE

      IEFLAG=0
      IWFLAG=0
      INFLAG=0

```

```

ISFLAG=0
ITFLAG=0
IBFLAG=0

ISTART=I
JSTART=J
KSTART=K

C -- SWEEP THE DOMAIN IN ALL SIX DIRECTIONS -----
C ----- SWEEP EAST IN X-DIRECTION

CALL LENGTH(UBNAME(N), 20, NUMCHA)
CALL IPREC(UBNAME(N)(1:NUMCHA), 'BLOCK', 'CENTERS', IPT,
&ILEN, JLEN, KLEN, CWORK, IWORK)

DO IE=ISTART, ILEN
  INODEP=IP(IE, JSTART, KSTART)
  INODEE=IPNODN(INODEP, 1)

  IF(SCAL(INODEE, 1, ISCVF).LE.(0.01)) THEN
    IEFLAG=IEFLAG+1
    IF(IEFLAG.EQ.1) THEN
      XE=0.5*(XP(INODEP)+XP(INODEE))
      GOTO 1000
    ENDIF
  ENDIF

  IF((IE.EQ.ILEN).AND.(IEFLAG.EQ.0)) THEN

    N2E = N
C DO WHILE LOOP TO CHECK ADJACENT BLOCKS
    KITERE=1
    DO WHILE (KITERE.LE.4)

      IF((N2E.GE.13).AND.(N2E.LE.16)) THEN
        XE=0.5*(XP(INODEP)+XP(INODEE))
        GOTO 1000
      ELSEIF((N2E.EQ.18).OR.(N2E.EQ.19).OR.(N2E.EQ.2)) THEN
        XE=0.5*(XP(INODEP)+XP(INODEE))
        GOTO 1000

C CONTINUE IN ADJACENT BLOCK
      ELSEIF((N2E.EQ.3).OR.(N2E.EQ.17)) THEN
        NADJE = N2E+1
      ELSEIF(N2E.EQ.20) THEN
        NADJE = N2E-18
      ELSEIF(N2E.EQ.1) THEN
        NADJE = N2E+4
      ELSEIF((N2E.GE.4).AND.(N2E.LE.12)) THEN
        NADJE = N2E+3
      ENDIF

      CALL LENGTH(UBNAME(NADJE), 20, NUMCHA)
      CALL IPREC(UBNAME(NADJE)(1:NUMCHA), 'BLOCK', 'CENTERS', IPT,
&ILEN, JLEN, KLEN, CWORK, IWORK)

```

```

DO IADJ=1,ILEN
INODEP=IP(IADJ,JSTART,KSTART)
INODEE=IPNODN(INODEP,1)

IF(SCAL(INODEE,1,ISCVF).LE.(0.1)) THEN
IEFLAG=IEFLAG+1
  IF(IEFLAG.EQ.1) THEN
    XE=0.5*(XP(INODEP)+XP(INODEE))
    GOTO 1000
  ENDIF
ENDIF

END DO

C REPLACE BLOCK NUMBER WITH ADJACENT BLOCK NUMBER AND CONTINUE
N2E = NADJE
KITERE=KITERE+1

C END DO-WHILE LOOP
END DO

ENDIF
END DO

1000 CONTINUE

C ----- SWEEP WEST IN X-DIRECTION

CALL LENGTH(UBNAME(N),20,NUMCHA)
CALL IPREC(UBNAME(N)(1:NUMCHA),'BLOCK','CENTERS',IPT,
&ILEN,JLEN,KLEN,CWORK,IWORK)

DO IW=ISTART,1,-1
INODEP=IP(IW,JSTART,KSTART)
INODEW=IPNODN(INODEP,4)

IF(SCAL(INODEW,1,ISCVF).LE.(0.1)) THEN
IWFLAG=IWFLAG+1
  IF(IWFLAG.EQ.1) THEN
    XW=0.5*(XP(INODEP)+XP(INODEW))
    GOTO 2000
  ENDIF
ENDIF

IF((IW.EQ.1).AND.(IWFLAG.EQ.0)) THEN

N2W=N
C DO WHILE LOOP TO CHECK ADJACENT BLOCKS
KITERW=1
DO WHILE (KITERW.LE.4)

IF((N2W.EQ.1).OR.(N2W.EQ.3).OR.(N2W.EQ.20).OR.(N2W.EQ.19)) THEN
XW=0.5*(XP(INODEP)+XP(INODEW))
GOTO 2000
ELSEIF((N2W.EQ.16).OR.(N2W.EQ.17).OR.(N2W.EQ.6)) THEN
XW=0.5*(XP(INODEP)+XP(INODEW))
GOTO 2000

```

```

C CONTINUE IN ADJACENT BLOCK
  ELSEIF(N2W.EQ.2) THEN
    NADJW = N2W+18
  ELSEIF((N2W.EQ.4).OR.(N2W.EQ.18)) THEN
    NADJW = N2W-1
  ELSEIF(N2W.EQ.5) THEN
    NADJW = N2W-4
  ELSEIF((N2W.GE.7).AND.(N2W.LE.15)) THEN
    NADJW = N2W-3
  ENDIF

  CALL LENGTH(UBNAME(NADJW),20,NUMCHA)
  CALL IPREC(UBNAME(NADJW)(1:NUMCHA),'BLOCK','CENTERS',IPT,
&ILEN,JLEN,KLEN,CWORK,IWORK)

  DO IADJ=ILEN,1,-1
    INODEP=IP(IADJ,JSTART,KSTART)
    INODEW=IPNODN(INODEP,4)

    IF(SCAL(INODEW,1,ISCVF).LE.(0.1)) THEN
      IWFLAG=IWFLAG+1
      IF(IWFLAG.EQ.1) THEN
        XW=0.5*(XP(INODEP)+XP(INODEW))
        GOTO 2000
      ENDIF
    ENDIF

  END DO

C REPLACE BLOCK NUMBER WITH ADJACENT BLOCK NUMBER AND CONTINUE
  N2W = NADJW
  KITERW=KITERW+1

C END DO-WHILE LOOP
  END DO

  ENDIF
  END DO

2000 CONTINUE

C ----- SWEEP NORTH IN Y-DIRECTION

  CALL LENGTH(UBNAME(N),20,NUMCHA)
  CALL IPREC(UBNAME(N)(1:NUMCHA),'BLOCK','CENTERS',IPT,
&ILEN,JLEN,KLEN,CWORK,IWORK)

  DO JN=JSTART,JLEN
    INODEP=IP(ISTART,JN,KSTART)
    INODEN=IPNODN(INODEP,2)

    IF(SCAL(INODEN,1,ISCVF).GE.(0.99)) THEN
      INFLAG=INFLAG+1
      IF(INFLAG.EQ.1) THEN

```

```

        YN=0.5*(YP(INODEP)+YP(INODEN))
        GOTO 3000
    ENDIF
ENDIF

IF((JN.EQ.JLEN).AND.(INFLAG.EQ.0)) THEN

    N2N=N
C DO WHILE LOOP TO CHECK ADJACENT BLOCKS
    KITERN=1
    DO WHILE (KITERN.LE.4)

        IF((N2N.EQ.20).OR.(N2N.EQ.3).OR.(N2N.EQ.7).OR.(N2N.EQ.10)) THEN
            YN=0.5*(YP(INODEP)+YP(INODEN))
            GOTO 3000
        ELSEIF((N2N.EQ.17).OR.(N2N.EQ.18).OR.(N2N.EQ.4)) THEN
            YN=0.5*(YP(INODEP)+YP(INODEN))
            GOTO 3000
        ELSEIF((N2N.EQ.1).OR.(N2N.EQ.5).OR.(N2N.EQ.11).OR.(N2N.EQ.14))
THEN
            YN=0.5*(YP(INODEP)+YP(INODEN))
            GOTO 3000

C CONTINUE IN ADJACENT BLOCK
        ELSEIF(N2N.EQ.19) THEN
            NADJN = N2N-17
        ELSEIF((N2N.EQ.2).OR.(N2N.EQ.6).OR.(N2N.EQ.12).OR.(N2N.EQ.15))
THEN
            NADJN = N2N-1
        ELSEIF((N2N.EQ.8).OR.(N2N.EQ.9)) THEN
            NADJN = N2N-1
        ELSEIF(N2N.EQ.13) THEN
            NADJN = N2N+3
        ELSEIF(N2N.EQ.16) THEN
            NADJN = N2N+1
        ENDIF

        CALL LENGTH(UBNAME(NADJN),20,NUMCHA)
        CALL IPREC(UBNAME(NADJN)(1:NUMCHA),'BLOCK','CENTERS',IPT,
&ILEN,JLEN,KLEN,CWORK,IWORK)

        DO JADJ=1,JLEN
            INODEP=IP(ISTART,JADJ,KSTART)
            INODEN=IPNODN(INODEP,2)

            IF(SCAL(INODEN,1,ISCVF).LE.(0.1)) THEN
                INFLAG=INFLAG+1
                IF(INFLAG.EQ.1) THEN
                    YN=0.5*(YP(INODEP)+YP(INODEN))
                    GOTO 3000
                ENDIF
            ENDIF
        END DO
    END DO

```

```

C REPLACE BLOCK NUMBER WITH ADJACENT BLOCK NUMBER AND CONTINUE
  N2N = NADJN
  KITERN=KITERN+1

C END DO-WHILE LOOP
  END DO

  ENDIF
  END DO

3000 CONTINUE

C ----- SWEEP SOUTH IN Y-DIRECTION

  CALL LENGTH(UBNAME(N), 20, NUMCHA)
  CALL IPREC(UBNAME(N)(1:NUMCHA), 'BLOCK', 'CENTERS', IPT,
&ILEN, JLEN, KLEN, CWORK, IWORK)

  DO JS=JSTART, 1, -1
    INODEP=IP(ISTART, JS, KSTART)
    INODES=IPNODN(INODEP, 5)

    IF(SCAL(INODES, 1, ISCVF).LE.(0.01)) THEN
      ISFLAG=ISFLAG+1
      IF(ISFLAG.EQ.1) THEN
        YS=0.5*(YP(INODEP)+YP(INODES))
        GOTO 4000
      ENDIF
    ENDIF

    IF((JS.EQ.1).AND.(ISFLAG.EQ.0)) THEN

      N2S=N
C DO WHILE LOOP TO CHECK ADJACENT BLOCKS
      KITERS=1
      DO WHILE (KITERS.LE.4)

        IF((N2S.EQ.20).OR.(N2S.EQ.19).OR.(N2S.EQ.6).OR.(N2S.EQ.9)) THEN
          YS=0.5*(YP(INODEP)+YP(INODES))
          GOTO 4000
        ELSEIF((N2S.EQ.12).OR.(N2S.EQ.15).OR.(N2S.EQ.18)) THEN
          YS=0.5*(YP(INODEP)+YP(INODES))
          GOTO 4000
        ELSEIF((N2S.EQ.3).OR.(N2S.EQ.4).OR.(N2S.EQ.10).OR.(N2S.EQ.13))
THEN
          YS=0.5*(YP(INODEP)+YP(INODES))
          GOTO 4000

C CONTINUE IN ADJACENT BLOCK
        ELSEIF((N2S.EQ.1).OR.(N2S.EQ.5).OR.(N2S.EQ.11).OR.(N2S.EQ.14))
THEN
          NADJS = N2S+1

```

```

ELSEIF(N2S.EQ.2) THEN
NADJS = N2S+17
ELSEIF((N2S.EQ.7).OR.(N2S.EQ.8)) THEN
NADJS = N2S+1
ELSEIF(N2S.EQ.17) THEN
NADJS = N2S-1
ELSEIF(N2S.EQ.16) THEN
NADJS = N2S-3
ENDIF

CALL LENGTH(UBNAME(NADJS),20,NUMCHA)
CALL IPREC(UBNAME(NADJS)(1:NUMCHA),'BLOCK','CENTERS',IPT,
&ILEN,JLEN,KLEN,CWORK,IWORK)

DO JADJ=JLEN,1,-1
INODEP=IP(ISTART,JADJ,KSTART)
INODES=IPNODN(INODEP,5)

IF(SCAL(INODES,1,ISCVF).LE.(0.1)) THEN
ISFLAG=ISFLAG+1
IF(ISFLAG.EQ.1) THEN
YS=0.5*(YP(INODEP)+YP(INODES))
GOTO 4000
ENDIF
ENDIF

END DO

C REPLACE BLOCK NUMBER WITH ADJACENT BLOCK NUMBER AND CONTINUE
N2S = NADJS
KITERS=KITERS+1

C END DO-WHILE LOOP
END DO

ENDIF
END DO

4000 CONTINUE

C ----- CALCULATE THE THREE MIXED-FLUID THICKNESSES LOCALLY

SCAL(INODE,1,ISCMX)=(XE-XW)
SCAL(INODE,1,ISCMY)=(YN-YS)
SCAL(INODE,1,ISCMZ)=0.0

C --- ENDIF FOR LOCAL VOLUME FRACTION CHECK
ENDIF

END DO
END DO
END DO
END DO
C*****

```

Following the determination of the mixed fluid thickness in each coordinate direction, the gradient Richardson number is calculated in each computational cell. Here, the density and velocity gradients are determined using subroutine UGRDNT, and the boundary specifiers, given by USRD CELLID, determine whether a one-sided difference should be used for cells adjacent to a boundary or patch (e.g. a wall).

```

C*****
C***** CALCULATE THE GRADIENT RICHARDSON NUMBER *****
C*****

C LOOP OVER ALL THE BLOCKS
  DO N=1,UNB

C GET THE THREE DIMENSIONAL ADDRESSES OF THE CELLS
  CALL LENGTH(UBNAME(N),20,NUMCHA)
  CALL IPREC(UBNAME(N)(1:NUMCHA),'BLOCK','CENTERS',IPT,ILEN,JLEN,
&KLEN,CWORK,IWORK)

  DO K=1,KLEN
  DO I=1,ILEN
  DO J=1,JLEN

    INODE = IP(I,J,K)
    INODEH = IP(I,J+1,K)
    INODEL = IP(I,J-1,K)
    INODES = IPNODN(INODE,5)           !CFX NUMBER FOR SOUTH NODE
    INODEN = IPNODN(INODE,2)           !CFX NUMBER FOR NORTH NODE
    IFACES = IPFACN(INODE,5)           !CFX NUMBER FOR THE SOUTH FACE
    UWGTS = WFACT(IFACES)               !THE SOUTH INTERPOLATING FACTOR
    IFACEN = IPFACN(INODE,2)           !CFX NUMBER FOR THE NORTH FACE
    UWGTN = WFACT(IFACEN)               !THE NORTH INTERPOLATING FACTOR
    UBCSP = INT(SCAL(INODE,1,ISCCI))    !THE BOUNDARY SPECIFIER

C CALCULATE THE U,W, DENSITY GRADIENTS IN THE Y-DIRECTION

C DERIVATIVE FOR AN AVERAGE CELL
  IF(UBCSP.EQ.1) THEN
    CALL UGRDNT(U(INODE,1),U(INODEN,1),U(INODES,1),YP(INODE),
& YP(INODEN),YP(INODES),UWGTN,UWGTS,UDUDY)
    CALL UGRDNT(W(INODE,1),W(INODEN,1),W(INODES,1),YP(INODE),
& YP(INODEN),YP(INODES),UWGTN,UWGTS,UDWDY)
    CALL UGRDNT(DEN(INODE,1),DEN(INODEN,1),DEN(INODES,1),YP(INODE),
& YP(INODEN),YP(INODES),UWGTN,UWGTS,UDRDY)

C DERIVATIVE FOR A CELL THAT IS NEXT TO A HIGH WALL OR BOUNDARY
  ELSEIF((UBCSP.EQ.2).OR.(UBCSP.EQ.4)) THEN
    CALL UGRDNT(U(INODE,1),U(INODE,1),U(INODES,1),YP(INODE),
& YP(INODE),YP(INODES),UWGTN,UWGTS,UDUDY)
    CALL UGRDNT(W(INODE,1),W(INODE,1),W(INODES,1),YP(INODE),
& YP(INODE),YP(INODES),UWGTN,UWGTS,UDWDY)
    CALL UGRDNT(DEN(INODE,1),DEN(INODE,1),DEN(INODES,1),YP(INODE),
& YP(INODE),YP(INODES),UWGTN,UWGTS,UDRDY)

```

```

C DERIVATIVE FOR A CELL THAT IS NEXT TO A LOW WALL OR BOUNDARY
  ELSEIF((UBCSP.EQ.3).OR.(UBCSP.EQ.5)) THEN
    CALL UGRDNT(U(INODE,1),U(INODEN,1),U(INODE,1),YP(INODE),
&  YP(INODEN),YP(INODE),UWGTN,UWGTS,UDUDY)
    CALL UGRDNT(W(INODE,1),W(INODEN,1),W(INODE,1),YP(INODE),
&  YP(INODEN),YP(INODE),UWGTN,UWGTS,UDWDY)
    CALL UGRDNT(DEN(INODE,1),DEN(INODEN,1),DEN(INODE,1),YP(INODE),
&  YP(INODEN),YP(INODE),UWGTN,UWGTS,UDRDY)
    END IF

C CALCULATE THE GRADIENT RICHARDSON NUMBER
  UBUOY=-9.81/MAX(URHOF,DEN(INODE,1))
  UNUMO=(UBUOY*UDRDY)
  UDENO=MAX(1E-6,((UDUDY*UDUDY)+(UDWDY*UDWDY)))
  SCAL(INODE,1,ISCGR)=MIN(15.0,MAX(0.000001,(UNUMO/UDENO)))

  END DO
  END DO
  END DO
  END DO

```

The next portion is for the actual calculation of the droplet diameter in each cell based on the value of the gradient Richardson number and using the appropriate length scales. This is done as follows:

```

C*****
C***** CALCULATE THE DROPLET DIAMETER *****
C*****

  DO N=1,UNB

    CALL LENGTH(UBNAME(N),20,NUMCHA)
    CALL IPREC(UBNAME(N)(1:NUMCHA),'BLOCK','CENTERS',IPT,ILEN,JLEN,
&KLEN,CWORK,IWORK)

    DO K=1,KLEN
      DO I=1,ILEN
        DO J=1,JLEN

          INODE = IP(I,J,K)

          IF(SCAL(INODE,1,ISCVF).LE.(0.00001)) THEN
            SCAL(INODE,1,ISCDP) = 0.0
          ELSEIF(SCAL(INODE,1,ISCVF).GT.(0.00001)) THEN
C----- DETERMINE THE APPROPRIATE CHARACTERISTIC LENGTH SCALE

            UTURB=(TE(INODE,1)**(3/2))/MAX(ED(INODE,1),1E-10)
            DMX=SCAL(INODE,1,ISCMX)
            DMY=SCAL(INODE,1,ISCMY)
            DMZ=SCAL(INODE,1,ISCMZ)
            DWALL=SCAL(INODE,1,ISCDW)
            UDMMAX=MAX(DMX,DMY,DMZ)
            IF(UDMMAX.EQ.0) THEN

```

```

        IF (TE ( INODE , 1 ) . EQ . 0 ) UCHLEN = DWALL
        IF (TE ( INODE , 1 ) . GT . 0 ) UCHLEN = MIN ( UTURB , DWALL )
ELSEIF ( UDMMAX . GT . 0 ) THEN
    DMMIN = MIN ( DMX , DMY , DMZ )
    IF ( DMMIN . GT . 0 ) THEN
        IF (TE ( INODE , 1 ) . EQ . 0 ) UCHLEN = MIN ( DMMIN , DWALL )
        IF (TE ( INODE , 1 ) . GT . 0 ) UCHLEN = MIN ( DMMIN , UTURB , DWALL )
    ELSEIF ( DMMIN . EQ . 0 ) THEN
        IF ( DMX . EQ . 0 ) THEN
            MINX = MIN ( DMY , DMZ )
            IF ( MINX . EQ . 0 ) UDMMIN = MAX ( DMY , DMZ )
            IF ( MINX . GT . 0 ) UDMMIN = MINX
        ELSEIF ( DMY . EQ . 0 ) THEN
            MINY = MIN ( DMX , DMZ )
            IF ( MINY . EQ . 0 ) UDMMIN = MAX ( DMX , DMZ )
            IF ( MINY . GT . 0 ) UDMMIN = MINY
        ELSEIF ( DMZ . EQ . 0 ) THEN
            MINZ = MIN ( DMX , DMY )
            IF ( MINZ . EQ . 0 ) UDMMIN = MAX ( DMX , DMY )
            IF ( MINZ . GT . 0 ) UDMMIN = MINZ
        ENDIF
    IF (TE ( INODE , 1 ) . EQ . 0 ) UCHLEN = MIN ( UDMMIN , DWALL )
    IF (TE ( INODE , 1 ) . GT . 0 ) UCHLEN = MIN ( UDMMIN , UTURB , DWALL )
    ENDIF
ENDIF
ENDIF

C-----
C ----- DROP DIAMETER CALCULATIONS -----

        IF ( SCAL ( INODE , 1 , ISCGR ) . LE . ( 0 . 2 ) ) THEN
            CONST = 4 . 0 * ( ( 1 - SCAL ( INODE , 1 , ISCVF ) ) ** 0 . 1 )
            UDPCALC = CONST * ( TE ( INODE , 1 ) ** ( 3 / 2 ) ) / MAX ( ED ( INODE , 1 ) ,
1E-10)
            SCAL ( INODE , 1 , ISCDP ) = MIN ( UDPCALC , ( 0 . 5 * DMY ) , DWALL )

        ELSEIF ( SCAL ( INODE , 1 , ISCGR ) . GT . ( 0 . 2 ) . AND .
&SCAL ( INODE , 1 , ISCGR ) . LE . ( 7 . 5 ) ) THEN
            CONST = 15 . 0 * ( ( 1 - SCAL ( INODE , 1 , ISCVF ) ) ** 0 . 1 )
            UDPCALC = CONST * UCHLEN * ( SCAL ( INODE , 1 , ISCGR ) ** ( 0 . 89 ) )
            SCAL ( INODE , 1 , ISCDP ) = MIN ( UDPCALC , ( 0 . 5 * DMY ) , DWALL )

        ELSEIF ( SCAL ( INODE , 1 , ISCGR ) . GT . ( 7 . 5 ) ) THEN
            SCAL ( INODE , 1 , ISCDP ) = 0 . 0
        ENDIF
    ENDIF

    END DO
    END DO
    END DO
    END DO

```

If the flag to use the droplet model has not been set, then the scalar array for the droplet diameter is filled using the constant average value set in UBCND, UDIAP.

```

C*****
C***** CONSTANT AVERAGE DROPLET DIAMETER *****
C*****

C IF FLAG NOT SET THEN USE CONSTANT, AVERAGE DROPLET DIAMETER
  ELSEIF(UDYNM.EQ.0) THEN

    DO N=1,UNB
      CALL LENGTH(UBNAME(N),20,NUMCHA)
      CALL IPREC(UBNAME(N)(1:NUMCHA),'BLOCK','CENTERS',IPT,ILEN,JLEN,
&KLEN,CWORK,IWORK)

      DO K=1,KLEN
        DO I=1,ILEN
          DO J=1,JLEN

            INODE = IP(I,J,K)
            SCAL(INODE,1,ISCDP) = UDIAP

          END DO
        END DO
      END DO
    END DO

C ENDIF FOR FLAG TO USE DYNAMIC DROPLET DIAMETER
  ENDIF

C*****

```

The next portion of CFX subroutine USRSRC is for setting the source terms in the scalar transport equation, which is a function of the slip velocity. Here, the slip velocity is given by

$$u_s = (1 - r_a)^m \cdot u_\infty$$

where u_∞ is the terminal velocity for a single particle in an infinite medium, given by

$$u_\infty = \left(\frac{4gd_p}{3C_D} \right)^{1/2} \left(\frac{\Delta \mathbf{r}}{\mathbf{r}_w} \right)^{1/2}$$

and the drag coefficient is given by

$$C_D = \frac{18}{\text{Re}_p^{0.6}}$$

as discussed in Section 3.3. Then, the source term that appears in the scalar transport equation is given by

$$S = -\frac{\partial}{\partial x_i} \left[\frac{\mathbf{r}_a \mathbf{f}(1-\mathbf{f})}{\mathbf{f} + R(1-\mathbf{f})} u_s \right]$$

where $R = \rho_\alpha/\rho_\beta$ represents the ratio of the unmixed phase densities.

One note should be made here concerning the boundedness of the volume fraction as it relates to the slip velocity in setting the scalar source term. It was found that the formulation given by

$$S|_s = \text{Min} \left[\text{Max}(S|_s, 0.0), \mathbf{b} \frac{\mathbf{r}_i V_i (1-\mathbf{f}_i)}{\Delta t A_s \mathbf{f}_s}, \mathbf{b} \frac{\mathbf{r}_{i-1} V_{i-1} (\mathbf{f}_{i-1})}{\Delta t A_s \mathbf{f}_s} \right]$$

$$S|_n = \text{Min} \left[\text{Max}(S|_n, 0.0), \mathbf{b} \frac{\mathbf{r}_{i+1} V_{i+1} (\mathbf{f}_{i+1})}{\Delta t A_n \mathbf{f}_n}, \mathbf{b} \frac{\mathbf{r}_i V_i (1-\mathbf{f}_i)}{\Delta t A_n \mathbf{f}_n} \right]$$

is very useful in ensuring boundedness by allowing any values of the scalar, ϕ , above one or less than zero to be corrected during the course of the outer iterations in the solver. Essentially, this is a physical limitation, which dictates that the active cell cannot donate more scalar than it has to an adjacent cell, and that the adjacent cell cannot receive more scalar than it can displace. The extent to which this limitation is enforced is determined by the boundedness parameter, β (e.g. $\beta=0.9$ means only 90% of the total fuel volume in the active cell can be donated, or 90% of the total water volume in the adjacent cell can be displaced).

The nomenclature used above is as follows: V is the cell volume, A is the area normal to the slip velocity, ϕ is the scalar, Δt is the time step used in the discretization, and β is the boundedness parameter that the user sets as USBND in UBCND. Subscripts s and n refer to the south and north faces on a control cell and the subscript i refers to the cell in question, with $i+1$ indicating a cell located above cell i and $i-1$ indicating a cell below cell i . The subscript m refers to the mixture, and the subscript β refers to the heavy phase (i.e. the water). It can be seen that the correction provided by these equations is conservative in that it can only spatially redistribute the scalar, not destroy or produce it.

Another issue that may be of some concern to the user involves how the flux due to the slip velocity is calculated in the vertical direction when the grids are non-orthogonal. The solution to this problem is facilitated by the fact that CFX stores the three area components on each of the six faces. Hence when the flux due to the slip velocity is calculated in the vertical direction, only the area component normal to the vertical direction is used.

It should also be mentioned that if the user wants to set different relationships for the slip velocity it should be done in the following loop where the source terms are set in the scalar transport equation.

```

C*****
C***** SFST MODELS *****
C*****

C SET SOURCE TERMS IF FLAGS HAVE BEEN SET AND IF EQUATION IS BEING
SOLVED
  IF ( ((USFST.EQ.1).AND.(CALIAS.EQ.'SCALAR PHI'))
    & .OR. ((UKEPS.EQ.1).AND.(CALIAS.EQ.'K'
    & .OR. ((UKEPS.EQ.1).AND.(CALIAS.EQ.'EPSILON' )) ) THEN

C*****
C***** SCALAR EQUATION SOURCE TERM *****
C*****

      IF((CALIAS.EQ.'SCALAR PHI').AND.(NITER.GE.USADD)) THEN
C START THE LOOP OVER ALL THE BLOCKS

      DO N=1,UNB
      CALL LENGTH(UBNAME(N),20,NUMCHA)
      CALL IPREC(UBNAME(N)(1:NUMCHA),'BLOCK','CENTERS',IPT,ILEN,JLEN,
&KLEN,CWORK,IWORK)

      DO K = 1, KLEN
      DO J = 1, JLEN
      DO I = 1, ILEN

      INODE = IP(I,J,K)
      INODES = IPNODN(INODE,5)
      INODEN = IPNODN(INODE,2)
      UBCSP = INT(SCAL(INODE,1,ISCCI))

C VERTICAL AREA AND INTERPOLATING FACTORS
      IFACES=IPFACN(INODE,5)           !THE SOUTH FACE
      USRAS=AREA(IFACES,2)           !THE SOUTH AREA
      UWGTS=WFACT(IFACES)           !THE SOUTH INTERPOLATING FACTOR
      IFACEN=IPFACN(INODE,2)        !THE NORTH FACE
      USRAN=AREA(IFACEN,2)          !THE NORTH AREA
      UWGTN=WFACT(IFACEN)           !THE NORTH INTERPOLATING FACTOR

C CALCULATE THE VALUES OF STUFF AT THE SOUTH FACE
      IF((UBCSP.EQ.1).OR.(UBCSP.EQ.2).OR.(UBCSP.EQ.4)) THEN
      !INTERPOLATE DROPLET DIAMETER
          UDIAPS=(1.-UWGTS)*SCAL(INODE,1,ISCDP)+
&          (UWGTS)*SCAL(INODES,1,ISCDP)

      !INTERPOLATE THE DENSITY AND SCALAR
          UTHETS = (1.-UWGTS)*SCAL(INODE,1,ISCAL)+
&          (UWGTS)*SCAL(INODES,1,ISCAL)
          UDENS = (1.-UWGTS)*DEN(INODE,1)+(UWGTS)*DEN(INODES,1)
          UVFS = (1.-UWGTS)*SCAL(INODE,1,ISCVF)+
&          (UWGTS)*SCAL(INODE,1,ISCVF)

      !SLIP VELOCITY
          IF(UDIAPS.LE.0.000001) THEN
          USLIPS=0.0
          ELSE

```

```

!CALCULATE THE TERMINAL VELOCITY
UCON1=(4*9.81*(UDIAPS**(1.6)))/(54*UVISW**(0.6))
UCON2=((URHOW-URHOF)/(URHOW**(0.4))
UTERM = (UCON1*UCON2)**(0.71429)

USLIPS = ((1-UVFS)**(UEXP1))*UTERM

        ENDIF
END IF

IF(UBCSP.EQ.5) THEN
!SET ZERO DERIVATIVE CONDITION IF BOUNDARY IS OUTLET OR INLET
        UDIAPS = SCAL(INODE,1,ISCDP)
        UTHETS = SCAL(INODE,1,ISCAL)
        UDENS = DEN(INODE,1)
        UVFS=SCAL(INODE,1,ISCVF)

!SLIP VELOCITY
        IF(UDIAPS.LE.0.000001) THEN
                USLIPS=0.0
        ELSE

!CALCULATE THE TERMINAL VELOCITY
UCON1=(4*9.81*(UDIAPS**(1.6)))/(54*UVISW**(0.6))
UCON2=((URHOW-URHOF)/(URHOW**(0.4))
UTERM = (UCON1*UCON2)**(0.71429)

USLIPS = ((1-UVFS)**(UEXP1))*UTERM

        ENDIF
END IF

IF((UBCSP.EQ.3).OR.(UBCSP.EQ.0)) THEN
!SET EQUAL TO ZERO IF BOUNDARY IS A WALL
UDIAPS=0.0
UTHETS=0.0
UDENS=0.0
USLIPS=0.0
END IF

C CALCULATE THE VALUES OF STUFF AT THE NORTH FACE
IF((UBCSP.EQ.1).OR.(UBCSP.EQ.3).OR.(UBCSP.EQ.5)) THEN
!INTERPOLATE DROPLET DIAMETER
UDIAPN=(1.UWGTN)*SCAL(INODE,1,ISCDP)+(UWGTN)*SCAL(INODEN,1,ISCDP)

!INTERPOLATE THE DEN AND SCALARS
UTHETN = (1.-UWGTN)*SCAL(INODE,1,ISCAL)+
&(UWGTN)*SCAL(INODEN,1,ISCAL)
UDENN = (1.-UWGTN)*DEN(INODE,1)+(UWGTN)*DEN(INODEN,1)
UVFN = (1.-UWGTN)*SCAL(INODE,1,ISCVF)+
&(UWGTN)*SCAL(INODE,1,ISCVF)

!INTERPLOLATE SLIP VELOCITY
        IF(UDIAPN.LE.0.000001) THEN
                USLIPN=0.0
        ELSE

```

```

!CALCULATE THE TERMINAL VELOCITY
UCON1=(4*9.81*(UDIAPN**(1.6)))/(54*UVISW**(0.6))
UCON2=((URHOW-URHOF)/(URHOW**(0.4)))
UTERM = (UCON1*UCON2)**(0.71429)

USLIPN = ((1-UVFN)**(UEXP1))*UTERM

        ENDIF
END IF

IF(UBCSP.EQ.4) THEN
    UDIAPN=SCAL(INODE,1,ISCDP)
    UTHETN = SCAL(INODE,1,ISCAL)
    UDENN = DEN(INODE,1)
    UVFN=SCAL(INODE,1,ISCVF)

!SLIP VELOCITY
    IF(UDIAPN.LE.0.000001) THEN
        USLIPN=0.0
    ELSE

!CALCULATE THE TERMINAL VELOCITY
        UCON1=(4*9.81*(UDIAPN**(1.6)))/(54*UVISW**(0.6))
        UCON2=((URHOW-URHOF)/(URHOW**(0.4)))
        UTERM = (UCON1*UCON2)**(0.71429)

        USLIPN = ((1-UVFN)**(UEXP1))*UTERM

                ENDIF
    END IF

    IF((UBCSP.EQ.2).OR.(UBCSP.EQ.0)) THEN
        UDIAPN=0.0
        UTHETN=0.0
        UDENN=0.0
        USLIPN=0.0
    END IF

C LIMIT THE SCALAR SOURCE TO GIVE BOUNDED VOLUME FRACTIONS
C SOUTH SOURCE
    IF((UBCSP.EQ.1).OR.(UBCSP.EQ.2).OR.(UBCSP.EQ.4)) THEN
        UCON1 = URHOF*UTHETS*(1-UTHETS)*USLIPS
        UCON2 = UTHETS+(URHOF/URHOW)*(1-UTHETS)
        USLS1=USRAS*(UCON1/UCON2)

        USLS2=USBND*DEN(INODE,1)*VOL(INODE)*(1.-SCAL(INODE,1,ISCAL))/(DT)
        USLS3=USBND*DEN(INODES,1)*VOL(INODES)*SCAL(INODES,1,ISCAL))/(DT)
        USSRC=MIN(USLS2,USLS3,MAX(0.0,USLS1))
    END IF

    IF(UBCSP.EQ.5) THEN
        UCON1 = URHOF*UTHETS*(1-UTHETS)*USLIPS
        UCON2 = UTHETS+(URHOF/URHOW)*(1-UTHETS)
        USLS1=USRAS*(UCON1/UCON2)

```

```

USLS2=USBND*DEN(INODE,1)*VOL(INODE)*(1.-SCAL(INODE,1,ISCAL))/(DT)
USSRC=MIN(USLS2,MAX(0.0,USLS1))
END IF

IF((UBCSP.EQ.3).OR.(UBCSP.EQ.0)) THEN
USSRC=0.0
END IF

C NORTH SOURCE
IF((UBCSP.EQ.1).OR.(UBCSP.EQ.3).OR.(UBCSP.EQ.5)) THEN
UCON1 = URHOF*UTHETN*(1-UTHETN)*USLIPN
UCON2 = UTHETN+(URHOF/URHOW)*(1-UTHETN)
USLN1=USRAS*(UCON1/UCON2)

USLN2=USBND*DEN(INODEN,1)*VOL(INODEN)*(1-
SCAL(INODEN,1,ISCAL))/(DT)
USLN3=USBND*DEN(INODE,1)*VOL(INODE)*SCAL(INODE,1,ISCAL))/(DT)
UNSRC=MIN(USLN2,USLN3,MAX(0.0,USLN1))
END IF

IF(UBCSP.EQ.4) THEN
UCON1 = URHOF*UTHETN*(1-UTHETN)*USLIPN
UCON2 = UTHETN+(URHOF/URHOW)*(1-UTHETN)
USLN1=USRAS*(UCON1/UCON2)

USLN3=USBND*DEN(INODE,1)*(VOL(INODE)*(SCAL(INODE,1,ISCAL)))/(DT)
UNSRC=MIN(USLN3,MAX(0.0,USLN1))
END IF

IF((UBCSP.EQ.2).OR.(UBCSP.EQ.0)) THEN
UNSRC=0.0
END IF

C CALCULATE AND SET THE SOURCE INTO THE CFX SOURCE ARRAY
USRCS=(USSRC-UNSRC)
SU(INODE,1)=SU(INODE,1)+USRCS

END DO
END DO
END DO

END DO

END IF

```

Following this, the source terms are set in the k and ϵ equations. These represent turbulent production/destruction due to buoyancy effects, and were discussed in Section 3.2.

```

C*****
C ***** K AND EPSILON SOURCE TERM *****
C*****

IF( ((CALIAS.EQ.'K').AND.(NITER.GE.UTADD))
& .OR.((CALIAS.EQ.'EPSILON').AND.(NITER.GE.UTADD))) THEN

```

```

C LOOP OVER THE CELLS
  DO N=1,UNB

    CALL LENGTH(UBNAME(N),20,NUMCHA)
    CALL IPREC(UBNAME(N)(1:NUMCHA),'BLOCK','CENTERS',IPT,ILEN,JLEN,
&KLEN,CWORK,IWORK)

    DO K = 1, KLEN
    DO J = 1, JLEN
    DO I = 1, ILEN

      INODE = IP(I,J,K)
      INODES = IPNODN(INODE,5)      !CFX NUMBER FOR SOUTH NODE
      INODEN = IPNODN(INODE,2)     !CFX NUMBER FOR NORTH NODE
      IFACE=IPFACN(INODE,5)        !CFX NUMBER FOR THE SOUTH FACE
      UWGTS=WFACT(IFACE)           !THE SOUTH INTERPOLATING FACTOR
      IFACE=IPFACN(INODE,2)        !CFX NUMBER FOR THE NORTH FACE
      UWGTN=WFACT(IFACE)           !THE NORTH INTERPOLATING FACTOR
      UBCSP = INT(SCAL(INODE,1,ISCCI))

C CALCULATE THE DENSITY DERIVATIVE IN THE VERTICAL DIRECTION
      !DERIVATIVE FOR AN AVERAGE CELL
      IF(UBCSP.EQ.1) THEN
        CALL UGRDNT(DEN(INODE,1),DEN(INODEN,1),DEN(INODES,1),
& YP(INODE),YP(INODEN),YP(INODES),UWGTN,UWGTS,UDRDY)
        END IF

        !DERIVATIVE FOR A CELL THAT IS NEXT TO A HIGH WALL OR BOUNDARY
        IF((UBCSP.EQ.2).OR.(UBCSP.EQ.4)) THEN
          CALL UGRDNT(DEN(INODE,1),DEN(INODE,1),DEN(INODES,1),
& YP(INODE),YP(INODEN),YP(INODES),UWGTN,UWGTS,UDRDY)
          END IF

          !DERIVATIVE FOR A CELL THAT IS NEXT TO A LOW WALL OR BOUNDARY
          IF((UBCSP.EQ.3).OR.(UBCSP.EQ.5)) THEN
            CALL UGRDNT(DEN(INODE,1),DEN(INODEN,1),DEN(INODE,1),
& YP(INODE),YP(INODEN),YP(INODES),UWGTN,UWGTS,UDRDY)
            END IF

C CALCULATE THE K AND EPSILON SOURCE TERMS
            UVIS = VIS(INODE,1)
            UDEN = MAX(URHOF,MIN(URHOW,DEN(INODE,1)))
            UTE = TE(INODE,1)
            UEPS = ED(INODE,1)

C AVOID DIVIDING BY ZERO (ASSUME IF K IS VERY SMALL EPSILON IS VERY
SMALL)
            IF(UTE.GT.0.000001) THEN
              UEOK = UEPS/UTE
            END IF
            IF(UTE.LT.0.000001) THEN
              UEOK = 1.0
            END IF

C CALCULATE K SOURCE (UNITS ARE (KG M^2/S^2)/S )
            USRCK = UVIS*9.81*UDRDY/(UTPN*UDEN)

```

```

C LIMIT K SUCH THAT SOURCE CANNOT REMOVE MORE RHO*K FROM A CELL THAN 75
PERCENT
  USRCKL = -0.75*UTE*UDEN/DT
  USRCK = MAX(USRCKL,USRCK)

C CALCULATE EPSILON SOURCE (UNITS ARE (KG M^2/S^3)/S )
  USRCE = 1.44*UEOK*(MAX(0.0,USRCK))

C SET THE SOURCE IN THE K EQUATION
  IF((CALIAS.EQ.'K').AND.(NITER.GE.UTADD)) THEN
    SU(INODE,1) = SU(INODE,1) + USRCK*VOL(INODE)
  END IF

C SET THE SOURCE IN THE EPSILON EQUATION
  IF((CALIAS.EQ.'EPSILON').AND.(NITER.GE.UTADD)) THEN
    SU(INODE,1) = SU(INODE,1) + USRCE*VOL(INODE)
  END IF

  END DO
  END DO
  END DO

  END DO

  END IF

C*****
C***** END THE IF STATEMENTS TO SET THE SOURCES *****
C*****
  END IF

C*****
C***** END OF SOURCE TERMS *****
C*****

```

This completes the implementation of the SFST and DFE models. Further details concerning the different arrays and utility routines used can be found in the CFX Users Manual [12].

Appendix C: Details on Shear Flow Data Reduction Program

To acquire the appropriate data for the various plots from the shear flow simulations, a data reduction program was written by Matthew Umbel [37]. This program was then modified to account for the altered definition of the mixed fluid thickness as discussed previously in Section 6.3. For each simulation performed, an output file was generated directly from CFX-4 that contained vertical line data for the volume fraction, density and streamwise velocity for each horizontal position as specified in subroutine UBCND. Recall that in UBCND, the user specifies the *i* index location to begin writing the data, the final location, and the total number of dumps (see Appendix B.3.3).

After the simulation has finished, the output file generated by CFX is modified to include certain specifications at the beginning of the file. They are added to the file in list format in the following form:

```
1 fuel density (kg/m3)
2 water density (kg/m3)
3 fuel inlet flowrate (gpm)
4 water inlet flowrate (gpm)
5 height of lower layer (m)
6 height of upper layer (m)
7 width of test apparatus (m)
8 horizontal length over which shearing takes place (m)
9 height of test apparatus at shear flow section (m)
10 mean droplet size (m)
11 number of vertical sets of data
12 number of points in each set of data
13 LOW VALUE OF Y TO BEGIN CALCULATING PARAMETERS AT
14 HIGH VALUE OF Y TO BEGIN CALCULATING PARAMETERS AT
15 LOW VALUE OF X IN PERCENT TO BEGIN CALCULATING PARAMETERS AT
16 HIGH VALUE OF X IN PERCENT TO BEGIN CALCULATING PARAMETERS AT
```

Following this one time list, the *x*-location of each vertical profile is written, followed by columns containing the mixture density, volume fraction, vertical location, and streamwise velocity. The data reduction program then reads in all of the relevant information at each streamwise location, and performs several calculations to determine the important parameters, and then output each in a data file in a format readable by TECPLOT, which was used to generate the plots. At each *x*-location, the program calculates the interfacial thickness (defined as the distance between where the volume fraction is 0.1 and 0.9), the mixed fluid thickness (here defined as the distance between where the volume fraction is 0.03 and 0.97, as discussed previously), the vertical location of the fluid interface, and the maximum gradient Richardson number. It also calculates the gradient Richardson number, density gradient, and streamwise velocity gradient as a function of *y* at each streamwise location.

The FORTRAN used to perform the data reduction is given below.

```

C*****
C***** THE KATZ DATA REDUCTION PROGRAM *****
C*****

C WRITTEN BY: MATTHEW ROBERT UMBEL
C DATE: 9/26/98

C MODIFIED: 9/8/99
C ALTERED DEFINITION OF THE MIXED FLUID THICKNESS: 0.03 - 0.97

C DECLARE VARIABLES
C RHOF:      FUEL DENSITY
C RHOW:      WATER DENSITY
C VELINF:    VELOCITY OF FUEL AT UPPER INLET
C VELINW:    VELOCITY OF WATER AT LOWER INLET
C HLOW:      HEIGHT OF LOWER INLET
C HHIGH:     HEIGHT OF UPPER INLET
C XSHOT:     LONGITUDINAL LOCATION OF DATA SET
C DELLOW:    Y LOCATION TO LOWER EDGE OF INTERFACIAL THICKNESS
C DELHI:     Y LOCATION TO UPPER EDGE OF INTERFACIAL THICKNESS
C HCLLOW:    Y LOCATION TO LOWER EDGE OF MIXED FLUID THICKNESS
C HCHI:      Y LOCATION TO UPPER EDGE OF MIXED FLUID THICKNESS
C HCLOW:     THICKNESS OF LOWER CONCENTRATION BOUNDARY LAYER
C HCHIGH:    THICKNESS OF UPPER CONCENTRATION BOUNDARY LAYER
C YINTER:    Y LOCATION TO CONCENTRATION INTERFACE
C YINTRV:    Y LOCATION TO VELOCITY INTERFACE
C NSHOT:     NUMBER OF VERTICAL SETS OF DATA
C NPOINT:    NUMBER OF POINTS IN EACH SET OF DATA
C DUDYMX:    MAXIMUM VELOCITY GRADIENT IN THE DATA
C HGT:       HEIGHT OF TEST APPARATUS AT SHEAR FLOW SECTION
C DEL:       INTERFACIAL THICKNESS
C DELM:      MIXED FLUID THICKNESS
C DELMA:     AVERAGE MIXED FLUID THICKNESS
C QINF:      FUEL INLET FLOWRATE
C QINW:      WATER INLET FLOWRATE
C BUOYA:     BUOYANCY PARAMETER
C WIDT:      WIDTH OF TEST APPARATUS
C DP:        DROPLET SIZE
C LSHEAR:    HORIZONTAL LENGTH OVER WHICH SHEARING TOOK PLACE
C YLOW:      LOW VALUE OF Y TO BEGIN CALCULATING PARAMETERS AT
C YHIGH:     HIGH VALUE OF Y TO BEGIN CALCULATING PARAMETERS AT
C XLOW:      LOW VALUE OF X IN PERCENT TO BEGIN CALCULATING PARAMETERS
C XHIGH:     HIGH VALUE OF X IN PERCENT TO BEGIN CALCULATING
PARAMETERS AT
C XCONC:     VARIABLE WITH NORMALIZED X VALUES
C DRDY:      DERIVATIVE OF DENSITY WRT VERTICAL
C DUDY:      DERIVATIVE OF U VELOCITY WRT VERTICAL
C DELI:      INTERFACIAL OFFSET
C GRMX:      MAXIMUM GRADIENT RICHARDSON NUMBER

C DECLARE THE REALS
      REAL RHOF,RHOW,VELINF,VELINW,HLOW,HHIGH,XSHOT,
&DELOW,DELHI,HCLOW,HCHIGH,HGT,HCLLOW,HCHI,DRDY,DUDY,
&DUDYMX,BUOYA,WIDT,DP,LSHEAR,RHO,FUELVF,Y,VEL,YG,GRICH,
&TEMPG,DEL,DELM,YINTER,YINTRV,DUMMY,XTOSTR,PERC,
&DELRHO,DELUVL,DELHGT,GRMX

```

```

C DECLARE INTEGERS
    INTEGER I , J , K , N , NSHOT , NPOINT , CNTRX , CNTRY

C DECLARE CHARACTERS
    CHARACTER*50 INSTRING

C DIMENSION ARRAYS
    DIMENSION RHO(300) , FUELVF(300) , Y(300) , VEL(300) , YG(300) , GRMX(300) ,
    &GRICH(300) , TEMPG(300) , DEL(300) , DELM(300) , YINTRV(300) ,
    &YINTER(300) , XCONC(300) , HCHIGH(300) , HCLOW(300) , DUDY(300) , DRDY(300)

C GET THE NAME OF THE INPUT FILE
    PRINT* , 'ENTER THE NAME OF THE INPUT FILE: '
    READ* , INSTRING

C OPEN THE INPUT FILE AND CREATE THE FILES FOR OUTPUT
    OPEN(10 , FILE=INSTRING , STATUS='OLD' )
    OPEN(11 , FILE='GRY.DAT' , STATUS='NEW' )
    OPEN(12 , FILE='GRMX.DAT' , STATUS='NEW' )
    OPEN(13 , FILE='DELX.DAT' , STATUS='NEW' )
    OPEN(14 , FILE='DELMX.DAT' , STATUS='NEW' )
    OPEN(15 , FILE='OUTPUT.TXT' , STATUS='NEW' )
    OPEN(16 , FILE='YINTR.DAT' , STATUS='NEW' )
    OPEN(17 , FILE='HCBL.DAT' , STATUS='NEW' )
    OPEN(18 , FILE='DUDY.DAT' , STATUS='NEW' )
    OPEN(19 , FILE='DRDY.DAT' , STATUS='NEW' )

C READ THE RELEVANT "ONE TIME" VARIABLES
    READ(10 , *) RHOF , RHOW , QINF , QINW , HLOW , HHIGH , WIDT , LSHEAR , HGT ,
    &DP , NSHOT , NPOINT , YLOW , YHIGH , XLOW , XHIGH

C CALCULATE INITIAL PARAMETERS
    BUOYA = 981.0*(RHOW-RHOF)/RHOF
    VELINW = 100.*(QINW * 1./15850.)/(HLOW *WIDT)
    VELINF = 100.*(QINF * 1./15850.)/(HHIGH*WIDT)
    HHIGH = HHIGH*100.0
    HLOW = HLOW*100.0
    WIDT = WIDT*100.0
    DP = DP*100.0
    LSHEAR = LSHEAR*100.0

    XTOSTR = 0.725
    CNTRX = 0
    CNTRY = 0

C WRITE THE RELEVANT ONE TIME PARAMETERS TO THE OUTPUT FILE
    WRITE(15,99)'INPUT FILE NAME: ' , INSTRING
    WRITE(15,100)' '
    WRITE(15,101)'FUEL DENSITY (KG/M^3)           = ' , RHOF
    WRITE(15,101)'WATER DENSITY (KG/M^3)         = ' , RHOW
    WRITE(15,101)'FUEL INLET FLOWRATE (GPM)       = ' , QINF
    WRITE(15,101)'WATER INLET FLOWRATE (GPM)     = ' , QINW
    WRITE(15,101)'FUEL INLET VELOCITY (CM/S)     = ' , VELINF
    WRITE(15,101)'WATER INLET VELOCITY (CM/S)    = ' , VELINW
    WRITE(15,101)'FUEL INLET HEIGHT (CM)         = ' , HHIGH
    WRITE(15,101)'WATER INLET HEIGHT (CM)        = ' , HLOW
    WRITE(15,101)'HORIZONTAL SHEAR DOMAIN (CM)   = ' , LSHEAR

```

```

WRITE(15,101)'BUOYANCY (CM/S^2)           =', BUOYA
WRITE(15,101)'AVERAGE DROPLET SIZE (CM)   =', DP
WRITE(15,101)'LOWEST Y/H VALUE IN Y DOMAIN =', YLOW/HGT
WRITE(15,101)'HIGHEST Y/H VALUE IN Y DOMAIN =', YHIGH/HGT
WRITE(15,101)'LOWEST X/L VALUE IN X DOMAIN =', XLOW
WRITE(15,101)'HIGHEST X/L VALUE IN X DOMAIN =', XHIGH

C WRITE OUT THE HEADINGS TO TECPLOT FILE FOR VARIABLES THAT ARE F(X)
WRITE(11,100) 'VARIABLES="RIG", "Y" '
WRITE(12,100) 'VARIABLES="X/L", "RIGMAX" '
WRITE(12,100) 'ZONE T="MAX GRADRICH" '
WRITE(13,100) 'VARIABLES="X/L", "DEL" '
WRITE(13,100) 'ZONE T="DEL" '
WRITE(14,100) 'VARIABLES="X/L", "DELM" '
WRITE(14,100) 'ZONE T="MIXED THICKNESS" '
WRITE(16,100) 'VARIABLES="X/L", "YINTR", "YVELINTR" '
WRITE(16,100) 'ZONE T="INTERFACES" '
WRITE(17,100) 'VARIABLES="X/L", "HCLOW", "HCHIGH" '
WRITE(17,100) 'ZONE T="CONC BNDRY LAYERS" '
WRITE(18,100) 'VARIABLES="DUDY", "Y" '
WRITE(19,100) 'VARIABLES="DRDY", "Y" '

C ***** BEGIN LOOP TO READ IN SETS OF DATA *****
DO K=1,NSHOT
READ(10,*) XSHOT
READ(10,*) (RHO(I),FUELVF(I),Y(I),VEL(I),DUMMY, I=1,NPOINT)

PERC = 1.0 - (XSHOT-XTOSTR)*100.0/LSHEAR

C IF THE X VALUE IS IN RANGE BEGIN CALCULATIONS
IF( (PERC.GE.XLOW).AND.(PERC.LE.XHIGH) ) THEN
CNTRX=CNTRX+1
XCONC(CNTRX) = PERC
CNTRY=0

C ***** BEGIN THE 1ST LOOP OVER THE VERTICAL DATA *****
DO J=1,NPOINT

C IF THE Y VALUE IS IN RANGE BEGIN CALCULATIONS
IF( (Y(J).GE.YLOW).AND.(Y(J).LE.YHIGH) ) THEN
CNTRY=CNTRY+1

C FIND THE Y LOCATION TO THE LOWER EDGE OF THE INTERFACIAL THICKNESS
IF((FUELVF(J).LT.0.1).AND.(FUELVF(J+1).GT.0.1)) THEN
CALL INTRPL(Y(J+1),Y(J),FUELVF(J+1),FUELVF(J),0.1,DELLOW)
END IF
C FIND THE Y LOCATION TO THE UPPER EDGE OF THE INTERFACIAL THICKNESS
IF((FUELVF(J).LT.0.9).AND.(FUELVF(J+1).GT.0.9)) THEN
CALL INTRPL(Y(J+1),Y(J),FUELVF(J+1),FUELVF(J),0.9,DELHI)
END IF
C USE VALUES TO FIND Y LOCATION OF INTERFACE AND INTERFACIAL THICKNESS
YINTER(CNTRX)=100.0*(DELOW + 0.5*(DELHI-DELOW))
DEL(CNTRX) = 100.0*(DELHI-DELOW)

```

```

C FIND THE Y LOCATION TO THE LOWER EDGE OF THE CONC BOUNDARY LAYER
  IF((FUELVF(J).LT.0.03).AND.(FUELVF(J+1).GT.0.03)) THEN
    CALL INTRPL(Y(J+1),Y(J),FUELVF(J+1),FUELVF(J),0.03,HCLLOW)
  END IF
C FIND THE Y LOCATION TO THE UPPER EDGE OF THE CONC BOUNDARY LAYER
  IF((FUELVF(J).LT.0.97).AND.(FUELVF(J+1).GT.0.97)) THEN
    CALL INTRPL(Y(J+1),Y(J),FUELVF(J+1),FUELVF(J),0.97,HCHI)
  END IF
C USE VALUES TO FIND MIXED FLUID THICKNESS
  DELM(CNTRX)=100.0*(HCHI-HCLLOW)

C CALCULATE THE DENSITY AND VELOCITY GRADIENTS IN THE VERTICAL
DIRECTION

  DELRHO = RHO(J+1) - RHO(J-1)
  DELUVL = VEL(J+1) - VEL(J-1)
  DELHGT = Y(J+1) - Y(J-1)
  DRDY(CNTRY) = DELRHO/DELHGT
  DUDY(CNTRY) = DELUVL/DELHGT
  YG(CNTRY) = 100.0*(Y(J+1)+Y(J-1))*0.5

C FIND THE Y LOCATION OF THE VELOCITY INTERFACE (VEL=0.0)
  IF((VEL(J).LT.0.0).AND.(VEL(J+1).GT.0.0)) THEN
    CALL INTRPL(Y(J+1),Y(J),VEL(J+1),VEL(J),0.00,YINTRV(CNTRX))
    YINTRV(CNTRX)=100.0*YINTRV(CNTRX)
  END IF

C END THE IF SETTING THE BOUNDS ON THE Y RANGE
  END IF

C***** END THE 1ST LOOP OVER THE VERTICAL DATA *****
  END DO

C ***** BEGIN THE 2ND LOOP OVER THE VERTICAL DATA *****
C CALCULATE THE GRADIENT RICHARDSON NUMBER
  CNTRY=0
  DO J=1,NPOINT
C IF THE Y VALUE IS IN RANGE BEGIN CALCULATIONS
  IF( (Y(J).GE.YLOW).AND.(Y(J).LE.YHIGH) ) THEN
    CNTRY=CNTRY+1

    IF((Y(J).GT.HCLLOW).AND.(Y(J).LT.HCHI)) THEN
      TEMPG(CNTRY)=-9.81*DRDY(CNTRY)/(RHO(J)*DUDY(CNTRY)*DUDY(CNTRY))
    ELSE
      TEMPG(CNTRY)=0.0
    END IF

  END IF
  END DO
C***** END THE 2ND LOOP OVER THE VERTICAL DATA *****

```

```

C SMOOTH THE GRADIENT RICHARDSON NUMBER USING 1D DIFFUSION EQUATION
  DO J=2,CNTRY-1
    DY = 0.5*(YG(J+1)-YG(J-1))
    IF(J.EQ.2) DELTA=1.1*DY
    DELTA = MIN(DY,DELTA)
  END DO

  DT = 0.10*DELTA*DELTA

  DO N=1,5
    DO J=2,CNTRY-1
      DY = 0.5*(YG(J+1)-YG(J-1))
      GRICH(J) = (1. - 2.*DT/(DY*DY))*(TEMPG(J) )+
&      ( DT/(DY*DY) )*(TEMPG(J+1) + TEMPG(J-1) )
    END DO

    DO J=1,CNTRY
      TEMPG(J)=GRICH(J)
    END DO
  END DO

C DETERMINE THE SIZE OF THE CONCENTRATION BOUNDARY LAYERS
  HCHIGH(CNTRX) = 100.*HCHI - YINTER(CNTRX)
  HCLOW(CNTRX) = YINTER(CNTRX) - 100.*HCLLOW

C WRITE OUT THE HEADER TO TECPLOT FILE FOR GRICH,DUDY,DRDY AT X
LOCATIONS
  WRITE(11,105) 'ZONE T=" X/L = ',PERC,'"'
  WRITE(11,103) 'I=',CNTRY,',J=1,K=1,F=POINT'
  WRITE(18,105) 'ZONE T=" X/L = ',PERC,'"'
  WRITE(18,103) 'I=',CNTRY,',J=1,K=1,F=POINT'
  WRITE(19,105) 'ZONE T=" X/L = ',PERC,'"'
  WRITE(19,103) 'I=',CNTRY,',J=1,K=1,F=POINT'

C CALCULATE THE MAXIMUM DUDY AND WRITE THE F(Y) DATA TO FILE
  DUDYMX=0.0
  GRMX(CNTRX) = 0.0

  DO J=1,CNTRY
    WRITE(11,106) GRICH(J),YG(J)
    WRITE(18,106) DUDY(J),YG(J)
    WRITE(19,106) DRDY(J),YG(J)

    DUDYMX = MAX(DUDYMX,ABS(DUDY(J)))
    GRMX(CNTRX) = MAX(GRMX(CNTRX),ABS(GRICH(J)))
  END DO

C CALCULATE PARAMETERS THAT ARE COMBINATIONS OF OTHER PARAMETERS
  DELI = ABS(YINTER(CNTRX) - YINTRV(CNTRX))

C WRITE THE PARAMETERS TO THE OUTPUT FILE
  WRITE(15,100)' '
  WRITE(15,101)'X/L = ',PERC
  WRITE(15,101)'INTERFACE LOCATION (CM) = ',YINTER(CNTRX)
  WRITE(15,101)'VEL INTERFACE LOCATION (CM) = ',YINTRV(CNTRX)

```

```

WRITE(15,101)'INTERFACIAL OFFSET (CM)           = ',DELI
WRITE(15,101)'INTERFACIAL THICKNESS (CM)       = ',DEL(CNTRX)
WRITE(15,101)'MIXED LAYER THICKNESS (CM)      = ',DELM(CNTRX)
WRITE(15,101)'LOWER CONC BL THICKNESS (CM)    = ',HCLOW(CNTRX)
WRITE(15,101)'UPPER CONC BL THICKNESS (CM)    = ',HCHIGH(CNTRX)
WRITE(15,101)'MAXIMUM VELOCITY GRAD (1/S)     = ',DUDYMX
WRITE(15,101)'MAXIMUM GRADIENT RICHARDSON     = ',GRMX(CNTRX)

C*****END THE IF SETTING THE BOUNDS ON THE X RANGE*****
  END IF

C***** END THE DO LOOP OVER THE SETS OF DATA *****
  END DO

C WRITE OUT THE NUMBER OF SHOTS AND POINTS THAT DATA WAS CALCULATED
FROM
  WRITE(15,100)' '
  WRITE(15,102)'NSHOT                               = ', CNTRX
  WRITE(15,102)'NPOINT AT LAST DATA SHOT          = ', CNTRY
  WRITE(15,100)' '

C WRITE THE HEADERS TO THE TECPLOT FILE FOR THE PARAM(X) DATA
  WRITE(12,103) 'I=',CNTRX,',J=1,K=1,F=POINT'
  WRITE(13,103) 'I=',CNTRX,',J=1,K=1,F=POINT'
  WRITE(14,103) 'I=',CNTRX,',J=1,K=1,F=POINT'
  WRITE(16,103) 'I=',CNTRX,',J=1,K=1,F=POINT'
  WRITE(17,103) 'I=',CNTRX,',J=1,K=1,F=POINT'

C WRITE THE DATA TO THE TECPLOT OUTPUT FILES FOR PARAM(X) DATA
  DO I=1,CNTRX
    WRITE(12,106)XCONC(I),GRMX(I)
    WRITE(13,106)XCONC(I),DEL(I)
    WRITE(14,106)XCONC(I),DELM(I)
    WRITE(16,107)XCONC(I),YINTER(I),YINTRV(I)
    WRITE(17,107)XCONC(I),HCLOW(I),HCHIGH(I)
  END DO

99  FORMAT(A,A)
100 FORMAT(A)
101 FORMAT(A,F15.7)
102 FORMAT(A,I7)
103 FORMAT(A,I3,A)
104 FORMAT(A,F11.5,A)
105 FORMAT(A,F7.5,A)
106 FORMAT(F15.6,F15.7)
107 FORMAT(F15.6,F15.7,F15.7)

```

```

C END TO MAIN PROGRAM
  END

C*****
C***** SUBROUTINES *****
C*****

C DEFINE SUBROUTINE TO INTERPOLATE
  SUBROUTINE INTRPL(XH,XL,PHIH,PHIL,PHIX,X)

C DEFINE REAL STUFF
  REAL XH,XL,PHIH,PHIL,X,PHIX

  X = XL + (XH-XL)/(PHIH-PHIL)*(PHIX-PHIL)

  END

```